Risk Estimation of Rocking Components Subjected to Ground Motions



María García Espinosa

Linacre College

University of Oxford

A thesis submitted for the degree of

Doctor of Philosophy

Trinity Term 2018

Abstract

The behaviour of a rocking object has fascinated the scientific community for many years. This is partly because its study is applicable to a wide variety of structural and non-structural elements, i.e., hospital equipment, industrial technology, bridge piers or art preservation. Rocking motion typically occurs in objects that are unrestrained at their base and are disturbed from their equilibrium position. However, despite the intuitive nature of rocking motion, it is in fact a highly complex dynamic problem in which sliding, uplifting, geometry, material non linearities and impacts also affect the behaviour.

Understanding of the mechanisms that may lead to failure of rocking bodies is of significant importance to quantifying and minimizing the associated risk. The most common model to describe the rocking problem is the Inverted Pendulum Model, IPM, proposed by Housner in 1963, which has been followed by multiple researchers. However, the IPM explicit makes the assumption that the contact forces are concentrated at the edges. While this concept is usually true for bodies which physical feet at their edges, it is not valid for bodies which have a flat base.

Moreover, for reasons related to safety, characterizing the risk of these rocking elements subjected to ground motions is of increasing importance. Nonetheless, the mode of failure of these objects is mainly related to exceeding displacement or rotation limits. Consequently, several of the existing frameworks to estimate the risk may not be applicable. As a result, the survival of a rocking element during a ground motion is not a function of a single dominant frequency or the

peak amplitude of the input. Hence, the risk of rocking elements requires the generation of realistic inputs to subject to the deterministic models.

This thesis develops a suitable dynamic model for relaxing the previous assumption of the IPM. Its effect is discussed numerically and experimentally showing that the associated uncertainty propagates to the conclusion of whether a rocking body would survive or fail when subjected to a ground excitation.

Additionally, a study of the rocking response of artifacts subjected to sound induced vibration is presented. The effect of these sound vibrations using different instruments is illustrated through the stability of artifacts. Conclusions are drawn regarding whether the case or the music source should be selected to protect the museum artifacts and which kind of music affects more the stability of these objects.

Finally, the earthquake generation problem is examined. The novel technique of implementing rejection methods with earthquakes generated from the Karhunen-Loève expansion as well as an estimation of seismological properties from the accelerogram are developed. This work will then focus on generating ground records compatible with seismological and design characteristics for the purpose of generating probability of failure curves for rocking bodies. Based on these results and to directly compare with design requirements, an innovate technique to produce the probability of failure for a lifespan is proposed. Examples comparing earthquake generation models illustrate the nowadays most optimal method for rocking bodies.

Acknowledgements

My Ph.D has been one of the most significant academic challenger I have ever had to face. Without the support, patience and guidance of the following people, this study would not have been completed. It is therefore to them that I owe my deepest gratitude.

First of all, I would like to thanks to my supervisor Professor Manolis Chatzis and the financial support of the EC, FP7-PEOPLE-2013, Marie Curie, Career Integration Grant, 'RERCSGM', project number 618359 for provide me the opportunity to study in such a prestigious university as Oxford is. I also want to thank him for sharing his knowledge on the field and for his guidance and support throughout this thesis. Besides my advisor, I would like to thanks to Professor Andrew Smyth and Dr Raphael Greenbaum, for their commitment during my period in Columbia University, and to my internal examiners Professor Martin William and Professor Tony Blakeborough for their guidance during my years of research.

My always sincere gratitude also goes to Professor Pierfrancesco Cacciola who undertook to act as my Master dissertation advisor. His enthusiasm, happiness and commitment have been always a role mode for me. A great thanks also goes to Professor José Antonio Cabezas and Professor Pablo Moreno for their help, advice and knowledge through all my academic life.

Last thanks but no least, I would love to thank to my family. My parents, Dr Pablo and Isabel, who have always supported, encouraged and believed in me in all my endeavours. I could not do anything without them. My sisters and brother, Alicia, Sara and Pablete, who

have always supported me and cheering me up. Also to these little ones who always draw a smile on me, Marina and Gonzalo, and the future ones coming (Bosco and Alma). Finally, to my partner Pablo Zataraín who has been an essential pillar during these years.

Contents

1 Introduction **9**

1.1 Motivation 9

1.2 Literature review: Deterministic models 11

1.3 Literature review: Earthquake generation models 13

1.4 Dissertation Outline 17

Part I **20**

2 Examining the energy loss in the Inverted Pendulum Model **21**

2.1 Introduction 21

2.2 Model and Assumptions 22

2.2.1 Dynamic Model 22

2.2.2 Numerical Simulation. 28

2.3 Deterministic effect of λ on the stability of the body 29

2.4 Quantifying the Probability of Failure. 36

2.4.1 Probabilistic models for the effect of λ on the stability of the body. . . 36

2.4.2 Effect of the Uncertainty of λ in the estimate of the outcome. 39

2.5 Stability Analysis: Multiple-Pulses 42

2.6 Conclusions 46

3 Experimental investigation of the effect of base geometry on the response

of rocking bodies **48**

3.1 Introduction 48

3.2 Impulse distribution and base geometry 49

3.3 Experimental set up 54

3.4 Experimental investigation 58

3.5 Calibration of the IPM using the experimental results. 65

3.5.1 Probability of agreements 65

3.5.2 Bayesian updating 71

3.6 Discussion and conclusions 73

4 Examining the energy loss in systems of stacked rocking bodies **76**

4.1 Introduction 76

4.2 Model and assumptions 77

4.2.1 Dynamic model: Rocking patterns for two stacked blocks 77

4.2.2 Kinematics and equations of motion 79

4.2.3 Change of pattern without impact 81

4.2.4 Transitions between patterns with impact 84

4.2.5 Numerical Formulation 94

4.3 Stability diagrams 94

4.3.1 Change of pattern 96

4.3.2 Effect of λ_i 102

4.3.3 Effect of body dimensions. 106

4.4 Conclusions 110

5 Rocking response of artifacts subjected to sound induced vibrations **112**

5.1 Introduction 112

5.2 Classifications of motions of a body. 113

5.3 A review of sound induced vibration 115
5.4 Physical signal model 117
5.5 Analysis of Museums set up 118
5.6 Amplification factors 121
5.7 Effect of music notes on the stability of the body 123
5.7.1 Input of the model 123
5.7.2 Rigid case and cantilever shelf: $H(\omega) = 1$ 125
5.7.3 Flexible case and cantilever shelve: $H(\omega) \neq 1$ 126
5.7.4 Vibration mitigation 129
5.7.5 Slide-Rocking 131
5.8 Conclusions 132

Part II **134**

6 Review of existing earthquake generation models **135**

6.1 Introduction 135
6.2 Principal axes components 136
6.3 Stochastic process through a PSD 137
6.3.1 Kanai-Tajimi Clough-Penzien Spectrum 138
6.3.2 Spectral Representation Method 138
6.3.3 Spectrum matching 140
6.4 Hybrid approaches 142
6.4.1 Simulation of uniaxial ground motions 142
6.4.2 Simulation of biaxial ground motions 145
6.5 Data driven approach 146
6.6 Conclusion 149

7 KL expansion with a specified earthquake and site characteristics 150

7.1 Introduction 150

7.2 Estimation of M, R_{rup} and V_s 151

7.2.1 Strong motion database 152

7.2.2 Methodology to develop predictive equations 152

7.2.3 Empirical equations 154

7.3 Rejection Methods 157

7.3.1 Threshold method 158

7.3.2 Envelope distribution sampling method 160

7.4 Estimation of $\hat{\mathbb{M}}$ 163

7.5 Application of rejection methods 167

7.5.1 Threshold model for the selection of ground motions 167

7.5.2 Envelope distribution sampling method for the ground motions selection 170

7.6 Comparison between the envelope method and RK-N 174

7.6.1 Peak Ordinates and ρ_c 175

7.6.2 Elastic response spectrum 176

7.6.3 Temporal characteristics 179

7.6.4 Spectral characteristics 181

7.7 Conclusion 183

8 Seismic risk analysis of rocking bodies 185

8.1 Introduction 185

8.2 Planar response of a Rocking Body 186

8.3 Engineering risk seismic analysis 188

8.3.1 Probability of failure curves versus intensity measures 189

8.3.2 Probability of failure over a period of interest 189

8.3.3 Lifespan 191

8.3.4 Defining parameters α_g and β_g 192

8.4 Seismic risk evaluation 193

8.4.1 Probability of failure curves using stochastic models. 194

8.4.2 Probability of failure curves using hybrid approaches. 198

8.5 Conclusions 220

9 Conclusions and future work **224**

9.1 A summary of the conclusions 224

9.2 Future work 226

Appendices **228**

Nomenclature

Greek symbols and maths

$+$	After impact
$- \rightarrow +$	During impact
$-$	Before impact
α	Slenderness of the block
α_g	Gutenberg and Richter parameter
β	Angle between l and the side of the block
β'	Angle between l' and the side of the block
β_g	Gutenberg and Richter parameter
β_R	Vector of regression coefficients from RK-N model
χ	Random angle with respect of ψ
$\ddot{y}_g$	Vertical ground acceleration
$\ddot{\theta}$	Angular acceleration
$\ddot{x}_g$	Horizontal ground acceleration
δ	Standard deviation error
$\Delta\omega$	Sampling steps of ω
$\dot{\theta}$	Angular velocity
$\dot{x}$	Horizontal velocity
$\dot{y}$	Vertical velocity
$\dot{y}_d$	Vertical velocity of a point at a distance d
ε	Vector of regression coefficients
ε_μ	Relative mean error
η	Zero mean white noise errors
$\hat{}$	Refer to an estimate value
κ	Vector of regression coefficients from the estimation of M, R_{rup}, V_s

λ Distance from the post-impact corner to the centroid of a distribution

λ^* Point on the stability diagram belonging to the predefined region will fail

λ^*_{40}, λ^*_{60} values of λ^* that would correspond to a probability of failure of 40% and 60%

$\mathbb{A}$ Refers to any intensity measure

$\mathbb{F}^j_{x_i}$, $\mathbb{F}^j_{y_i}$ Force j applied to body i along the directions x and y

$\mathbb{K}$ Threshold value

$\mathbb{M}$ Vector containing physical characteristics of an earthquake

$\mathbb{M}^j_{G_i}$ Moment j applied to body i with respect to its centre of mass G_i

K Representation of a cycloidal pulse

$\mathscr{F}$ Refers to a selected predictive formula

$\mathscr{N}_\phi$ Multivariate Gaussian distribution

$\mathscr{N}_t$ Target Multivariate Gaussian distribution

$\mathscr{Q}$ Representation of a non-linear function

$\mathscr{S}_p$ Proposal probability distribution

μ Mean

μ_a Mean of the accepted distribution of the v_c

μ_f Coefficient of friction

μ_T Truncated mean

μ_t Mean of the target distribution of the v_c

μ_u Untruncated mean

ω Frequency

ω' Frequency of the filter

ω_f Filter frequency

ω_g Frequency of the ground

ω_n Natural frequency

ω_u Angular frequency

ω_{mid}	Middle frequency
Φ	Cumulative Density Function
ϕ	Probability Density Function
ϕ_b	Angle between axis x and I
Φ_N	Cumulative Density Function of the Normal Gaussian distribution
ϕ_N	Probability Density Function of the Normal Gaussian distribution
Φ_T	Cumulative Density Function of the truncated Gaussian distribution
ϕ_T	Probability Density Function of the truncated Gaussian distribution
Φ_U	Cumulative Density Function of the uniform distribution
ϕ_U	Probability Density Function of the uniform distribution
Ψ	Random phase angles
ψ	Rotational angle of ground motion components
ρ_c	Vector parameters
Σ	Covariance matrix
σ	Standard deviation
Σ_a	Covariance matrix of the accepted distribution of the v_c
Σ_e	Covariance matrix
Σ_t	Covariance matrix of the target distribution of the v_c
σ_T	Truncated standard deviation
σ_u	Untruncated standard deviation
τ	Random time
θ	Angular displacement
$\tilde{}$	Refer to a target value
ε_{KL}	Error of the model-KL
φ	Time modulation function
ρ	Correlation coefficient
ς_e	Coefficients of the KL expansion

ξ	Damping ratio
ξ_f	Filter damping
ξ_g	Damping of the soil
a	Refers to the PGA
a_1, a_2	Orthogonal horizontal components of ground acceleration
a_g	Design ground acceleration
$A_{c\omega}$	Acceleration of the case
$A_{g\omega}$	Relative acceleration output
B	Refers to the block
b	Half width
C	Constant of the envelope criterion
c	$1, 2, ..., 6$
c_p	Poison distribution parameter
C_E	Correlation coefficients
D	Threshold distance
d	Distance from the corner to f_y
d_1, d_2	Two random points at the base of the block
D_e	Eigenvalues
D_{5-95}	Effective duration of the record
E	Sum of two errors, ε_{KL} and S
E_χ	Uniaxial earthquake
e_c	Regression vector error
E_I	Major components of a biaxial input
E_l	Successive earthquakes occurring
E_{II}	Intermediate components of a biaxial input
E_{No}	Vector composed by the principal and intermediate component of the generated time histories

f_c	Frequency of the case
F_j	External force vector applied on a point at a vectorial distance r_j
f_r	Frequency of the rack
F_x	Horizontal D'Alembert force
f_x	Horizontal reaction of the ground
F_y	Vertical D'Alembert force
f_y	Vertical reaction of the ground
f_{xi}, f_{yi}	Tangential and normal interface forces occurring at interface i
G	Center of mass
$G(\omega)$	TK-CP PSD
h	Half base
$H(\omega)$	$H_1(\omega)H_2(\omega)$
$H^{\pm}_{i\to P_j}$	Angular momentum of body i with respect to point P_i
$H_1(\omega)$	Frequency response functions of the case
$H_2(\omega)$	Frequency response functions of the rack
I	Major component
i	$1,2,...$
I_0	Moment of inertia about one of the corners
I_a	Arias Intensity
I_G	Moment of inertia about the center of mass
II	Intermediate component
j	1,...,n_f
j_d	Impulse applied at d
J_x	Horizontal equivalent impulse
J_y	Vertical equivalent impulse
k	Refers to the earthquakes Kobe, Hachinohe, Northridge and EC-8
L	Evidence

l	Distance between 0_1 and 0_2
l'	Distance between 0_1 and $0_2^{'}$
L_M	Depth to the hypocenter measure from the epicenter
L_T	Value of interest for the lifespan
L_t	Lifespan variable
M	Magnitude of the seismic event
m	Mass of a single block
M_m	Mass of two blocks
M_{event}	Magnitude of a specific event
N	Data points that tends to infinity
n	Acceleration samples
N_c	Number of cycles of the pulse
n_e	Number of earthquakes that a block survives
N_F	Number of inputs that fail
n_f	Number of applied forces
N_I	Total number of impacts
N_M	Number of earthquakes greater than a magnitude
N_o	Number of synthetic earthquakes
N_S	Number of inputs that survive
N_T	Number of inputs
N_t	Number of failures that have occurred at a time t
o	$1, ..., N_o$
p	Maximum number of eigenvalues
P_F	Probability of failure
P_i	Points of application of the vertical impulse
P_M	Probability of surviving a magnitude
P_S	Probability of survival

$P_{E_{Bka}}(\lambda)$ Probability of agreement for a given earthquake, for a given PGA and for a given λ

$P_{E_{Bk}}(\lambda)$ Probability of agreement for a given earthquake for a given λ

p_s Air wave

$P_{TB}(\lambda)$ Probability of agreement for an assumed value of λ for all the earthquakes

q Index that corresponds to different runs of a given E_{Bka} and A^q_{Bka}

q_d Impulsive forces

Q_i Generalised force

R Distance from one corner to the center of the block

r Reduction of energy factor

R_e Utility function

r_j Vectorial distance

r_t Reduction of energy factor for stacked bodies

R_U Correlation matrix KL expansion

R_{rup} Distance to the area of rupture

S Total residuals

s $s_1 s_2$

S_0 Constant PSD

s_1 Air pressure constant

s_2 Distance constant

$S_{\theta_i}, S_\beta, S_l, H_{\theta i}$ Signum functions

S_{est} Residuals

T Period

t Time

T_k Kinetic energy

t_{mid} Time to the middle of the strong shaking phase

U Vector of length $2n$

u Dimension of Σ_e

u_0 Amplitude

$unif$ Sample from a uniform distribution

v_c Vector of auxiliary variables

V_e Eigenvectors

V_i Relative velocity to the ground of the center of mass of the block i

V_s Shear velocity

w Width

x Horizontal axis

x_c Displacement of the case

x_r Displacement of the rack

y Vertical axis

Abbreviations

CSM Concentrated Springs Model

DEM Discrete Element Method

DOF Degree of freedom

F Failure

FECO Block with feet at the corners

FLBA Block with a flat base

GV Gasparini and VanMarcke

IPM Inverted Pendulum Model

KL Karhunen-loeve expansion

KL-ER Case I Karhunen-loeve expansion with the Envelope model with three parameters

KL-ER Case II Karhunen-loeve expansion with the Envelope model with six parameters

KL-T Karhunen-loeve expansion with the Threshold model

KT-CP	Kanai-Tajimi Clough-Penzien
P	Probability
PGA	Peak Ground Acceleration
PGD	Peak Ground Displacement
PGV	Peak Ground Velocity
PSD	Spectral Density function
RK-N	Rezaeian and Der Kerughian
S	Survival
SF	Scaled factors
SRM	Spectral Representation Method
WM	Winkler Model

Chapter 1

Introduction

1.1 Motivation

A wide range of structural and non-structural elements are not fixed or bolted to their support medium as shown in Figure 1.1 and hence, they are free to experience large displacements and rotations, when subjected to ground motions. These objects may overall be characterized as rocking. Until recently, the rocking problem has been developed by using a number of simplifying assumptions such as sliding and uplifting are neglected. Nonetheless, the rocking problem is not as simple as it looks. It is a highly complex dynamic problem in which the materials and geometric properties also affect its behaviour.

Even the simplest case of planar rocking has been a challenge to the rocking community. For this modelling approach, the body and the base are usually considered to be rigid, the body rocks with respect to either of the corner points and a physical impact law is used to define the time instance at which the rocking corner changes. Because the model defines a pin at each corner, its dynamic model assumes that the contact forces are concentrated at the edges and that the body cannot slide and uplift. Nonetheless, in reality, rocking bodies can slide and uplift, the body and the base are deformable and the forces are not always concentrated at the corners, i.e., a body with a flat base.



Figure 1.1 – Some rocking bodies.

While sliding, uplifting and the deformability of the body and base can be minimised mechanically, distinguishing between different base geometries of the block is of extreme importance, because the behaviour of such elements during impacts is critical to their overall response. Thus, understanding the mechanisms behind the process that might produce failure (when the body topples) is the key to fully comprehending this phenomenon.

The impact occurs while the body rocks from one corner to the other. Therefore, during impact, the rigid body would experience an impulse distribution along its contact surfaces with an equivalent vertical impulse located at its centroid. This centroid could be anywhere and it directly affects the loss of energy. Thus, to accurately describe the rocking motion, the model should account for a random location of the vertical impulse.

Furthermore, natural hazards such earthquakes can produce detrimental effects on their performance during their life-cycles. The effect of these phenomena is a problem of significant importance in the stability of rocking bodies. Characterising the risk includes an ensemble of ground motions to generate probability of failure curves as well as a procedure to evaluate the risk in terms of lifespans. Hence, there is a need of finding suitable deterministic and stochastic models that allow for estimating the ground motion related risk of such objects.

However, not just earthquakes can cause the failure of rocking bodies. Nowadays, muse-

ums complain about their artifacts moving from theirs positions or even overturning. One reason could be the type of excitation that an artifact is subjected. The difference between the past and present museum is that these days, it seems to be common for museums to host music concerts. Therefore, a study of the rocking response of artifacts subjected to sound induced vibration is also needed to fully understand this phenomenon.

1.2 Literature review: Deterministic models

The first dynamic model, IPM, for rocking was suggested by Housner [1] in 1963 after the Chilean Earthquakes, where a number of slender structures survived, while apparently more stable structures were severely damaged. Housner modelled the response of rocking bodies as inverted pendulums of equivalent properties. For this modelling approach, several assumptions must be introduced: the body and the base are considered to be rigid, sliding and uplift are neglected, the response is planar and the loss of energy which only occurs during impacts is exclusively described by the dimensions of the body. The effects of some of the previous assumptions of the IPM [1] on the stability of rocking bodies have been studied by a series of authors.

An alternative formulation of the IPM model was developed by Prieto and Lourenzo [2] who assuming a finite interval for the impulse force, they unified the governing equations. Plaut et al. [3] defined the IPM model for symmetric and asymmetric blocks for a horizontal or tilted foundation. Ishiyama [4] created a numerical two Degree Of Freedom (DOF) model and classified the motion of a rigid body in rest, slide, slide rocking, translation jump and rotation jump. Shenton and Jones [5] improved the model of Ishiyama. Pompei et al. [6] formulated the criteria for the transition from rocking to sliding by an analytical approach for specific inputs. They demonstrated that neglecting sliding can lead to errors in the study of the rocking body. Experimentally, it was demonstrated by Lipscombe and Pellegrino [7] that the free rocking response of small aspect ratio bodies substantially depends on the uplifting

after each impact. Hence, the IPM does not fully describe the behaviour of such objects.

The deformability of the ground was relaxed by Psycharis and Jennings [8] who considered two foundation models: Winkler Model (WM) and Concentrate Spring Model (CSM). Both models have the property that the springs cannot be in tension and viscous damping is used. Thus, the dissipation of energy is achieved through vertical dampers and not through an Impact model. The model had 2DOF, vertical and rotational, however, sliding and uplift are neglected. Koh and Spanos [9] simulated a non-linear formulation of the equation of motion for the rocking and bouncing of the block on a WM. Also, the center point of the base is constrained horizontally. Hence, only small angles of rotation are allowed and only 2DOF are taken into account (vertical and rotational). Palmeri and Makris [10] proposed a model on viscoelastic foundation and Chatzis and Smyth [11] proposed two models in which the effects of geometric non-linearities, ground deformability, sliding and uplifting were included.

Some ancient structures built with rocking columns act as multiple rocking bodies where the columns are free to rock, slide or uplift. Allen et al. [12] were the first to address the dynamic behaviour of two stacked rigid prims. Spanos and Roussis [13] focused on the behaviour of two stacked rigid bodies. Kounadis et al. [14] also proposed a similar model with two rigid blocks in which a step by step solution was employed analytically in Mathematica. Makris and Vassiliou [15] studied the rocking response defined for an array of free- standing columns capped with a simply supported rigid beam. This study shows that the multibody system may be more stable when the supported beam is heavier. Papaloizou and Kromodromos [16] arrived to the same conclusion using Discrete Element Methods (DEM).

Zulli and Contento [17] developed a 3D extension of the IPM. The body and the base are rigid assuming no bouncing and sliding between them. They also introduce the eccentricity of the center of the mass. Chatzis and Smith [18] proposed an expansion of their 2D model developed in [11] to 3D. This model examined a rigid prism on a deformable base using a WM and a CSM in which geometric non-linearities are included. Moreover, sliding and uplifting

take part on the study creating a 6DOF system.

However, it is often claimed that the effect of these omitted phenomena can be minimized mechanically. For example, sliding may be minimized using a high friction material between the body and the base, while the effects of deformability are substantially smaller for relatively stiff materials for the body and the support medium, the chance of the body being in a free flight mode is reduced as it becomes more slender and assuming that all the excitations are horizontal, while the out of plane response of the body can be minimized if the perpendicular dimension of the base of the body, the length, is substantially greater to the dimension of the in plane dimension of the base, the width. Nevertheless, even if the effects of the previous phenomena are minimized, the IPM as introduced by Housner [1] makes an explicit assumption about the energy lost during impacts: the location of the vertical impulsive force generated during impact is assumed to be at the future rocking corner. Therefore, the angular momentum is conserved about this point.

Existing works in the literature have used alternative assumptions about the loss of energy during impacts: Kalliontzis et al. [19], Zhang et al. [20], Yim et al.[21], Dimitrakopoulos and DeJong [22], Voyagaki et al. [23], ElGawady et al [24]. These are usually expressed through the use of alternative values for the reduction of energy factor. While some of those works have attributed the use of different reduction factors to the effect of the ignored phenomena, i.e., sliding, uplift, deformability and the three-dimensional nature of the response, it should be noted that their inclusion would result in a substantially different dynamic behaviour including dynamic patterns that could not be predicted by the IPM for any assumed value of the reduction of energy factor.

1.3 Literature review: Earthquake generation models

A common objective of Earthquake Engineering is to predict the response of a structure subjected to a ground motion. In the case of rocking bodies, their stability while are subjected

to ground motions is a problem of significant importance, as for example observed by Nigbor et al. [25] in the Loma Prieta earthquake in 1989 where many art objects were damaged. The dynamic response of rocking elements during ground motions is strongly non-linear. These objects differ to standard structural systems in that their primary mode of failure is mainly associated to displacement- rather than stress- based criteria of failure, and that their response is mainly associated to rigid body rather than deformation modes. Consequently, several of the existing methodologies to study the risk associated to structures are not applicable, as they are usually focused on systems that are geometrically linear and whose failure is associated with fracture or yield. A remedy for this is to study the risk associated to rocking bodies using the more general approach of creating probability of failure curves.

Estimating the failure of rocking bodies subjected to ground motions requires the generation or selection of a reasonable number of earthquakes to accurately estimate the probability of failure and create probability of failure curves by varying an intensity measure. Hence, one of the key challenges in this problem is how these ground motions are produced. Studies of the response of rocking bodies subjected to cycloidal pulses have shown a series of interesting properties of the system as, for example, Shenton and Jones [5], Zhang and Makris [26] and Plaut and Virgin [3]. However, ground motions cannot in general be perfectly approximated with idealized pulses.

The ideal case is to use recorded earthquakes however, those, with the exception of few regions, cannot be found in abundance. Authors as Baker [27, 28] have developed models that select recorded earthquakes for a structure of interest. This selection is done by using a target resonance period of a linear system. However, rocking bodies do not have a resonance period and hence, this method is not applicable. In addition to the problem, once the selection is made, the amount of earthquakes is limited due to the small number of recorded earthquakes per area. In order to solve this problem, Jayaram et al. [29] presented a selection algorithm for matching a target response spectrum of a linear system. Nevertheless, scaling earthquakes

has a significant impact on the results of the dynamic analysis as explained by Shields [30]. The frequency characteristics of ground motions are in reality coupled with the intensity of the motion.

The limitations in the number of available recorded earthquakes can be alleviated through the generation of artificial motions. The methods to achieve so in the literature can be grouped into: stochastic, seismological, hybrid and data-driven models.

Commonly, stochastic models are formulated through the definition of the statistical properties of the underlying random process. A popular means of achieving so is through defining a Power Spectral Density function (PSD) such as the Kanai-Tajimi Clough Penzien (KT-CP) PSD [31]. Time histories can then be generated, for example by using the Spectral Representation method (SRM) presented by Shinozuka and Deodatis [32]. To account for the non-stationarity of the ground motions, a time modulation function defined by Jennings [33] is used. There are, however, methodologies that generate processes from a stochastic processes that are fully non stationary as, for example, Rezaeian and Der Kiureghian [34]. Such approaches result into models that are very easy to use but often hard to associate to physical or design quantities.

To alleviate this problem, there are other stochastic models that generate artificial earthquakes compatible with a design response spectrum such as Gasparini and Vanmarcke [35] and Cacciola and Deodatis [36]. The goal of such methods is to make sure that the response of each single time history matches the target spectrum. However, this is not true in nature. This disadvantage has minimal effects for linear systems as it dissipates all frequencies around the resonance frequency. In contrast, rocking bodies do not have a resonance period and all frequencies are equally important, in particular, low ones.

Seismological models such as Aki [37] and Brune [38] often focus in simulating the seismic wave and the wave propagation. These models provide a broad band of parameters for the generation of ground motions. Such parameters are based on the properties of the rupture

and the geometry between the fault and the studied location such as the magnitude, distance from the plane of the fault, depth of the hypocenter and the type of the movement along the fault surface. Examples of those are Miyake et al. [39], Ruiz et al. [40] and Mavroeidis and Papageorgiou [41]. Recently, seismological models have been successful in matching properties of large recorded earthquakes as presented by Aochi and Fukuyama [42] and Olsen et al. [43]. Such methods however also have a common property: frequently their outputs are not time histories, but response spectra ordinates. To produce the time histories necessary for studying a rocking system, one would need to use a model such as the one of Gasparini and Vanmarcke [35]. Therefore, all the disadvantages previously defined would also hold on these methods.

Hybrid approaches are based on a mixture of stochastic and seismological models. These methods relate site and earthquake characteristics to the model through regression analysis. Examples of those are: Rezaeian and Der Kiureghian [44], Pousse et al. [45], Sabetta and Plugiese [46], Vlachos et al. [47] and Alamilla et al. [48]. These approaches are enclosed to predefined equations which might not correspond to the underlying physical model, i.e., in Sabetta and Plugiese [46] there is an underestimation of the variability inherent in real ground motions for specific earthquake and site characteristics. For the stochastic part, these hybrid approaches assume modulation functions to address spectral and temporal characteristics of the excitation, which again might not correspond to the underlying physical model.

Contrasting with stochastic models, data driven approaches such as the KL expansion do not require the definition of a mathematical or stochastic model of the underlying process. Data-driven approaches allow enriching a set of recorded accelerograms as presented by Zentner and Poiron [49], Smyth and Masri [50] and Olivier and Smyth [51]. They feed a non-Gaussian probabilistic model with recorded earthquakes. However, since the generation is completely achieved through data, there are no physical checks on the method. Also, to utilize the method a good number of recorded motions has to be available.

Nonetheless, ground motions are a three dimensional (3D) phenomenon hence, it should be expected that the motion of the rocking bodies certainly includes 3D displacements and rotations. Therefore, defining the earthquake excitation in a 3D manner has the advantage of getting a more realistic response. A procedure to treat the concepts of principal axes in ground motions is presented by Penzien and Watabe [52].

Estimating the risk of rocking bodies not only requires the generation of a suitable number of time histories, but also the knowledge of the potential seismic activity of a region. A design engineer might have access to a design response spectrum, might know the seismicity of a region, or might have a number of real recorded earthquakes. In that sense, earthquake generation models can be also catalogued into three different groups depending on the information on the seismicity of a region that they use: in terms of design codes, seismological data or real recorded earthquakes. While real recorded earthquakes is probably the less feasible solution due to the lack of earthquakes per area, seismological data of the region can be obtained with models based on empirical data as the one presented by Abrahamson [53] and international seismic codes provide target response spectrum defined for linear systems such as Eurocode 8 and FEMA [54, 55]. Each of the earthquake generation models previously presented can be linked to one of these tools.

1.4 Dissertation Outline

The first part of this dissertation deals with the effect of the energy loss on the dynamic problem of rigid bodies. The second part deals with the characterization of the seismic risk of these elements.

In Chapter 2, the location of the equivalent impulse between the body and the ground is considered as a random variable with a related uncertainty. For this aim, a single body is simulated using the Inverted Pendulum Model (IPM) of [1]. The momentum equations are, therefore, reformulated. The IPM of [1] considers the reaction forces at the corners hence,

the vertical impulse is located there. However, it is of interest to experimentally proof that, indeed, for bodies with a flat base this location is further from the future rocking corner. It is the aim of Chapter 3 to show the effect that different base geometries produce in a rocking body with the description of the energy loss of the IPM. Experimental results are calibrated to find the optimal position of the vertical impulse for each body.

In Chapter 4, Chapter 2 is extended to the case of stacked bodies. Particularly, it studies the potential location of the vertical impulses at the interfaces between the two bodies and between the lower body and the ground for the different types of impacts occurring in this system. In both Chapter 2 and 4, the effect of this uncertainty is considered while subjecting the rocking systems to cycloidal pulses.

In Chapter 5, the behaviour of rocking bodies in museums while background music is played is presented. In this Chapter, the artifact is located in different set ups and stability diagrams illustrate which system or instrument provides the best performance.

In part II, to quantify the risk of rocking bodies, probability of failure curves are used. For this aim, there is a need of selecting or generating an ensemble of time histories. It is the purpose of Chapter 6 to summarize the most common earthquake generation and selection models in the literature. The advantages and disadvantages of each of them in terms of rocking bodies are explained. To alleviate these disadvantages the KL expansion which does not use any predefined model is proposed. In Chapter 7, two novel techniques are presented. First, since the KL expansion generates earthquakes without caring about their physical characteristics, a regression model is presented to obtain seismological properties from the accelerograms. Second, to generate probability of failure curves, earthquakes are selected for an intensity measure with rejection techniques. Two rejection procedures are presented which depend on the criterion to select the earthquakes. The advantages and disadvantages of each them are presented, as well as a comparison with the models developed in [44, 56].

Finally, it is the aim of Chapter 8 to create probability of failure curves for the earthquake

generation models presented in Chapters 6 and 7. Earthquakes are generated using these approaches and applied to a rocking body that is simulated using IPM [1]. The probability of failure curves are created for varying intensity measures. A comparison between models is also presented. This framework is then extended to produce the probability of failure against a lifespan of interest. This is illustrated using suitably chosen examples and its ability to predict the probability of failure of a rocking body in an area and period of interest.

This dissertation concludes by summarising its significant contributions and outlining the course of future research in Chapter 9.

Part I

Chapter 2

Examining the energy loss in the Inverted Pendulum Model

This work is part of a paper that was coauthored with Professor Manolis N. Chatzis and Professor Andrew W. Smyth and was published in the Journal of Engineering Mechanics [57].

2.1 Introduction

It was previously mentioned that the first dynamic model for rocking was suggested by Housner [1]. For this modelling approach, several assumptions were introduced: the body and the base are rigid, sliding is neglected, uplift cannot occur, the motion is two-dimensional and the loss of energy only occurs during impacts and is exclusively described by the dimensions of the body.

The effect of some of the previous assumptions on the stability of rocking bodies has been studied in a series of papers [4, 5, 13, 10, 11, 18, 17]. It is often claimed that the effect of these omitted phenomena can be minimized mechanically in a design of a rocking body. Nevertheless, even if the effect of the previous phenomena is minimized, the IPM as

introduced by [1], makes an explicit assumption about the energy lost during impact. In the IPM, the location of this impact is assumed to be at the future rocking corner. Therefore, the angular momentum is conserved about this point. This Chapter shows that conserving momentum with respect to the future rocking corner is not the only admissible solution to the problem, even if the examined body is such so that the ignored phenomena have indeed a minimal effect on its response. It is shown in this Chapter that the vertical impulse during an impact may be applied in any position between the future rocking corner and the midpoint of the base, without violating the rest of the assumptions. This position can, hence, be considered as a random variable with a related uncertainty.

Stability diagrams, which show a range of combinations of amplitudes and frequencies that produce the failure of a block, are developed for a rigid body subjected to ground excitations in the form of single, double and triple harmonic pulses. Conclusions are drawn on the effect of the position of the vertical impulse on the stability of the body. To quantify the propagation of the uncertainty on the stability of the body, a probabilistic approach is developed using the dynamic properties of the stability of a rocking body. The approach is initially formulated for the stability of rocking bodies subjected to single cycloidal pulses as in [26] and then extended to the case of multiple pulses [3].

2.2 Model and Assumptions

The purpose of this Section is to review the IPM and reformulate it to introduce the uncertainty of the vertical impulse. The numerical simulation is also explained.

2.2.1 Dynamic Model

This Section provides a brief description of the IPM [1]. The rocking body and the properties used in the following equations are defined in Figure 2.1. In this Chapter the convention which is used for the axes is shown in Figure 2.1, with x and y being the horizontal and vertical axis

respectively, and θ the rotation. The block can be fully defined by its mass m, its moment of inertia I_0 about one of the two corners 0 and $0'$, while b and h are the half-width and half-height of the body, respectively. Furthermore, R is the distance from a corner to the centre of mass, $R = \sqrt{h^2 + b^2}$. The slenderness of the block is defined by the angle $\alpha = \arctan \frac{b}{h}$. Depending on the sign of θ the body rocks with respect to the corresponding corner, and hence can be simulated by a pendulum whose pin is located at that corner as shown in Figure 2.1. This of course implies, that the body cannot slide, or experience a free-flight mode, that both the body and the ground are rigid, and that the response of the body is strictly planar, which are assumptions that are adopted in this thesis.

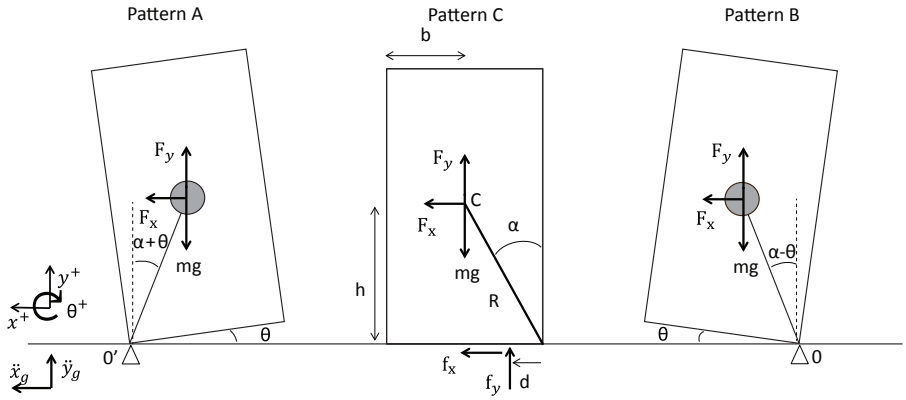

Figure 2.1 – Inverted Pendulum model defined by [1] for a free-standing rocking block.

The motion of the body is defined through three patterns. Patterns A and B are the pendulum patterns corresponding to $\theta < 0$ and $\theta > 0$ respectively, while pattern C is the static pattern $\theta = 0$ and $\dot{\theta} = 0$, i.e., when the body is at rest. The block is subjected to a positive horizontal, $\ddot{x}_g$, and vertical, $\ddot{y}_g$, ground accelerations. F_x and F_y are D'Alembert fictitious forces defined by $F_x = -m\ddot{x}_g$ and $F_y = -m\ddot{y}_g$. The ground is experiencing only translational accelerations and not rotational as for example examined in [58]. If moments are taken about the centre of rotation 0 or $0'$, the equations of motion, using Newton's second

law, are respectively:

$$\begin{aligned}\ddot{\theta} &= -p^2 \sin(\alpha - \theta) + \frac{m\ddot{x}_g}{I_0} R\cos(\alpha - \theta) - \frac{m\ddot{y}_g}{I_0} R\sin(\alpha - \theta) \text{ for } \theta > 0 \\ \ddot{\theta} &= p^2 \sin(\alpha + \theta) + \frac{m\ddot{x}_g}{I_0} R\cos(\alpha + \theta) + \frac{m\ddot{y}_g}{I_0} R\sin(\alpha + \theta) \text{ for } \theta < 0\end{aligned} \tag{2.1}$$

where $p^2 = m\,g\,R/I_0$.

In the static pattern the ground applies to the body horizontal and vertical reactions, f_x and f_y respectively, so that the static equilibrium is retained. The vertical reaction f_y is applied at a distance d measured, by convention, from the right corner 0. Since it is assumed that the ground cannot provide any tensile forces, the position of the vertical reaction force is bounded between the two corners, hence: $0 \leq d \leq 2\,b$. If the obtained value of d is outside those limits, then the static equilibrium cannot be retained, as it is assumed that the ground interface is unable to provide tensile forces. Hence, as $d = 0$ or $d = 2\,b$ the body transitions from the static pattern to patterns B or A, respectively.

In order to switch between patterns A and B, an impact occurs as is shown in Figure 2.2. This transition takes place when $\theta = 0$. During this impact, the body experiences impulsive forces. The corresponding resultants of the horizontal and vertical impulses are defined as J_x and J_y respectively.

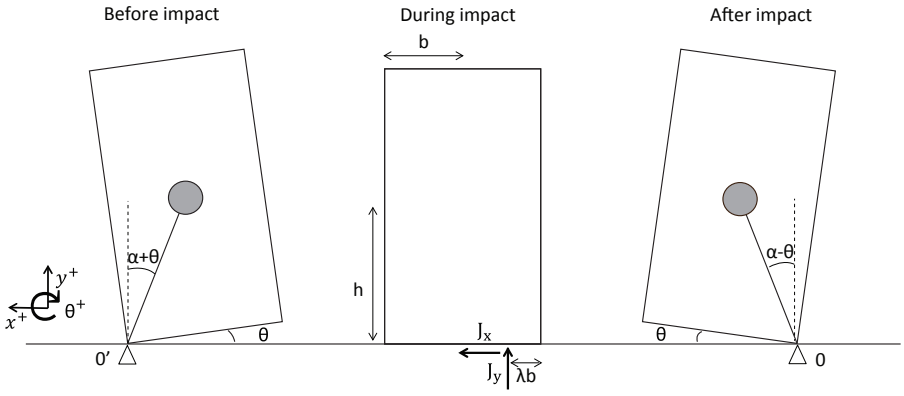

Figure 2.2 – Impact of the body and resulting horizontal and vertical impulses J_x and J_y, applied at a distance λ from the future rocking corner.

The assumption of conserving momentum with respect to the future rocking corner during impacts, is equivalent to assuming that the vertical impulse acts on that corner. To obtain J_y a distribution of vertical impulses along the base of the body has to be assumed. The restrictions for that distribution are that the distributed impulses are applied at the contact interface, i.e. between the two corners, and that they correspond to compressive impulsive forces. For the purposes of illustration of the following Figure 2.3 and without any loss of generality, a flat base is assumed for the body and hence the distributed impulses can be applied at any point between the two corners.

Figure 2.3 represents one of the infinitely many admissible distributions that could be considered for the distributed vertical impulses. Since the body is rigid, the distribution can be completely represented by the resultant impulse J_y, which is located at the centroid of the distribution. This centroid, without any loss of generality, may be at a distance $\lambda\, b$ measured from the post-impact rocking corner towards the pre-impact rocking corner. The exact geometry of the base plays an important role in the response of the body as has been shown in [11, 59]. A non-flat multi-contact base would result in a non-continuous impulse distribution along the base. Nonetheless, this does not influence any of the results of the Chapter as the continuous nature of the distribution of the impulses is not made use of. For Figure 2.3 the pre- and post-impact rocking corners are assumed to be $0'$ and 0 respectively. The requirement for all forces from the interface to be compressive, including impulsive forces and the corresponding impulses result in the following constraints: $J_y > 0$ and $0 \leq \lambda \leq 2$. The latter constraint translates to the centroid being between the two corner points.

Formulating the momentum equations linking the time instances after and before the

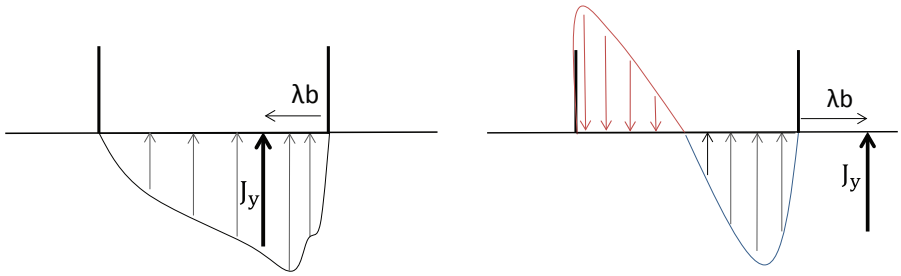

(a) Physically possible (b) Non-physically possible

Figure 2.3 – a) One of the infinitely many admissible distributions to describe the vertical impulse during impact. J_y is the vertical impulse. b) The red distribution corresponds to tensile forcees which is a violation of the non-tensile assumption. J_x is neglected in this Figure.

impact as in Figure 2.2, the following three momentum equations are obtained:

$$\begin{aligned} m\dot{x}^+ &= m\dot{x}^- + J_x \\ m\dot{y}^+ &= m\dot{y}^- + J_y \\ I_G\dot{\theta}^+ &= I_G\dot{\theta}^- - (b - \lambda\, b)J_y\, sign(\dot{\theta}^-) + h\, J_x \end{aligned} \tag{2.2}$$

where $\dot{x}^+$, $\dot{y}^+$, $\dot{\theta}^+$ and $\dot{x}^-$, $\dot{y}^-$, $\dot{\theta}^-$ are: the horizontal, vertical and angular velocity after and before impact and I_G is the moment of inertia about the centre of the block. The *sign* in equation (2.2) accounts for whether the future rocking corner is 0 or 0′, with $sign(\dot{\theta}^-)$ being + or − respectively. Due to the pendulum kinematic constraints:

$$\dot{x}^+ = -h\,\dot{\theta}^+ \qquad\qquad \dot{y}^+ = b\,\|\dot{\theta}^+\| \tag{2.3}$$

$$\dot{x}^- = -h\,\dot{\theta}^- \qquad\qquad \dot{y}^- = -b\,\|\dot{\theta}^-\| \tag{2.4}$$

Thus, the unknowns of the system are $\dot{\theta}^+$, J_y, J_x and λ. To find a solution of the system, it is necessary to assume the value of one of the unknowns, for example, λ. While this is often assumed to be equal to zero in the literature, it is important to note that there would not be any violation of the momentum equations assuming any value for λ. But if one takes into account the previous discussion, any value of $\lambda \in [0, 2]$ could be used. The angular velocity

after impact is defined through the reduction of energy factor, r, which relates the kinetic energy before and after impact.

$$r = \frac{\left(\dot{\theta}^{+}\right)^{2}}{\left(\dot{\theta}^{-}\right)^{2}} = \left(\frac{1 - \frac{3}{4}(2-\lambda)\sin^{2}\alpha}{1 - \frac{3}{4}\lambda\sin^{2}\alpha}\right)^{2} \tag{2.5}$$

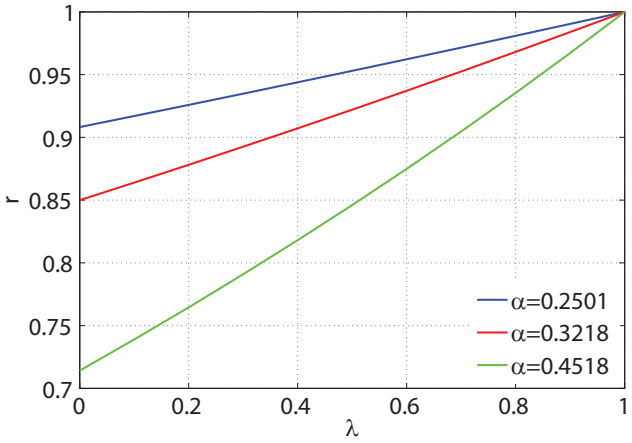

Figure 2.4 – r over λ for different slenderness.

Leading to the equation: $\dot{\theta}^{+} = \sqrt{r}\dot{\theta}^{-}$. It can be seen from equation (2.5) that if $\lambda > 1$, then $r > 1$, hence energy is generated during the impact, which is not physically possible in this problem where the ground experiences only translational accelerations. This is also observed in Figure 2.4 in which $r = 1$ when $\lambda = 1$ for any α. Thus, two material assumptions, the lack of tensile forces from the interface and that there cannot be an increase of the energy during an impact, result in λ taking an admissible value in the interval $[0, 1]$. Any value of $\lambda \in [0, 1]$ is completely compatible with the assumptions made in the IPM. To this point it should be noted that researchers have suggested the use of values of smaller reduction of energy factors than the one suggested by Housner in [1], or equivalently have suggested negative values for λ, to account for additional loss of energy during impact potentially due to the ignored sliding, bouncing, deformability of the ground, or the three dimensional nature of the response. However, if those assumptions were to be violated, the dynamic response of the body would include additional dynamic patterns, whose effect on the response cannot be approximated by an IPM for any value of λ. In other words, one should either use a model

capable of taking into account those phenomena, or if these phenomena can be neglected then an IPM can be used assuming that $\lambda \in [0, 1]$. This work assumes the latter.

Finally, it should be noted that the occurring $\sqrt{r} = \frac{1-\frac{3}{4}(2-\lambda)\sin^2\alpha}{1-\frac{3}{4}\lambda\sin^2\alpha}$ should be positive. Negative solutions do not make physical sense and they would result in a free-flight pattern that is incompatible with the IPM. This Chapter will deal with bodies of aspect ratio h/b so that $\sqrt{r}$ is positive even for $\lambda = 0$. As algebraically $\sqrt{r}$ becomes larger for larger values of λ, this guarantees that $\sqrt{r} > 0$ for any of the bodies and values of λ examined in this Chapter.

2.2.2 Numerical Simulation.

To integrate this model over time, the dynamic equations in (2.1) are brought to state-space form (equation 2.6 for $\theta < 0$) and are integrated over time using a variable time stepping Runge-Kutta 4-5 pair as presented in [60]. This algorithm uses a 4th order Runge-Kutta to propagate the solution over time and performs a comparison versus the prediction obtained from the 5th order Runge-Kutta estimating an error from the difference of the two methods. The time step is varied in order to retain the estimated relative and absolute error within some bounds.

$$\begin{aligned} \dot{x}_1 =& x(2) \\ \dot{x}_2 =& p^2 sin(\alpha + x(1)) + \frac{m\ddot{x}_g R}{I_0}(cos(\alpha + x(1)) + \frac{m\ddot{y}_g R}{I_0}(sin(\alpha + x(1)) \end{aligned} \tag{2.6}$$

Unlike typical equations of motion, the ones describing the behaviour of the IPM are not smooth, i.e., infinitely differentiable as there is a switch of the state-space equations from one pattern to the other. Additionally, the velocity state $\dot{\theta}$ is discontinuous around the time instance of an impact. In order to switch from one pattern to the other an event driven function algorithm is suggested in [61], that allows for stopping the integration around a specific time instance at which an event is located. In this problem, the events are the transitions between patterns and the detection of toppling, i.e., failure, of the body, i.e., $\|\theta\| = \pi/2$. Those are tracked online by the algorithm as implemented in Matlab's ode45 solver with the Events option [62]. Each time a transition between patterns is detected, the

algorithm stops the integration and switches the state-space equations used to account for the new pattern. Furthermore, if the detected event was an impact then the velocity of the body is modified according to equation (2.5), to account for the loss of energy during the impact.

Equation (2.5) implies that eventually $\dot{\theta}$ tends to zero but never becomes numerically equal to zero. In other words, in theory the body can never go back to the static pattern from one of the two pendulum patterns. This however, is impractical in terms of the time integration and may lead to numerical instabilities when equation (2.5) is applied to values of the pre-impact velocity, or equivalently the kinetic energy just before the impact E_k, close to the machine tolerance (10^{-9}). To avoid that and ensure stability and robustness of the algorithm, a condition is imposed after an impact event regarding the minimum value of the kinetic energy of the body: if the energy of a body after impact is smaller than this minimum value, then the static pattern is enforced as shown in Figure 2.5. The integration continues until a new switch is located, or until the stopping criteria for integration are met. These stopping criteria are either that toppling of the body was detected, or that the upper bound of the requested time window of integration was met, i.e., the body survived this excitation. Figure 2.5 shows the numerical implementation.

2.3 Deterministic effect of λ on the stability of the body

As stated in the previous Section 2.2, λ has an associated uncertainty. The source of this uncertainty is the lack of modeling the contact physics in the IPM, which allows for an infinite number of admissible distributions for the vertical impulses. This can be thought of as a 'structural' uncertainty of the IPM. This Section examines how different values of λ affect the stability of a rocking body when subjected to a ground acceleration $\ddot{x}_g$. Initially, a single cycloidal pulse stability analysis is conducted, similar to the one presented in [26]. A free standing block with p=2.1401 and $\alpha = 0.2501$ [26], as shown in Figure 2.1, is subjected

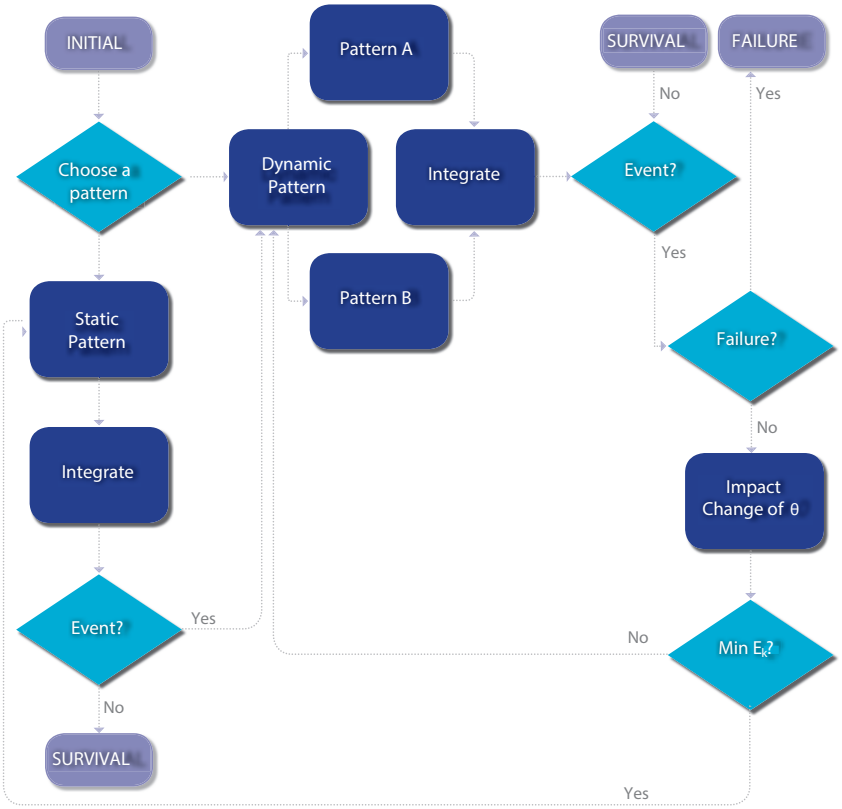

Figure 2.5 – Schematic explanation of the time integration scheme used.

to single cycle sinusoidal, cosinoidal and square pulses for a range of angular frequencies ω_u and amplitude u_0:

$$\begin{aligned} \ddot{x}_g &= 0, && \text{if t>T} \\ \ddot{x}_g &= u_0 \mathrm{K}\left(\omega_u t\right), && \text{if } 0 \leq \text{t} \leq \text{T} \end{aligned} \tag{2.7}$$

where $T = \frac{2\pi}{\omega_u}$, K is either of the functions sin, cos, square for the sinusoidal, cosinoidal and square pulses respectively, with the square function being defined as the following periodic function with period T:

$$\begin{aligned} \text{square}(\omega_u t) &= +1, \quad \text{if} \quad 0 < t < T/2 \\ \text{square}(\omega_u t) &= -1, \quad \text{if} \quad T/2 < t < T \end{aligned} \tag{2.8}$$

As noted in [26], three areas can be observed in a stability diagram of a body subjected to single cycloidal pulses: survival, failure after a single impact and failure without impact. Stability diagrams are generated in Figure 2.6(a) showing these areas for a range of combinations of u_0 and ω_u for a sinusoidal pulse. Note that there are no failures for $\frac{u_0}{\tan(\alpha)\, g} < 1$, because

this is the critical value to initiate rocking. The non-linearity of the problem is apparent by the fact that there are pulses of constant frequency, for which as the amplitude of the pulse, $\frac{u_0}{\alpha g}$, is increased the block goes from the stable region to the unstable (failure with impact), re-transitions to the stable region and has a final transition to the unstable region (failure without impact).

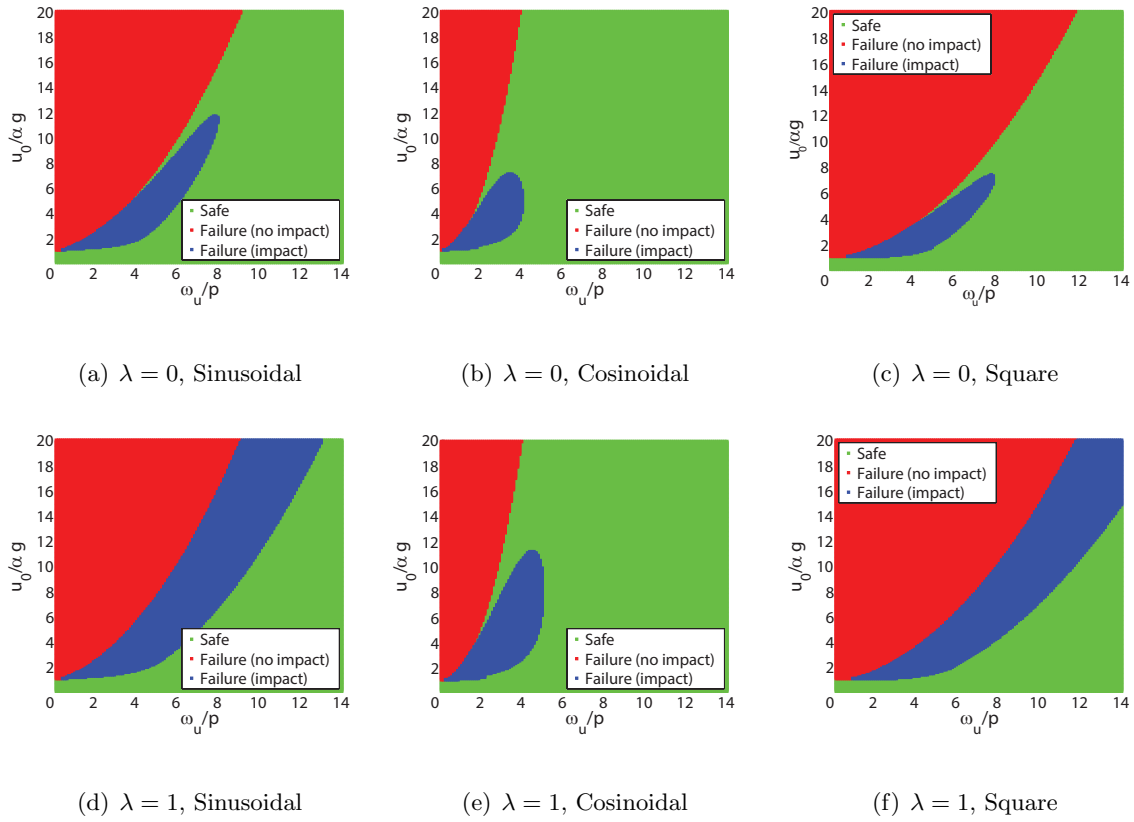

(a) $\lambda = 0$, Sinusoidal (b) $\lambda = 0$, Cosinoidal (c) $\lambda = 0$, Square

(d) $\lambda = 1$, Sinusoidal (e) $\lambda = 1$, Cosinoidal (f) $\lambda = 1$, Square

Figure 2.6 – Overturning Acceleration Spectrum of Free standing block subjected to a single sinusoidal (a, d), cosinoidal (b, e) and square (c, f) acceleration pulse with frequency ω_u, p=2.1401 and $\alpha = 0.2501$.

Thanks to the similarity property described in [26, 22] the results for the diagram are applicable to bodies which have the same aspect ratio but potentially different size, as expressed through R, as long as the same value of ω_u/p is examined. It should further be noted that, as indicated in this Chapter, an additional parameter required for ensuring similarity between two such bodies is the assumption of the same value of λ for both of them. In [26],

it was assumed that the vertical impulse during an impact is applied at the future rocking corner, i.e., $\lambda = 0$. However, as discussed in Section 2.2, λ can attain values between zero and one. Figure 2.6 shows the stability diagrams for all three types of pulses for values of $\lambda = 0$ and $\lambda = 1$. A significant increase of the failure with impact can be observed in all three cases, as λ goes from zero to one. This is reasonable, as larger values of λ correspond to a smaller loss of energy during impacts and specifically the extreme case of $\lambda = 1$ case corresponds to conservation of energy during impacts. For the cosinoidal pulse, as can be seen in Figures 2.6(b) and 2.6(e), the single impact instability region is smaller than in Figure 2.6(a) and 2.6(d) and the boundary between non-impact and safety regions is steeper. On the other hand the square pulse, presents similarities to the sinusoidal pulse as can be seen in Figure 2.6(c) and 2.6(f).

As expected, the area of failure without impact is unaffected by λ. This behaviour can be observed for any aspect ratio h/b and for the purpose of illustrating this, two different aspect ratios are used in Figure 2.7 for all three pulses. Figure 2.7 represents the boundaries between survival and failure for different vales of λ. As the assumed value of λ is increased the area of failure with impact is expanding by including more pairs of u_0 and ω_u. This significant behaviour means that, for a given pair of values ω_u and u_0 in the area defined between the boundary lines for the areas of failure with impact for $\lambda = 0$ and $\lambda = 1$, a body which fails for a given value of λ also fails for higher values of λ. Hence, for the case of single cycle pulses, there is a value of $\lambda = \lambda^*$, such that a point on the stability diagram belonging to the predefined region fails for any $\lambda > \lambda^*$ and survive for $\lambda < \lambda^*$:

$$\begin{aligned} &\text{if } \lambda < \lambda^* \rightarrow \text{ SURVIVAL} \\ &\text{if } \lambda \geq \lambda^* \rightarrow \text{ FAILURE} \end{aligned} \tag{2.9}$$

It should also be observed that points in the diagram that fail for $\lambda = 0$, fail for any of the allowable values of λ. Notice that the survival or failure of the remaining points on the stability diagram, outside the area defined earlier, does not depend on the value of λ.

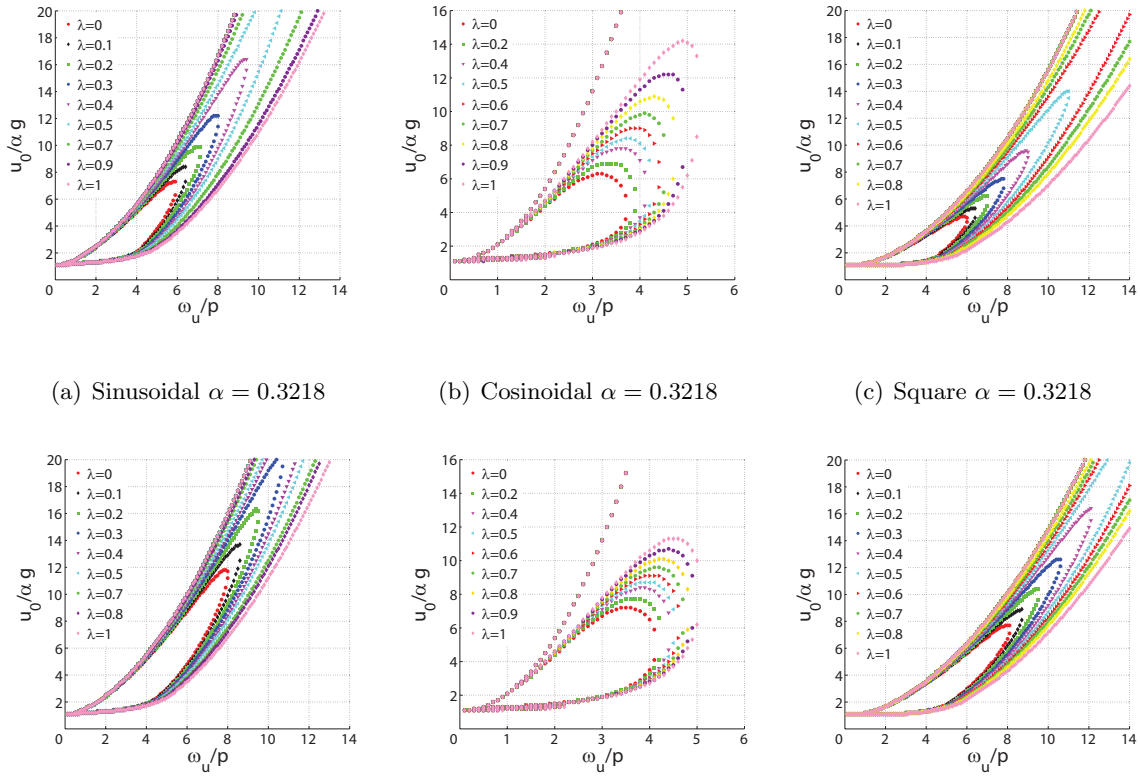

(a) Sinusoidal $\alpha = 0.3218$ (b) Cosinoidal $\alpha = 0.3218$ (c) Square $\alpha = 0.3218$

(d) Sinusoidal $\alpha = 0.2501$ (e) Cosinoidal $\alpha = 0.2501$ (f) Square $\alpha = 0.2501$

Figure 2.7 – Boundary regions which separate the area of failure with impact from the failure without impact and survival. The block is subjected to a single sinusoidal (a, d) cosinoidal (b, e) and (c, f) square acceleration pulse with $p = 2.1401$ for $\alpha = 0.3218$ and $\alpha = 0.2501$.

Following the property defined in equation (2.9), the bisection method is applied to calculate λ^*, i.e., the value of λ signifying the transition between failure and survival. The bisection method detects this transition with the precision of a tolerance imposed (tolerance= 10^{-3}). Figure 2.8 shows the corresponding values of λ^* for a single sinusoidal, cosinoidal and square pulse. It can be observed that the mapping of λ^* to an (ω_u, u_0) pair depends on the type of the input.

Figure 2.9 shows a comparison between the three pulses for the cases of $\lambda = 0$ and $\lambda = 1$. Notably, the square pulse results in a higher range of u_0 and ω_u values that signify failure. On the other hand, the cosinoidal pulse seems to have a usually safer behaviour than the sinusoidal and square pulses maybe because of the phase. However, there are areas on the

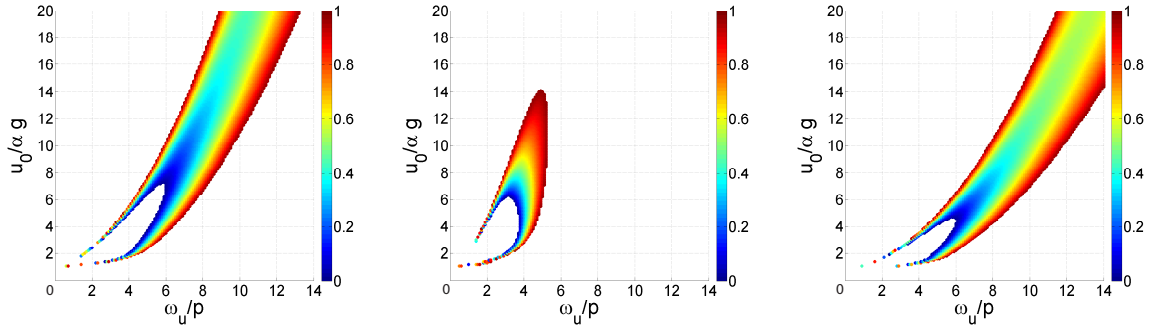

(a) Sinusoidal $\alpha = 0.3218$ (b) Cosinoidal $\alpha = 0.3218$ (c) Square $\alpha = 0.3218$

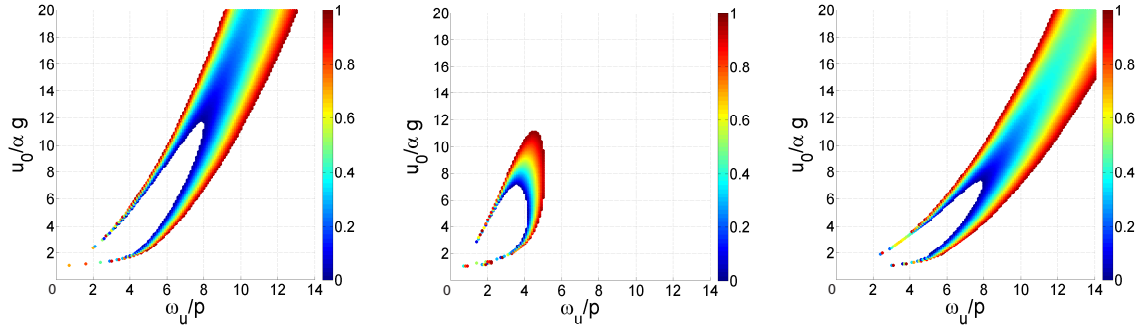

(d) Sinusoidal $\alpha = 0.2501$ (e) Cosinoidal $\alpha = 0.2501$ (f) Square $\alpha = 0.2501$

Figure 2.8 – Values of λ^* of a free standing block with a constant frequency parameter $p = 2.1401$ subjected to a single sinusoidal for a) $\alpha = 0.3218$ and d) $\alpha = 0.2501$, to a cosinoidal for b) $\alpha = 0.3218$ and e) $\alpha = 0.2501$ and to a square pulse for c) $\alpha = 0.2501$ and f) $\alpha = 0.1244$.

diagram for which any of the three inputs may result in failure and the other two to safety. For example, the cosinoidal pulse fails for the case of $\lambda = 0$, $\omega_u = 4p$ and $u_0 = 3.7\alpha g$, while the square pulse survives. Comparing the cosinoidal and the sinusoidal pulses for the case of $\lambda = 0$ for $\omega_u = 4p$ and $u_0 = 5.9\alpha g$, the former fails but not the latter. In general, for a specific value of ω_u, u_0 and λ, due to the non-linearity of the problem, there are areas where the survival or failure of the body will depend on the type of the input.

At this point, it can be observed that variations of the value of λ significantly change the failure with impact areas. In the literature [26], it is claimed that $\lambda = 0$, hence according to equation (2.5) the smallest allowable value of r is used. However, this Chapter has already

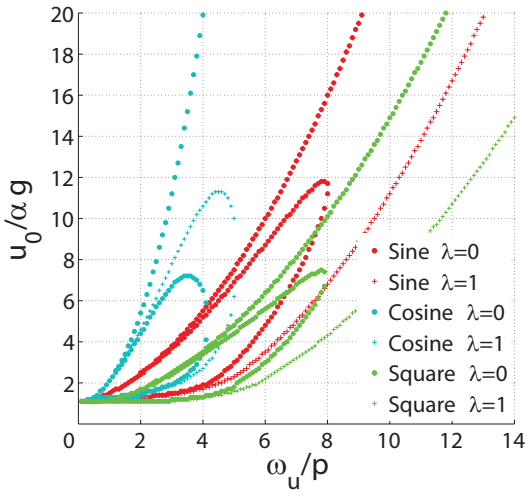

Figure 2.9 – Overturning Acceleration Spectrum for a single sinusoidal, cosinoidal and square pulse for values of $\lambda = 0$ and $\lambda = 1$ subjected to a rigid body with $p = 2.1401$ and $\alpha = 0.2501$.

demonstrated that the body has a greater tendency to collapse as the value of λ is increased. Hence, assuming that $\lambda = 0$, is a non-conservative assumption. It should further be noted that in Figure 2.6(a) when ω_u/p is small, the minimum overturning acceleration for failure is given by the lower limit of the failure with impact area. As the frequency of the input pulse is increased, this area disappears and hence the minimum amplitude for failure is given by the boundary of the failure with no impact area. Hence at some frequency, there is a jump of the minimum acceleration for overturning. This is a favourable property as the required amplitude for overturning the body for an input beyond that transition frequency is substantially larger. Nevertheless, the value of this transition frequency increases as λ is increased, as shown in Figure 2.7, reducing the range of these favourable, in terms of the required amplitude of overturning, frequencies.

For the remainder of this Chapter, the following dimensions are adopted $p = 2.1401$ and $\alpha = 0.3218$ which correspond to h=1.5240 m, b=0.5080 m and $h/b = 3$.

2.4 Quantifying the Probability of Failure.

This Section aims to introduce λ as a random variable and a investigation of its effect is carried out.

2.4.1 Probabilistic models for the effect of λ on the stability of the body.

Based on the previous discussion in Section 2.2, λ is a random variable between zero and one and hence it is associated with some probability of occurrence. As a result, the outcome of a body being subjected to a single cycloidal pulse of a specific u_0 and ω_u is also linked with a corresponding probability of survival/failure. While there are points in the stability diagram, i.e., pairs of values (ω_u, u_0), that fail or survive for any of the possible values of λ, there are also points for which, the deterministic property defined on equation (2.9) correspond to a probability property: the probability of the body failing or surviving is only the probability of λ being smaller or greater than λ^*:

$$\begin{aligned} P\left(\lambda > \lambda^*\right) &= \text{PROBABILITY OF FAILURE} \\ P\left(\lambda < \lambda^*\right) &= \text{PROBABILITY OF SURVIVAL} \end{aligned} \tag{2.10}$$

In this Chapter, two types of distributions, defined in terms of the mean, μ, and the standard deviation, σ, are used for modelling λ: uniform which corresponds to the assumption that any value of λ between zero and one is equally possible, and truncated Gaussian distributions which has the limits $\mu = 0.5$ and $\sigma = 0.5$, respectively. Assuming a value of μ closer to a value implies that this is expected as the most probable value of λ, while σ quantifies the dispersion of a set of values. Thus a σ closer to zero indicates that the expected values of λ are closer to the mean. An increase of the value of σ indicates that there is smaller certainty about the expected value of λ. Equations (2.11) and (2.12) refer to the Probability Density Function (ϕ), $\phi_U(\lambda)$, and Cumulative Density Function (Φ), $\Phi_U(\lambda)$, of the Uniform

Distribution.

$$\phi_U(\lambda) = \begin{cases} 1 & \text{for } 0 \leq \lambda \leq 1, \\ 0 & \text{for } \lambda < 0 \text{ or } \lambda > 1 \end{cases} \tag{2.11}$$

$$\Phi_U(\lambda) = \begin{cases} 0 & \text{for } \lambda < 0, \\ \lambda & \text{for } \lambda \in [0, 1), \\ 1 & \text{for } \lambda \geq 1 \end{cases} \tag{2.12}$$

It is often convenient to define a truncated Gaussian in terms of an untruncated Gaussian of μ_u and σ_u. The truncated Gaussian distribution is defined as follow:

$$\phi_T(\lambda; \mu_u, \sigma_u, 0, 1) = \frac{\phi_N(\xi_T)}{\Phi_N(\beta_T) - \Phi_N(\alpha_T)} \tag{2.13}$$

$$\Phi_T(\lambda; \mu_u, \sigma_u, 0, 1) = \frac{\Phi_N(\xi_T) - \Phi_N(\alpha_T)}{\Phi_N(\beta_T) - \Phi_N(\alpha_T)} \tag{2.14}$$

$$\mu_T = \mu_u + \frac{\phi_N(\alpha_T) - \phi_N(\beta_T)}{\Phi_N(\alpha_T) - \Phi_N(\beta_T)} \sigma_u \tag{2.15}$$

$$\sigma_T = \sigma_u^2 \left(1 + \frac{\alpha_T \phi_N(\alpha_T) - \beta_T \phi_N(\beta_T)}{\Phi_N(\alpha_T) - \Phi_N(\beta_T)} - \left(\frac{\phi_N(\alpha_T) - \phi_N(\beta_T)}{\Phi_N(\alpha_T) - \Phi_N(\beta_T)} \right)^2 \right) \tag{2.16}$$

where μ_u and σ_u are the values of the untruncated Gaussian distribution, $\xi_T = \frac{x - \mu_u}{\sigma_u}$, $\alpha_T = \frac{0 - \mu_u}{\sigma_u}$ and $\beta_T = \frac{1 - \mu_u}{\sigma_u}$,$[0, 1]$ are the limited values, ϕ_N and Φ_N are the ϕ the Φ of the normal Gaussian distribution ($\mu = 0$ and $\sigma = 1$), respectively.

The probability of failure of the body for a range of values of u_0 and ω_u is then calculated. Monte Carlo simulations are used to calculate the probability of failure. A number of random samples of λ are generated and the probability of failure is calculated for each value of u_0 and ω_u and for a given distribution. The number of generated samples of λ is increased until convergence is achieved. For the case of the uniform distribution, the random values are modelled using the 'rand' tool from Matlab which generates uniformly distributed random numbers. For the truncated Gaussian distribution, the algorithm described in [63] is used to

generate samples. The probability of failure is calculated for a pair of u_0 and ω_u, as the sum of all observed failures divided by the number of samples of λ.

Alternatively, the probability of survival or failure can be defined directly using the property of equation (2.10). In this approach, having defined the values of λ^*, for a body of a given aspect ratio and type of input, one can then apply equation (2.10) for each pair of points (u_0 and ω_0) to generate the corresponding probability of survival/failure in the area of points for which equations (2.9) and (2.10) are applicable.

The advantage of the second approach is that the second step, i.e., the transition from the λ^* mapping to the probability of failure does not require any further dynamic simulations, but only the calculation of the associated probabilities, that solely depend on the assumed distributions and the values of λ^* corresponding to each point. This probability can, for the cases examined, be calculated analytically. This results in an overall substantial reduction of calculation cost in comparison to the Monte Carlo approach. It should be noted that the Monte Carlo simulations mentioned in this Chapter use 1000 samples.

For any single cycloidal pulse input, it can be observed, as for example in Figure 2.6, that the area of failure without impact does not change for different values of λ. Hence, the probability of failure in these areas is 100%. Because λ cannot be greater than one, the area that corresponds to survival for the case of $\lambda = 1$ has a probability of failure of 0%. Hence, as in previous Sections, only the points for which equations (2.9) and (2.10) are applicable, are analysed. Figure 2.10 compares the Monte Carlo Simulations versus the defined probabilistic approach for a single cosinoidal pulse. It can be seen that there is an excellent match between the two methods. In fact the difference between the two methods is controlled by the number of samples used for the Monte Carlo method and the error tolerance chosen for numerically estimating equation (2.10). By increasing the former and reducing the latter a desired difference tolerance between the two methods can be achieved. The same can be verified regardless of the input, dimensions of the body or the distribution assumed

for λ.

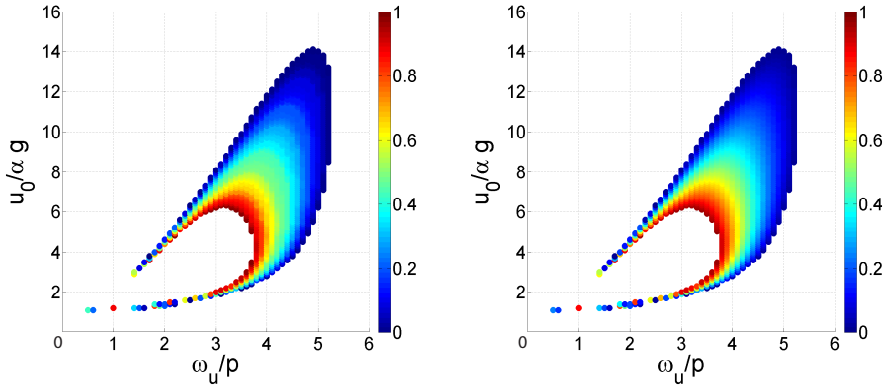

(a) Monte Carlo Simulations (b) Probabilistic approach

Figure 2.10 – Probability of Failure for one cosinoidal pulse using (a) Monte Carlo Simulations and (b) the Probabilistic approach for a body with $p = 2.1401$ and $\alpha = 0.3218$.

2.4.2 Effect of the Uncertainty of λ in the estimate of the outcome.

The probability of failure of the body for a single cosinoidal pulse input, assuming truncated Gaussian distributions of λ corresponding to different values of μ and σ are compared in Figure 2.11. Increasing μ and keeping σ constant as in Figures 2.11(a) and 2.11(c) or 2.11(b) and 2.11(d), the area of points with probability of failure close to 100% increases. This is in agreement with what was presented in Section 2.3, as higher values of μ correspond to a higher expected value of λ. On the other hand, increasing σ and keeping μ constant, as in Figures 2.11(a) and 2.11(b) or 2.11(c) and 2.11(d), results in reducing the size of areas with an almost constant probability of failure.

In Figure 2.11 there are points whose probability of failure is very close to 50%. A probability of failure of 50% means that there is as much certainty about the outcome using the mode, as that which occurs by flipping a coin. Thus, there is a very large uncertainty to the model's prediction on whether the body is expect to survive or fail. The same practically holds for a range of probabilities close to 50%, e.g. $40 - 60\%$. Hence, points in the diagram

with probabilities of failure in that range should be further examined.

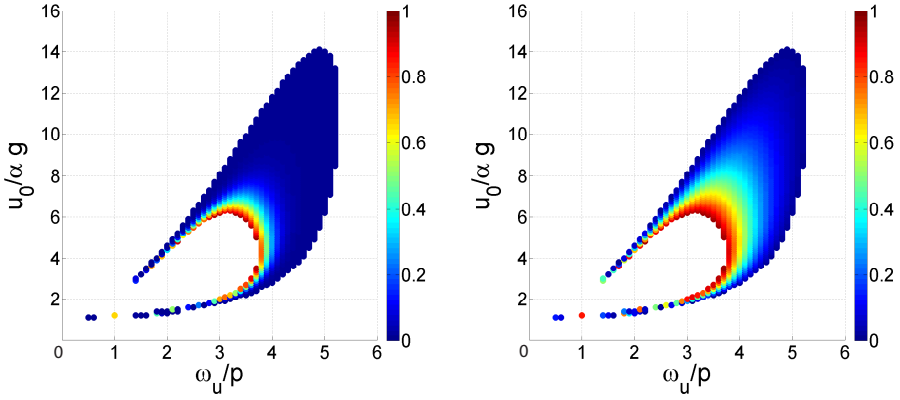

(a) $\mu = 0.2$ and $\sigma = 0.15$

(b) $\mu = 0.2$ and $\sigma = 0.5$

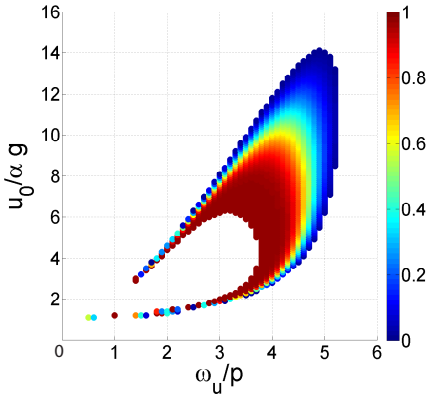

(c) $\mu = 0.8$ and $\sigma = 0.15$

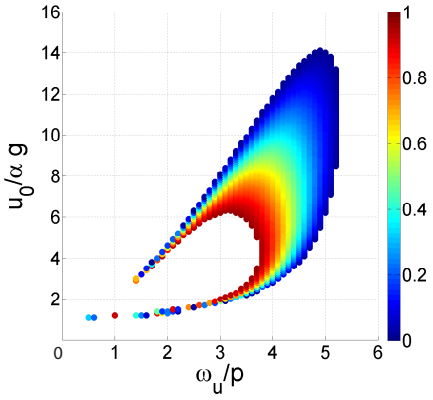

(d) $\mu = 0.8$ and $\sigma = 0.5$

Figure 2.11 – Probability of Failure for a single cosinoidal pulse using the truncated Gaussian distribution with a) $\mu = 0.2$ and $\sigma = 0.15$, b) $\mu = 0.2$ and $\sigma = 0.5$, c) $\mu = 0.8$ and $\sigma = 0.15$ and d) $\mu = 0.8$ and $\sigma = 0.5$ for a body with $p = 2.1401$ and $\alpha = 0.3218$.

In attempting to understand the effect of the assumed distribution of λ on the region of points with the aforementioned range of probabilities of failure, the Φ for assumed Truncated Gaussian distributions of λ occurring from different values of μ and σ are illustrated in Figure 2.12(a). The vertical axis represents the probability of λ being greater than the value indicated in the horizontal axis. Those distributions are used in the stability analysis of a body with $\alpha = 0.2501$ and $p = 0.3218$ subjected to a single cycloidal pulse ground excitation with the results shown in 2.12(b). A point in the region of the stability diagram that satisfies

the property of equation (2.10) has a probability of failure of $X\%$, if $1 - \Phi(\lambda^*) = X\%$. For the reasons explained earlier it is hence beneficial to define in Figure 2.12(a), the values of λ^* that correspond to a probability of failure of 40% and 60%, the corresponding values of λ^* are denoted as λ^*_{60} and λ^*_{40}, respectively.

In Figure 2.12(a) the values of λ^*_{40} and λ^*_{60} for each distribution are selected. The values are shown in Table 2.1. In Figure 2.12(b), the points which correspond to λ^* values equal to λ^*_{60} and λ^*_{40} are represented with lines. These lines are also the boundaries of the points of this uncertain region between 40% and 60% probability of failure for each distribution. The dashed line represents the 60% boundaries and the continuous line the 40% boundary. In Table 2.1, for $\mu = 0.2$, the λ^*_{60} value decreases as σ is increased. However, for λ^*_{40}, the decrease is smaller. From Figure 2.8(b), it can be observed that the values of λ^* decrease when moving towards the bottom left corner, and increase while moving towards the upper right corner. The same behaviour is observed in the Figure 2.12(b). The 60% line moves towards the bottom left corner as σ is increased and is almost constant for the 40% line. Hence, the region of the points with probabilities between 40% and 60% expands towards the bottom left corner. In Table 2.1, for $\mu = 0.8$, λ^*_{60} is almost constant whereas λ^*_{40} increases as σ is increased. In Figure 2.12(b), the uncertain region extends towards the upper right corner as σ is increased. In Table 2.1, for values of $\mu = 0.5$, the probability of λ^* increases and decreases symmetrically as the uniform distribution is approached, matching with what is observed in Figure 2.12(b) where the uncertain region expands in both directions as σ is increased.

It was shown in the previous paragraph, how one can determine the behaviour of this uncertain region of points with probabilities between 40% and 60%, using only the λ^* for a specific body and excitation and the Φ for the assumed distribution of λ.

Table 2.1 – λ^* values for $40-60\%$ for truncated distributions of different μ and σ.

μ	σ	λ^*_{40}	λ^*_{60}
0.2	0.06	0.2254	0.1781
	0.15	0.2116	0.1326
0.5	0.1	0.5260	0.4260
	0.25	0.5743	0.4750
0.8	0.06	0.8051	0.7949
	0.14	0.8604	0.7836

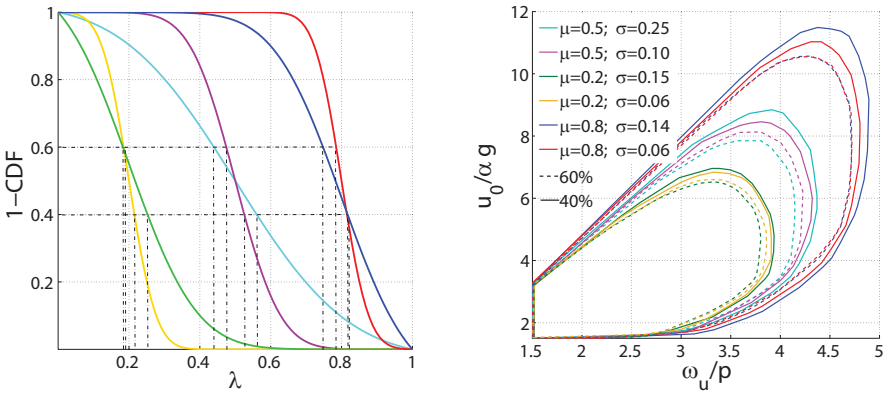

(a) Φ (b) Boundaries of probability of 40%-60%

Figure 2.12 – Φ (a) and λ^* boundaries for probabilities between $40-60\%$ (b) for a rigid body subjected to a single cosinoidal pulse for a body with $p = 2.1401$ and $\alpha = 0.3218$.

2.5 Stability Analysis: Multiple-Pulses

This Section is an extension of single pulses to multiple pulses. To this end, the body is subjected to double and triple cycloidal pulses, by modifying equation (2.7) to:

$$\begin{aligned} \ddot{x}_g &= 0, && \text{if } t > N_c T \\ \ddot{x}_g &= u_0 \mathrm{K}\left(\omega_u t\right), && \text{if } 0 \leq t \leq N_c T \end{aligned} \tag{2.17}$$

where N_c is the number of cycles of the pulse. Figure 2.13 illustrates areas of failure with

impact for different values of λ subjected to double sinusoidal and cosinoidal pulses.

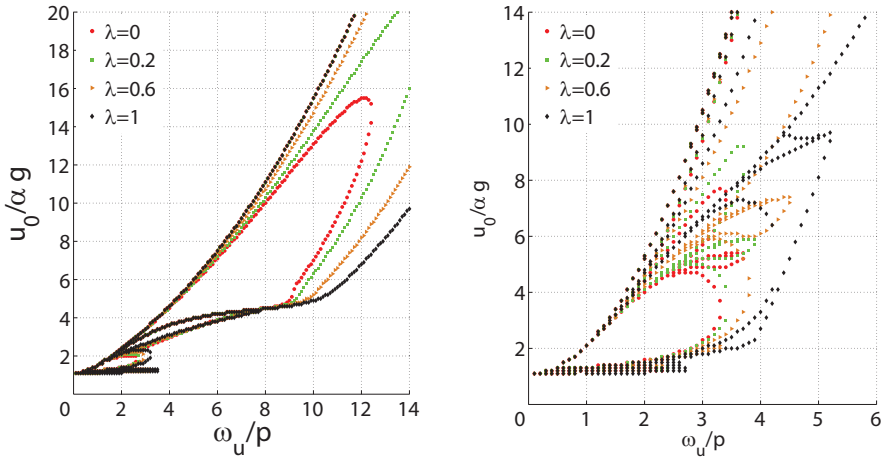

(a) Sine Pulse (b) Cosine Pulse

Figure 2.13 – Boundaries separating the area of failure with impact from the failure without impact and survival for a body with $p = 2.1401$ and $\alpha = 0.3218$. The block is subjected to a) double sinusoidal pulse and b) double cosinoidal pulse.

It should be noticed that not all points agree with the property described on (2.9). For example, in Figure 2.13(a) for a double sinusoidal pulse input some points fail for $\lambda = 0$ while they do not for greater values of λ. And in general, for a pair of u_0 and ω_u, there are points for which the body fails for a value of λ, λ_2, and survives for another value of λ, λ_1, even when $\lambda_1 > \lambda_2$. The same phenomenon can be observed in Figure 2.13(b) for a double cosinoidal pulse input. For $\omega_u = 3.5p$ and $u_0 = 5\alpha g$, $\lambda = 0$ the body fails, whereas for $\lambda = 0.2$ it survives. Hence, for each ω_u and u_0, there might be multiple transitions from survival to failure as the value of λ increases. This is illustrated in Figure 2.14. Those transitions essentially correspond to multiple roots in accordance to what was defined for single pulses in Section 2.3.

Since equation (2.9) not being applicable for this case, two methods are investigated for determining the probability of failure of the body: *i*) a multiroot finding method *ii*) Monte Carlo Simulations. The latter is practically the same as explained in Section 2.4.1, where the

probability of failure for a point on the stability diagram is calculated as the sum of all the occurrences of failure over the total number of samples of λ used.

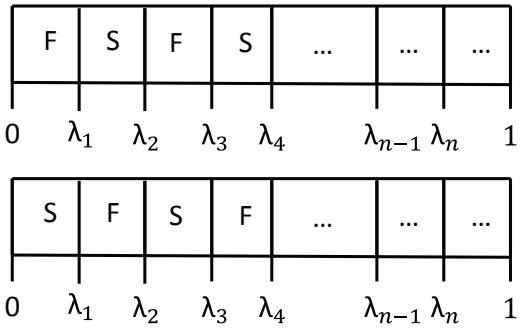

Figure 2.14 – Graph explaining the two possible cases when using the multiroot finding method.

A multiroot finding method is used based on a modification of what was presented in 2.4.1 for single pulses. This method determines for a pair of ω_u and u_0 all the corresponding roots, i.e., values of λ, λ^*, for which there is a transition from survival (S) to failure (F) and vice-versa, as shown in Figure 2.14. Once all roots for a pair of values of ω_u and u_0 are found, the probability of survival or failure is determined depending on whether the body fails or survives for $\lambda = 0$: Following Figure 2.14, if the body fails for $\lambda = 0$, the probability of survivals is defined as in equation (2.18). Otherwise, the probability of survival is defined as in equation (2.19).

$$\begin{aligned} P_S &= P((0 < \lambda < \lambda_1^*) \cup (\lambda_2^* < \lambda < \lambda_3^*) \cup \cdots) \\ &= P(0 < \lambda < \lambda_1^*) + P(\lambda_2^* < \lambda < \lambda_3^*) \cdots \end{aligned} \tag{2.18}$$

$$\begin{aligned} P_S &= P((\lambda_1^* < \lambda < \lambda_2^*) \cup (\lambda_3^* < \lambda < \lambda_4^*) \cup \cdots) \\ &= P(\lambda_1^* < \lambda < \lambda_2^*) + P(\lambda_3^* < \lambda < \lambda_4^*) \cdots \end{aligned} \tag{2.19}$$

Figures 2.15(a) and 2.15(b) compare Monte Carlo simulations against the multiroot finding method, for calculating the probability of failure for a body subjected to 2 cycoidal pulses, under the assumption that the values of λ follow the uniform distribution. It can be seen

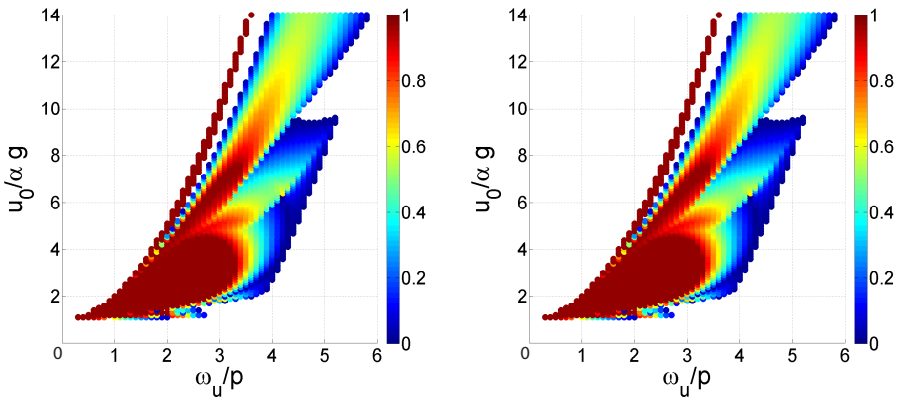

(a) Monte Carlo simulations (b) Multiroots finding method

Figure 2.15 – Probabilistic approach for the Uniform Distribution for two cosinoidal pulses using a) Monte Carlo simulations and b) Multiroots finding method for a body with $p = 2.1401$ and $\alpha = 0.3218$.

that there is an excellent match between the two methods and the same can be observed for any underlying assumed distribution of λ or assumed multi-cycle cycloidal input. Using the multiroot method suggested, the probability of the body failing or surviving can be easily and quickly determined without the need for further dynamic simulations once the roots have been calculated, even if the assumed distribution of λ changes. Hence, Monte Carlo simulations and the associated computational cost may be avoided.

Comparing the single pulses against the multiple pulses, it can be noticed that similar trends in terms of the probabilities of failure can be observed. Despite the fact that equations (2.9) and (2.10) are not applicable any more, the probability of failure still depends on the assumed distribution of λ as can be seen in Figures 2.16(a) and 2.16(b) where a uniform and Truncated Gaussian distribution of λ are compared when the body is subjected to three cosinoidal pulses.

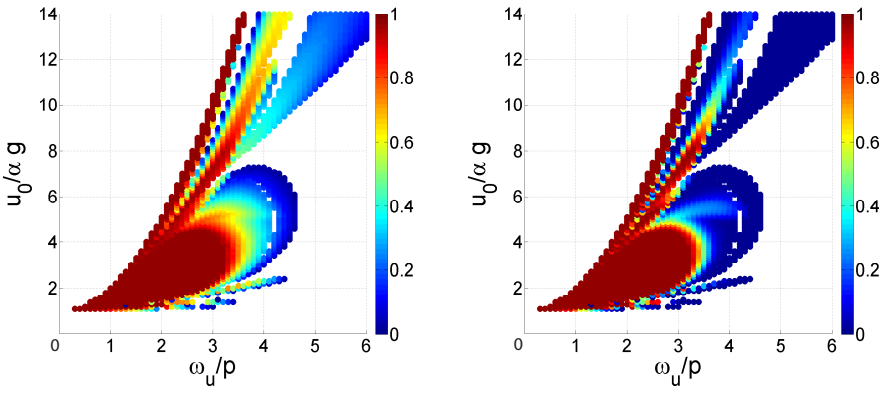

(a) Uniform Distribution

(b) Truncated Distribution

Figure 2.16 – Probabilistic approach for the Uniform Distribution for three cosinoidal pulses using the multiroot finding method using a) the uniform distribution and b) the Truncated Gaussian with $\mu = 0.2$, $\sigma = 0.15$ for a body with $p = 2.1401$ and $\alpha = 0.3218$.

2.6 Conclusions

This Chapter discusses the assumptions involved in modelling the loss of energy during impact in the IPM, even if sliding, uplift, ground deformability and the three dimensional nature of the response can indeed be neglected. It is shown that the location of the vertical impulse during impact could be applied at any point between the post-impact rocking corner of the body and the midpoint of the base without violating any of the assumptions of the model. It was illustrated that the assumption for the value of λ significantly affects the stability of rocking bodies and that the assumption of $\lambda = 0$, common in the literature, is the least conservative assumption compatible with the assumptions of the IPM. A property of the dynamic system was highlighted, where increasing the value of λ for a point in the stability diagram results in expanding the area of failure with impact monotonically.

Defining λ as random variable, the probability of failure of the body is quantified. A probabilistic method based on the dynamic behaviour of the system, defined in equation (2.10), was introduced to calculate efficiently the probability of failure of a rocking body. The method was verified against Monte-Carlo Simulations. It was shown that there may

be points in the stability diagram whose probability of failure is close to 50% and hence the prediction of the model on whether the body survives or fails is associated with a large uncertainty. The size and location of this uncertain region was shown to be dependent on the assumed distribution of λ.

The previous were then extended in terms of stability of a body subjected to multiple pulses. A method was developed to calculate the corresponding probability of failure of the body by extending the probabilistic method presented for the case of multiple transitions between survival and failure. It was again shown that the uncertainty in λ has a significant effect in the stability of a rocking body.

Chapter 3

Experimental investigation of the effect of base geometry on the response of rocking bodies

3.1 Introduction

The dynamic model of the IPM assumes that the contact forces are concentrated at the edges. Nonetheless, as explored in Chapter 2 the forces are not always concentrated at the corners, i.e., a body with a flat base. Whether the forces are concentrated at the edges [64, 10, 65, 8, 11, 18], or distributed along the base [8, 11, 18, 66], is an important distinction in the literature. A relevant conclusion between the effect of concentrated and distributed forces was observed in [11]: a 2D concentrated model was shown to be more stable than a 2D distributed model.

In [11] it was further discussed that the models with concentrated forces are an accurate representation of bodies with feet at the edges whereas distributed forces of bodies with a flat base. Therefore, it should be expected that a body with feet would be more stable than a body with a flat base. This is further demonstrated in this Chapter by studying

experimentally the behaviour of two almost identical bodies apart from their base geometry: one has a flat base (FLBA) while the other has concentrated feet along the two bottom edges (FECO).

Experiments in rocking are not very common as they come with some difficulties: first, the challenges of contact sensing methods for measuring the rocking motion of a rigid block, such as accelerometers sensing large peak accelerations during the impact, which do not correspond with the behaviour of the body. Second, the highly sensitive phenomena on the response of the shake table to identical waveforms [67, 68]. Even though a few papers have experimentally investigated the assumptions of the IPM: uplifting in [7, 69], sliding in [70], a three dimensional (3D) model in [71, 72] and the influence on the response of the bodies for different interface material in [73]; there is not an experimental investigation which studies the effect of different base geometries.

It is therefore the goal of this Chapter to show the effect that different base geometries produce in a rocking body with the description of the energy loss of the IPM. It was shown in Chapter 2 that this energy loss is connected to the base geometry. This is be demonstrated theoretically through this Chapter associating the base geometries with the impulse distribution during impact. Experimental results are calibrated to find the optimal position of the vertical impulse for each body. It is then concluded that the location of the vertical impulse for FECO is close to the future rocking corner, result that is close to the default assumption of the IPM. Therefore, the assumption of the IPM might not be a good estimation while studying a body with flat base.

3.2 Impulse distribution and base geometry

The purpose of this Section is to theoretically present that variations on the base geometry of the block modify the impulse distribution during an impact. In Section 2.2.1, it is assumed that the impact is instantaneous and that the contact force is impulsive. This impulse is

equal to the change of momentum. Hence, the impact dynamics are an algebraic relation between velocities and impulse described by the impulse momentum equations.

Consider the rigid block rocking from the corner $0'$ to 0 as illustrated in Figure 2.2. The rocking corner before impact is $0'$ and the future rocking corner is 0. The velocities along the base of the body resulting before, after and at a random time, τ, during the impact are shown in Figure 3.1(a), 3.1(b) and 3.1(c) and are represented by the superscripts +, -, and $-\rightarrow+$, respectively.

The analysis of this Section is based on the fundamental idea that the velocities occurring follow a linear function of the distance d. While in reality the velocity might not be linear, it renders the proof of this Section easier. In Figure 3.1(a), the vertical velocity of a point at distance d from, $0'$, is denoted as $\dot{y}^{-}_{(d)}$ for the velocity before impact at time $\tau = t^{-}$, in Figure 3.1(c) as $\dot{y}^{+}_{(d)}$ for the velocity after impact at time $\tau = t^{+}$. The velocity during impact in Figure 3.1(b) is defined at a point d at time τ bounded by $[t^{-}t^{+}]$ as $\dot{y}^{-\rightarrow+}_{(d,\tau)}$.

Just before the impact $\dot{y}^{-}_{0'} = 0$, while the velocity at any point, d, varies linearly with respect to d. This is shown in Figure 3.1(a) where all points have a downwards and hence, negative velocity with the magnitude being maximum at 0 and denoted as $\dot{y}^{-}_{0}$. After impact $\dot{y}^{+}_{0} = 0$, while the velocity of any point, d, varies linearly as shown in Figure 3.1(c). Therefore, all points have an upwards and positive velocity with the magnitude being maximum at $0'$ and denoted as $\dot{y}^{+}_{0'}$. It is observed that $\dot{y}^{+}_{(d)}$ and $\dot{y}^{-}_{(d)}$ algebraically decrease with d.

During the impact, the velocities are bounded between pre and post impact velocities. Therefore, the velocity at corner $0'$ changes from zero to positive, while conversely for corner 0 it changes from negative to zero as shown in Figure 3.1(b). Due to the previous assumption of the velocity behaving in a linear manner, $\dot{y}^{-\rightarrow+}_{(d,\tau)}$ is enforced to vary linearly over τ.

During impact, the contact interface applies impulsive forces, q_d, at a distance d from $0'$. It is assumed in this model that the contact interface force at point d can be approximated by an element that resists $\dot{y}^{-\rightarrow+}_{(d,\tau)}$ and that this element provides an opposite impulsive force

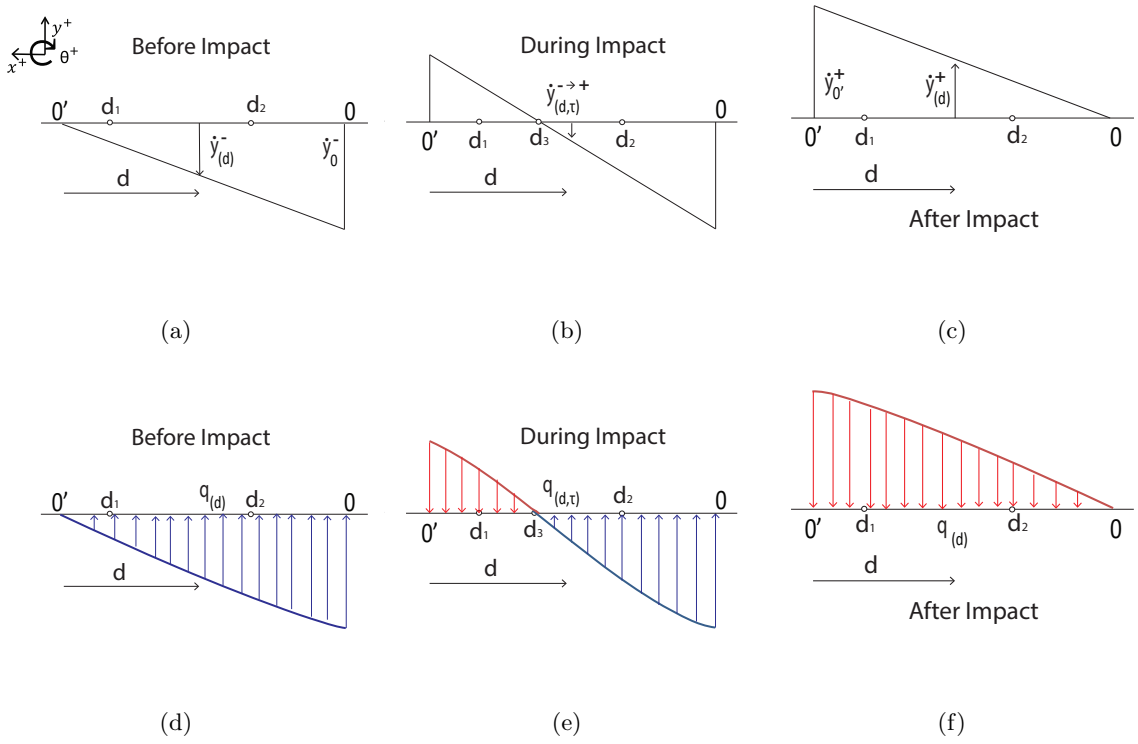

Figure 3.1 – Velocity distributions from Figure 2.2 a) before impact, b) during impact and c) after impact. Force distribution d) before impact, e) during impact and f) after impact. The red arrows represent the tensile forces.

to the velocity of any point d. Before the impact $\dot{y}^{-}_{(d)} < 0$ hence, the impulsive force $q_{(d)}$ is upwards (compressive force) as shown in Figure 3.1(d) while after impact $\dot{y}^{+}_{(d)} > 0$ hence, the impulsive force is downwards (tensile forces) as illustrated in Figure 3.1(f). However, the tensile forces cannot be applied by the contact interface and are instead zero. These tensile forces are represented in Figure 3.1 with red arrows.

Without loss of generality, it can be stated that during impact the impulsive forces applied at a location d at time τ are given by a non-linear function, $\mathscr{Q}$, of $\dot{y}_{(d,\tau)}$. This is expressed in the general form:

$$\begin{aligned} q_{(d,\tau)} &= \mathscr{Q}(\dot{y}_{(d,\tau)}) \qquad \dot{y}_{(d,\tau)} < 0 \\ q_{(d,\tau)} &= 0 \qquad\qquad\quad \dot{y}_{(d,\tau)} > 0 \end{aligned} \tag{3.1}$$

Previously, it was stated that, a specific time instance, the velocity, $\dot{y}^{-\rightarrow+}_{(d,\tau)}$, increases with

d. It is then observed that the forces from equation (3.1) monotonically increase with the velocity: the smallest the velocity is algebraically, the larger the impulsive force is. For instance, in Figures 3.1(b) and 3.1(e), the highest $\dot{y}^{-\rightarrow+}_{(d,\tau)}$ and $q_{(d,\tau)}$ is at corner 0 whereas $q_{(d,\tau)} = 0$ is from corner $0'$ to point d_3 as $\dot{y}^{-\rightarrow+}_{(d,\tau)} > 0$. As a result, the impulsive forces increase with the distance d. For example, consider the two points d_1 and d_2 with $d_1 < d_2$ in Figure 3.1(e), it is then easy to deduce that $q_{(d_1,\tau)} < q_{(d_2,\tau)}$.

The integration of the impulsive force $\int_{t^-}^{t^+} q_d$ gives the impulse j_d. Consider again the two points d_1 and d_2 with $d_1 < d_2$. The impulse of each point is defined as $j_{d_1} = \int_{\tau=0}^{\tau=\tau_1} q_{(d_1,\tau)} d\tau$ and $j_{d_2} = \int_{\tau=0}^{\tau=\tau_2} q_{(d_2,\tau)} d\tau$. Comparing both integrals and using $q_{(d_1,\tau)} < q_{(d_2,\tau)}$, it is then observed that $j_{d_1} < j_{d_2}$. Therefore, the impulse distribution also increases with d in a monotonic non-linear manner.

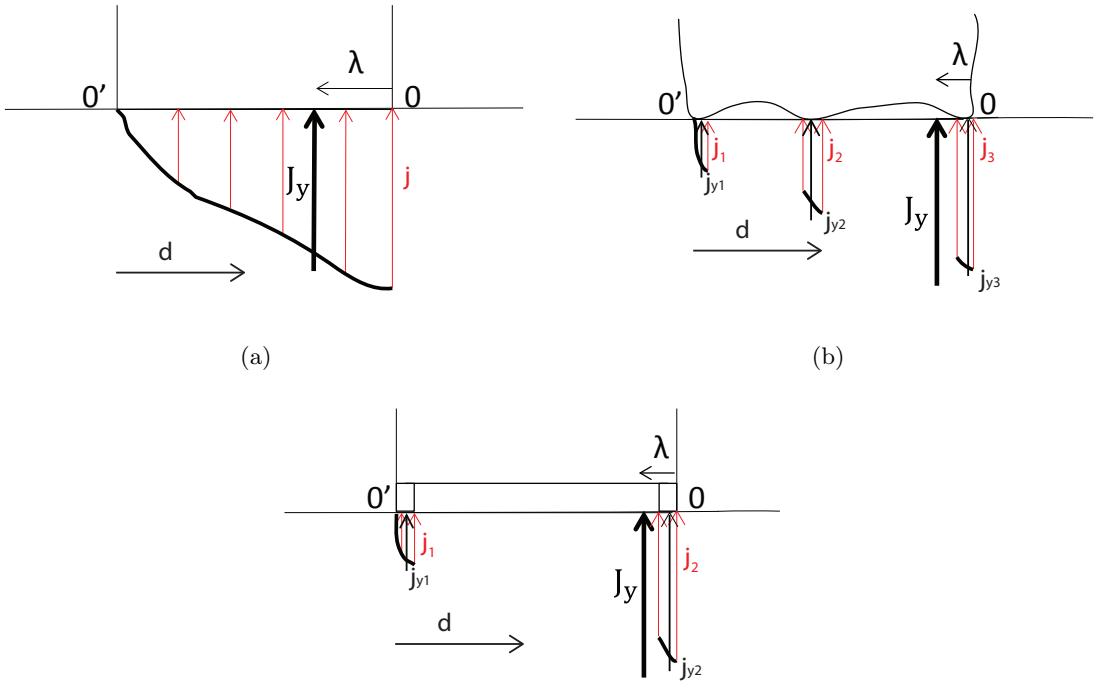

Figure 3.2 – Impulse distribution for a) a flat base, b) a body with three feet and c) a body with feet at the edges.

Figure 3.2 illustrates some examples of the impulse distribution, j, for different contact

interfaces. In Figure 3.2(a), the base of the block is flat hence, the contact interface is between corners $0'$ and 0. The impulse distribution, j, appears all along the base, growing towards corner 0 and being maximum at this corner. If the block has a non-flat base, the base and the ground have multiple contact interfaces as illustrated in Figures 3.2(b) and 3.2(c). Therefore, there is an impulse distribution, j_i, where i refers to the contact interface i. This impulse distribution grows towards corner 0. This is presented in Figures 3.2(b) and 3.2(c). The impulse distributions of a contact interface i can be replaced by an equivalent impulse J_{yi} applied at a distance λ of the centroid of the distribution as illustrated in Figures 3.2(a), 3.2(b) and 3.2(c).

This location λ of J_y varies depending on the base geometry. For flat base bodies as in Figure 3.2(a), J_y is located at a distance λ from the future rocking corner. Thus, at each interface i the centroid of the equivalent distribution is closer to the future rocking corner. For the cases with multiple j_i, an equivalent impulse j_{yi} for each contact interface is considered to then obtain J_y as illustrated in Figures 3.2(b) and 3.2(c). If the length of each feet is the same as in Figure 3.2(c), J_{y_1} is smaller than J_{y2}. Thus, J_y is located at a distance λ substantially closer to 0. Therefore, interfaces close to the future rocking corner have large impulses. For the aim of Figures 3.2(b) and 3.2(c), J_y has been located a bit further from corner 0, however, it is expected that in reality J_y is placed inside the right foot.

It can then be claimed that a large contact interface ends up in a J_y located between the middle base and the future rocking corner while small contact interfaces, as a body with feet, move J_y close to the future rocking corner. Thus, it is expected that bodies with a flat base have a large λ than bodies with multiple contact interfaces as a body with feet at the edges. It can then be concluded that, mechanically, the value of λ can be forced to be anywhere on half the base of the block by simply modifying the contact interface between the ground and the block.

3.3 Experimental set up

This Section describes the experimental set up. All rocking motion experiments were performed on the shake table in Columbia University's Carleton Laboratory (Figure 3.3). The shake table allows for uniaxial horizontal displacements. It is constructed by ANCO R-142 (ANCO Engineers, Inc., Boulder, Colorado) with a 10 t hydraulic actuator controlled by an MTS 793 FlexTest SE (MTS Systems Corporation, Eden Prairie, Minnesota) configured for displacement control. The table has a maximum stroke of ± 0.127 m, maximum velocity of 1.524 m/s, and maximum acceleration of 3 g at the maximum payload of 2 t and is calibrated for operational use in the range of $0 - 100$ Hz.

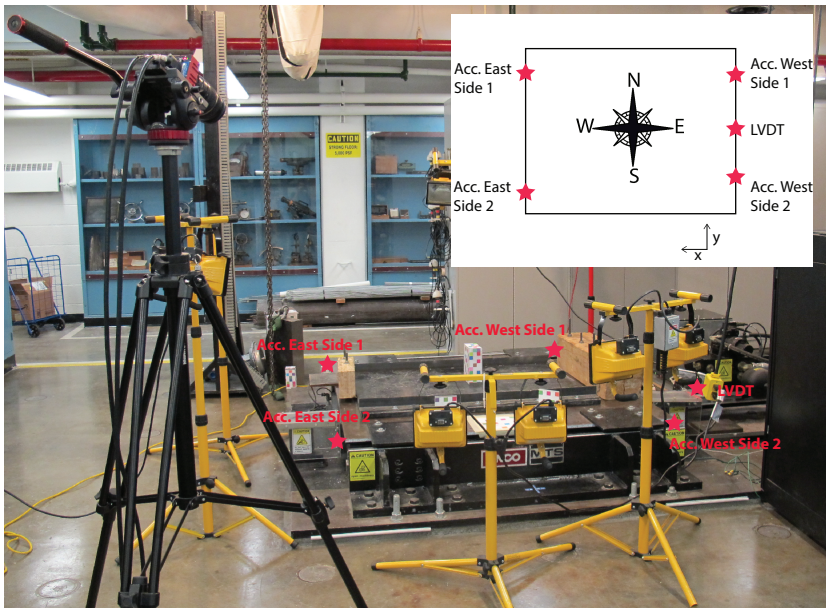

Figure 3.3 – A photograph of the experimental set up.

Additionally, the table is equipped with a Data Physics SignalStar (Data Physics Corporation, San Jose, California [74]) outer loop acceleration controller which was used to calibrate the response of the table versus the desired acceleration ground motions. Acceleration time histories used as an input to the shake table outer controller for all the experiments performed are a realisation from the events: Kobe, Northridge, Hachinohe and one earthquake generated using Eurocode 8 [54] as shown in Figure 3.4.

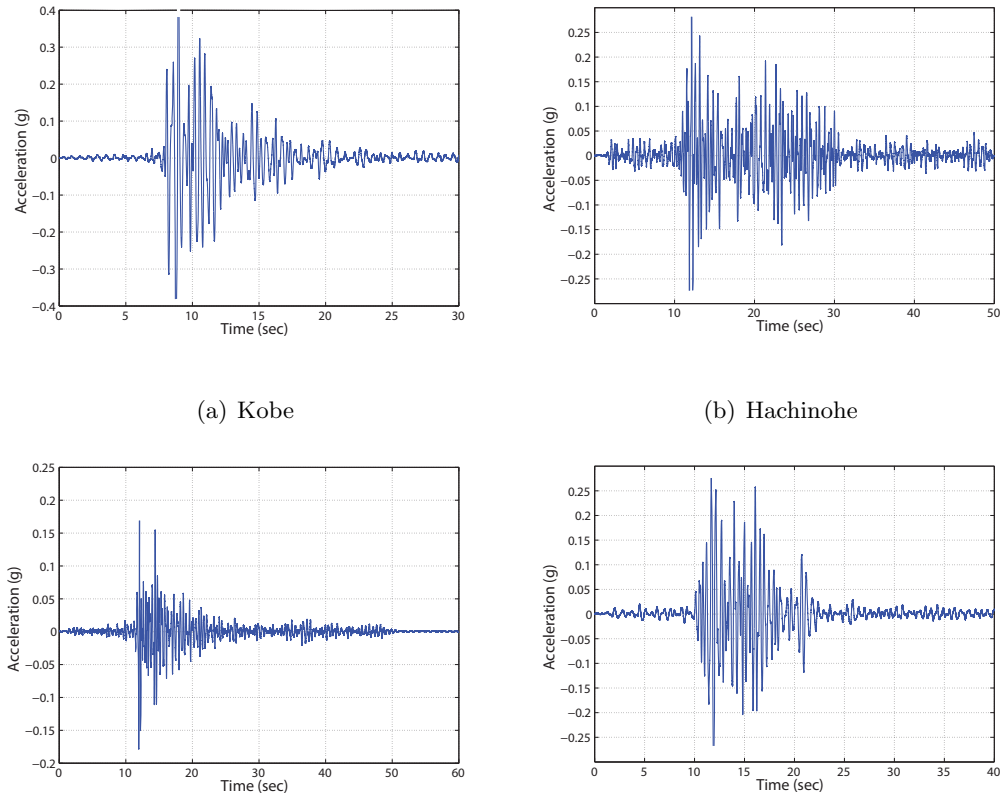

(a) Kobe

(b) Hachinohe

(c) Northridge

(d) EC 8

Figure 3.4 – Output acceleration time histories of the shake table for a) Kobe, b) Hachinohe, c) Northridge and d) EC-8.

The records were uniformly scaled to obtain peak accelerations between 0.2 g and 1.4 g. To determine the optimal signal input for the shake table, an iterative process is imposed based on minimising the error between the desired and obtained shake table acceleration (measured by the controller's accelerometer). The latter was repeated for each time history used as an input each time that it was scaled. To conserve repeatability, this optimisation process for each time history is saved and used for all the runs. References to each of the earthquake inputs are shown in Figure 3.4 for peak accelerations of 0.2g. However, as stated in [75, 76], the dynamic combination between the actuator and the shake table are unable to exactly replicate the inputs.

Four accelerometers are used to record the table motion. The sensors are called: ac-

celerometers West Side 1 and East Side 1 and West Side (2) and East Side (2) and their location on the table is shown in Figure 3.3. All accelerometers have a sensitivity of 100 mV/g except Acc. West Side 1 that has a sensitivity of 1000 mV/g. All sensors have a frequency range of 0.06 - 450 Hz. They were attached to the table as illustrated at the top left part of Figure 3.3, which presents the shake table orientation as seen from above. A National Institute of Standards and Technology (NIST) traceable linear variable differential transformer (LVDT) was used to measure the shake table displacement along the axis of excitation. The experimental set up is shown in Figure 3.3. Note that in Figure 3.3 lights and camera are presented but their results have not been used in this study.

In this work two bodies of almost identical dimensions, cut from solid steel stock, shown in Figure 3.5, with different base geometries are studied experimentally. FLBA, is a rectangular block with a flat base which had been cut from solid steel stock. Its dimensions are 70 x 200.17 x 140.24 mm as in Figure 3.5(a). The second body, FECO, is a rectangular block with dimensions of 70.08 x 200.10 x 140.12 mm. Two steel angles were placed along the two bottom edges of the second body, resulting in the geometry shown in Figure 3.5(b). The effect is the modification of the base geometry of the body so that it now practically has two 'feet' with dimensions 140.12 x 3.32 x 2.94 mm. The manufactured blocks are illustrated in Figure 3.6. For videogrammetry purposes [72], paper sheets with printed targets were placed on the block faces. These have negligible weight in comparison to the blocks.

The blocks were placed on a rubber mat, 0.94 x 1.2 m and 0.0254 m thick, placed on top of the shake table surface to serve as a foundation and protect the table surface from hard impacts. It reduces the high peak accelerations occurring at impact time between two metal surfaces. This foundation is considered practically rigid due to the ratio between the stiffness of the rubber mat and the small mass of each block. The weight of each block is 15.40 Kg and 15.42 Kg for FLBA and FECO, respectively. The rubber mat has a durometer of 80 and a stiffness per unit area of $2.482e10^5$ KN/m/m^2 [77]. Thus, the static deflection is $6.21e10^{-6}$

mm and 6.20e10^{-6} mm for FECO and FLBA, respectively. Therefore, the assumption of the rubber mat being practically rigid is justifiable.

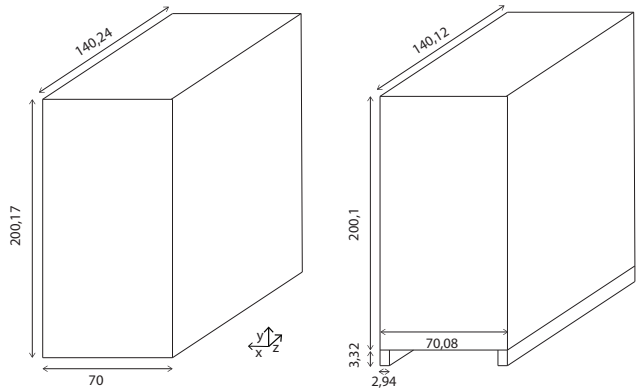

(a) FLBA (b) FECO

Figure 3.5 – Physical dimensions of blocks a) FLBA, b) FECO used in the experiments. Dimensions are shown in mm.

It should further be noted through comparing the two bodies in Figure 3.5 that their dimensions are practically identical, with FECO being slightly taller due to the added feet. While the difference is not significant, if it did have any effect it would be of making FECO slightly more prone to failure than FLBA. However, it is later shown that in the experiments the FLBA was shown to be more prone to fail. Hence, the fact that FECO is slightly more slender has not affected the main conclusions of this work.

The blocks are manufactured to be symmetric rectangular prisms in correspondence to the assumptions of the deterministic model used in Section 2.2.1. To avoid the 3D rocking response [18] the third dimension of both bodies, w, is substantially bigger than the width, b, and comparable to the height, h, as it can be seen in Figure 3.5. Moreover, before each run the bodies are placed so that the dimension parallel to their width, b, is parallel to the axis of excitation.

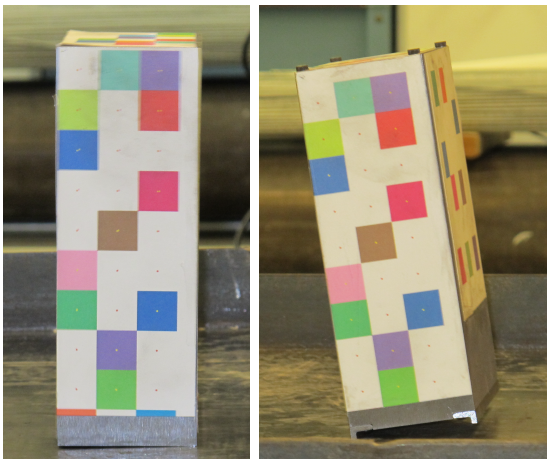

(a) FLBA (b) FECO

Figure 3.6 – Photograph of the rocking blocks a) Flat body, b) Body with feet.

3.4 Experimental investigation

This Section examines how the two different base geometries affect the stability of the rocking bodies when subjected to ground accelerations. For this aim, some experiments executed on FLBA and FECO, previously described, are referred. Each block is placed on the table by its own and is subjected to the selected set of earthquakes at different peak amplitudes. Each realization of an earthquake is referred by its target PGA from now on.

To ensure reproducibility of the experiment, all results are repeated at least three times for a given earthquake and PGA. If all these result in survival (or failure), it is considered that the block survives (or fails). In contrast, if the first three runs end in a mix between survival and failure, more runs are conducted until at least a total of three survivals or three failures are observed.

For any given earthquake, a transition PGA is referred from here after as a PGA for which the survival/failure status of the body is different than the immediately smaller examined PGA. For reasons of brevity, in this work, S and F refer to the body surviving or failing during a run, respectively. Following what was stated earlier for a specific PGA of an earthquake, if all the runs lead to survival or failure, the result is denoted a S or F, respectively. If more

Table 3.1 – Kobe

KOBE				
PGA (g)	**Flat Base**		**Feet Base**	
	Test	**Outcome**	**Test**	**Outcome**
0.2	SSS	S	SSS	S
0.3	SSS	S	SSS	S
0.35	FFF	F	SFFSFFF	F*
0.4	FFF	F	SFFSSFSS	S*
0.5	FFF	F	FFF	F
0.6	FFF	F	FSSFS	S*
0.7	FFF	F	FFF	F
0.9	FFF	F	FFF	F
1	FFF	F	FFF	F

Table 3.2 – Hachinohe

HACHINOHE				
PGA (g)	**Flat Base**		**Feet Base**	
	Test	**Outcome**	**Test**	**Outcome**
0.2	SSS	S	SSS	S
0.3	SSS	S	SSS	S
0.35	SSS	S	SFSSFSS	S*
0.4	FFFSFF	F*	FSSSS	S*
0.45	FFF	F	FFF	F
0.6	FFF	F	FFF	F
1	FFF	F	FFF	F
1.1	FFF	F	FFF	F

than three runs, are necessary for a PGA, then if three S or F are observed, the result is indicated by a superscript *, i.e., S^* or F^*, respectively. The superscript * indicates that it is likely that the examined PGA is within the vicinity of a transition PGA. The experimental

Table 3.3 – Northridge

Northridge				
PGA (g)	**Flat Base**		**Feet Base**	
	Test	**Outcome**	**Test**	**Outcome**
0.3	SSS	S	SSS	S
0.4	SSS	S	SSS	S
0.7	SFSSSS	S*	FFSFSSF	S*
0.9	FSFSSFS	S*	SSFSS	S*
1	FFF	F	FFSFF	F*
1.05	FSSFS	F*	SSSS	S
1.1	FFF	F	FFF	F
1.4	FFF	F	FFF	F

Table 3.4 – EC-8

EC-8				
PGA (g)	**Flat Base**		**Feet Base**	
	Test	**Outcome**	**Test**	**Outcome**
0.2	SSS	S	SSS	S
0.45	SSS	S	SSS	S
0.5	FSFSFFSSF	F*	SSS	S
0.6	FFF	F	SSFSS	S*
0.7	FFFF	F	FSFSSSFFF	F*
1	FFF	F	FFF	F
1.4	FFF	F	FFF	F

results for each block for each earthquake are illustrated in Tables 3.1 to 3.4 and Table 3.5 summarises the transitions observed. Each Table refers to a different earthquake in its title and rows correspond to the different PGAs. The column called outcome specifies the conclusion drawn for each of the PGAs.

Table 3.5 – Transitions

Earthquake	Transitions	FLCA	FECO
Kobe	1	0.3 → 0.35	0.3 → 0.35
	2	-	0.35 → 0.4
	3	-	0.4 → 0.5
	4	-	0.5→ 0.6
	5	-	0.6 → 0.7
Hachinohe	1	0.35 → 0.4	0.4 → 0.45
Northridge	1	0.9 → 1	0.9 → 1
	2	-	1 → 1.05
	3	-	1.05 → 1.1
EC-8	1	0.45 → 0.5	0.6 → 0.7

Previous studies [68, 67] have pointed out some factors that could explain different survival/failure outcomes among runs for the same body subjected to a specific earthquake and PGA, such as: accumulation of damage, ambient vibration, misalignment of the block and differences in the acceleration of the shake table. However, for this set of conducted experiments, damage of the blocks or the rubber was not observed, the ambient vibration of the lab was insignificant as experiments were not run in parallel to other vibration inducing experiments, and the blocks were re-aligned before each run. While the surface of the rubber support is slightly inhomogeneous, it appears that the small differences of the actual table accelerations between different runs are the major source of this lack of exact reproducibility of the outcomes. Figure 3.7(b) illustrates a zoom of two time histories recorded from Acc. East Side 1 for Kobe earthquake for $PGA = 0.6$ g for two different tests. The differences between them are clearly observed as is the lack of reproducibility of the table for the same target PGA.

It has been demonstrated that the actual PGAs from the table are slightly different.

However, these small variations might or might not affect a body. For example, consider the case of FLBA with Kobe earthquake, FLBA fails from $PGA = 0.35$ g to $PGA = 1$ g in all the tests as observed in Table 3.1, hence, it should not be expected that this lack in reproducibility would affect the response when a body consistently survives or fails. In contrast, these variations might affect a body that has transitions around a PGA. For example, consider now FECO with also Kobe earthquake. In Table 3.1 is shown that FECO has a transition for a $PGA = 0.6$ g. Observe that five tests were done for FECO, for which the body fails twice and survives the rest. Therefore, these variations matter in this case. Note that not only the PGA changes, the time history, the waveform and the frequency content are also slightly different.

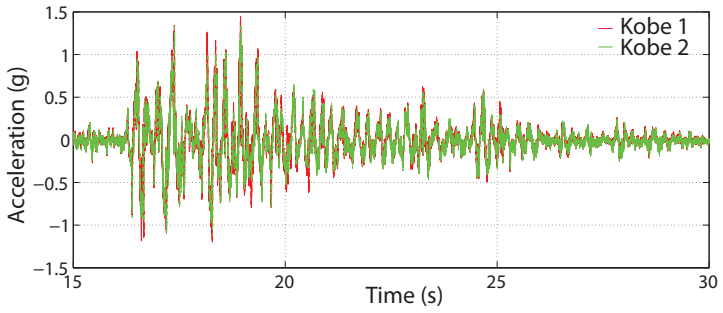

(a)

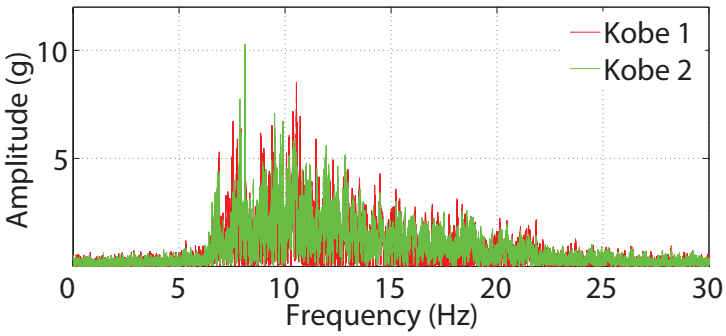

(b)

Figure 3.7 – a) Comparison between two signals recorded from the shake table for the same PGA for Kobe earthquake. Zoom from $t = 12$ s to $t = 14$ s. b) Frequency domain of the signals.

Comparing the results presented in Tables 3.1 to 3.4, it is clearly observed that FLBA is less stable than FECO. For any value of PGA of an earthquake for which FLBA survives, FECO also survives. However, there are multiple combinations of earthquakes and PGA for which FECO survives but FLBA does not.

In terms of the transitions summarised in Table 3.5, it can be seen while using Kobe earthquake that the FLBA fails from $PGA = 0.35$ g whereas FECO has several transitions between failure and survival as the PGA is increased. It is observed that also Northridge has several transitions between survival and failure and re-transitions from failure to survival. The fact that there may be more than one transition amplitude for a sinusoidal acceleration input of a given frequency has been observed in [3, 26]. Figures 3.8(a) and 3.8(b) represent the stability diagram of a rocking body with dimensions as FLBA and FECO subjected to a single sinusoidal acceleration pulse under the assumed values of $\lambda = 0$ and $\lambda = 0.3$, respectively. The stability diagram occurs by varying the frequency ω_u and amplitude of the sinusoidal pulse a_g in the horizontal and vertical axis, respectively, and denoting the outcome of the body in terms of survival or failure. For example, in both cases for $\omega_u/p = 4$, as $u_0/\alpha g$ is increased, the body goes from survival to failure with impacts, to then re-transition to survival and a final transition to failure. While the earthquakes used in the experiments are not single sinusoidal pulses, a similar phenomenon is observed in Table 3.5 where for a given target waveform the PGA scaling leads to transitions. For example, for FECO in Table 3.5, as the value of the PGA is increased from 0.2 g to 1 g, the block experiences three transitions from survival to failure at the following PGAs.

However, it can also be observed in Table 3.5 that there are earthquakes with no more than one transition between survival and failure as for example Hachinohe. This can be associated qualitatively to Figure 3.8(a), where such cases occur for pulses of larger frequencies. Therefore, it is likely that the block is in an area where there is no more than one transition as for example in Figure 3.8(a) for $\omega_u/p = 1$ or $\omega_u/p > 5.5$. To approximately know where

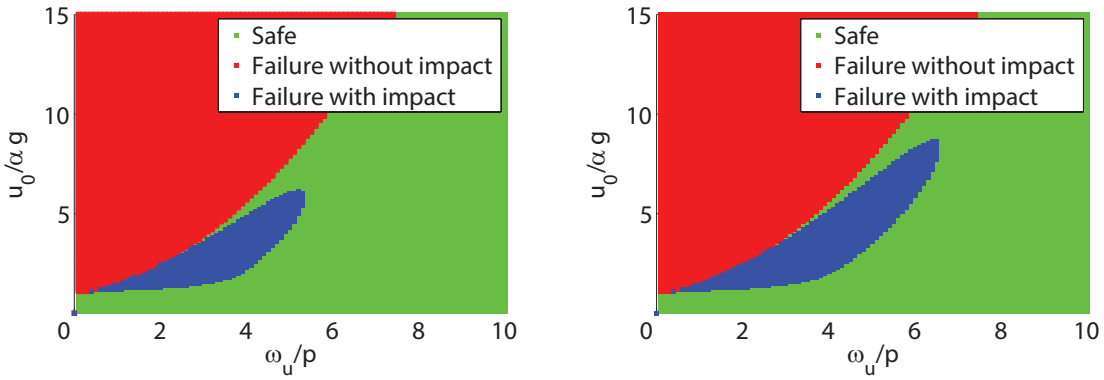

(a) $\lambda = 0$ (b) $\lambda = 0.3$

Figure 3.8 – Stability diagrams for a single sinusoidal pulse using the IPM for a) $\lambda = 0$ using the dimensions of FECO and b) $\lambda = 0.3$ using the dimensions of FLBA.

this earthquake is located on the stability diagram, the fast Fourier transform is obtained showing that, in fact, Hachinohe is located for $\omega_u/p > 5.5$. Similarly, for EC-8 earthquake, both blocks have only one transition between survival and failure.

It is also of interest to comment on the effect of the earthquakes. From Table 3.5 it is clearly observed that Kobe is the most catastrophic earthquake. Both blocks fail for the first time for a low value of $PGA = 0.35$ g. This behaviour is followed by Hachinohe, for which FLBA fails for $PGA = 0.4$ g and FECO for $PGA = 0.45$ g, EC-8, for which FLBA fails for $PGA = 0.5$ g and FECO for $PGA = 0.7$ g and Northridge for which both blocks fail for $PGA = 1$ g. In terms of transitions, the Kobe earthquake seems to be more sensitive to the changes of amplitudes. Five different transitions were observed for FECO. It also has narrow transitions for lower PGAs contrasting with Northridge which has narrow transitions for greater PGAs. It is therefore observed from Table 3.5 that Kobe is the earthquake that produces the most failures and that Northridge is the safest one for both blocks.

To sum up, experimental results comparing FLBA and FECO conclude that despite FECO being slightly slender than FLBA, FECO is more stable than FLBA.

3.5 Calibration of the IPM using the experimental results.

As it was explained in Section 2.2.1, the energy loss is expressed through the parameter λ. Hence, the objective of this Section is to find the most likely value for FECO and FLBA based on the experimental results. To achieve that, the accelerations recorded on the shake table during each experiment is used as the input in equation (2.1) and the results occurring for different λ are compared versus the actual survival/failure outcome of that run.

An example of signal recorded from the accelerometers with a sampling frequency of 2500 Hz is shown in Figure 3.9 for Kobe PGA=0.35 g when FECO is placed on the table. In the Figure, the recordings from Acc. West Side 2, Acc. East Side 1 and Acc. East Side 2 are illustrated. It is observed that the signals recorded from the accelerometers present high-frequency components, i.e., Acc. East Side 1 has three high frequency components at 23.49, 23.98 and 29.34 s. These frequency components would correspond to large displacements that may not be accurate measurements. Indeed, they are not rigid body accelerations and correspond to a local high frequency deformation of the table due to the impact. It should be noted that the deterministic model cannot handle deformation accelerations as inputs. Therefore, these high frequency components need to be removed.

In order to alleviate this problem, a Finite Impulse Response (FIR) lowpass filter with a cut-off frequency of 100 Hz is applied. The filtering is achieved in Matlab using the *filtfilt* command [78]. Consider again Figure 3.9, it is observed on the figure that the high frequency components appearing in the recorded time history from, i.e., Acc. East Side 1 are removed when the filter is applied.

3.5.1 Probability of agreements

The aims of this Section are to investigate whether the assumed value of λ affects the IPM prediction on the outcome of a run, and observe the frequency of agreements of the theoretical model for a given λ versus the experimental results. Subsequently an optimal value of λ is

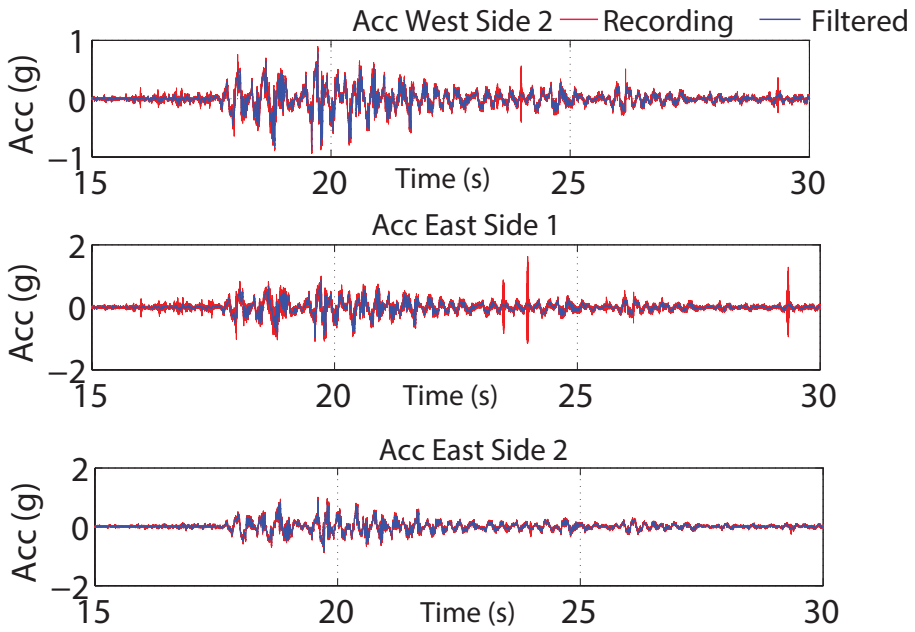

Figure 3.9 – Recording of Kobe 0.35 g and the obtained record after removing the noise signal.

defined in this Section as the one that maximizes the frequency of agreements.

The input that is used in the model in equation (2.1) is the accelerometer that produced the least noticeable high frequency components during that test. The signal is further filtered as previously mentioned. This signal is selected out of the three accelerometers used. Different values of λ (with an interval of 0.1) are used and the outcome of the body for that value of λ is recorded to see whether the bodies survive or fail for each test. This process is repeated for each of the runs presented in Tables 3.1, 3.2, 3.3 and 3.4 and the agreement between the model and the run is noted. Then the probability of agreement for a given earthquake, for a given PGA and for a given λ is defined as:

$$P_{E_{Bka}}(\lambda) = \frac{\sum_{q=1}^{Q_{E_{Bka}}} A^q_{E_Bka}(\lambda)}{Q_{E_Bka}} \tag{3.2}$$

where B refers to FECO or FLBA, $k = 1, 2, 3, 4$ corresponds to the earthquakes Kobe, Hachinohe, Northridge or EC-8, respectively, a refers to the corresponding PGA of that run, $q = 1, ..., Q_{E_{Bka}}$ is the index that corresponds to different runs of a given E_{Bka} and $A^q_{E_{Bka}}$

denotes the agreement or disagreement of the model for that assumed value of λ with the outcome of run q for the examined E_{Bka}.

Figure 3.10(a) illustrates the results obtained from Kobe for FLBA using equation (3.2). It is observed that for a PGA greater than 0.4 g any λ completely agrees with the experimental result. A similar result occurs for $PGA = 0.2$ g for all λs. In contrast, λ has a significant effect on $P_{E_{Bka}}(\lambda)$ for PGA$<$ 0.4 g. For example, in Figure 3.10(a) for a $PGA = 0.35$ each λ disagrees with the experimental result. Similarly, Figure 3.10(b) presents $P_{E_{Bka}}(\lambda)$ for FECO. In this case, it is observed that all $P_{E_{Bka}}(\lambda)$ does not depend at all on the value of λ (only results for $\lambda = 0$ and $\lambda = 0.2$ are illustrated as the results for all values are indistinguishable). Note that in Figure 3.10(b) for PGAs between $[0.2-0.4]$ g, 0.5 g and between $[0.7-1]$ g, there is a complete agreement of the IPM with experimental results regardless of the assumed λ. Equally for the remaining values, there is a level of disagreement that cannot be corrected by assuming a different value of λ. For the latter cases, it is expected that some of the other assumptions of the IPM are not satisfied, for example the assumption that the body behaves like a pendulum in the dynamic patterns.

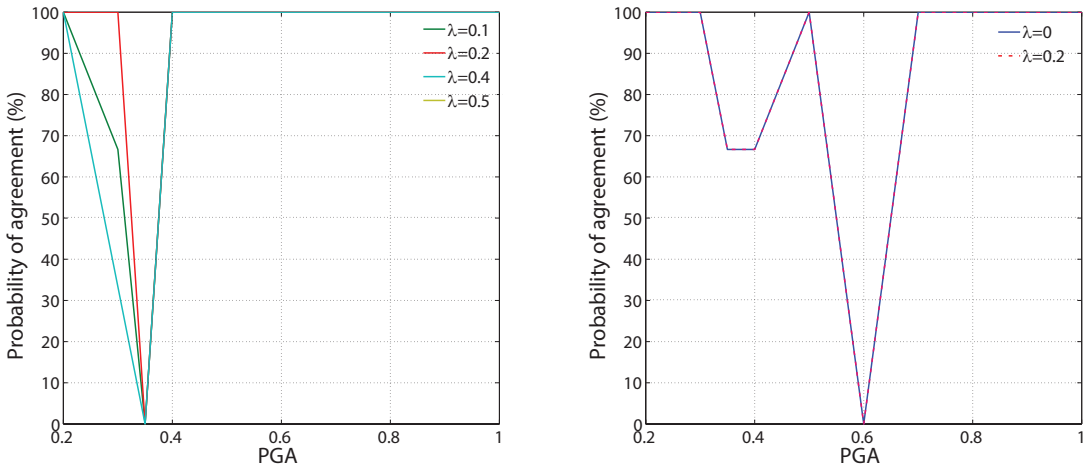

(a) Kobe FLBA

(b) Kobe FECO

Figure 3.10 – $P_{E_{Bka}}(\lambda)$ a) FLBA, b) FECO. The probability is presented in percentage.

The above cases result in not having any single value of λ for which the experimen-

tal results are obtained for any run. Assuming that all PGAs are equally important, the probability of agreement of a potential λ for an earthquake, k, can be calculated as:

$$P_{E_{Bk}}(\lambda) = \frac{\sum_{i=1}^{I_{E_{Bka}}} P^{i}_{E_{Bka}}(\lambda)}{I_{E_{Bka}}} \tag{3.3}$$

where $I_{E_{Bka}}$ is the total number of PGAs examined per earthquake used which varies for each earthquake. Similarly, a probability of agreement for an assumed value of λ for all the earthquakes is obtained as follows:

$$P_{TB}(\lambda) = \frac{\sum_{k=1}^{k=4} P_{E_{Bk}}(\lambda) I_{E_{Bka}}}{\sum_{k=1}^{k=4} I_{E_{Bka}}} \tag{3.4}$$

Having defined, $P_{E_{Bk}}(\lambda)$ and $P_{TB}(\lambda)$, it can be considered that an optimal value of λ for a given earthquake for each of the bodies occurs by the value of λ maximizing $P_{E_{Bk}}(\lambda)$. A criterion that can be used to obtain an optimal value of λ overall for each body is that of maximizing $P_{TB}(\lambda)$. Figure 3.11(a) illustrates $P_{E_{Bk}}(\lambda)$ and $P_{TB}(\lambda)$ for FECO, for different earthquakes. It is observed that in Figure 3.11(a) each earthquake results in a different optimal value of λ. For example, when FECO is subjected to the recordings of Kobe, all values of λ in the range $[0 - 0.5]$ appear to be equally likely with $P_{E_{Bk}}(\lambda) = 85\%$. Similarly, for EC-8 values of λ in the range $[0 - 0.9]$ appear to be equally likely, however the $P_{E_{Bk}}(\lambda)$ is smaller, 62%. In contrast, when recordings of Hachinohe and Northridge are used, λ appears to have values that maximize $P_{E_{Bk}}(\lambda)$ at $\lambda = 0.3$ and $\lambda = 0.1$, respectively. Using equation (3.4), the most likely value of λ for FECO, regardless of the earthquake, was found to be $\lambda = 0.1$.

A similar procedure is followed for FLBA. Figure 3.11(b) shows these results. When FLBA is subjected to the recordings of Kobe, there is a range of most likely values of λ between $[0 - 0.25]$ and for EC-8 the most likely values are between $[0 - 0.9]$, whereas for the recordings of Hachinohe λ has its most potential value at 0.3 which turns out to be the same when FLBA is subjected to Northridge recordings. It is then observed that the most potential value of λ, regardless of the event, was found to be at $\lambda = 0.3$ for FLBA.

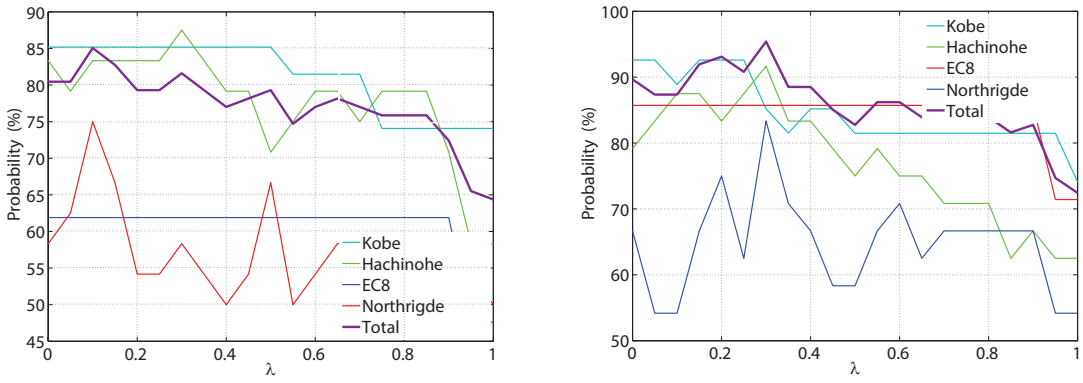

(a) FECO

(b) FLBA

Figure 3.11 – $P_{E_{Bk}}(\lambda)$ and $P_{TB}(\lambda)$ for a) FECO and b) FLBA, for each event and the for the total events.

It is observed in Figure 3.11, that for any of the bodies, the optimal value of λ depends on the examined earthquake. This is reasonable as λ is a function of the pre-impact velocity $\dot{\theta}^{-}$. Obviously, each earthquake leads to multiple impacts with different $\dot{\theta}^{-}$. Therefore, λ differs per input.

It is also of interest to find out if there is any optimal value of λ with greater accuracy than 0.1 that maximizes this frequency of agreements for each body regardless of the earthquake. To this end, a derivative-free-method in MATLAB called *fminsearch* was used. In order to find the optimal value of λ around the peak observed in Figure 3.11, the initial conditions were set as $\lambda = 0.3$ and $\lambda = 0.1$ for the FLBA and FECO, respectively. The optimization procedure leads to $\lambda = 0.242$ and $\lambda = 0.105$ for FLBA and FECO, respectively.

It was pointed out that equation (3.3) takes into account all the PGAs as if each of them were equally important. However, it was observed in Figure 3.10 that for a specific test, there are PGAs for which the body survives or fails regardless of the λ. Also, there are specific PGAs for which the result is different from the experimental outcome regardless of the value of λ. To avoid these, equation (3.3) is calculated by excluding PGAs in which λ has no effect:

$$P^*_{E_{Bk}}(\lambda) = \frac{\sum_{i=1}^{I_{E^*_{Bka}}} P^i_{E^*_{Bka}}(\lambda)}{I_{E^*_{Bka}}} \tag{3.5}$$

where the symbol $*$ refers, in this case, to the subset of earthquakes selected.

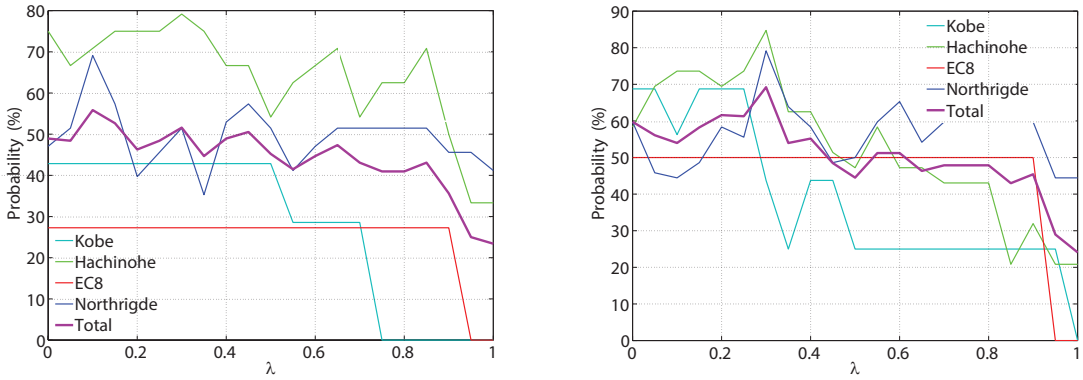

(a) FECO (b) FLBA

Figure 3.12 – Potential value of λ for a subset of PGA a) FECO and b) FLBA, for each event and for the total events.

In attempting to understand the effect of the aforementioned condition, Figure 3.12 illustrated $P^*_{E_{Bk}}(\lambda)$ for both blocks. The same observations from Figure 3.11 practically hold for the subset: each earthquake results in a different optimal value of λ. For example, when FECO is subjected to the recordings of Kobe, all values of λ in the range $[0-0.5]$ appear to be equally likely with $P^*_{E_{Bk}}(\lambda) = 42\%$. Similarly for EC8 values of λ in the range $[0-0.9]$ appear to be equally likely, however the $P_{E_{Bk}}(\lambda)$ is smaller, 28%. In contrast, when recordings of Hachinohe and Northridge are used, λ appears to have values that maximize $P^*_{E_{Bk}}(\lambda)$ at $\lambda = 0.3$ and $\lambda = 0.1$, respectively. Using equation (3.4), the most likely value of λ for FECO, regardless of the earthquake, was found to be $\lambda = 0.1$.

Similarly, Figure 3.12(b) shows the potential value of λ for the FLBA. Both earthquake recordings, Hachinohe and Northridge, have their optimal value of λ at 0.3 whereas recordings from Kobe and EC-8 have an interval of possible potential values. Finally, the potential value of λ, regardless of the earthquake, is located at 0.3. It is observed that the most probable

value of λ for each body is in agreement with the previous result where all the PGA were taken into account. However, even if for the subset of earthquakes $P^*_{E_{Bk}}(\lambda)$ decreases this is not really a problem as this Section aims to find the optimal value of λ for the experimental data.

An optimization procedure is also applied to the subset of earthquakes to find the potential value of λ with greater accuracy than 0.1. As expected, the optimization procedure also leads to the same optimal value of λ than when all the signals were used. Therefore, implementing the subset and all the signals ends in obtaining the same optimal values of λ.

3.5.2 Bayesian updating

At the beginning of this Section, it was illustrated in Figure 3.9 that the signals recorded by the accelerometers are not identical. This was attributed to the deformation of the shake table due to the impacts with the body. As a result, there is a physical noise contaminating about the pure rigid body acceleration signal of the table. This noise is assumed to be a zero mean Gaussian noise. The properties of this noise were estimated by comparing the individual signals to the mean of the three signals, which was considered to be a better representation of the table rigid body acceleration. The occurring mean of square ratio (RMS) appears to be in the range between 3% to 8% depending on the test. In order to take this process noise into account, one hundred noise signals with a RMS of 5% were generated and added to the corresponding average signal. Thus, for each of the runs in Tables 3.1, 3.2, 3.3 and 3.4, the deterministic model was subjected to those signals leading to a probability of prediction from the model rather than a deterministic outcome.

The generated inputs per test are subjected to the IPM and the probability of failure, P_F, and the probability of survival P_S are calculated as follows:

$$\begin{aligned} P_F(\lambda) &= N_F/N_T \\ P_S(\lambda) &= N_S/N_T \end{aligned} \tag{3.6}$$

where N_F and N_S denote the number of inputs which fail or survive, respectively and N_T is the total number of inputs, in this case, one hundred.

To find the optimal values of λ, the Bayesian updating procedure is implemented [79]. In this problem, λ is a continuous variable hence, only ϕ is defined. Thus, using Bayes' rule $\phi(\lambda = \lambda_i)$ given the evidence, L, is defined as:

$$\phi(\lambda = \lambda_i | L_{1,\dots,Q}) = \frac{R_e(\lambda_i)\phi(\lambda = \lambda_i | L_{1,\dots,Q-1})}{\int_{\lambda=0}^{\lambda=1} R_e(\lambda)\phi(\lambda | L_{1,\dots,Q-1})d\lambda} \tag{3.7}$$

where R_e is the utility function depending on the observed evidence from the experiment: if the body fails $R_e = P_F(\lambda_i)$ and if it survives $R_e = P_S(\lambda_i)$. $\phi(\lambda = \lambda_i | L_{1,\dots,Q-1})$ is the prior which is assumed to be uniformly distributed for the first iteration. For the following cases, $\phi(\lambda = \lambda_i | L_{1,\dots,Q-1})$ is updated with the previous posterior, $\phi(\lambda = \lambda_i | L_{1,\dots,Q})$.

The probability density function for each block using equation (3.7) is shown in Figure 3.13. The value of λ that maximizes the ϕ, i.e., the likelihood of each body is $\lambda = 0.225$ and $\lambda = 0.025$ for FLBA and FECO, respectively. It is clearly observed that both of them have a sharp maximum, meaning that the data is leading the method to be relatively confident about the result. In Figure 3.13 a further zoom in the area of the peaks is provided where the ϕ is further discretized for an increment of λ equal to 0.023. The values of λ that maximise the likelihood and hence, the optimal values of λ are $\lambda = 0.221$ and $\lambda = 0.025$ for FLBA and FECO, respectively.

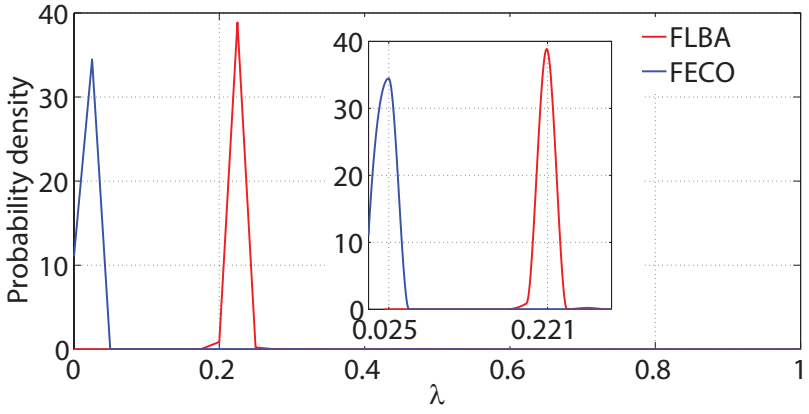

Figure 3.13 – Probability density functions for FLBA and FECO using Bayesian updating.

The Bayesian updating procedure was also studied only for the subset of signals defined on the previous Section; similar to what was observed in the previous Section, taking into account this subset does not change the most likely values of λ. For this reason, the figure is no longer shown as again the values of λ that maximise the likelihood are $\lambda = 0.221$ and $\lambda = 0.025$ for FLBA and FECO, respectively.

This Sections shows how one can determine the density distribution of this uncertainty related to λ using only Bayesian inference. Implementing the optimization procedure for FLBA, the optimal value of λ is 0.242 whereas with the Bayesian updating procedure $\lambda = 0.221$. Therefore, it can be assumed that in any case the optimal value of λ for FLBA is between 0.211 and 0.242. For FECO, the optimization procedure ended in an optimal value of $\lambda = 0.105$ while with the Bayesian updating procedure $\lambda = 0.025$. Thus, for FECO, the optimal value of λ might be between 0.025 and 0.105. However, the results of the Bayesian update are more trustful because the physical noise of the acceleration of the signals is taken into account.

3.6 Discussion and conclusions

It has been shown through this Chapter that, experimentally, the base geometry affects the stability. FECO locates the vertical impulse closer to the future rocking corner than FLBA. Based on the optimal values of λ obtained in the Bayesian updating approach, stability diagrams for a single sinusoidal pulse are produced as in Chapter 2. Figure 3.14(a) represents the boundary lines between survival and failure for $\lambda = 0.025$ and $\lambda = 0.221$. The common assumption used in the literature of $\lambda = 0$ is also illustrated in the figure. The similarity of the curves between $\lambda = 0$ and $\lambda = 0.025$ and the differences between $\lambda = 0$ and $\lambda = 0.221$ is clearly observed. Therefore, the common assumption in the literature appears to be suitable for FECO but not for FLBA for which $\lambda = 0$ is a non-conservative assumption. It is hence of extreme importance to identify the value of λ.

The optimal values obtained in this work are for the bodies presented and the inputs used. However, these values might be different if a body has different dimensions and if the support base material was different. For instance, during the process of these presented experiments, both blocks were also placed on a steel mat; it appeared that FLBA was failing more often than when it was placed on the rubber mat indicating that the value of λ further increases when the steel mat is used. In [57], stability diagrams for different values of λ are illustrated showing that, in fact, as λ increases the block is more prone to fail. Therefore, the need of identifying the value of λ for FLBA was observed even for the steel mat.

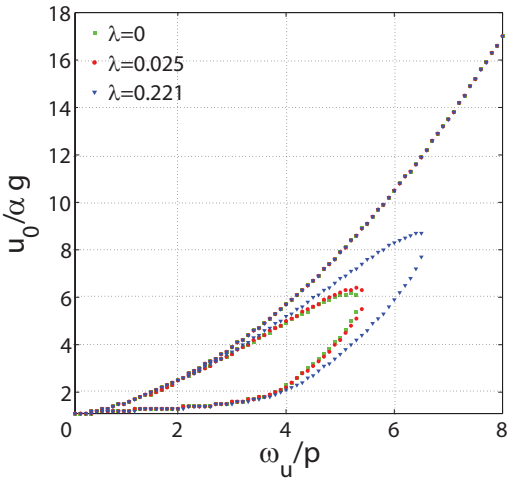

(a)

Figure 3.14 – Failure-safety boundaries for a single sinusoidal pulse. $\lambda = 0$, $\lambda = 0.025$ and $\lambda = 0.221$ using the dimensions of the FECO and FLBA, respectively.

Moreover, the manufactured blocks from this paper can be modelled using the Concentrated spring model (CSM) and the Winkler Model (WM). The latter allows for a continuous force distribution around the base, similar to the FLBA, and the former only at the corners, similar to the limited area of allowable forces near the corners occurring for FECO. The similarity between FECO and CSM and between FLBA and WM has been noted in [11]. It was observed that for a very stiff support medium, the CSM produces results similar to the IPM with $\lambda = 0$ in terms of the stability of the body. Also, it was shown that the WM, for

planar rocking, appears to be less stable. Note that the previous observation between IPM for $\lambda = 0$ and CSM further requires that the effect of sliding, uplifting and the 3D nature of the body are neglected.

It was also shown in [11], that a mismatch between the IPM for $\lambda = 0$ and the WM when the value of the shear modulus was increased. The potential reason might be explained through the results of this paper. The optimal value of λ for the FLBA studied in this Chapter was shown to be 0.221, hence, it appears to be possible that the WM stability diagram for a high value of the shear modulus and neglecting sliding, uplifting and the 3D motion become closer to the IPM with an optimal value of λ for the block. However, in [57] when the value of λ is increased, the line which separates the areas of failure without impact and the areas of survival does not change, so it does not depend on λ. In contrast, for the WM [11], this line varies. Therefore, there would still not be an excellent match between IPM and WM for a flat base block even if the value of λ is increased. To address this issue, it is necessary to modify the equations of motion for the dynamic pattern of the IPM for flat base bodies [19].

To sum up, experimental and numerical investigations in this Chapter have shown that the base geometry has an important effect on the response of the bodies. It is often claimed in the literature that while using the IPM [1] $\lambda = 0$; however, it should only be considered that λ is close to zero if the body investigated has feet at the corners. The effect on the variability of this location was studied in Chapters 2 and 4 showing that the stability of the body decreases as λ increases.

Chapter 4

Examining the energy loss in systems of stacked rocking bodies

This work is part of a paper that was coauthored with Professor Manolis N. Chatzis, Professor Martin S. Williams and Christopher Needham and was published in the Journal of Engineering Mechanics [80].

4.1 Introduction

The rocking response becomes increasingly rich as more rigid modes are enabled, as when having assemblies of rocking bodies. The latter is a case in several situations, such as the case of stacked rocking bodies found in museums composing of artifacts on pedestals. Assemblies of two stacked rocking bodies can be found in several seismically active regions and hence their behaviour when subjected to ground motions is of interest.

The work of Housner [1] has been extended to rocking models for the dynamic behaviour of the assembly of two stacked rigid bodies. The associated conditions for failure of such systems have been studied in [12] in which failure is defined when at least one of the bodies topples. A complete formulation of the non-linear equations of motion using Newton's laws

or Lagrange's method have been developed in [81] and [13], respectively. Both focused on the derivation of the equation of motion for the consecutive transition from one pattern of motion to another making use of the assumption introduced by Housner: that of conserving angular momentum with respect to the future rocking corner. A multi-block model was developed in [14] where the simplified assumption of no loss of energy during impacts for each body in the system was adopted. Other type of rocking systems have been presented for rocking frames in [15, 82], for rocking bodies on base isolation in [83, 84], for rocking bodies with casters in [85, 86] and for a statue-pedestal system in [87].

However, as explained in Chapter 2, there is an inherent assumption of the IPM which is not guaranteed to be satisfied, that of conserving angular momentum with respect to the future rocking corner and the resulting loss of energy during impacts [57]. This Chapter hence extends the work presented in Chapter 2 to the case of stacked bodies. In particular, the Chapter investigates the potential location of the vertical impulses at the interfaces between the two bodies and between the lower body and the ground for the different types of impacts occurring in this system. The effect of this location on the overall stability of the top body and the system is studied.

4.2 Model and assumptions

The purpose of this Section is to extend the IPM model to a system of two bodies. The patterns as well as the equations to change of patterns with and without impact are presented. Finally, the numerical simulation is explained.

4.2.1 Dynamic model: Rocking patterns for two stacked blocks

This Section extends the IPM to the case of two stacked rigid blocks, symmetric about the vertical axis. The geometry and notation for this case is shown in Figure 4.1(a), and is consistent with that used by [13]. The blocks each have a mass m_i, where $i = 1$ corresponds

to the bottom body and $i = 2$ to the upper. The moment of inertia of body i about its centre of mass, G_i, is denoted as I_{G_i}. Their half-height and half-width are defined respectively as h_i and b_i. The right bottom corners of the blocks are denoted as 0_i and the left $0_i'$. The distance between the centres of mass and 0_i is defined as R_i and the angle between R_i and the side of the corresponding block as α_i. The distances between corners 0_1 and 0_2 is l and the angle between l and the side of the block is β. The distance between 0_1 and $0_2'$ is l' and the angle between l' and the side of the block is β'. The rotation of each body is defined to be positive clockwise and denoted as θ_1 and θ_2 for the bottom and top body respectively. When the bodies are fully connected, the moment of inertia of the system about its centre of mass, G, is represented as I_G, the distance between the centre of mass and 0_1 is defined as R and the angle between R and the side as α.

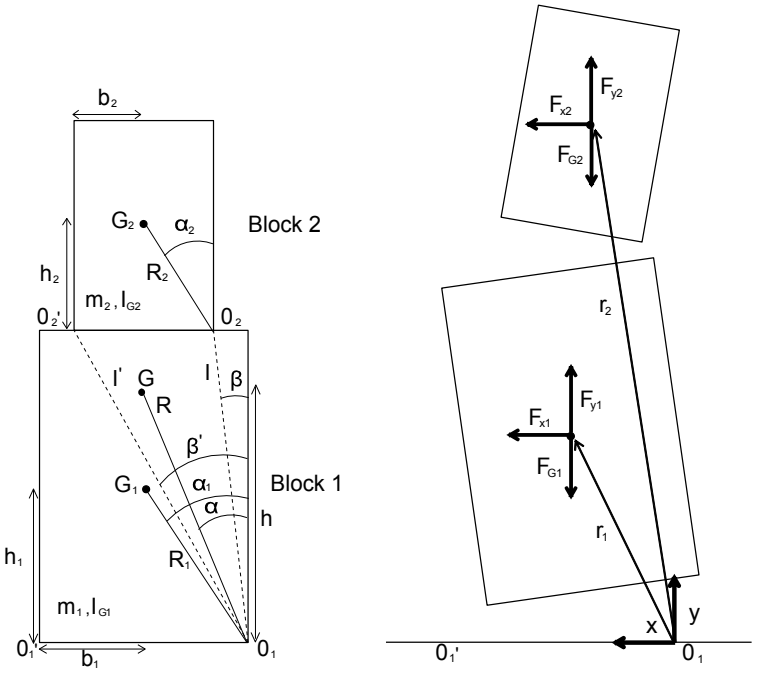

(a) (b)

Figure 4.1 – a) Geometry of two stacked blocks. b) Forces and kinematics of the bodies. Note that this model does not allow uplifting, the separation from the ground is only for illustration reasons.

There are eight possible dynamic rocking patterns for the stacked rocking bodies, aside from the static configuration where both bodies are at rest corresponding to the case shown in Figure 4.1(a). There are four basic categories of dynamic patterns, as illustrated in Figure 4.2, indicated by a numerical index, each with two symmetrical sub-patterns that are indicated by the letters a and b. Depending on the sign of θ_1 and $\theta_2 - \theta_1$ respectively, the bottom and top bodies rock with respect to one of their bottom corners. The cases for which θ_1 or $\theta_2 - \theta_1$ become equal to zero result in the bottom or top contact interface respectively being the line segment between the two bottom corners of the bottom and top body respectively. This situation is referred to from hereafter by denoting the corresponding interface as 'active'. Following the assumptions of the IPM, each body can then be simulated as a pendulum whose pin is located at that corner. Therefore, as in the case of a single body, this implies that the bodies cannot slide or experience free-flight, the ground and bodies are rigid, and the response of the system is strictly planar.

4.2.2 Kinematics and equations of motion

Based on the previous assumptions any pattern can be described using at most two generalised coordinates, θ_1 and θ_2. The equations of motion for any pattern can then be derived using Lagrange's method [88]. In its generalised form this is given by:

$$\frac{d}{dt}\left(\frac{\partial T_k}{\partial \dot{\theta}_i}\right) - \frac{\partial T_k}{\partial \theta_i} = Q_i \qquad\qquad Q_i = \sum_{j=1}^{n_f} F_j \frac{\partial r_j}{\partial \theta_i} \tag{4.1}$$

where T_k is the kinetic energy of the system, Q_i is the generalised force, n_f is the number of applied forces, F_j is an external force vector applied on a point at a vectorial distance r_j from 0_1 as shown in Figure 4.1(b). The forces that are applied here correspond to the gravitational forces applied to the two bodies $m_i\, g$ and the inertial forces due to a horizontal ground acceleration $\ddot{x}_g$. The kinetic energy of the system is given by:

$$T_k = \frac{1}{2}\sum_{i=1}^{2}(m_i V_i^2 + I_{Gi}\dot{\theta}_i^2) \qquad\qquad V_i^2 = \dot{x}_i^2 + \dot{y}_i^2 \tag{4.2}$$

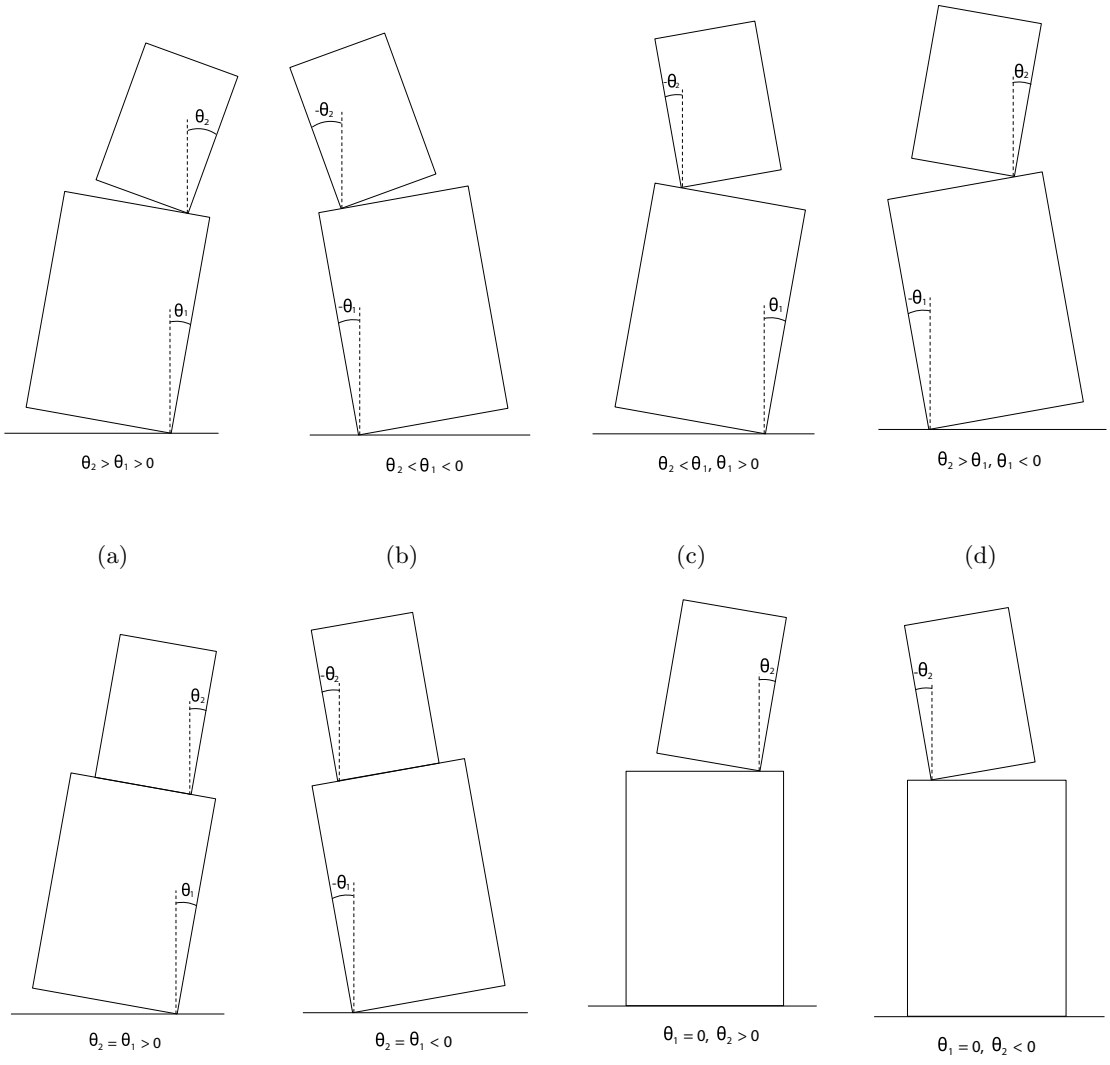

Figure 4.2 – All possible dynamic patterns of rocking for two stacked blocks. a) Pattern 1a, b) Pattern 1b, c) Pattern 2a, d) Pattern 2b, e) Pattern 3a, f) Pattern 3b, g) Pattern 4a and h) Pattern 4b.

where V_i is the velocity of the centre of mass of the block i relative to the ground. Hence, the translational kinetic energy appearing in equation (4.2) is not equal to the total translational energy of the body. This is due to the fact that the ground accelerations are used in equation (4.2) as inertia forces [85].

Using the coordinate system defined in Figure 4.1(b), the positions of the centres of mass of the blocks G_1 and G_2 are given, for patterns 1a, 1b, 2a, 2b, 4a and 4b, by the following

equations:

$$x_1 = H_{\theta_i} 2b_1 + S_{\theta_1} R_1 \sin(\alpha_1 - S_{\theta_1}\theta_1) \qquad y_1 = R_1 \cos(\alpha_1 - S_{\theta_1}\theta_1) \tag{4.3}$$

$$\begin{aligned} x_2 = {} & H_{\theta_i} 2b_1 + S_{\theta_1} S_l \sin(\theta_1 - S_{\theta_1} S_\beta) \\ & + S_{\theta_2} R_2 \sin(\alpha_2 - S_{\theta_2}\theta_2) \end{aligned} \qquad y_2 = S_l \cos(\theta_1 - S_{\theta_1} S_\beta) + R_2 \cos(\alpha_2 - S_{\theta_2}\theta_2) \tag{4.4}$$

The signum function S_{θ_i}, S_β, H_{θ_i} and S_l are defined as:

$$S_{\theta_i} = \begin{cases} 1 & \text{for } \theta_i \geq 0, \\ -1 & \text{for } \theta_i < 0 \end{cases} \qquad S_\beta = \begin{cases} \beta & \text{for } \theta_1 > 0, \theta_2 > 0 \text{ or } \theta_1 < 0, \theta_2 < 0, \\ \beta' & \text{for } \theta_1 > 0, \theta_2 < 0 \text{ or } \theta_1 < 0, \theta_2 > 0, \end{cases} \tag{4.5}$$

$$H_{\theta_i} = \begin{cases} 0 & \text{for } \theta_i \geq 0, \\ 1 & \text{for } \theta_i < 0 \end{cases} \qquad S_l = \begin{cases} l & \text{for } \theta_1 > 0, \theta_2 > 0 \text{ or } \theta_1 < 0, \theta_2 < 0, \\ l' & \text{for } \theta_1 > 0, \theta_2 < 0 \text{ or } \theta_1 < 0, \theta_2 > 0, \end{cases} \tag{4.6}$$

For the case of pattern 3, as $\theta_2 = \theta_1$ the equivalent centre of mass of the system, G, is shown in Figure 4.1(a) and its position is defined as:

$$x_G = H_{\theta_i} 2b_1 + S_{\theta_1} R \sin(\alpha - S_{\theta_1}\theta_1) \qquad y_G = R \cos(\alpha - S_{\theta_1}\theta_1) \tag{4.7}$$

where $R = \sqrt{h^2 + b_1^2}$, $h = \frac{m_1 h_1 + m_2(2h_1 + h_2)}{M_m}$, $M_m = m_1 + m_2$ and $I_G = I_{G_1} + I_{G_2} + m_1 (h - h_1)^2 + m_2 (h - h_2)^2$. To use equation (4.1) for this case only one generalised coordinate, e.g. θ_1 is used after replacing $\theta_2 = \theta_1$, before calculating the energy of the system $T_k = \frac{1}{2}(M_m V_G^2 + I_{Gi}\dot{\theta}_i^2)$. Similarly for pattern 4 one uses only θ_2 as a generalised coordinate and takes into account that $\theta_1 = 0$ before using equation (4.2). The equation of motions for all the possible cases are presented in [13], and are omitted in this Chapter for brevity.

The rocking motion of the system involves transitions from one pattern to another. Those transitions may occur with or without an impact and are described in the following Sections.

4.2.3 Change of pattern without impact

In this category, a change of patterns occurs without an impact. In fact, as is described in this Section the transitions occur due to the inabilities of the contact interfaces to provide

tensile stresses. This is of course an extension of the assumption that was used in the IPM and allows for the transition between the static and dynamic patterns as described in [57].

It is useful to cluster different patterns depending on whether the contact interfaces between the bottom body and the ground and the one between the two bodies, which are referred to as bottom and top interface respectively, correspond to a point or a linear segment. The two contact interfaces are referred to as inactive or active, respectively. Taking into account the symmetry between patterns a and b the following three cases presented in Figure 4.3 are of interest.

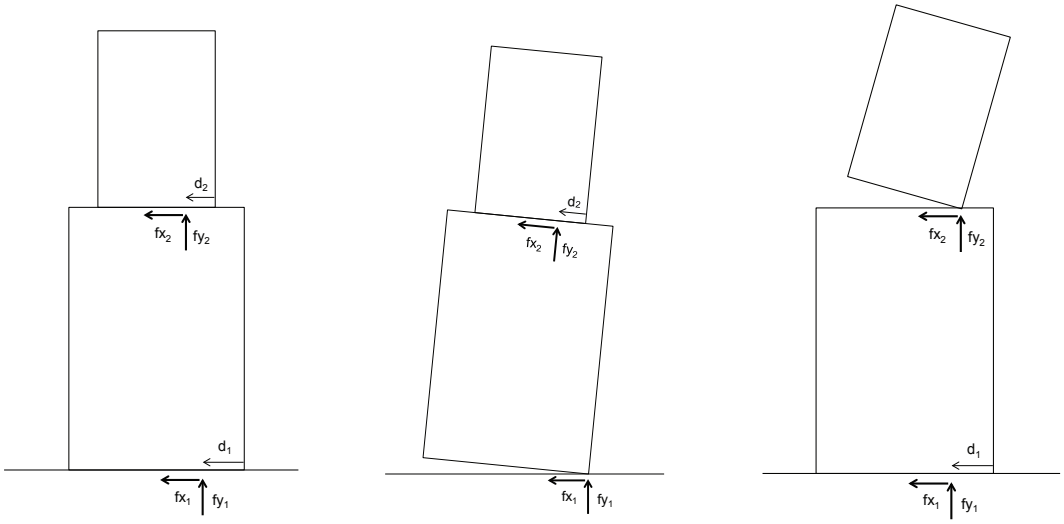

(a) (b) (c)

Figure 4.3 – All possible cases of the reactions forces. a) Both interfaces active, b) Bottom interface active and c) Top interface active.

In the case of Figure 4.3(a), which is the static pattern, both contact interfaces are active. Figure 4.3(b) corresponds to the case where the bottom interface is active and the top is inactive and while the figure shows pattern $4a$, the case is applicable to $4b$ as well. The last case is when the bottom interface is inactive and the top is active, Figure 4.3(c). Similarly, while Figure 4.3(c) corresponds directly to pattern $3a$ the discussion is applicable to $3b$ as well.

Figure 4.3 further shows the tangential and normal interface forces, f_{x_i} and f_{y_i}, occurring at interface i. For clarity, only the reaction forces applied to the body above the interface are drawn. It should be noted that when an interface is inactive, its reactions have to pass through the corresponding rocking corner. For an active interface however, the reaction forces could act at any point between the two corresponding corners. The distances along the interface from the right towards the left corner are denoted in Figure 4.3 as d_i.

Furthermore, $d_i/b_i \in [0, 2]$, i.e., the vertical reaction forces of an active interface have to be applied between the two corners. Otherwise the non-tensile forces assumption for the interfaces is violated. This now enables us to define the condition for transition between patterns without impact: A pattern is sustained when the reaction forces of each of the active interfaces remain between the corresponding corners. At the instant at which the reaction forces of an active interface are applied at one of the corners, i.e., $d_i \to 0$ or $d_i/b_i \to 2$ then a transition occurs to a corresponding pattern where the active interface of interest has been replaced with an inactive interface involving that corner. Hence, the transitions that are expected to occur and the corresponding conditions can be summarised in Table 4.1.

Table 4.1 – Required interface conditions for each rocking pattern.

Pattern	**Bottom**	**Top**
Pattern 1a	$d_1/b_1 \to 0$	$d_2/b_2 \to 0$
Pattern 1b	$d_1/b_1 \to 2$	$d_2/b_2 \to 2$
Pattern 2a	$d_1/b_1 \to 0$	$d_2/b_2 \to 2$
Pattern 2b	$d_1/b_1 \to 2$	$d_2/b_2 \to 0$
Pattern 3a	$d_1/b_1 \to 0$	$d_2/b_2 \in [0-2]$
Pattern 3b	$d_1/b_1 \to 2$	$d_2/b_2 \in [0-2]$
Pattern 4a	$d_1/b_1 \in [0-2]$	$d_2/b_2 \to 0$
Pattern 4b	$d_1/b_1 \in [0-2]$	$d_2/b_2 \to 2$

The parameters d_i, f_{x_i} and f_{y_i} can easily be obtained through Newton's equations of motion for the two bodies:

$$m_i\ddot{x}_i = \sum_j \mathbb{F}^j_{x_i} \qquad m_i\ddot{y}_i = \sum_j \mathbb{F}^j_{y_i} \qquad I_{G_i}\ddot{\theta}_i = \sum_j \mathbb{M}^j_{G_i} \tag{4.8}$$

where $\mathbb{F}^j_{x_i}$, $\mathbb{F}^j_{y_i}$ correspond to the force j applied to body i along the directions x and y respectively, and $\mathbb{M}^j_{G_i}$ correspond to the moment j applied to body i with respect to its centre of mass G_i. Solving the system of those equations is straightforward as the accelerations $\ddot{\theta}_i$ can be calculated first using the equations of motion (4.1).

This Section has described how transitions between patterns without impact can be described by tracking the values of d_i. The resulting transitions are equivalent to those defined in [13]. However, the approach presented here allows for easier implementation in algorithms that use Event detection (as discussed later) and a better understanding of the mechanics that leads to transitions.

4.2.4 Transitions between patterns with impact

In this category the change of patterns follows the event of an impact. An impact occurs when either θ_1 or $\theta_2 - \theta_1$ changes sign. The contact surfaces are considered to be rigid following the assumptions of the IPM, hence the duration of the impact is considered to be infinitesimally small. It is important to distinguish between three time instants: just before impact, denoted by the superscript $^-$, just after impact, associated denoted by the superscript $^+$, and a time instant during the infinitesimally small duration of the impact, referred to as the time instant of the impact. The pre- and post- impact instants are associated with one of the patterns in Figure 4.2. Table 4.2 shows the possible transitions; $P1$ and $P2$ refer to the points of application of the vertical impulses for the lower and upper interface, respectively. The arrow points at the distance of P_i from the corresponding future rocking corner of that interface.

It is important to note that during the impact the system does not belong to any pattern.

Table 4.2 – Default transitions from pre-impact to post-impact pattern.

Pattern	**Switch**	P_1	P_2
1a	2b	$0'_1 \xrightarrow{\lambda_1 b_1}$	$P_2 = 0_2$
1a	2a	$P_1 = 0_1$	$0'_2 \xrightarrow{\lambda_2 b_2}$
1b	2a	$\xleftarrow{\lambda_1 b_1} 0_1$	$0'_2 \xrightarrow{\lambda_2 b_2}$
1b	2b	$P_1 = 0'_1$	$\xleftarrow{\lambda_2 b_2} 0_2$
2a	1b	$\xleftarrow{\lambda_1 b_1} 0_1$	$P_2 = 0'_2$
2a	1a	$P_1 = 0_1$	$\xleftarrow{\lambda_2 b_2} 0_2$
2b	1a	$\xleftarrow{\lambda_1 b_1} 0_1$	$P_2 = 0_2$
2b	1b	$P_1 = 0'_1$	$0'_2 \xrightarrow{\lambda_2 b_2}$
3a	1b	$0'_1 \xrightarrow{\lambda_1 b_1}$	$0'_2 \xrightarrow{\lambda_2 b_2}$
3b	1a	$\xleftarrow{\lambda_1 b_1} 0_1$	$\xleftarrow{\lambda_2 b_2} 0_2$
4a	1b	$0'_1 \xrightarrow{\lambda_1 b_1}$	$0'_2 \xrightarrow{\lambda_2 b_2}$
4b	1a	$\xleftarrow{\lambda_1 b_1} 0_1$	$\xleftarrow{\lambda_2 b_2} 0_2$

Following the convention of the previous Section, the top or bottom contact interface is referred to as active or inactive during the impact depending on whether the contact interface corresponds to a line segment or a corner respectively. During an impact at least one of the two interfaces has to be active. Figure 4.4 describes three distinct cases that occur during impact.

During impact, impulsive forces are applied at both bodies from the contact interfaces. The corresponding tangential and normal impulses from contact interface i are denoted as J_{x_i} and J_{y_i}, respectively. For reasons of clarity only the impulses acting from the contact interface to the body above are drawn in Figure 4.4. It is important to note that for an inactive contact, as there is a single point of contact, the corresponding impulses have to pass through

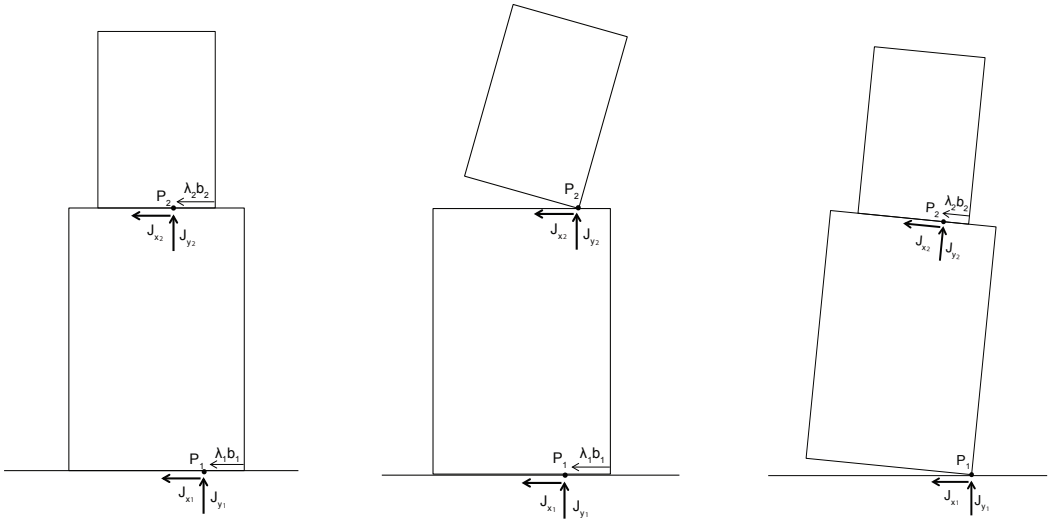

Figure 4.4 – Three characteristic cases during impact. a) Both interfaces active, b) Bottom interface active and c) Top interface active.

that point. For an active contact though, the resultant normal impulses may be applied at any point along the contact interface. This is accounted for using a corresponding tangential distance from the future rocking corner denoted as $\lambda_i\, b_i$, where $i = 1$ and 2 correspond to the bottom and top interface respectively. The following Figure 4.5 associates the resultant normal impulse J_{y_i} of contact interface i to the impulse distribution it replaces.

The assumption of non-tensile stresses used by the model in Section 2.2.1, which allows for the change of patterns without impact further leads to the lack of non-tensile impulses in the contact interfaces during an impact. As can be seen in Figure 4.5, and equivalently to what was shown for single rocking bodies in [57], the location of the resultant normal impulses has to be between the two corners or otherwise the assumption of non-tensile stresses is violated. As a result: $\lambda_i \in [0, 2]$.

An important difference with the work of [13] is that the assumption that $\lambda_i = 0$, i.e., angular momentum about the future rocking corner is conserved during impact, is not made. All values of λ_i between 0 and 2 are compatible with the assumptions underlying the model.

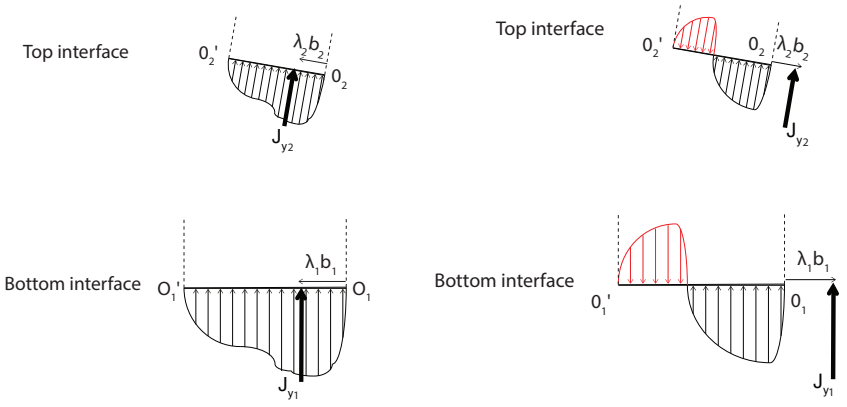

Figure 4.5 – a)Physically possible: One of the infinite admissible distributions to describe the vertical impulses during impact. b) Non-physically possible: Distribution showing the tensile stresses which are a violation of the non-tensile assumptions.

However, for a given type of impact, block dimensions and pre-impact velocities, some values of λ_i may result in an increase in the energy of the system during impact. Since this condition is physically impossible, such values of λ_i must be excluded. For single rocking blocks this restriction requires λ to be less than 1, but this is not necessarily the case for stacked blocks as systems can exchange energy. Nevertheless, in the following, the focus is limited to values of $0 \leq \lambda_i \leq 1$, while ensuring that the chosen values of λ_i do not lead to energy increase during any impact.

Having defined the location of the resultant contact impulses for each interface and for any transition, it should be highlighted that for body 2 the only external, non-zero, impulses applied at the body during the impact are J_{x_2} and J_{y_2}. Similarly for the system of the two rocking bodies, the impulses externally applied to the system are J_{x_1} and J_{y_1}. As a result, during any impact, the angular momentum of the upper body is conserved with respect to the point of application of J_{y_2}, P_2, and the angular momentum of the whole system is conserved with respect to the point of application of J_{y_1}, P_1. This is expressed in the following two

equations.

$$H^{+}_{2\to P_2} = H^{-}_{2\to P_2} \qquad \sum_{i=1}^{2} H^{+}_{i\to P_1} = \sum_{i=1}^{2} H^{-}_{i\to P_1} \tag{4.9}$$

where $H^{\pm}_{i\to P_j}$ corresponds to the angular momentum of body i with respect to point P_j defined as:

$$H^{\pm}_{i\to P_j} = I_{G_i}\,\dot{\theta}^{\pm}_i + m_i\,(\mathbf{r}_{P_j\to G_i} \times \mathbf{v}^{\pm}_{G_i}) \cdot \hat{\mathbf{k}} \tag{4.10}$$

This is now illustrated using Figure 4.6, where the system switches form pattern 3a to 1b. Angular momentum of the whole system is conserved about the impact point, at a distance $\lambda_1 b_1$ form $0'_1$. Leading to the following equation:

$$A_1\dot{\theta}^{-}_1 + B_1\dot{\theta}^{-}_2 = C_1\dot{\theta}^{+}_1 + D_1\dot{\theta}^{+}_2 \tag{4.11}$$

where,

$$A_1 = I_O - (2-\lambda_1)Mb_1^2$$

$$C_1 = I_{O1} - \lambda_1 m_1 b_1^2 + m_2 l(2h_1 + h_2)\cos\beta + (1-\lambda_1)m_2 l b_1 \sin\beta$$

$$B_1 = 0$$

$$D_1 = I_{G2} + m_2 R_2(2h_1 + h_2)\cos\alpha_2 + (1-\lambda_1)m_2 R_2 b_1 \sin\alpha_2$$

where $M = m_1 + m_2$, $I_O = I_{O1} + I_{G2} + m_2 R_{2O}^2$ and I_{0_i} are the moments of inertia of the blocks about their corners. Note that in this case both blocks behave as one, i.e., $\dot{\theta}^{-}_2 = \dot{\theta}^{-}_1$. A second equation can be derived by considering the conservation of angular momentum about P_2 for block 2 alone leading to:

$$A_2\dot{\theta}^{-}_1 + B_2\dot{\theta}^{-}_2 = C_2\dot{\theta}^{+}_1 + D_2\dot{\theta}^{+}_2 \tag{4.12}$$

where,

$$A_2 = I_{0_2} - \lambda_2 m_2 b_2^2 + m_2 l' h_2 \cos(\beta') - (1-\lambda_2)m_2 l' b_2 \sin(\beta')$$

$$B_2 = 0$$

$$C_2 = m_2 l h_2 \cos\beta + (1-\lambda_2)m_2 l b_2 \sin\beta$$

$$D_2 = I_{O2} - \lambda_2 m_2 b_2^2$$

The post impact velocities of the stacked bodies can be calculated by solving equations (4.11) and (4.12). Note that the solutions depend on the assumed values of λ_1 and λ_2.

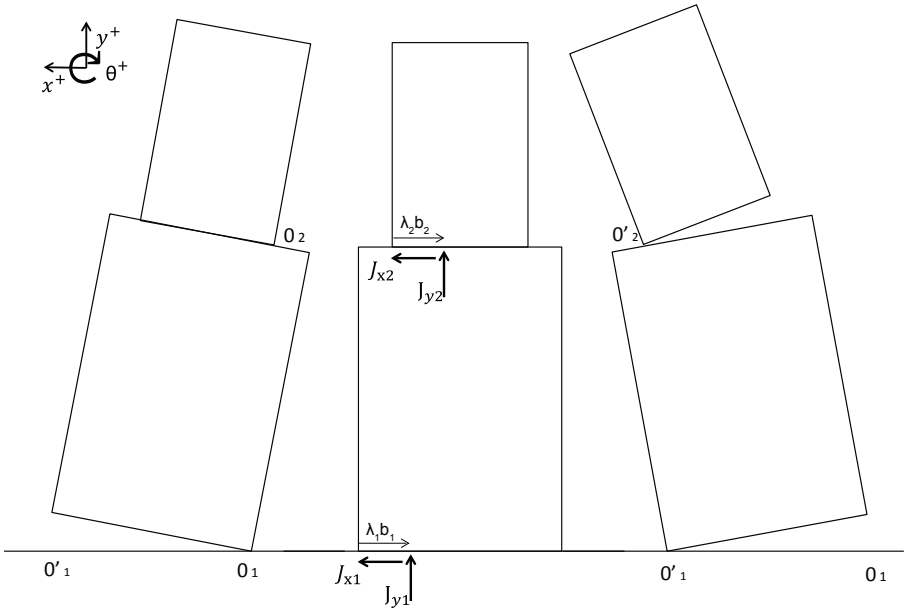

Figure 4.6 – Transition from pattern 3a to 1b.

The same procedure can be followed for all the transitions with impacts and the results can always be presented in the form of equations (4.11) and (4.12), with different expressions for the coefficients A_1, A_2, B_1, B_2, C_1, C_2 and D_1, D_2. Equations for the rest of the patterns transitions described in Table 4.1 are presented in the Appendix I: Momentum equations. The coefficients are functions of the dimensions of the two bodies and also potentially the rotations of the bodies, and finally are affected for any case by at least one of λ_1 and λ_2. If one sets $\lambda_1 = 0$ and $\lambda_2 = 0$ then the same expressions are obtained as those presented in [13]. It is evident from equations (4.11) and (4.12), that the post impact rotational velocities and hence the future trajectory of the body depend on the values of the assumed λ_i.

In this case, it should be noted that there is a design choice that can affect the values of λ_i at the two interfaces. This is either the introduction of an absorbing material between the two bodies around that interface, e.g., sorbothane rubber as in [89], or the use of physical feet at the corners as explained in [11, 57]. Assuming that the introduction of the rubber material does not substantially change the stiffness of the contact interface, its effect in the model examined here is an increased exchange of energy between the two bodies of that interface

[57]. This in essence corresponds to decreasing the corresponding value of λ_i at that interface. Hence, placement of the rubber material at the bottom or top interface decreases the value of λ_1 and λ_2 respectively towards zero in comparison to the value of those parameters for the original interface. Equally the works presented in [11, 57] describe of how placement of physical feet leads to decreasing the value of λ_i. This second option is mainly useful for the bottom interface.

Special transition cases

Consider again the case where the blocks are in pattern 3a and a transition with impact leading to pattern 1b occurs as shown in Figure 4.6. If after the impact $\dot{\theta}_2^+ - \dot{\theta}_1^+ < 0$, the transition to pattern 1b is possible. However, if the analysis results in $\dot{\theta}_2^+ - \dot{\theta}_1^+ > 0$, this results in a subsequent immediate impact activating the upper interface. These successive impacts with no progress of time are not physically possible and even mathematically lead to erroneous results. That is because pattern 1b is not well defined for $\theta_1 = \theta_2$ and $\dot{\theta}_2 - \dot{\theta}_1 > 0$. This situation may occur for several transitions with impact for which the sign of either $\dot{\theta}_1^+$ or $\dot{\theta}_2 - \dot{\theta}_1$, together with the post impact values of θ_1 and θ_2 are not compatible with the post impact pattern. Table 4.3 presents the necessary conditions on the post impact angular velocities for the different transitions with impact to be feasible.

If the conditions are violated then the investigated transition is not feasible. This case is also investigated in [13] and the treatment suggested is to instead switch to a post impact pattern for which the function that violated the sign condition, either $\dot{\theta}_1$ or $\dot{\theta}_2$, is zero. This results in changing the post impact pattern as also described in Table 4.3.

However, in order for the new post-impact patterns to be feasible either or both of the conditions, $\dot{\theta}_1 = 0$ or $\dot{\theta}_2 - \dot{\theta}_1 = 0$, have to be satisfied. Those conditions act in parallel with the momentum equations (4.10). As a result the values of λ_i cannot be chosen freely any more. Within the context of the work presented in [13] this means that during such

Table 4.3 – Special conditions for switching patterns. PI refers to Post-Impact.

Pattern	Expected Switch	PI condition	New PI condition	Switch	P_1	P_2
1a	2b	$\dot{\theta}_1^+ \geq 0$	$\dot{\theta}_1^+ = 0$	4a	$0_1' \xrightarrow{\lambda_1 b_1}$	$P_2 = 0_2$
1a	2a	$\dot{\theta}_2 \geq \dot{\theta}_1$	$\dot{\theta}_2 = \dot{\theta}_1$	3a	$P_1 = 0_1$	$0_2' \xrightarrow{\lambda_2 b_2}$
1b	2a	$\dot{\theta}_1^+ \leq 0$	$\dot{\theta}_1^+ = 0$	4b	$\xleftarrow{\lambda_1 b_1} 0_1$	$P_2 = 0_2'$
1b	2b	$\dot{\theta}_2 \leq \dot{\theta}_1$	$\dot{\theta}_2 = \dot{\theta}_1$	3b	$P_1 = 0_1'$	$\xleftarrow{\lambda_2 b_2} 0_2$
2a	1b	$\dot{\theta}_1^+ \geq 0$	$\dot{\theta}_1^+ = 0$	4b	$0_1' \xrightarrow{\lambda_1 b_1}$	$P_2 = 0_2'$
2a	1a	$\dot{\theta}_2^+ \geq \dot{\theta}_1^+$	$\dot{\theta}_2^+ = \dot{\theta}_1^+$	3a	$P_1 = 0_1$	$0_2' \xrightarrow{\lambda_2 b_2}$
2b	1a	$\dot{\theta}_1^+ \leq 0$	$\dot{\theta}_1^+ = 0$	4a	$\xleftarrow{\lambda_1 b_1} 0_1$	$P_2 = 0_2$
2b	1b	$\dot{\theta}_2^+ \leq \dot{\theta}_1^+$	$\dot{\theta}_2^+ = \dot{\theta}_1^+$	3b	$P_1 = 0_1'$	$\xleftarrow{\lambda_2 b_2} 0_2$
3a	1b	$\dot{\theta}_2^+ \geq \dot{\theta}_1^+$	$\dot{\theta}_2^+ = \dot{\theta}_1^+$	3b	$0_1' \xrightarrow{\lambda_1 b_1}$	$0_2' \xrightarrow{\lambda_2 b_2}$
3a	1b	$\dot{\theta}_1^+ \geq 0$	$\dot{\theta}_1^+ = 0$	4b	$0_1 \xrightarrow{\lambda_1 b_1}$	$0_2' \xrightarrow{\lambda_2 b_2}$
3b	1a	$\dot{\theta}_2^+ \leq \dot{\theta}_1^+$	$\dot{\theta}_2^+ = \dot{\theta}_1^+$	3a	$\xleftarrow{\lambda_1 b_1} 0_1$	$\xleftarrow{\lambda_2 b_2} 0_2$
3b	1a	$\dot{\theta}_1^+ \leq 0$	$\dot{\theta}_1^+ = 0$	4a	$\xleftarrow{\lambda_1 b_1} 0_1$	$\xleftarrow{\lambda_2 b_2} 0_2$
4a	1b	$\dot{\theta}_1^+ \geq 0$	$\dot{\theta}_1^+ = 0$	4b	$0_1' \xrightarrow{\lambda_1 b_1}$	$0_2' \xrightarrow{\lambda_2 b_2}$
4a	1b	$\dot{\theta}_1^+ \leq 0, \dot{\theta}_2^+ > \dot{\theta}_1^+$	$\dot{\theta}_2^+ = \dot{\theta}_1^+$	3b	$0_1' \xrightarrow{\lambda_1 b_1}$	$0_2' \xrightarrow{\lambda_2 b_2}$
4b	1a	$\dot{\theta}_1^+ \leq 0$	$\dot{\theta}_1^+ = 0$	4a	$\xleftarrow{\lambda_1 b_1} 0_1$	$\xleftarrow{\lambda_2 b_2} 0_2$
4b	1a	$\dot{\theta}_1^+ \geq 0, \dot{\theta}_2^+ < \dot{\theta}_1^+$	$\dot{\theta}_2^+ = \dot{\theta}_1^+$	3a	$\xleftarrow{\lambda_1 b_1} 0_1$	$\xleftarrow{\lambda_2 b_2} 0_2$

instances the assumption of conserving angular momentum with respect to a future rocking corner, i.e. $\lambda_i = 0$, cannot be satisfied for the active contact interface. This, of course, is not violating any of the assumptions of the model as described in this Chapter, it is however a further indication that even in the work of [13] values of λ_i other than zero are used for such cases. Within the context of the current work, such instances result in changing the corresponding λ_i to the specific value that guarantees the transition. Table 4.3 shows the points of application of the vertical impulses for both interface.

Going back to the example presented, to avoid the non-feasible post impact result $\dot{\theta}_2^+ - \dot{\theta}_1^+ > 0$, it is assumed that the system switches to pattern $3b$, $\dot{\theta}_2^+ = \dot{\theta}_1^+$. In this case the analysis reduces to a single rocking body analysis [57] and conservation of angular momentum of the whole system about the bottom impact force location yields:

$$\dot{\theta}_1^+ = \frac{I_0 - (2-\lambda_1)M_m b_1^2}{I_0 - \lambda_1 M b_1^2}\dot{\theta}_1^- \tag{4.13}$$

Equivalently one can obtain the same expression more generally by using the conservation of angular momentum equation for the system with respect to P_1 and replacing $\dot{\theta}_2^+ = \dot{\theta}_1^+$ for any value of λ_1. However, the conservation of angular momentum of the upper body, together with the condition $\dot{\theta}_2^+ = \dot{\theta}_1^+$, uniquely prescribe the value of λ_2:

$$\lambda_2 = \frac{A_3\dot{\theta}_1^- + B_3\dot{\theta}_1^+}{C_3\dot{\theta}_1^- + D_3\dot{\theta}_1^+} \tag{4.14}$$

$$A_3 = -(I_{0_2} + m_2 l' h_2 \cos\beta' - m_2 l' b_2 \sin\beta') \qquad B_3 = I_{0_2} + m_2 l h_2 \cos\beta + m_2 l b_2 \sin\beta$$

$$C_3 = m_2 b_2 (l' \sin\beta - b_2) \qquad D_3 = m_2 b_2 (l \sin\beta + b_2)$$

Note that, in equation (4.16) $\dot{\theta}_1^+$ is also a function of λ_1. This means that λ_2 has to have a very specific value given the value attained by λ_1, the dimensions of the body and the pre-impact velocities.

Similarly, it is possible that following the previously studied switch between patterns $3a \rightarrow 1b$, where after solving the momentum equations (4.10), $\dot{\theta}_1^+$ is found to be positive. As discussed earlier the solution suggested to tackle the occurring problem is through setting $\dot{\theta}_1^+ = 0$ and choosing pattern 4b. This can be seen in Figure 4.7.

For the above transition, the angular moment equations for the system (4.11) and the upper block (4.12) take the form:

$$A_1\dot{\theta}_1^- = D_1\dot{\theta}_2^+ \qquad A_2\dot{\theta}_1^- = D_2\dot{\theta}_2^+ \tag{4.15}$$

where A_1, A_2, D_1 and D_2 are previously defined.

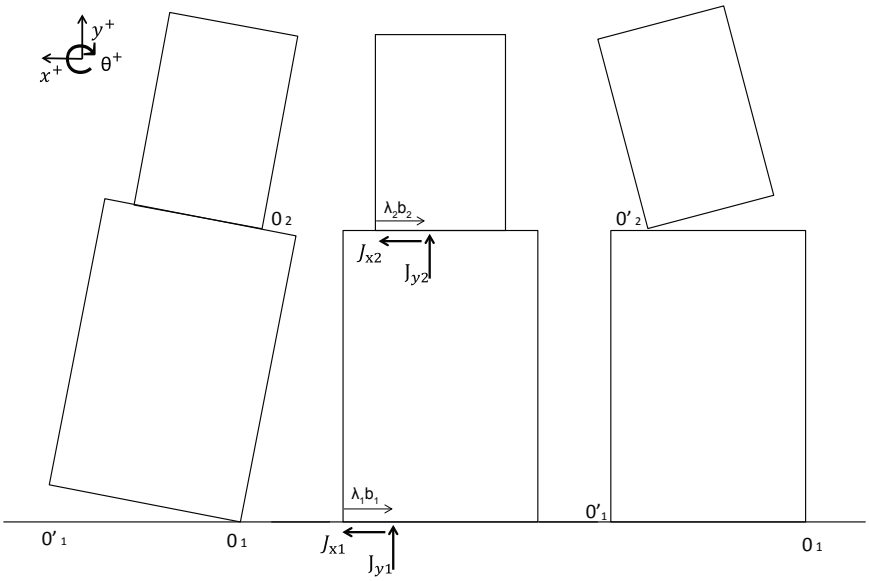

Figure 4.7 – Transition from pattern 3a to 4b.

In this transition both interfaces are active and hence, only λ_i are unknown. The locations of both contact points P_1 and P_2 are functions of the value of λ_1 and λ_2, respectively. There are now two momentum equations and three unknowns $\dot{\theta}_2^+$, λ_1 and λ_2. If one of the λ_i is specified the other is uniquely defined as the number of unknowns decreases to two. For example, if λ_2 is assumed, equations in (4.15) can be solved for $\dot{\theta}_2^+ = \frac{A_2}{D_2}\dot{\theta}_1^-$ and λ_1:

$$\lambda_1 = \frac{A_3\dot{\theta}_1^- + B_3\dot{\theta}_2^+}{C_3\dot{\theta}_1^- + D_3\dot{\theta}_2^+} \tag{4.16}$$

$$A_3 = I_O - 2Mb_1^2 \qquad B_3 = -(I_{G2} + m_2R_2(2h_1 + h_2)\cos\alpha_2 + m_2R_2b_1\sin\alpha_2)$$

$$C_3 = -(Mb_1^2) \qquad D_3 = m_2R_2b_1\sin\alpha_2$$

Similar computations apply to all transitions in this category. However, while this formulation alleviates the mathematical problems of the model, from a physical point of view it is questionable that the impulses are applied exactly at the locations that satisfy the additional constraints. Instead, it is more probable that when such situations are encountered some of the remaining assumptions on the post impact behaviour is violated. It has been

noticed in the literature that for the case of a single rocking body, the occurrence of such an instance, i.e., when the coefficient of restitution becomes negative, indicates that in reality the body bounces during impact [5, 90]. It is hence expected that equally in the case of stacked rocking bodies, the bodies around at least one of the contact interfaces are expected to become separated after the impact in the situations listed in Table 4.2. As a result, part of the system is expected to violate the assumption of no bouncing and hence proper study of the system in such scenarios requires the use of a model that takes free-flight and sliding modes into account, such as the extension of the models [5, 11].

Hence, for the remainder of this Chapter it is ensured that this problem does not occur for any of the systems and excitations studied.

4.2.5 Numerical Formulation

The numerical simulation of Chapter 2 for the single body case, is extended to two stacked bodies. The same tools from Matlab are used.

Figure 4.8 shows a flowchart of the design structure of the program. The 'simulation parameters' comprise of the geometrical parameters of the blocks, the initial conditions of the blocks and the base accelerations. 'Static state' is the case where $\theta_1 = \theta_2 = \dot{\theta}_1 = \dot{\theta}_2 = 0$. The condition to initiate the motion is determined at $d_i/b_i \to 0$ or/and $d_i/b_i \to 2$ depending on the pattern. Here, '$a(t)$ finished' is used to denote that the duration of the input is over. t_{end} is the predetermined simulation time, usually defined as the overall duration of excitation. The 'static pattern' is a dummy ode which simply outputs the conditions of the steady state until one of the conditions for initiation of rocking is satisfied.

4.3 Stability diagrams

Initially the stability of the system is investigated for ground accelerations having the form of an horizontal sinusoidal pulse as in [26, 57] and Chapter 2. This input, despite its simplicity,

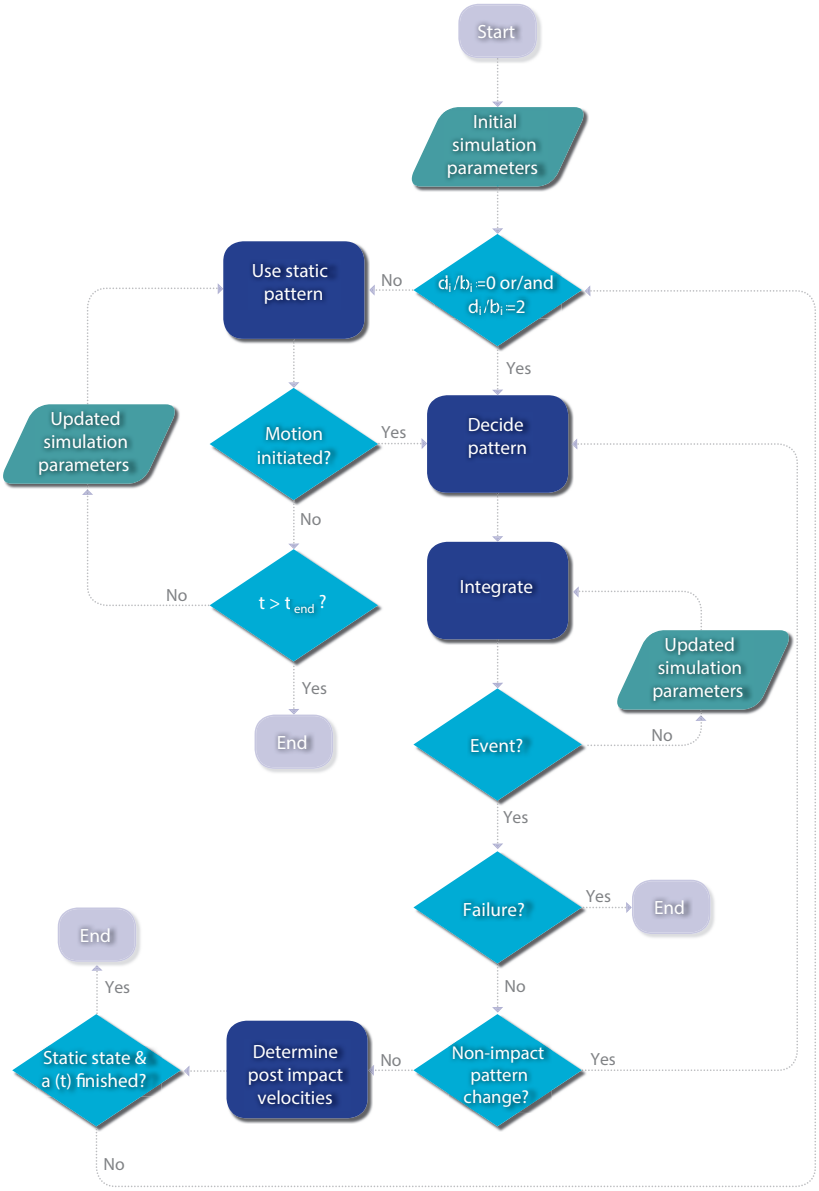

Figure 4.8 – Flowchart to show simulation coding structure

allows for demonstrating important features of the system [26, 3]. The blocks are subjected to single- and double-cycle sinusoids as defined in equation (2.17).

For the system examined here, the outcomes can be classified in terms of areas of u_0 and ω_u associated with: survival, failure with no impacts occurring, failure with impacts where only one of the two interfaces is active, or where both of them are active. Note that for all the areas for which an impact occurs, the values of λ_i related to the active interfaces during any of the impacts have an effect on the outcome. Finally, it may be of interest for

some system to further distinguish between failure of only the upper body which occurs when $|\theta_1 - \theta_2| = \pi/2$ and failure of the bottom body occurring when $\theta_1 = \pi/2$. The latter type of failure is certainly associated with failure of the system, as it is inevitable that past this point the upper body also topples.

4.3.1 Change of pattern

In this Section, a system of stacked bodies is subjected to single cycle horizontal sinusoidal acceleration pulses. Initially the investigated system involves two blocks that have the same aspect ratio $h_i/b_i = 3$ and dimensions: $h_1 = 60$ cm, $b_1 = 20$ cm, $h_2 = 15$ cm, $b_2 = 5$ cm. It is initially assumed that $\lambda_1 = \lambda_2 = 0$, i.e., the impulses are located at the future rocking corners. The stability diagram of the system is presented in Figure 4.9 where the horizontal and vertical axes are normalised with $p = 6.8215$ and $\alpha = 0.3218$ corresponding to the properties of block 2.

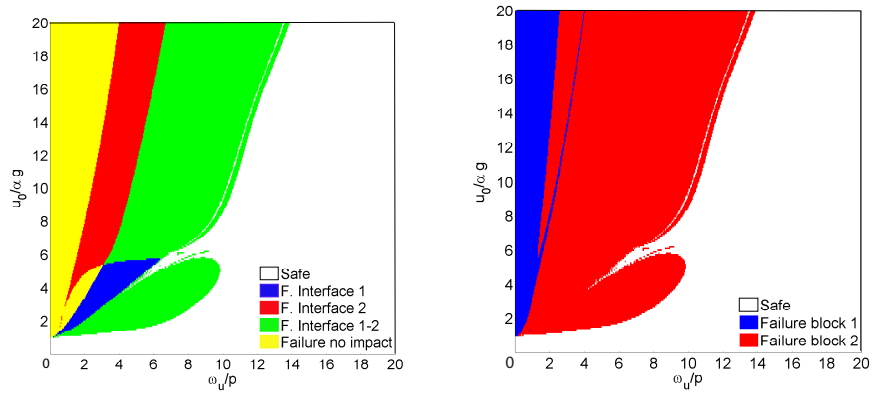

(a) (b)

Figure 4.9 – Diagrams of two stacked bodies with dimensions block 1: $h_1 = 0.6$, $b_1 = 0.2$ and block 2: $h_2 = 0.15$, $b_2 = 0.05$ with $\lambda_2 = 0$ and $\lambda_1 = 0$. The horizontal and vertical axes are normalised with $p = 6.8215$ and $\alpha = 0.3218$. a) History of impacts leading to failure, b) failure of upper and lower bodies.

Figure 4.9(a) presents the stability diagram separating the failure regions, depending on

whether there were any impacts prior to failure. If so, it further specifies which interfaces were active during any of those impacts. Figure 4.9(b) presents the stability diagram separating the failure regions depending on which body toppled first. The non-linearity of the problem is apparent in Figure 4.9(a) as for example for pulses of constant frequency, as the amplitude $u_0/(\alpha g)$ is increased the system may transition from survival, to failure with impact with both interfaces active, back to survival, followed by failure with only the bottom interface active, then re-transition to failure with both interfaces active and finally to failure, where only the top interface is active.

In Figure 4.9, as in the case of a single rocking body, for low amplitudes the body remains in the static pattern without ever transitioning to a dynamic pattern. For the system examined here the body always transitions first to pattern 3a and hence the amplitude that separates the static pattern from the dynamic patterns is $u_0/(\tan(b_1/h)g) < 1$. An additional region that resembles a behaviour encountered in the single body stability diagram is the region of points where failure occurs without impact. As an impact does not occur in that region, the outcome is not affected by the assumed value of λ_i. In the single rocking body case, the region of failure without impact has a lower boundary in terms of the amplitudes, but not an upper boundary. However, in this problem, the region can be separated into an upper lobe, where indeed increase of u_0 results in continuously remaining in this region, and a lower lobe where eventually as u_0 is increased an impact is experienced. Equally, if failure occurs with an interface i never becoming active, then the associated assumption on the value of λ_i does not influence the survival or failure of the body for that combination of u_0 and ω_u values.

In Figure 4.9(b) the failure regions are presented in terms of which is the first body that experiences toppling. It can be seen that the majority of the regions of failure are associated with toppling of the top body. In fact the region of failure for body 1 (and hence eventually the system) is a region of high amplitudes and low frequencies surrounded by a region of

where the top body fails first. A careful comparison of the outer boundaries of the area of failure for body 1 in Figure 4.9(b) versus the region of failure without impact in Figure 4.9(a) shows that the former matches the upper lobe of the latter.

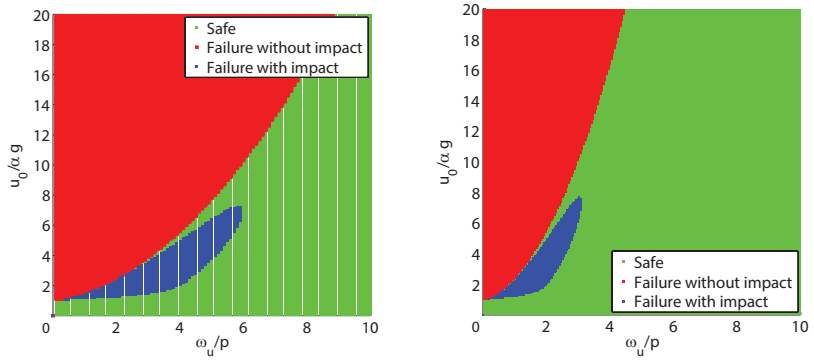

(a) Case B (b) Case C

Figure 4.10 – Stability diagrams for a) case B b) case C.

To understand this behaviour, consider the following two single-body rocking systems: when the bottom body is fixed but the upper body rocks, and when the two bodies always remain fully connected with the top interface active and this overall system rocks as one body. The former is referred to as case B and is associated with patterns $4a$ and $4b$, while the latter is referred to as case C and is associated with patterns $3a$ and $3b$. The original problem of both bodies rocking is referred to as case A. Figure 4.10 shows the stability diagrams for cases B and C, while Figure 4.11 draws comparisons with the stability of the system of stacked rocking bodies shown in Figure 4.9.

It can be seen in Figure 4.11 that, for the specific system studied and the assumption of λ_1 and λ_2 being zero, case C appears to be overall more stable. Case B is in general more stable than A, although there are areas in the diagram where the latter survives but the former is not. This investigation presented in Figure 4.11 is useful in terms of design, as for example the dimensions studied here could be encountered in the case of an artifact (body 2) situated on top of a pedestal (body 1). Then the design question would be of whether

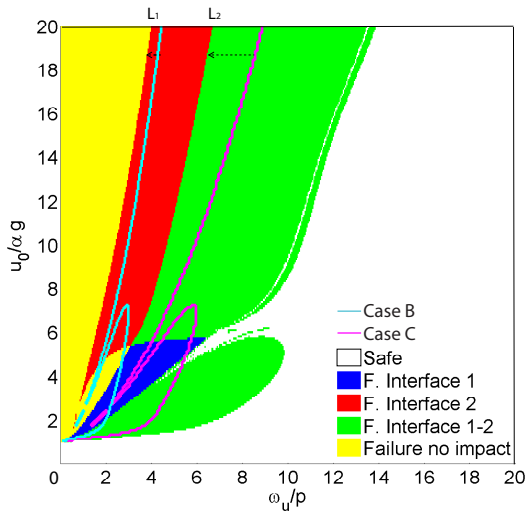

Figure 4.11 – Comparison of stacked bodies failure with single bodies. Stacked bodies dimensions: $h_1 = 0.6$, $b_1 = 0.2$ and $h_2 = 0.15$, $b_2 = 0.05$. The dimensions for the single rocking cases: Block 1 $h_1 = 0.6$, $b_1 = 0.2$ and Block 2 $h_1 = 0.15$, $b_1 = 0.05$. The horizontal and vertical axes are normalised with $p = 6.8215$ and $\alpha = 0.3218$. Note that the single body case, only the boundaries of failure without impact are presented. It is assumed for all cases that $\lambda = \lambda_i = 0$.

both bodies should be allowed to rock, the pedestal should be clamped on the floor, or the artifact should be clamped on the pedestal which would be allowed to rock. The three design scenarios correspond to cases A, B and C, respectively. It appears that for the case studied here the scenario of clamping the artifact to the pedestal results overall in less toppling of the system.

The upper lobe of the area of failure with no impact, where block 1 fails first, presented in Figure 4.9(a) can now be revisited. As the system experiences no impacts in this region of the u_o and ω_u map, the dynamics of the body are dictated by only two dynamic patterns: initially $3b$ (or $3a$) and potentially $1b$ (or $1a$). In case C, the area of failure with no impact is only dictated by pattern $3b$ (or $3a$). As pattern $1b$ is a pattern with similar dynamic properties to $3b$, it is no surprise that the upper lobe of the area of failure with no impact for

case A is very close to the boundary of the failure area with no impact for case C. It can then be considered that, qualitatively, the boundary of the no impact area for case C is translated for case A to the boundary of the upper lobe as indicated in Figure 4.11, which is referred to as L_1.

Similarly, it can be considered that the boundary of the area of failure without impact for case B is translated for case A to the line that separates the red and yellow regions of Figure 4.9(b) from the green and blue, which is referred to as L_2. Within the region defined by the translated lines, L_1 and L_2 the single rocking body cases indicate that the upper body is expected to topple to the right while the system of bodies rocking as one is expected to survive or topple to the left. Amongst the two types of failure it is substantially easier for the top body to topple to the right, as both bodies initially rotate towards the right. It is hence reasonable that within that region, it is the top body that fails first, without an impact occurring in the bottom interface. This region is further separated depending on whether there is an impact on the top interface. The bottom part corresponds to the lower lobe of the area of the failure with no impact that was observed in Figure 4.10(a).

While there are other regions in the diagram that inherit properties from the simplified single rocking cases B and C, the case of stacked rocking bodies exhibits richer dynamics and it would both erroneous and non conservative to try to approximate the behaviour of the stacked system by either of the two simplified single rocking cases.

As can be seen in 4.9(a) for the same frequency of the input pulse, different types of failure are encountered, as the amplitude changes. Examples of those are shown in Figure 4.12 for $\omega_u/p = 2$. When $u_0/(\alpha g) = 1.81$ the system fails with impact in both interfaces (Figure 4.9(a)) and block 2 topples (Figure 4.9(b)). The time histories for this case are illustrated in Figure 4.12(a) where the rotations θ_1 and $\theta_2 - \theta_1$ indicate that the bottom interface is activated during four impacts before block 2 topples after a single impact occurring at the top interface. For $u_0/(\alpha g) = 2.4$, the system only experiences impacts with the active interface

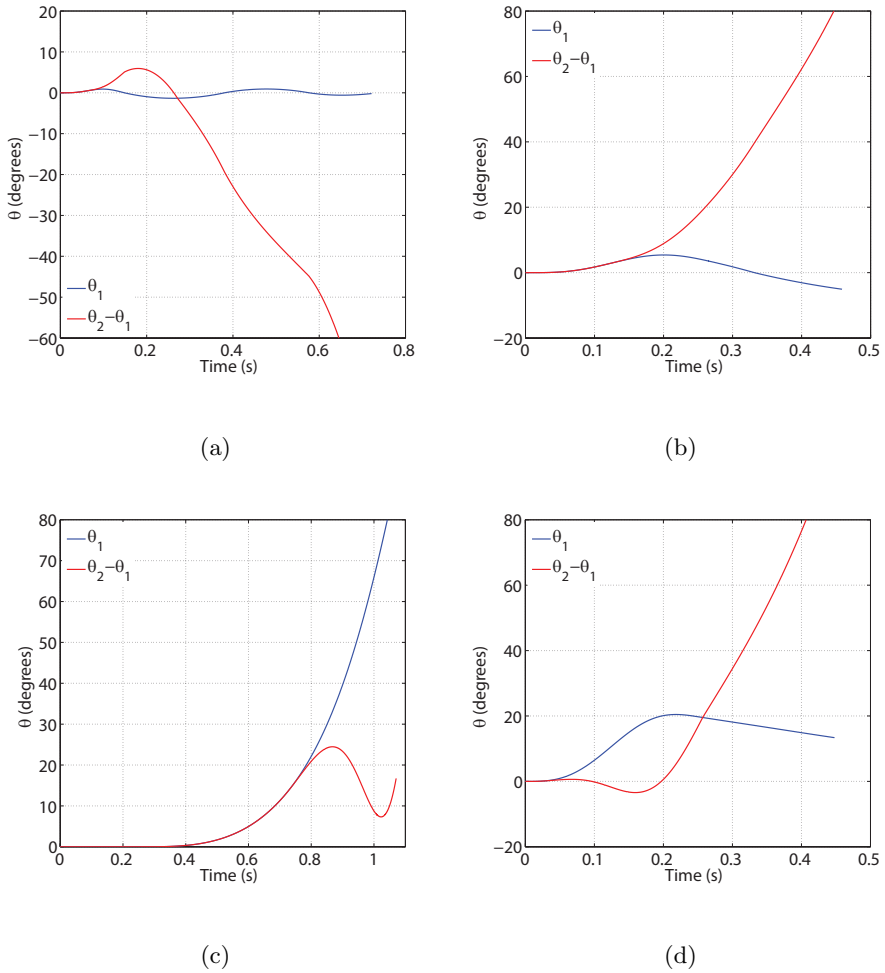

Figure 4.12 – Time histories for two stacked bodies with dimensions $h_1 = 0.6$, $b_1 = 0.2$, $h_2 = 0.2$, $b_2 = 0.05$ with $\lambda_1 = 0$ and $\lambda_2 = 0$ for a)Impact both bodies, $\omega_u/p = 2$, $u_0/(\alpha g) = 1.81$, b) Impact block 1, $\omega_u/p = 2$, $u_0/(\alpha g) = 2.4$, c) Failure no impact, $\omega_u/p = 2$, $u_0/(\alpha g) = 4.01$ and d) Impact block 2, $\omega_u/p = 2$, $u_0/(\alpha g) = 6.21$.

1 and block 2 topples without an impact activating interface 2. The time history for this case is illustrated in Figure 4.12(b). As the amplitude is increased to $u_0/(\alpha g) = 4.01$, the pattern of failure with no impact is achieved and block 1 fails thus the whole system fails. The time history for this case is shown in Figure 4.12(c). The last type of failure appears for $u_0/(\alpha g) = 6.21$ where only the top interface is activated with two impacts before overturning, Figure 4.12(d).

Finally, while in the case of a single rocking body there are only two patterns of failure,

i.e., the body toppling to the right or left, in this stacked body case there are several different patterns that may be active at the instance of failure. These are presented in Figure 4.13, together with the the condition of failure that was activated.

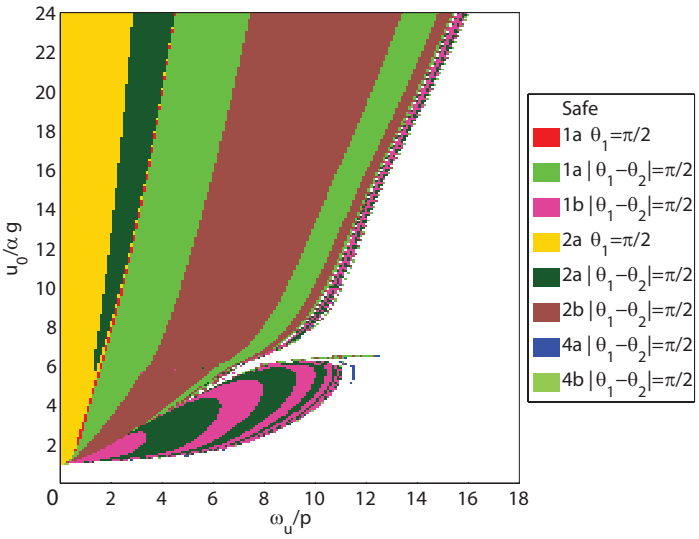

Figure 4.13 – Rocking patterns of failure of stacked bodies with dimensions $h_1 = 0.6$, $b_1 = 0.2$, $h_2 = 0.15$, $b_2 = 0.05$ with $\lambda_2 = 0$ and $\lambda_1 = 0$. The horizontal and vertical axes are normalised with $p = 6.8215$ and $\alpha = 0.3218$.

4.3.2 Effect of λ_i

The previous Section made the assumption that $\lambda_i = 0$. However, as discussed in the previous Chapters, there is an uncertainty over the locations of the vertical impulses and the values of λ_i. This Section examines how different values of λ_i affect the stability of the system of stacked rocking bodies when subjected to sinusoidal pulse type ground accelerations.

The values of λ_i can take values between 0 and 1. Figure 4.14 represents a sequence of stability diagrams in which the values of λ_2 and λ_1 have been increased. All cases are compared to the case of conserving angular momentum with respect to the future rocking corners, i.e., $\lambda_1 = \lambda_2 = 0$ (Figure 4.9).

Similarly to a single rocking body [57], a significant increase of the area of failure occurs as

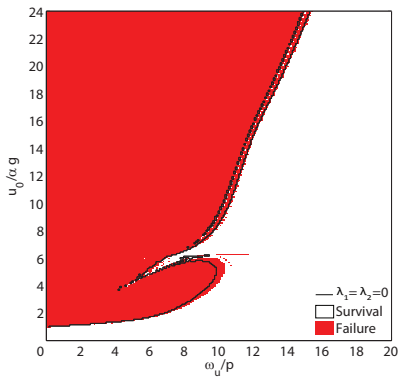

(a) $\lambda_1 = 0.3$, $\lambda_2 = 0$

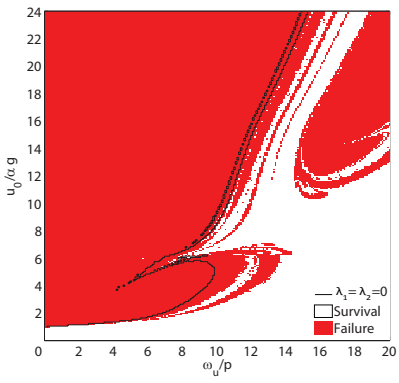

(b) $\lambda_1 = 0.9$, $\lambda_2 = 0$

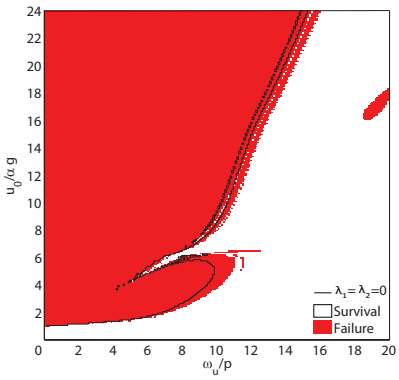

(c) $\lambda_1 = 0.3$, $\lambda_2 = 0.3$

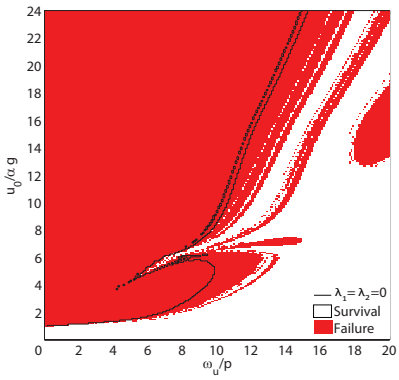

(d) $\lambda_1 = 0.3$, $\lambda_2 = 0.9$

Figure 4.14 – Stability diagram of two stacked bodies with dimensions $h_1 = 0.6$, $b_1 = 0.2$, $h_2 = 0.15$, $b_2 = 0.05$ for a) $\lambda_1 = 0.3$, $\lambda_2 = 0$, b) $\lambda_1 = 0.9$, $\lambda_2 = 0$ c) $\lambda_1 = 0.3$, $\lambda_2 = 0.3$ d) $\lambda_1 = 0.3$, $\lambda_2 = 0.9$. The horizontal and vertical axes are normalised with $p = 6.8215$ and $\alpha = 0.3218$. The boundaries between survival and failure when $\lambda_1 = 0$, $\lambda_2 = 0$ are plotted for explanation.

λ_1 is increased while retaining $\lambda_2 = 0$, as in the case of Figures 4.14(a) and 4.14(b). Similarly, the stability diagram is affected when only λ_2 is increased as in Figures 4.14(c) and 4.14(d). When either λ_1 or λ_2, or both are substantially increased to values near unity as in Figures 4.14(b) and 4.14(d), not only are the failure areas increased but there appear several areas in the diagram with multiple transitions between survival and failure. In these areas the outcome of the body is highly sensitive to the amplitude and frequency of the input, similar

to the observations made in [3, 91] for rocking systems with increased number of impacts. Time histories for θ_1 and $\theta_2 - \theta_1$ are shown in Figures 4.15(a) and Figures 4.15(b) when $\omega_u/p = 12$ and $u_0/(\alpha g) = 5.25$. It is clear in Figure 4.15 that the assumed values of both λ_i have a significant effect in the time history responses of the system. An additional effect in comparison to the single rocking body case studied in [57] is that the λ_i also affect the contact interfaces that become active during the excitation.

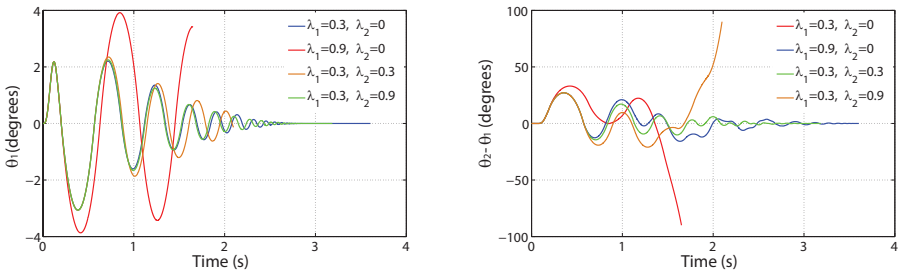

(a) θ_1 (b) $\theta_2 - \theta_1$

Figure 4.15 – Time histories for stacked bodies with dimensions $h_1 = 0.6$, $b_1 = 0.2$, $h_2 = 0.15$, $b_2 = 0.05$ when $\omega_u/p = 12$ and $u_0/(\alpha g) = 5.25$ for different values of λ_i for a) θ_1, b) $\theta_2 - \theta_1$.

In this problem the increased number of impacts is due to the change of the energy exchanged between the two bodies and the energy lost by the system to the ground, which are affected by λ_2 and λ_1 respectively. While these energies also depend on the pre-impact velocities, in general higher values of λ_1 and λ_2 lead to less loss of energy per impact. This can be illustrated by defining an average total reduction of energy factor for the system, r_t, as:

$$r_t = \sum_{i=1}^{N_I} \frac{\frac{T^+_{k1_i} + T^+_{k2_i}}{T^-_{k1_i} + T^-_{k2_i}}}{N_I} \tag{4.17}$$

where N_I is the number of impacts during the response of the system and $T^{\pm}_{kj_i}$ is the kinetic energy of body i for impact j before $^-$ and after $^+$ the impact.

The values of r_t for a range of values of $u_0/(\alpha g)$ and ω_u/p and for $\lambda_1 = \lambda_2 = 0$ and $\lambda_1 =$

0.6, $\lambda_2 = 0.3$ are shown in Figures 4.16(a) and 4.16(b) respectively. Both cases are compared with their corresponding boundaries between survival and failure. Note that the white color in Figure 4.16 corresponds to cases where the system fails without impact. Therefore, r_t cannot be defined.

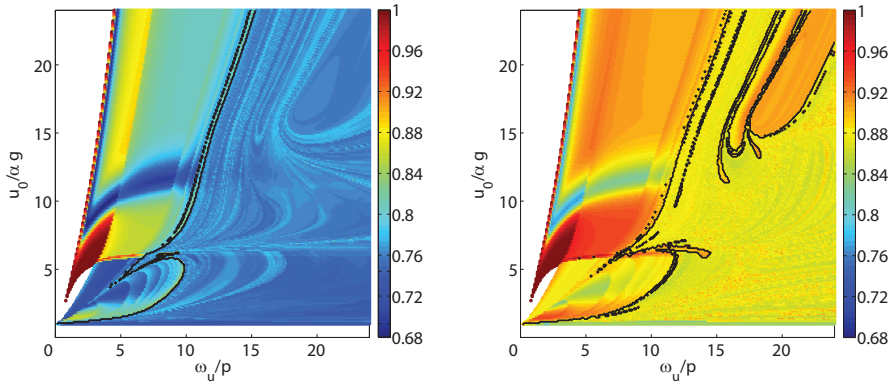

(a) $\lambda_1 = 0$, $\lambda_2 = 0$ (b) $\lambda_1 = 0.6$, $\lambda_2 = 0.3$

Figure 4.16 – Loss of energy factor r_t for the system. The dimensions of the bodies are $h_1 = 0.6$, $b_1 = 0.2$, $h_2 = 0.2$, $b_2 = 0.05$ for a) $\lambda_1 = 0$, $\lambda_2 = 0$ and b) $\lambda_1 = 0.6$, $\lambda_2 = 0.3$. Boundaries between survival and failure for both cases are plotted for explanation.The horizontal and vertical axes are normalised with $p = 6.8215$ and $\alpha = 0.3218$.

A comparison of Figure 4.16 with the corresponding stability diagrams in Figures 4.9 and 4.14(b) shows a good correspondence between the areas of high values of r_t, indicating small loss of energy, and failure.

Stability diagrams for subjecting the system to double pulses are shown in Figure 4.17(a) for $\lambda_1 = \lambda_2 = 0$, and Figure 4.17(b) for $\lambda_1 = 0.6$ and $\lambda_2 = 0.3$. As expected double pulses result in increasing the areas of failure in comparison to the single pulse case, even when both $\lambda_i = 0$. Figure 4.17(b) suggests that the effect of the assumed values of λ_i becomes of increasing importance as the number of pulse is increased and results to even further increasing the area of failure. A comparison between Figures 4.17(a) and 4.17(b), shows that the assumption of retaining angular momentum with respect to the future rocking corners

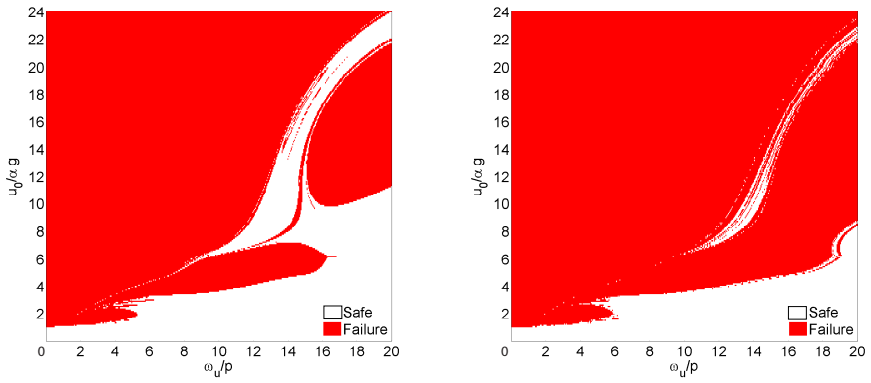

(a) $\lambda_1 = 0$, $\lambda_2 = 0$ (b) $\lambda_1 = 0.6$, $\lambda_2 = 0.3$

Figure 4.17 – Stability diagram of two stacked bodies subjected to two sinusoidal pulses. The dimensions of the bodies are $h_1 = 0.6$, $b_1 = 0.2$, $h_2 = 0.2$, $b_2 = 0.05$ for a) $\lambda_1 = 0$, $\lambda_2 = 0$ b) $\lambda_1 = 0.6$, $\lambda_2 = 0.3$. The horizontal and vertical axes are normalised with $p = 6.8215$ and $\alpha = 0.3218$.

can severely underestimate the tendency of the system of stacked bodies to fail for a double pulse excitation. Similar results can be obtained for further increasing the number of pulses.

4.3.3 Effect of body dimensions.

The model of stacked rocking bodies often has applications to museums where the bottom body corresponds to a pedestal with the upper body being a museum artifact. A design decision that often has to be taken in a museum has to do with the dimensions of the pedestal for a given artifact. This Section investigates the effect of the combined stability of the system for artifacts and pedestals of different size. Three different combinations of bottom and top bodies are examined, as summarised in Table 4.4. For the first two cases, the bottom body is kept the same with top body changing, corresponding to a situation where different artifacts are placed on the same pedestal. For the last two cases the dimensions of the bottom body are varied with the top body being the same; this corresponds to an investigation of using different pedestals for the same artifact. It is assumed that both bodies

have the same density and are not hollow. (The latter assumption may not necessarily be true for museum pedestals, some of which have hollow compartments.)

Table 4.4 – Dimensions for the different cases.

	Body 1			**Body 2**		
	h_1 [cm]	b_1 [cm]	h_1/b_1	h_2 [cm]	b_2 [cm]	h_2/b_2
Case 1	60	20	3	20	5	4
Case 2	60	20	3	15	5	3
Case 3	45	20	2.25	15	5	3

The three cases are subjected to a single cycle sinusoidal pulse ground acceleration as defined in equation (2.17) varying the frequency ω_u and the amplitude u_0 . Different values of λ_i are considered.

The stability diagrams for the three cases are presented in Figure 4.18, where the horizontal and vertical axes are normalised with $p = 6.8215$ and $\alpha = 0.3218$, corresponding to Block 2 for cases 2 and 3. In each figure, the lines presented correspond to the boundaries between survival and failure.

Figure 4.18(a) presents the boundaries of survival and failure for the three cases, when $\lambda_1 = \lambda_2 = 0$. Comparing cases 1 and 2, where block 1 has the same aspect ratio, case 2 appears overall as a safer solution. There are, however, combinations of ω_u/p and $u_0/(\alpha g)$ in which case 2 results in failure while case 1 results in survival e.g, for $\omega_u/p = 7.45$ and $u_0/(\alpha g) = 6.55$. Figure 4.18(b) shows the boundaries between failure and survival when $\lambda_1 = 0.6$ and $\lambda_2 = 0$. Contrasting with the case of $\lambda_i = 0$, case 1 now results in fewer pairs of u_0, ω_u that result in failure than case 2. However, there are still combinations of ω_u/p and $u_0/(\alpha g)$ where this situation reverses. Figure 4.18(c) illustrates the boundaries of failure and survival when $\lambda_1 = 0$ and $\lambda_2 = 0.6$. Similar to the case of $\lambda_i = 0$, case 2 appears the safer

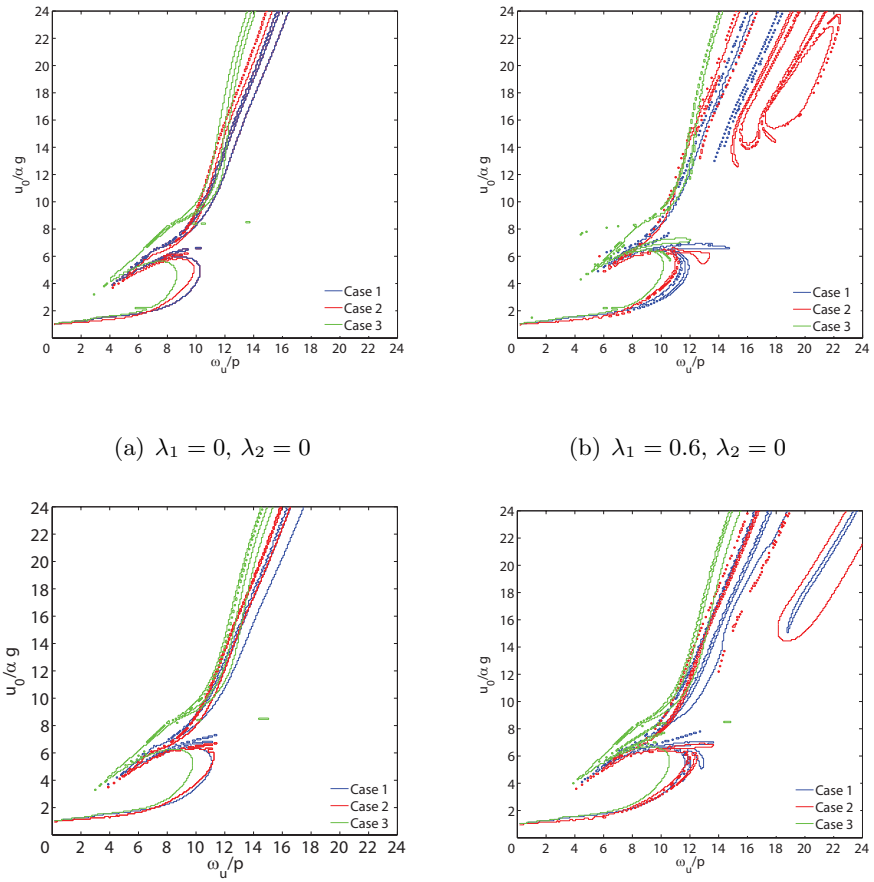

(a) $\lambda_1 = 0$, $\lambda_2 = 0$

(b) $\lambda_1 = 0.6$, $\lambda_2 = 0$

(c) $\lambda_1 = 0$, $\lambda_2 = 0.6$

(d) $\lambda_1 = 0.3$, $\lambda_2 = 0.6$

Figure 4.18 – Contour plots for a)$\lambda_1 = \lambda_2 = 0$ b) $\lambda_1 = 0.6$, $\lambda_2 = 0$, c) $\lambda_1 = 0$, $\lambda_2 = 0.6$ and d) $\lambda_1 = 0.3$, $\lambda_2 = 0.6$ for Stacked Bodies 1, 2 and 3 defined in Table 4.2.

solution as λ_2 is increased. When $\lambda_1 = 0.3$ and $\lambda_2 = 0.6$, Figure 4.18(d), there is no clear trend of one of the two solutions resulting in less failure. Hence, for a specific set of u_0 and ω_u the safest artifact, amongst the two studied here, depends on the values of λ_i. Equally, the optimal body in terms of decreasing the failures observed for the majority of ω_u and u_0 changes depending on the values of λ_i. However, as in the previous Section, for a given case it appears that an optimal situation occurs if $\lambda_1 = \lambda_2 = 0$. This would favour the use of absorbing materials in both interfaces, or the placement of feet on the pedestal.

Comparing now the cases where the dimensions of the pedestal are varied (case 2 and 3) it can be seen from Figure 4.18(a) that similar trends can be observed. While for $\lambda_1 = \lambda_2 = 0$

case 3 appears to be safer for the majority of the pairs of ω_u, u_0, there are combinations for which case 3 fails and case 2 survives, e.g., $\omega_u/p = 11.89$ and $u_0/(\alpha g) = 10.01$. Increasing the values of λ_i, Figures 4.18(b), 4.18(c) and 4.18(d), results in case 3 becoming safer than case 2 for most combinations of ω_u and u_0. Note that in these three Figures there are also combinations of ω_u/p and $u_0/(\alpha g)$ where case 3 fails and case 2 survives. Hence, again the optimal pedestal for a given artifact is a function of the properties of the excitation (u_0, ω_u) and the interface properties λ_1 and λ_2. Again however a decrease of the values of λ_i appears to improve each solution, i.e., either placing feet on the bottom of the pedestal or absorbing materials at both interfaces improves the overall stability of the system regardless of the pedestal chosen.

An alternative approach is to fix the pedestal to the ground, in which case the artifact behaves as a single rocking body. For this aim, the stability diagram for a single rocking body with the same dimensions as block 2 for cases 2 and 3 is compared with the stability diagrams of cases 2 and 3 in Figure 8.4.

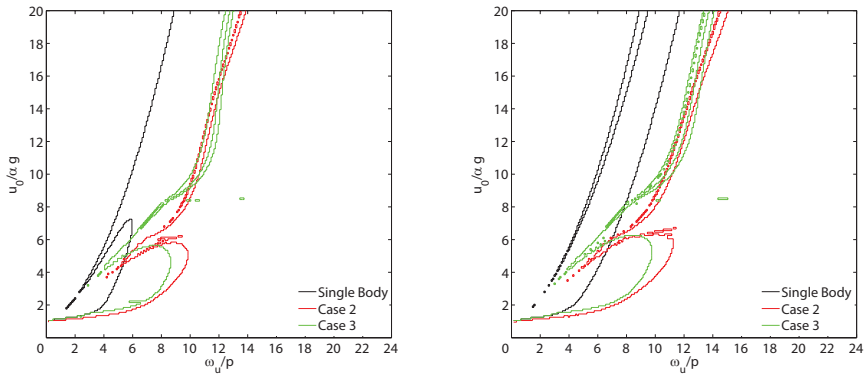

Figure 4.19 – Comparison of stacked bodies cases 2 and 3 and block 2 acting as a single body when a) $\lambda = \lambda_1 = \lambda_2 = 0$ and b) $\lambda = \lambda_2 = 0.6$, $\lambda_1 = 0$.

Although there are some pairs of ω_u, u_0 where case 3 appears to be safer than fixing the pedestal to the ground, the latter case appears to be safer for a wide range of values of ω_u, u_0.

This is true for both the case of $\lambda_1 = \lambda_2 = 0$, Figure 4.19(a), and for higher values of λ_2, e.g. $\lambda_2 = 0.6$ as in Figure 4.19(b). While, for the specific artifact it appears that fixing the pedestal to the ground is a favourable solution, in practice this has some limitations, such as the loss of mobility which is often a desirable feature in museums. Additionally, the pedestal was considered in the analysis as rigid, when in practice its flexibility may cause the acceleration at its top to be amplified in comparison to the input at the ground. Furthermore, in a museum there are several excitations that deviate substantially from the form of a single cycle sinusoidal base acceleration investigated here [89]. For example, accidental impact of visitors with the pedestal is a type of excitation that should be investigated where a non-fixed pedestal may potentially dissipate part of that energy by sliding.

4.4 Conclusions

This Chapter extends the discussion in Chapter 2 for the effect of the location of the vertical impulses during impact, to the case of two stacked rocking bodies. This Chapter considers the effects of this vertical impulse acting on interface i at a distance $\lambda_i\, b_i$, $\lambda_i \in [0, 1]$, from the future rocking corner.

To that end the momentum equations and transitions between patterns during impacts that were first derived in the work of [13] assuming $\lambda_1 = \lambda_2 = 0$ were re-derived. It was highlighted that the same non-tensile stresses assumption for the interface that defines the transitions without impact, implies that the vertical impulses have to be applied between the corner points of the rocking body above the interface. Additionally, it was shown that even in the original work of [13] there are situations where specific non-zero values of λ_i must be adopted so that the post-impact pattern is permissible. This Chapter argues that such cases instead result in loss of contact at one of the two interfaces, and hence free flight of part of the system. When such cases occur, a model that does not take into account such patterns should not be trusted.

The stability of the system subjected to simple single and double sinusoidal acceleration pulses was studied. As for the case of a single rocking body, it has shown that the common assumption in the literature, that $\lambda_i = 0$, is the least conservative scenario, as increasing the values of λ_i expands the area of failure. Higher values of λ_i result in multiple impacts prior to failure and, similar to the case of multiple pulses, introduce areas of ω_u and u_0 for which the stability of the body becomes sensitive on the exact values.

A practical study of the failure of different stacked bodies was performed. This study is applicable to, for example, museums where artifacts are placed on pedestals. For the systems studied, there is not a single solution which is the safest for all the combinations of ω_u/p and $u_0/(\alpha g)$. The optimal solution appears to be a function of the values of λ_i for the interfaces, which should be taken into account for design purposes. However, when $\lambda_i = 0$, the areas of failure tend to decrease. Hence, it appears that the use of energy absorbing materials in the contact interfaces, or of feet at the bottom of the bodies, whenever possible, result in usually safer solutions in terms of failure of the system through toppling.

Chapter 5

Rocking response of artifacts subjected to sound induced vibrations

5.1 Introduction

This thesis has focused on the stability diagram of rocking bodies subjected to earthquake type motion pulses. This Chapter is going to focus in another application which is museum artifacts.

In recent years, there has been a growing interest in the protection of cultural heritage artifacts. The vulnerability of museum exhibits under seismic action can have devastating consequences for the gallery. Unfortunately, there is a lack of seismic regulations regarding the protection of museum artifacts, even for countries with high seismic activity.

Because of this, a few investigations are related to seismic art object mitigation. One of the pioneers papers was [92]. This research focuses analytically and experimentally in the evaluation of seismic mitigation methods in the J. Paul Getty Museum in Malibu, California. Many Italian research groups have described the problem of the museums and have given

some simple rules for the design of display cases and other kinds of exhibitions [93]. An investigation on the identification of the artifact failure is presented in [94] which also proposed a methodology to preserve cultural heritage.

However, while the previous studies are focused on earthquakes, there is a need to investigate the day to day vibrations that each artifact of a museum is subjected to, i.e., constructions, traffic, people walking or music. In [89] different methods and procedures were developed to protect the art of The Metropolitan Museum of Art in New York while a construction was occurring in one of its galleries. Information on vibrations and its effects in museum artifacts were carried out in [95] along with recommending conservative limits for protection of artwork from construction vibration.

In this present Chapter, the effect of the background music in museum artifacts is investigated. In theory, music is a perfect sinusoidal but in reality the music notes are not and, moreover, depend on the instrument. Each instrument creates a different timbre; the flute produces sound through air, the piano through the hit of a string with a hammer and the guitar through the strum of one of its string. This causes that the vibration of a guitar to be different to the one produce by another instrument of a different family. It is therefore of interest to study the effect of some instruments on the stability of museum artifacts.

For the aim of the Chapter, the artifact is modelled through the extended IPM of [5] which allows the artifacts to not only rock but also slide, lift off and slide-rock. A representative museum scenario is selected and a simplified criterion of the music path travel is used in order to define the acceleration that the artifact is subjected to. Finally, the results are analysed to evaluate which system or instrument provides the best performance.

5.2 Classifications of motions of a body.

The purpose of this Section is to briefly explain the different patterns that a free standing rigid block experiences while subjected to a ground excitation. This Section is based on

the study of [5]. Therefore, only a review of the conditions to initiate the patterns as well as the conditions to switch between them are presented. For further information about the equations of motions and their derivation, the reader is referred to [5].

This analysis is restricted to a symmetric, rigid, rectangular block and horizontal ground acceleration as illustrated in Figure 5.1. Slide, slide-rock and free-flight modes are included in this study, aside from the static and rocking configuration explained in Section 2.2.1. The motion of the body is defined through six patterns summarised in Figure 5.1 where the block is subjected to horizontal, $\ddot{x}_g$, and vertical $\ddot{y}_g$ ground motion. Patterns A, B, C, D, E_A, E_B and F correspond respectively to the body experiencing pure rocking with respect to the left corner, pure rocking with respect to the right corner, rest, slide, slide-rock with respect to the left corner, slide-rock with respect to the right corner and free-flight mode. The conditions for each motion are presented in Table 5.1. For instance, for pattern D, pure slide, the angular displacement θ is zero whereas the horizontal velocity at the contact point $\dot{x}_0$ must be different than zero. Note that for all the patterns describe in Table 5.1, the vertical force, f_y is positive apart from the free flight mode.

Table 5.1 – Conditions to patterns

Pattern	A	B	C	D	E_A	E_B	F
θ	$\theta < 0$	$\theta > 0$	$\theta = 0$	$\theta = 0, \dot{\theta} = 0$	$\theta < 0$	$\theta > 0$	-
$\dot{x}_0$	$\dot{x}_0 = 0$	$\dot{x}_0 = 0$	$\dot{x}_0 = 0$	$\dot{x}_0 \neq 0$	$\dot{x}_0 \neq 0$	$\dot{x}_0 \neq 0$	-
f_y	$f_y > 0$	$f_y > 0$	$f_y > 0$	$f_y > 0$	$f_y > 0$	$f_y > 0$	$f_y < 0$

While the conditions for each pattern are previously defined, the conditions to switch between patterns are presented in Table 5.2. In the first column, the patterns before switching are presented whereas in the first row the future pattern is shown. For example, switching from pattern A, pure rocking with respect to the left corner, to pattern D, pure sliding occurs

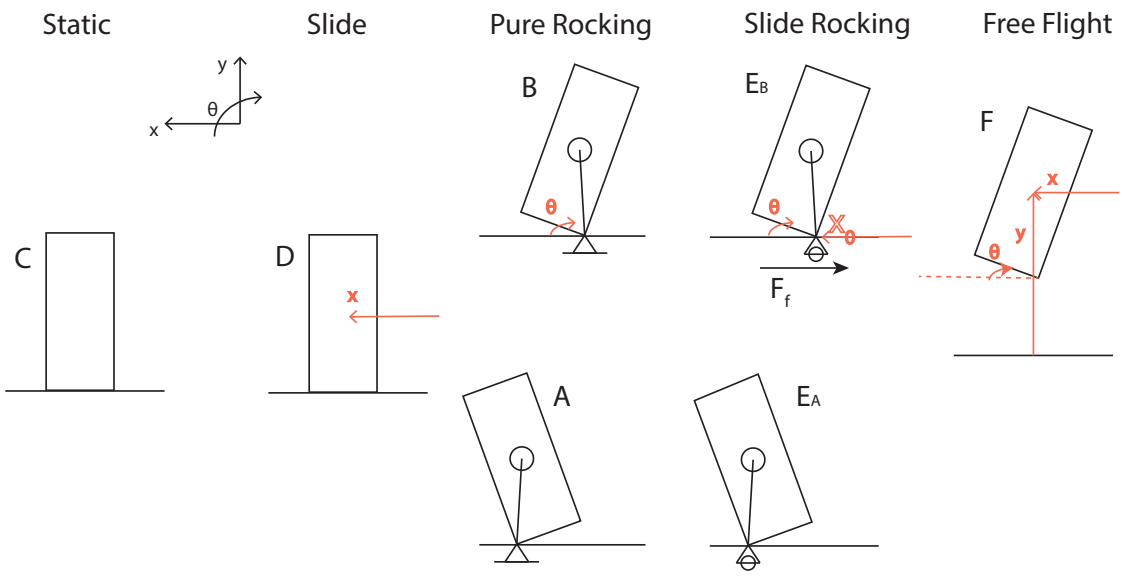

Figure 5.1 – Slide-Rocking Model defined by Shenton and Jones [5] for a free-standing rocking block.

when $\theta = 0$ and $\dot{x}_0 \neq 0$ or switching from pattern E_B to A, $\dot{x}_0 = 0$ and θ must change sign.

Table 5.2 – Events to go from one pattern to other

Pattern	A	B	C	D	E_A	E_B	F
A	-	$\theta > 0$	$\theta = 0$	$\theta = 0, \dot{x}_0 \neq 0$	$\dot{x}_0 \neq 0$	$\theta > 0, \dot{x}_0 \neq 0$	$f_y < 0$
B	$\theta < 0$	-	$\theta = 0$	$\theta = 0, \dot{x}_0 \neq 0$	$\theta < 0, \dot{x}_0 \neq 0$	$\dot{x}_0 \neq 0$	$f_y < 0$
C	$\theta < 0$	$\theta > 0$	-	$\dot{x}_0 \neq 0$	$\theta < 0, \dot{x}_0 \neq 0$	$\theta > 0, \dot{x}_0 \neq 0$	$f_y < 0$
D	$\theta < 0, \dot{x}_0 = 0$	$\theta > 0, \dot{x}_0 = 0$	$\theta = 0, \dot{x}_0 = 0$	-	$\theta < 0, \dot{x}_0 \neq 0$	$\theta > 0, \dot{x}_0 \neq 0$	$f_y < 0$
E_A	$\dot{x}_0 = 0$	$\theta > 0, \dot{x}_0 = 0$	$\theta = 0, \dot{x}_0 = 0$	$\theta = 0$	-	$\theta > 0$	$f_y < 0$
E_B	$\theta < 0, \dot{x}_0 = 0$	$\dot{x}_0 = 0$	$\theta = 0, \dot{x}_0 = 0$	$\theta = 0$	$\theta < 0$	-	$f_y < 0$
F	$\theta < 0, \dot{x}_0 = 0$	$\theta > 0, \dot{x}_0 = 0$	$\theta = 0, \dot{x}_0 = 0$	$\theta = 0, \dot{x}_0 \neq 0$	$\theta < 0, \dot{x}_0 \neq 0$	$\theta > 0, \dot{x}_0 \neq 0$	-
	$f_y > 0$	$f_y > 0$	$f_y > 0$	$f_y > 0$	$f_y > 0$	$f_y > 0$	-

5.3 A review of sound induced vibration

It is known that the shape of a waveform highly affects the response of a rocking body [57], it is therefore the aim of this Section to briefly explain how sound induced vibration is produced

from music instruments and why each of them produce a different wave pattern.

A sound wave is created as a result of a vibrating object which is the source of disturbance that moves through the medium. Musical instruments are formed into vibration when a person hits, strikes, plucks or strums. For example, a piano string is hit with a hammer when the pedal is played, a guitar string is plucked or strummed and a drum is hit with the drummer stick. By direct contact, these hits, strikes or plucks put energy into the instrument by disturbing the particles and forces of the objects into vibrational motion at their natural frequencies [96]. The result from the back and forth vibration of the particles through which the induced pressure wave is moving is the sound.

An instrument vibrates in such a manner that a standing wave pattern is formed within the object. Each natural frequency that an object or instrument produces has its own wave pattern. These patterns are only created at specific frequencies of vibration known as harmonic frequencies. For musical instruments and other objects, the harmonic frequencies are related to each other by simple whole number ratios.

For instance, consider a bass. Each end of a string is attached and fixed to the bass hence, it is unable to move and is called a node. Between each two nodes there is an area of high vibration called antinode. This is also called fundamental frequency or first harmonic of the instrument [96]. Figure 5.2(a) represents the waveforms of the first, second and third harmonic of a string. Observe that the second and third harmonics are produced by adding one or two more nodes, respectively. Also note that if a node is added, an antinode must also be added to maintain this alternation pattern behaviour. The patterns on Figure 5.2(a) are not the only patterns of vibration for a bass string. There are a infinite of patterns, by which the bass string could naturally vibrate, which are associated to each of its harmonic frequencies [97].

Nonetheless, the wave patterns of instruments are not generally possible to define as a simply harmonic motion. Instead, the oscillatory motion is a more complicated waveform

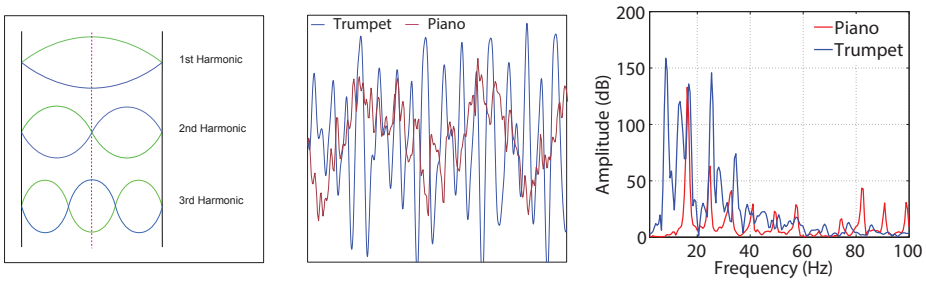

(a) (b) (c)

Figure 5.2 – a) Set of harmonics. b) Typical waveform produced by a trumpet and piano (C0 note). c) Spectrum of the series in b).

as illustrated in Figure 5.2(b) for a trumpet and piano. The reason is the overtones. These are the other frequencies besides the fundamental one that exists in musical instruments. These are illustrated in Figure 5.2(c). Different instruments produce different overtones. A combination of overtones forms the characteristic sound of the instrument. For example, in Figure 5.2(b) both waves have the same frequency, and therefore the same note. However, their overtones are different, and hence, their fundamental are different.

5.4 Physical signal model

Nowadays, the used of real instruments to produce music has become less popular due to the advance in physical signal models. A virtual instrument is typically much less expensive than the corresponding real one. Moreover, while real instruments can share common controllers, any virtual instrument effect can be quickly loaded on software. Nevertheless, the challenge of physical models is that they must really sound like the instrument or effect they are imitating [98]. It is therefore the purpose of this Section to briefly present the physical signal model used in this study.

There are many kinds of signal models to consider for musical instruments such as recordings, structured samplings, spectral models and virtual analog [98]. In this study, the music

is produced using FL Studio 12 software. Figure 5.3 simply represents the procedure that FL studio 12 follows to produce music. The real signal is first digitalised and sampled. After that, the signal is quantised and therefore noise is introduced. The quantisation noise depends on the input signal and it is inconsistent in amplitude and power, has distortion and an unpredictable spectral distribution. However, a dither noise which is a constructive noise (although uncontrollable), substitutes the noise produce by simple quantization. Dither replaces the noise with a random pattern noise characteristic of user selection which is not dependent on the input.

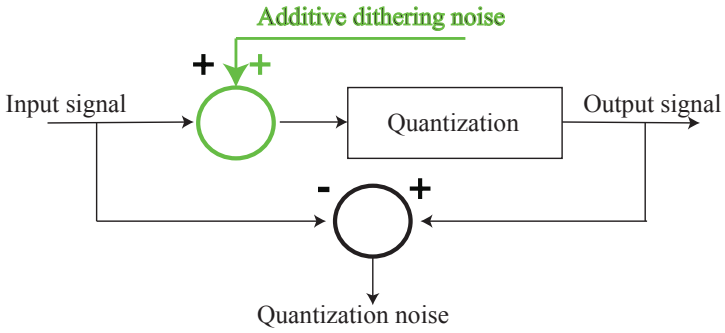

Figure 5.3 – Simplistic explicative diagram of how FL Studio 12 digitalised real signals.

5.5 Analysis of Museums set up

The purpose of this Section is to analyse the wave travel diagram for one of the most common museum scenarios where artifacts are displaced on cantilevered shelves as shown in Figure 5.4.

Sound waves can cause larger stresses on the artifacts or the object can topple or walk on the shelves or objects can hit neighbour artifacts while moving. Depending on the shape and mass distribution of the object and also the configurations of its mount, these vibrations might come in the form of increased bending, shear or bearing stresses [89]. The effect of these type of stresses on an artifact depend on the number of cycles as shown in [57].



Figure 5.4 – Typical case with cantilever shelves where objects are placed at the Ashmolean Museum in Oxford (U.K.).

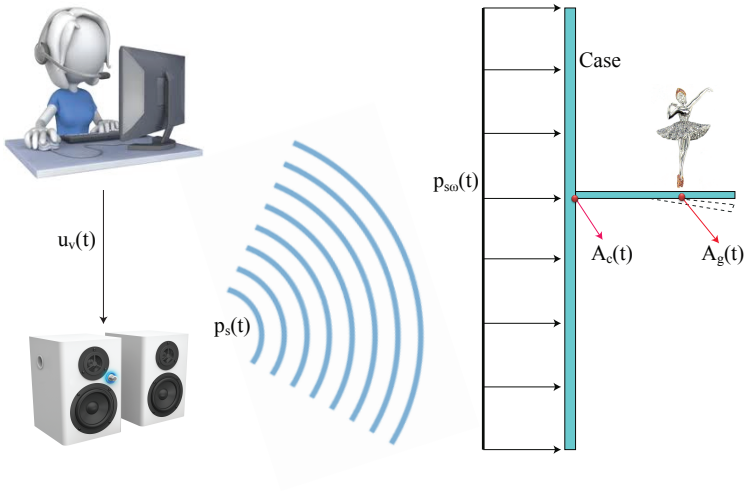

Figure 5.5 – Schematic explanation of a museum set up.

One of the most common museum set ups [99] is this situation of artifacts placed on cantilever shelves inside cases illustrated in Figure 5.4. This set up highlights the differences between motions relative to the original source of excitation. This is shown in Figure 5.5 in which a schematic explanation of this work is presented. A sound, $u_v(t)$ is digitally produced. It is then transformed into analog signal through the sound cord and it is sent to the speakers. The surface of the speakers vibrates transporting the sound in all directions. In this moment, the sound wave is transformed to air pressure wave $p_s(t)$. The pressure wave travels around until reaches a case where the artifact is placed. In the moment that the input, $p_{s\omega}(t)$, is in

touch with the case, it causes the acceleration of the case, $A_c(\omega)$, hence, the output. This acceleration travels through the cantilever shelve where the input is $A_c(\omega)$ and the output is the relative acceleration $A_g(\omega)$. Mathematically, this wave travel diagram can be defined with the following equations:

$$\begin{aligned} p_s(t) &= s_1 u_v(t) \\ p_{sw}(t) &= s_2 p_s(t) \\ A_c(\omega) &= H_1(\omega) p_{sw}(\omega) \\ A_g(\omega) &= H_2(\omega) A_c(\omega) \\ A_g(\omega) &= sH(\omega) U_v(\omega) \end{aligned} \tag{5.1}$$

where s_1, s_2 and s are the air pressure constant, the distant constant and the total of both, respectively. $H_1(\omega)$, $H_2(\omega)$ and $H(\omega)$ are frequency response functions in the frequency domain and hence, $H_1(\omega)$, $H_2(\omega)$ and $H(\omega) = H_1(\omega)\ H_2(\omega)$ are the frequency response functions of the case, rack and both, respectively, where ω is the input frequency. In order for this wave travel diagram to be possible, several assumptions are made:

- The speaker is assumed to be ideal therefore, sound waveforms are perfectly transformed to air pressure.
- The air pressure is a travelling wave and travels in any direction. However, it is assumed that there are not reflections from the environment.
- The case, rack and the artifact are three dynamic systems. However, by considering that the input and output of the case are not affected by the dynamics of the rack, it is assumed that the case is not affected by the dynamics of the rack. The same is assumed between the rack and the artifact. Thus the rack is not affected by the dynamics of the artifact.

5.6 Amplification factors

One of the most common scenarios in which vibrations may become more intensied is when objects are displayed on cantilevered shelves as illustrated in Figure 5.4. When the rack is a cantilever hanging perpendicularly from the case, the rack move horizontally deforming in the axial direction and the case deforms laterally. This situation presents a simple example of mechanical vibration, and highlights the distinct potential for amplication of motion relative to the original source excitation (the case). For the purposes of simplication, one may idealize a cantilevered shelf as simply a cantilevered beam with a mass on the end (a displayed object), as shown in Figure 5.5.

It is, therefore, the aim of this Section to study basic strategies to avoid large motions of the rack, $|x|_r$, relative to the shelf, $|x|_s$. These large or maximum motions are expressed as a ratio $|x|_s/|x|_r$ and depends on the frequency content with respect to the natural frequency of the shelf, whether is applied in a sustained or shorter transient manner and the amount of damping [89].

There are many basic strategies to reduce large motions such as avoid excitations near the natural frequency, or, if not, shifting the natural frequency of the object away from the excitation frequency [89] or increasing the damping ratio. For instance, Figure 5.6(a) illustrates the frequency response function, $H(\omega)$, for a harmonic excitation of a rack for different damping ratios. Observe that larger damping ratios reduce the ratio $|x|_s/|x|_r$.

Typically, one wants to lower the natural frequency of the object which is achieved adding a mass and/or softening the stiffness. This is presented in the Figure 5.6(b) where $\omega_n = 30$ Hz is increased and decreased to move the system.

In Figure 5.6, only the cantilever shelf was considered however, this shelf is excited because the air pressure waves arrive to the case producing an acceleration $A_c(\omega)$. Thus, both case and rack frequency response functions should be considered to find $A_g(\omega)$. Figure 5.7 represents the amplification factor when ξ is varied. Similar to Figure 5.6(a), larger damping ratios

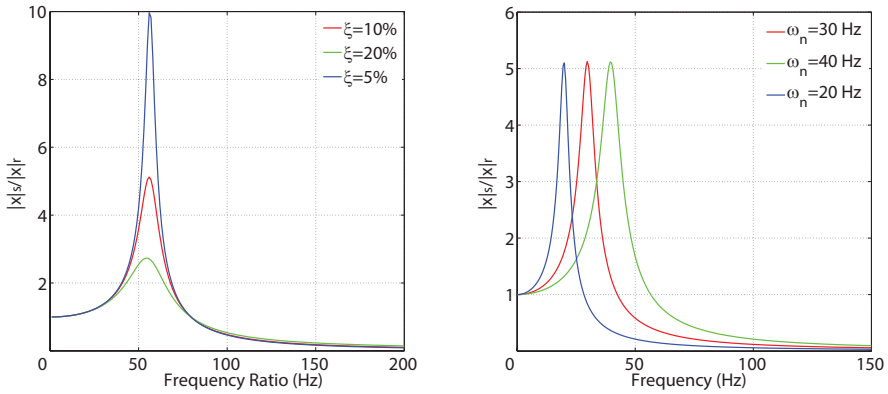

(a) (b)

Figure 5.6 – a) Comparison of the amplification response for different damping coefficients, $\omega_n = 50$ Hz. b) A comparison of a hypothetical situation where the system frequency is shifted for $\xi = 1\%$.

reduce the amplitude. To shift the natural frequencies to the right or left, the stiffness is increased or decreased, respectively by adding mass or softening the stiffness, as shown in Figure 5.7(b).

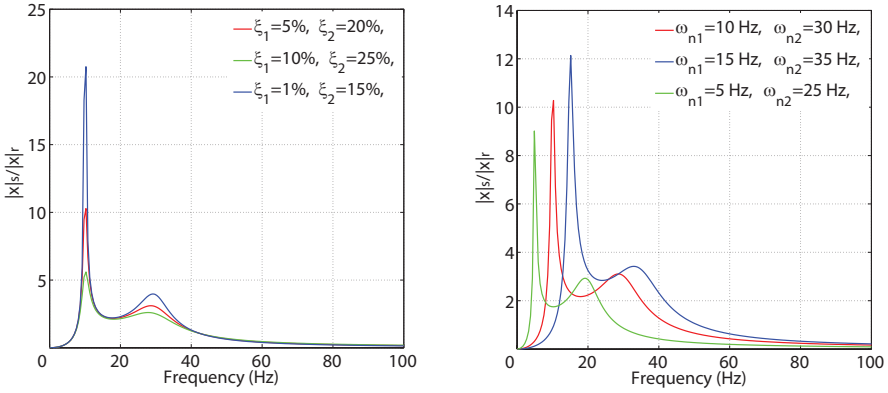

(a) (b)

Figure 5.7 – a) Comparison of the amplification response for different damping coefficients, $\omega_1 = 10$ Hz and $\omega_2 = 30$ Hz. b) A comparison of a hypothetical situation where the system frequency is shifted. $\xi_1 = 5\%$ and $\xi_2 = 20\%$. The number 1 and 2 refer to the case and rack, respectively.

Table 5.3 – Musical scale notes and frequencies.

Note	C0	D0	E0	F0	G0	A0	B0	C1	D1	E1
Freq. (Hz)	16.35	17.35	20.60	21.83	24.50	27.50	30.87	32.70	36.71	71.20

5.7 Effect of music notes on the stability of the body

This Section examines how the stability of a rocking body is affected when subjected to vibrations due to the acceleration of its ground induced by a music note. The body which is particularly investigated in this Section has the following characteristics: $b = 0.3$ cm, $h = 1$ cm, $p = 26.5466$ and $\alpha = 0.2915$ (Figure 2.1).

In the first part, the artifact is assumed to be placed or not in a rigid case and cantilever shelves. Secondly, the case and cantilever frequency response functions are taken into account. These simulations are done with the IPM of Section 2.2.1. Finally, the effect of sliding is investigated varying μ_f and the musical notes using the model presented in Section 5.2.

5.7.1 Input of the model

Musical notes are produced with FL Studio 12 software. Musical scale goes from C0 to B8 notes, with C0 having the lowest frequency (16.35Hz) and B8 the highest (7902.13 Hz). However, in [57, 26], it was observed that the stability of rocking bodies is affected by low frequency components (these depend on the body dimensions). Thus, this study is only focused in notes from C0 to E1, corresponding to the lower frequency notes. Table 5.3 illustrates the frequency of each of the notes used in this study.

The body is excited by four instruments (piano, organ, bass and synthesiser). Figure 5.8 illustrates the waveform of the C0 note of these instruments and Figure 5.9 the frequency domain of those signals. Observe that each instrument has a different waveform and that none of them is a perfect sinusoidal.

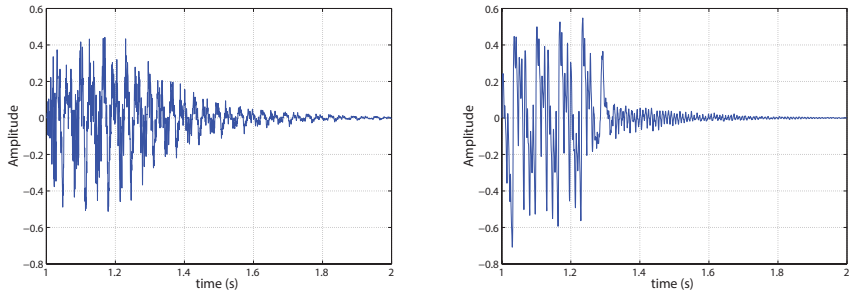

(a) Piano C_0

(b) Organ C_0

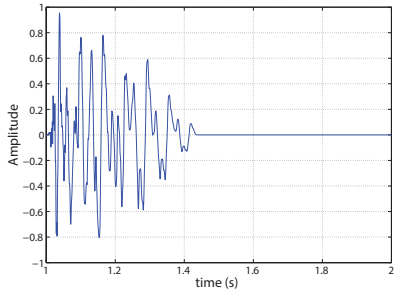

(c) Bass C_0

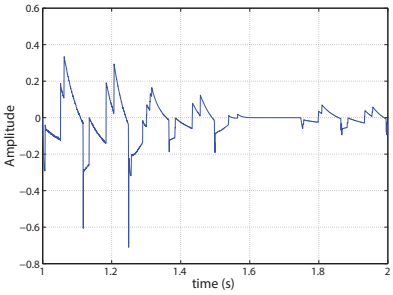

(d) Synthesizer C_0

Figure 5.8 – Waveform for the a) Piano C0, b) Organ C0, c) Bass C0 and d) Synthesizer C0.

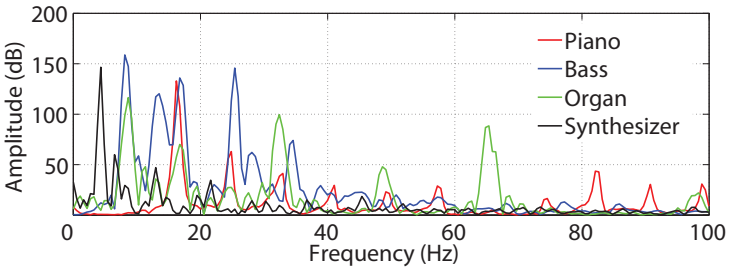

Figure 5.9 – Power spectrum of the Piano, Bass, Organ and Synthesizer, C0 note.

Through this Section, results are presented in the form of stability diagrams. In this Chapter, instead of using cycloidal pulses, the waveforms corresponding to notes are used. Hence, the horizontal axis is spaced according to the theoretical fundamental frequency of each note. Similar to previous Chapters, the outcome of the body is denoted in terms of survival or failure. Stability diagrams are calculated using as an input these music notes between C0 to E1 for each selected instrument. Note first that the frequency incremental

step between music notes is not homogeneous as shown in Table 5.3 and second, that the amplitude u_0 represents the volume of the speaker which varies uniformly until it provides a corresponding ground acceleration of 4.6 g.

5.7.2 Rigid case and cantilever shelf: $H(\omega) = 1$

This Section assumes that $H(\omega) = 1$ hence, that the case and rack are infinitesimally rigid. Figure 5.10 illustrates the stability diagrams of a rocking body subjected to the notes of different instruments. Note that there are no failures for $\frac{u_0}{tan(\alpha g)} < 1$, because it is the critical value to initiate the motion. The difference between instruments is clearly observed. While the piano is the safest instrument, the synthesiser is more prone to failure than the others. This is expected as the waveform between both instruments are extremely different as shown in Figures 5.8(a) and 5.8(d). This is similar observed for the square pulse in Chapter 2 where more areas of failure where observed, than for a sinusoidal or cosinoidal pulse. The reason is that the waveforms of the synthesiser and square pulse have strong drifts (ups and downs) on their form.

Figures 5.10(b) and 5.10(c) illustrate the stability diagrams of the organ and the bass, respectively. In contrast to the piano diagram, where only a few cases of failure appear at small frequencies and high amplitudes, the bass and the organ have more combinations of $u_0/\alpha g$ and music notes that produce the failure of the artifact. It is observed that for both instruments, the areas of failure decrease as the musical notes increase (the frequency also increases). However, the organ is more prone to failure at higher frequency notes (between B1 and E1) than the bass, for which the body appears to survive. These results confirm that the waveform of the vibration that the artifact is subjected to matters. This fact is in accordance with results shown in Chapter 2 where different cycloidal pulses have different areas of failure and survival.

This Section has pointed out how different waveforms affect the stability of an artifact

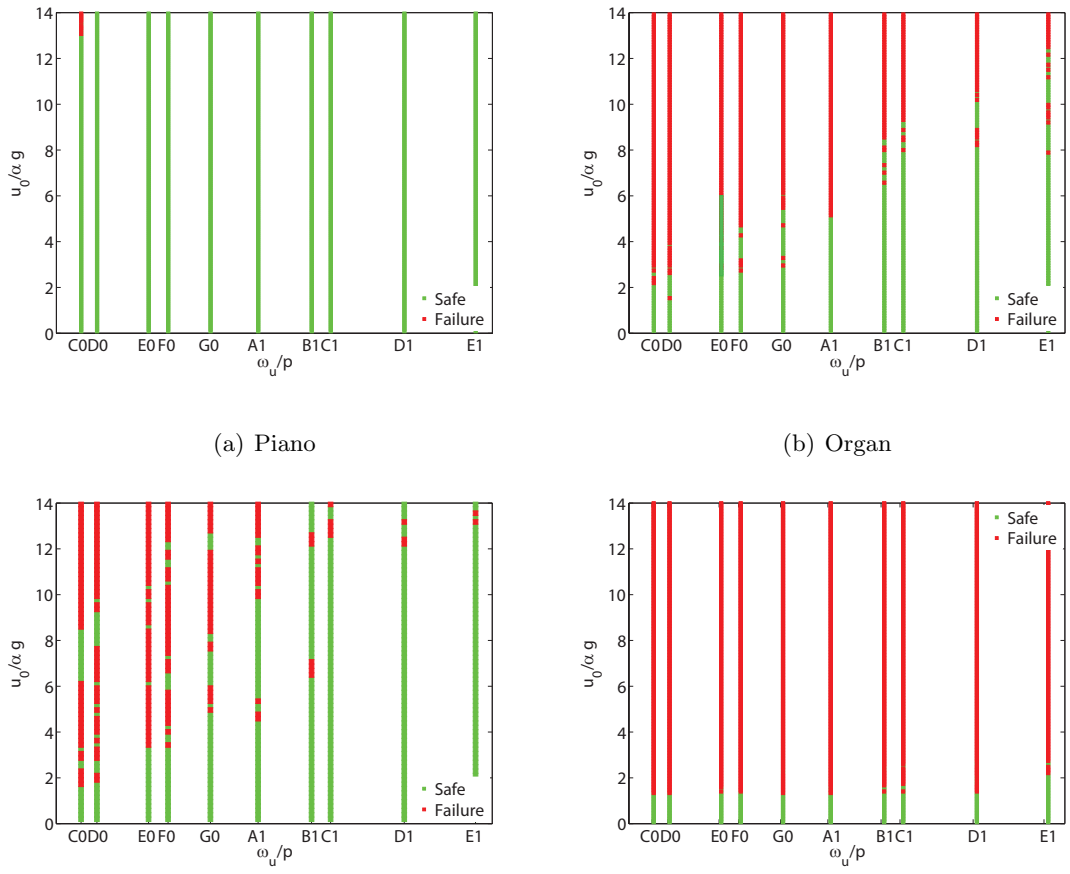

(a) Piano

(b) Organ

(c) Bass

(d) Synthesizer

Figure 5.10 – Stability diagrams when $H(\omega) = 1$ for a) piano, b) organ, c) bass and d) synthesizer.

when it is located in a stiff case and cantilever. It is observed that even waveforms that look similar, i.e., the piano or the organ, produce a completely different behaviour. Moreover, the nowadays common technique of creating artificial music with synthesisers has proved to be the least safe in terms of the stability of the artifact.

5.7.3 Flexible case and cantilever shelve: $H(\omega) \neq 1$

The previous Section examined the stability diagram when $H(\omega) = 1$ hence, it is of interest to include the case and the cantilever shelf, $H(\omega) \neq 1$. This corresponds to a more realistic scenario than that of the previous Section. For this purpose, reasonable values of the natural

frequency of the case, f_c, and the rack, f_r, are chosen to be 10 Hz and 30 Hz, respectively. Figure 5.11(a) and 5.11(b) show the overall frequency response functions $H_1(\omega)$ and $H_2(\omega)$ for the case and the rack, respectively. Figure 5.11(c) shows the frequency response function of both $H(\omega)$ which amplifies frequencies between [8-42] Hz.

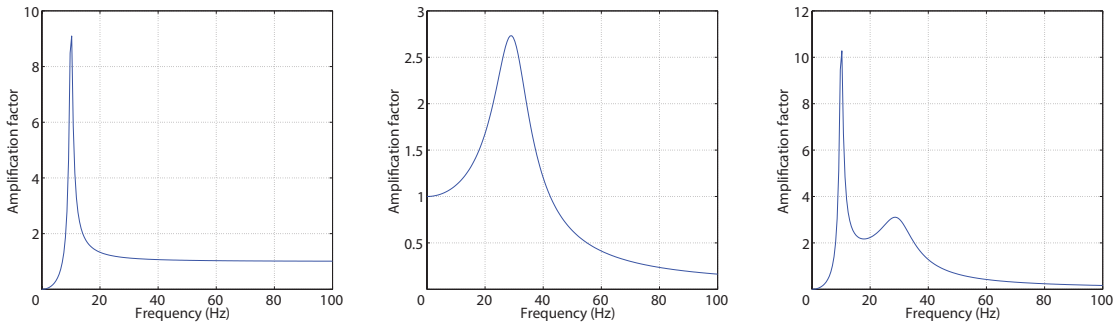

(a) Case (b) Rack (c) H

Figure 5.11 – frequency response function for a) case b) rack and c) both.

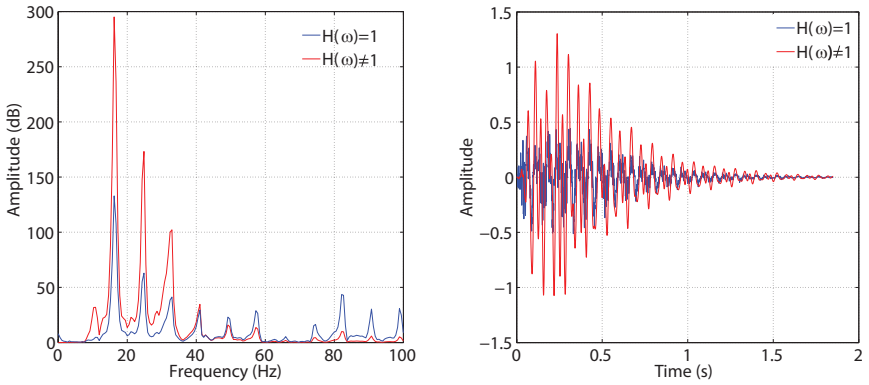

(a) Frequency Domain (b) Time Domain

Figure 5.12 – Comparison of the organ C0 note using the frequency responsefunction $H(\omega) \neq 1$ and $H(\omega) = 1$. a) Frequency domain b) time domain

Each musical note for each instrument is then transformed using these frequency response functions to take into account the case and the rack. An illustration of the change of the musical note while implementing $H(\omega)$ is illustrated in Figure 5.12 for the piano note C0. Figure 5.12(a) shows frequency domain of the signal and Figure 5.12(b) shows the time

domain. Both Figures also illustrate the signal when $H(\omega) = 1$. It is observed that $H(\omega)$ amplifies frequencies between 8-42 Hz and therefore, maximizes the low frequency notes.

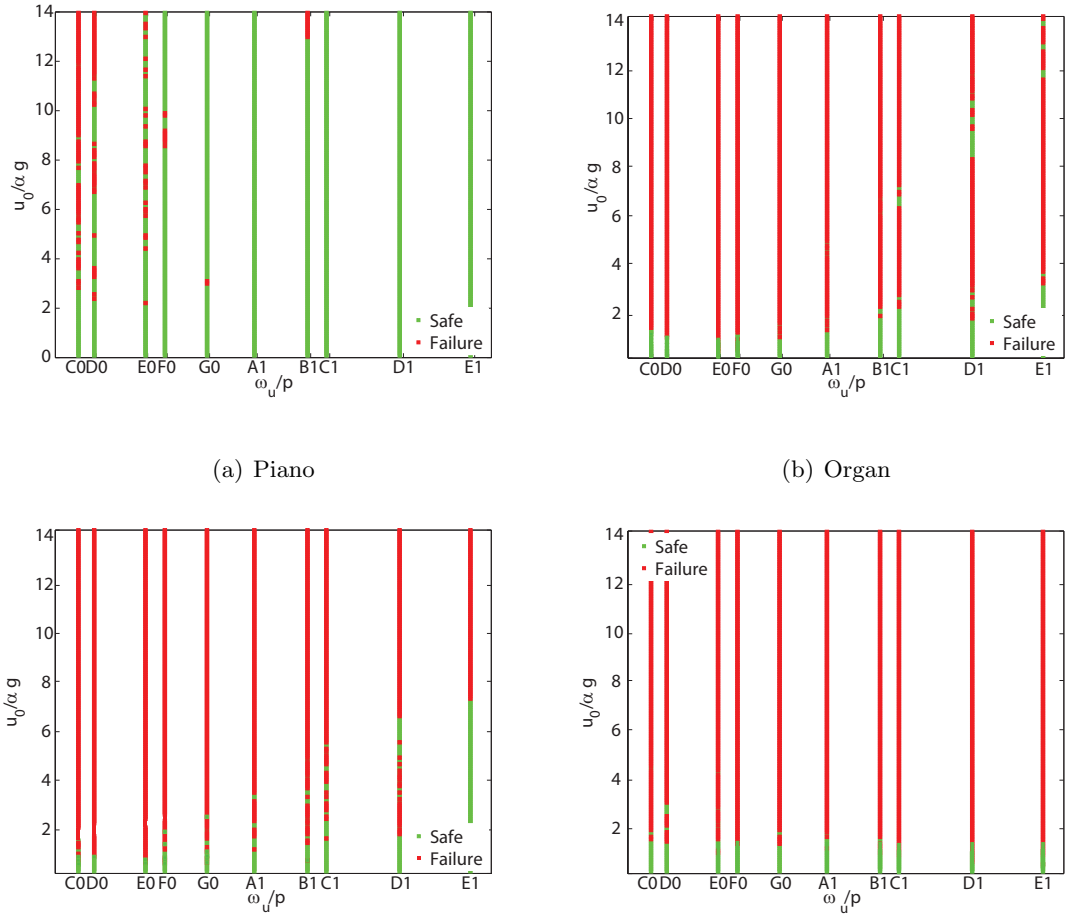

(a) Piano

(b) Organ

(c) Bass

(d) Synthesizer

Figure 5.13 – Stability diagrams when $H(\omega) \neq 1$ for a) piano, b) organ, c) bass and d) synthesizer.

Figures 5.13(a), 5.13(b), 5.13(c) and 5.13(d) represent the stability diagrams for the piano, organ, bass and synthesizer, respectively, with the $H(\omega)$ presented in Figure 5.11(c). Comparing with Figures 5.10(a), 5.10(b) 5.10(c) and 5.10(d), it is observed that the area of failure has increased for all cases. In Figure 5.10, the worst scenario was caused by the synthesiser for which most values of ω_u and u_0 fail. However, it is noticed that introducing the case and the rack, the bass and the organ also produces failure for most of the combinations of ω_u and u_0 as shown in Figures 5.13(b) and 5.13(c). This is as a consequence of the case

and the rack amplifying low frequency components for which rocking bodies are more prone to fail.

It has been illustrated in this Section that the amplification of the frequency of the notes through frequency response functions with realistic f_c and f_r could result in an increase of the areas of failure on the stability diagrams of the instruments studied. It is the aim of the next Section to try to find a reduction of these areas of failure when the case and the rack are taken into account.

5.7.4 Vibration mitigation

It was illustrated in the previous Section that using realistic values of f_c and f_r the artifact could become prone to failure. It is therefore of interest to try to find a realistic design of the case and the rack that ends in an improvement of the stability of the artifact.

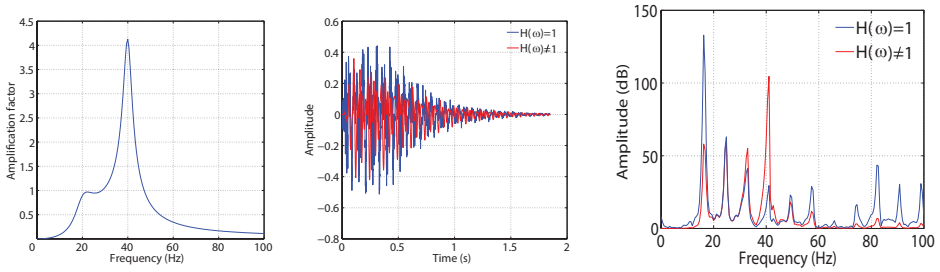

(a) $H(\omega)$ (b) Time Domain (c) Spectrum

Figure 5.14 – a) frequency response function when $f_c = 40$ Hz and $f_r = 20$ Hz. b) Comparison between the Piano note C0 with and without frequency response function c) Frequency domain.

In Figure 5.11(c), the rack and the case amplify frequencies between 0-42 Hz. Thus, in order to reduce the failure, the case frequency should be increased to shift the frequency response function to the right, mitigating all frequencies bellow its frequency. In a similar manner, the frequency of the rack is decreased therefore, its frequency response function is moved to the left. Thus, the combination of both, rack and case, decreases the behaviour of

f_r and also the low frequency content of the signal. With this intention, the case and the rack are modelled to have $f_c = 40$ Hz and $f_r = 20$ Hz respectively. The overall frequency response function $H(\omega)$ is shown in Figure 5.14(a). Observe that in contrast to Figure 5.11(c), the frequencies are amplified between 20 Hz and 40 Hz, and the maximum amplification factor is obtained at 40 Hz. The acceleration of the piano note C0 when this new $H(\omega)$ is applied is illustrated in Figure 5.14(b) and 5.14(c) in time and frequency domain, respectively. Both, $H(\omega) = 1$ and $H(\omega) \neq 1$, are presented in the Figure in time domain. Note that in this case, both signals have a similar amplitude.

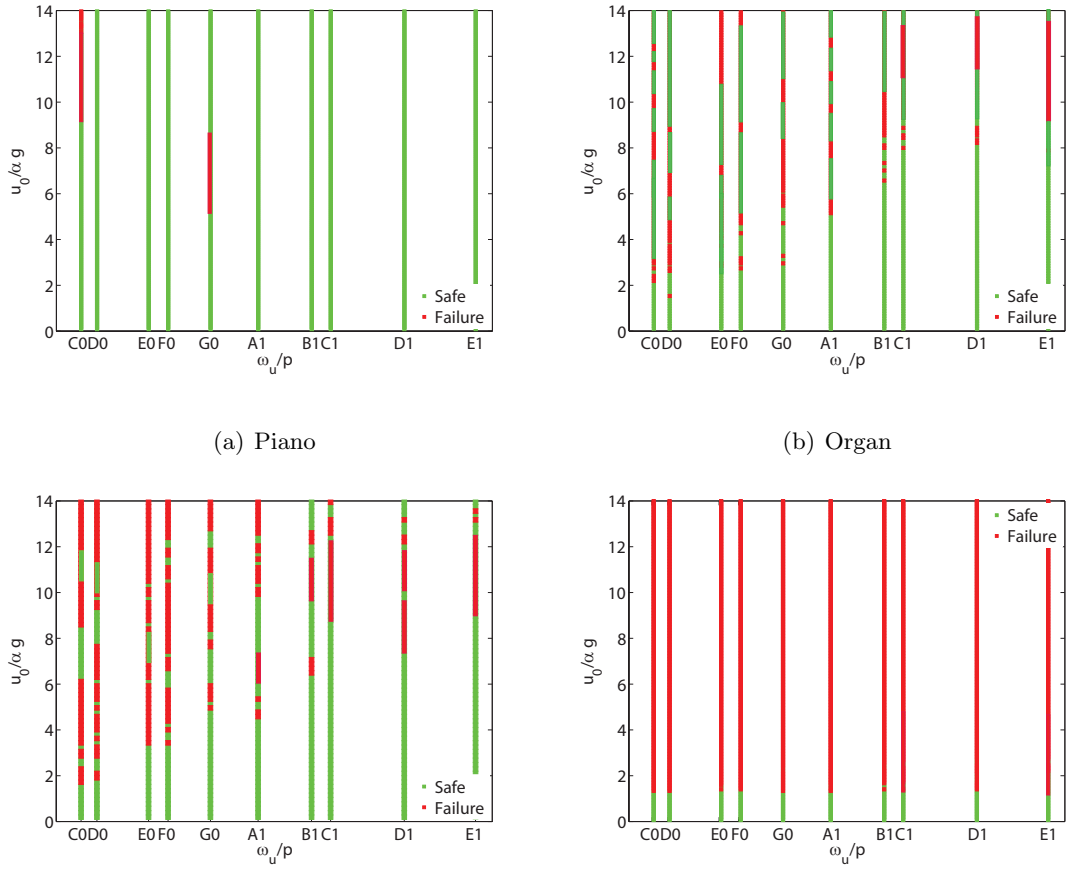

(a) Piano

(b) Organ

(c) Bass

(d) Synthesizer

Figure 5.15 – Stability diagrams when $H(\omega) \neq 1$ and $f_c = 40$ Hz and $f_r = 20$ Hz for a) piano, b) organ, c) bass and d) synthesizer.

Figure 5.15 illustrates the stability diagrams for each of the instruments presented in this

work when $f_c = 40$ Hz and $f_r = 20$ Hz for each musical note. Compared with Figure 5.13, it is observed that each instrument has reduced the areas of failure on the stability diagrams. In Figure 5.15(a), the piano stability diagram becomes slightly different than the stability diagram when $H(\omega) = 1$ in Figure 5.10(a) and considerably safer compared with Figure 5.13(a). A similar behaviour is observed for the bass: while in Figure 5.15(c) the areas of failure decrease in comparison with Figure 5.13(c), Figure 5.10(c) still has safer areas than Figure 5.15(c). Equally, the bass stability diagram reduces its areas of failure while decreasing the frequency of the rack and increasing the frequency of the case. However, there is not a strong variation on the stability diagram of the synthesizer between the case presented in this Section and in Sections 5.7.2 and 5.7.3. This is probably due to its waveform having strong drifts.

This Section has illustrated basic strategies for avoiding large amplifications to reduce the failure of the artifacts. However, the problem is that when moving the resonance to higher frequencies, rocking stops being the problem. Although other parameters neglected in the models become the problem, such as the deformation of the artifact.

5.7.5 Slide-Rocking

In the previous Sections, the focus was in the failure produced by toppling. In contrast, it is the aim of this Section to obtain a preliminary view of the influence of the coefficient of friction on the sliding kinematics while increasing the frequency.

Figure 5.16(a) illustrates the maximum displacement for each $u_0/\alpha g$ for some piano musical notes using $\mu_f = 0.3$. As expected, as $u_0/\alpha g$ increases, the body slides more. Also, while the frequency of the notes increases, sliding decreases. Since low frequency notes produce more displacements to the artifact, it is of interest to study the effect of different coefficients of friction for the lowest frequency. Figure 5.16(b) represents the sliding of the body for a single hit of the piano music note C0 for different coefficients of friction. It can be seen that

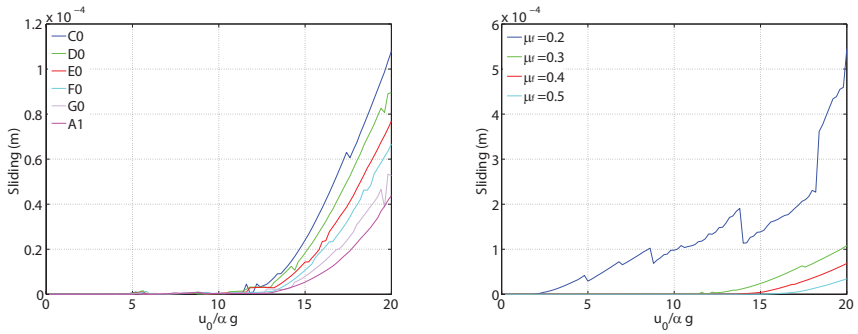

(a) Piano (b) Piano

Figure 5.16 – Sliding behaviour of a rocking body for one single hit using a) different piano notes b) different μ_f for the piano C0.

as the coefficient of friction increases, sliding decreases.

The effects of sliding due to the vibration produced by a drum is studied in Figure 5.17. The waveform of 18 successive drum hits is illustrated in Figure 5.17(a). First, the influence of μ_f when the artifact is subjected to only one drum hit is studied. In agreement with Figure 5.16(b), Figure 5.17(b) illustrates that a small μ_f induces larger displacements on the artifact even for small values of $u_0/\alpha g$. It is also observed that the drum produces larger displacements on the artifact than the piano. Second, the artifact is subjected to 4.2 s of drum hits (18 hits) with a $\mu_f = 0.3$ and $u_0/\alpha g = 20$. The results are presented in Figure 5.17(c). Note that the fluctuations observed in the Figure refer to the artifact moving to the right and left. Comparing the total displacement between one hit and 18 hits, the artifact moves 1 mm more with the sequence of drum hits.

5.8 Conclusions

A practical application derives from the presented investigation. The movement of museum artifacts has become a more recent problem due to the use of powerful speakers as well as the use of computer generated music.

A study of a rigid rectangular body subjected to sound induced vibrations was presented

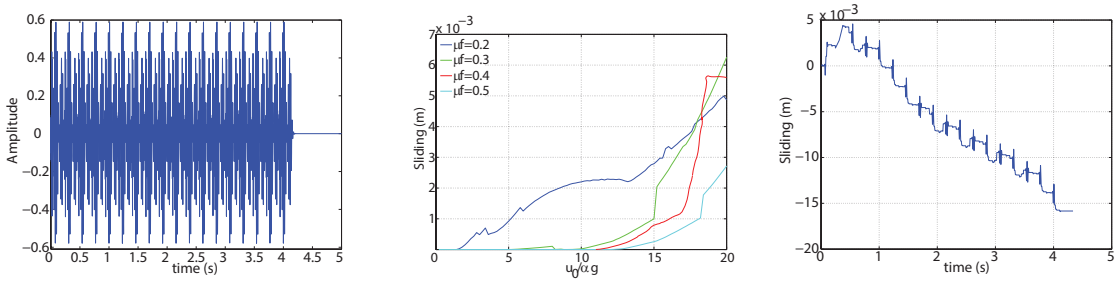

(a) Drum Successive hits (b) Drum one hit (c) Response for successive hits

Figure 5.17 – a) Successive hits using a drum, b) sliding one hit and c) sliding multiple hits.

in this Chapter. A methodology to induce the music source to the rigid body was proposed. The methodology takes into account the air pressure and the frequency of the rack and the case where the body is placed. This was tested not only when the rack and the case are flexible but also considering that both are completely rigid. Both studies ended in the importance of the waveform. For instance, the synthesiser produces failure for each musical note while the piano, organ and bass produce more failure at low frequency notes.

A case for reducing the failure when the rack and case are flexible was also presented. Conclusions were drawn regarding whether it is better to increase or decrease the natural frequencies of the case and rack in order to reduce the frequency content of the musical notes.

Investigations on the displacement of the rigid body due to music notes have been carried out. Two instruments were tested, the piano and the drum. Both end in the displacement growing when the coefficient of friction is reduced. More displacement was also observed at lower frequency notes.

Part II

Chapter 6

Review of existing earthquake generation models

6.1 Introduction

One of the main goals of this thesis is to generate time histories for the estimation of the risk of rocking bodies. The response of a rocking block subjected to cycloidal pulses was examined in Chapters 2 and 4. However, ground motions cannot in generally be approximated by idealized pulses as the ones examined so far. Therefore, one would need a model that produces a large amount of realistic earthquakes. Thus, it is presented in this Chapter a briefly explanation of some common earthquake generation models in the literature. The advantages and disadvantages of each of the models for rocking bodies is discussed through the Chapter as well as the design connection of each of them.

Moreover, since ground motions are a 3D, this Chapter first pertains to treat the concepts of principal axes in ground motions presented in [52].

6.2 Principal axes components

The investigation of the dynamic response of structural systems to earthquake excitation requires the use of ground motion. Time histories recorded at a station are a set of three records, one of them being in the vertical direction and two in the horizontal plane. The direction at which the components are recorded in the horizontal plane does not have a specific orientation with respect to the fault. It is therefore the aim of this Section to briefly explain the work of [52] which defines a set of three translational components of the ground motion which includes major, intermediate and minor principal axes. These axes are uncorrelated and their intensities have a decreasing order. Neglecting rotational components, consider a set of orthogonal horizontal components of ground acceleration $a_1(t)$ and $a_2(t)$. The correlation coefficient between both components over the time interval $\tau_1 < t < \tau_2$ as [56]:

$$\varrho_{a_1(t),a_2(t)} = \frac{\int_{\tau_1}^{\tau_2} a_1(t)a_2(t)dt}{\sqrt{\int_{\tau_1}^{\tau_2} a_1(t)^2 dt \int_{\tau_1}^{\tau_2} a_2(t)^2 dt}} \tag{6.1}$$

In [52], it is observed that this temporal correlation coefficient between a pair of components over a time interval does not significantly change for different time segments. Thus, it could be computed for the entire length of the record. However, the correlation coefficient depends on the direction in which the motions are recorded. It varies if the ground motion components are rotated by an angle ψ. Hence, it is a function of the rotation angle $\varrho_{a_1(t),a_2(t)\psi}$. For that reason in [52] the principal axes of a time history are the directions along which $\varrho_{a_1(t),a_2(t)\psi} = 0$. The principal components are the components along these axes.

Due to the dependence on the intensity of the motions of the principal components, it is decided to use the Arias intensity to sort the components between the major and intermediate [100]. Therefore, the component with the larger Arias intensity is defined as the major component whereas the smaller Arias intensity defines the intermediate component.

$$I_a = \int_0^t \ddot{x}_g^2(t)dt \tag{6.2}$$

Consider again $a_1(t)$ and $a_2(t)$ representing a pair of orthogonal horizontal acceleration

in the recorded directions and $a_{1,\psi}(t)$ and $a_{2,\psi}(t)$ the components clockwise rotated by an angle ψ as illustrated in Figure 6.1. The orthogonal transformation is defined by:

$$\begin{bmatrix} a_{1,\psi}(t) \\ a_{2,\psi}(t) \end{bmatrix} = \begin{bmatrix} cos\psi & sin\psi \\ -sin\psi & cos\psi \end{bmatrix} \begin{bmatrix} a_1(t) \\ a_2(t) \end{bmatrix} \tag{6.3}$$

Therefore, real recorded earthquakes are rotated according to equation 6.3. The rotation angle ψ is obtained such as $\varrho_{a_1(t),a_2(t)} = 0$. Using simple derivations [56] shows that $\hat{\psi}$ is given by:

$$\hat{\psi} = 0.5 \tan^{-1}\left(\frac{2\varrho_{a_1 a_2}\sigma_{a_1}\sigma_{a_2}}{\sigma_{a_1}^2 - \sigma_{a_2}^2}\right) + k\frac{\pi}{2} \tag{6.4}$$

where $\sigma_{a_i} = \int_0^{t_n} a_i(t)^2 dt$ and k is chosen such that $\hat{\psi}$ falls in the first quadrant. Using equations 6.3 and 6.4 the rotated components $a_{1,\psi}(t)$ and $a_{2,\psi}(t)$ are implemented to develop the principal components database.

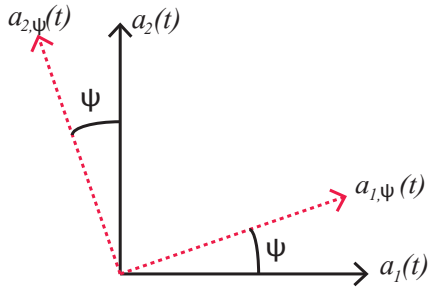

Figure 6.1 – Rotation of orthogonal horizontal components by angle ψ.

6.3 Stochastic process through a PSD

The most common approach to generate artificial earthquakes with stochastic models is representing the underlying random stochastic process through a PSD. It is the purpose of this Section to introduce the KT-CP [31] and SRM [32]. Finally, in order to generate earthquakes compatible with design tools, the Gasparini and Vanmarcke (GV) procedure is presented [35].

6.3.1 Kanai-Tajimi Clough-Penzien Spectrum

A PSD shows the strength of the variations (energy) as a function of the radial frequency ω. In other words, it shows at which frequencies variations are strong and at which are weak [101]. One of the most commonly used parametric forms for the PSD is the Kanai-Tajimi spectrum [102]. This original equation idealises the ground acceleration as a stationary random process. The underlying physical model of this PSD refers to the acceleration of a mass corresponding to a column of soil supported by a spring and a damper connected in parallel. Their base is assumed to be the bedrock. The Kanai-Tajimi PSD passes a white process through a soil filter with frequency ω_g and damping ξ_g, but the velocity and displacement spectra of the acceleration spectrum are not defined as ω tends to infinite [103]. Thus, it produces infinite variances for ground velocity and displacement. This has been solved by [31] who passed the Kanai-Tajimi spectrum through an additional filter with parameters ω_f and ξ_f and described the power spectrum of ground accelerations which yield finite variances for velocities and displacements as it is shown in the following equation:

$$G(\omega) = S_0 \frac{\left(1 + 4\xi_g^2 \left(\frac{\omega}{\omega_g}\right)^2\right)}{\left(1 - \left(\frac{\omega}{\omega_g}\right)^2\right)^2 + 4\xi_g^2 \left(\frac{\omega}{\omega_g}\right)^2} \frac{\left(\frac{\omega}{\omega_f}\right)^4}{\left(1 - \left(\frac{\omega}{\omega_f}\right)^2\right)^2 + 4\xi_f^2 \left(\frac{\omega}{\omega_f}\right)^2} \tag{6.5}$$

where S_0 is a constant power spectral intensity of the bedrock excitation. The parameters ω_g and ξ_g are estimated for three soil types by Ellingwood and Batts [104]. ω_f and ξ_f are positive parameters related to a high-pass filter that ensures finite velocities when $\omega = 0$. These parameters are estimated in [105] for each of the three soils. Equation 6.5 is known as the KT-CP PSD.

6.3.2 Spectral Representation Method

The SRM is used to generate synthetic ground motions from a given PSD [32]. In this method, f_0 is defined as a one-dimensional and uni-variate (1D-1V) stationary process with mean value equal to zero and two-sided power spectral density function $S_{f_0 f_0}(\omega)$. The stochastic process

$\ddot{x}_g$ can be simulated by infinite series by introducing the limit $N \to \infty$:

$$\ddot{x}_g = \sqrt{2} \sum_{n=0}^{N-1} A_n cos(\omega_n t + \psi_n) \tag{6.6}$$

$$\begin{aligned} A_n &= (2S_{f_0 f_0}(\omega_n)\Delta\omega)^{(1/2)}, \qquad n = 0, 1, 2, ..., N-1 \\ \omega_n &= n\Delta\omega \qquad\qquad n = 0, 1, 2, ..., N-1 \end{aligned} \tag{6.7}$$

where $\Delta\omega = \omega_u/N$, $A_0 = 0$ and $S_{f_0 f_0}(0) = 0$. The simulation formula in equation 6.6 generates a discrete ground time history $f(t)$ from a PSD function $S_{f_0 f_0}$, up to a cut-off frequency ω_u, beyond which $S_{f_0 f_0}$ is assumed to be zero for mathematical and physical reasons. The power spectrum is divided in n intervals with sampling step $\Delta\omega$. The Ψ_0, Ψ_1, Ψ_2, ..., Ψ_{N-1} are independent random phase angles distributed uniformly over the interval $[0, 2\pi]$.

To introduce the non-stationarity nature of the process, a time modulation function $\varphi(t)$ developed by [33] is applied. Through the use of this time envelope shown in Figure 6.2 in equation 6.8, the stationary stochastic process is converted into a non-stationary one. Figure 6.3 shows the difference between stationary and non-stationary stochastic processes.

$$\varphi(t) = \left\{ \begin{array}{ll} t/t_1 & t < t_1 \\ 1 & t_1 \leq t \leq t_2 \\ e^{-c(t-t_2)} & t > t_2 \end{array} \right\} \tag{6.8}$$

The KT-CP PSD using the SRM generates records using as an input ω_g, ξ_g, ω_f, ξ_f and S_0. However, while the values of ω_g, ξ_g, ω_f and ξ_f are given by estimations of the soil properties in [104], the value of S_0 refers to the intensity of the white noise at the rock level. Therefore, due to the lack of these measurements, a designer could not use this model directly to generate probability of failure curves. To alleviate this problem, there are other stochastic models that generate artificial earthquakes compatible with a design response spectrum [35, 36].

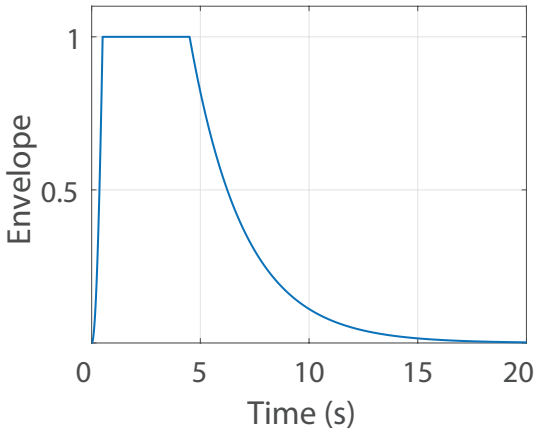

Figure 6.2 – Jenning envelope $t_1 = 1$, $t_2 = 9$ and $c = 0.2$.

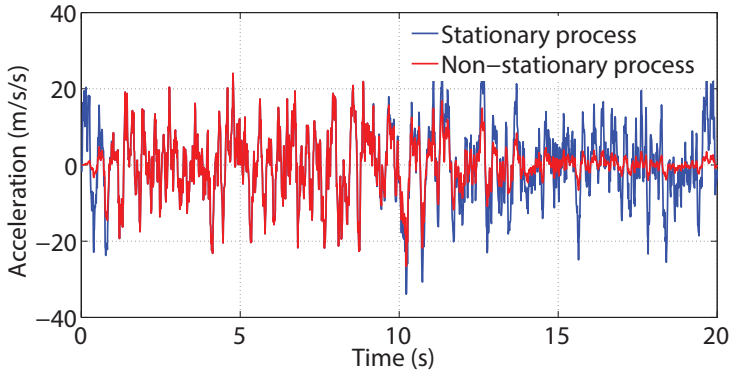

Figure 6.3 – Stationary and non-stationary stochastic process using SRM.

6.3.3 Spectrum matching

International seismic codes provide guidance on the selection or simulation of time histories to fit a design target spectrum [54]. The most common approaches for developing sets of ground motions that match on average the design response spectrum are, scaling earthquakes and spectrum matching using time or frequency approaches. However, while artificial earthquakes can be scaled to match the target response spectrum, scaling real earthquakes has mathematical and physical issues [106]: a weak earthquake is not generated by the same process as a strong one. Moreover, the areas of frequencies differ between both types of earthquakes. While a strong earthquake usually has a narrow band of frequencies, the weaker behaves similar to white noise recordings. Therefore, only a procedure to match artificially generated

earthquakes with a target response is presented in this Section.

One of the most common target spectrum match procedures is the GV [35]. This methodology involves adjusting the underlying PSD of each of the ground motion accelerograms to make them compatible with the target. The idea of the method is explained in Figure 6.4. It can be seen for the chart that first each ground motion is generated using a model. The synthetic record then excites to a Single Degree of Freedom (SDOF) and the corresponding response is calculated and compared against the target response. Iteratively, the PSD is adjusted using scaled factors (SF) until it matches with the target spectrum. A common quantitative measure of the overall match of the spectrum obtained from generated ground motion accelerograms to the target spectrum, is the squares ratio between the spectral accelerations of the response and design spectrum [29]. Thus, a set of scaling factors can be identified for each ground motion to minimize the error over a specified period range. It is important to note that each generated earthquake has its own PSD which is the function that is constantly adjusted using scaled factors to minimize the difference between the target and the response spectrum.

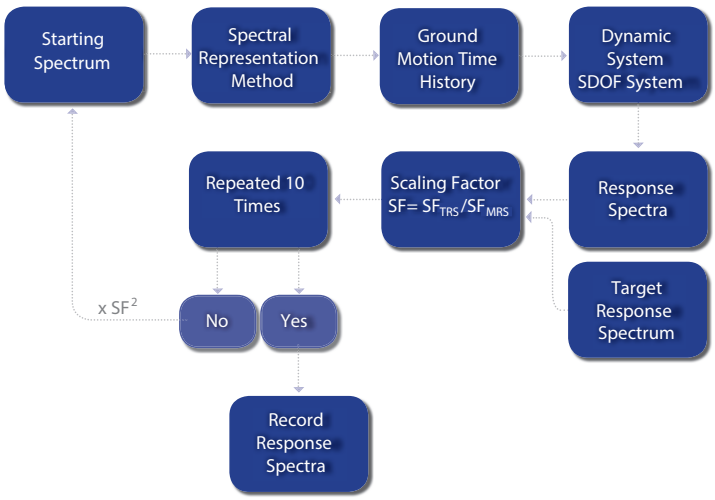

Figure 6.4 – Adapted Gasparini and Vanmarcke method [35].

The GV procedure can be used directly with design codes as it exactly matches the individual response spectra with the design spectrum with the only requirement of using an

elastic response spectrum as an input. As a consequence, the underlying PSD of each generated earthquake has the same spectra when it is known that each earthquake has a different spectrum. However, while there is a unique way to go from a number of spectra to the mean spectra, there is not a feasible way to go from mean spectra to individual one. Consequently, implementing GV procedure, synthetic spectra matches the target spectrum, ending in an overestimation or/and underestimation of the spectra of each of the time histories.

6.4 Hybrid approaches

In this Section, the model presented by Rezaeian and Der Kerughian (RK-N) in [44, 56] is explained. The method allows for generating ground records compatible with seismological properties such as the magnitude of the seismic event M, the shear velocity of the support ground, V_s, the type of the fault, F, (corresponding to normal or strike slip) and the closest distance from the recording site to the rupture area [107], R_{rup}. Figure 6.5 illustrates a schematic representation of the rupture plane where L_M defines the depth of the hypocenter measured from the epicenter. It should further be noted that in [44] the depth, L_M, is not one of the input parameters to the model. However, despite this fact, the model still takes its effect into account. The generated earthquakes, in reality, correspond to a distribution of L_M that is compatible with the selected list of earthquakes, for a chosen M, R_{rup} and V_s.

In the following brief synopsis, the method is presented for the generation of uniaxial [44] and biaxial ground [56] motion components. Both methods use a list of selected earthquakes from [108] with magnitudes larger than 6 as inputs to the regression analysis. A time shift to avoid long stretches of zero motion in the recorded earthquake is implemented in [44, 56].

6.4.1 Simulation of uniaxial ground motions

To obtain ground motions using the method developed in [44] the steps shown in Figure 6.6 are followed:

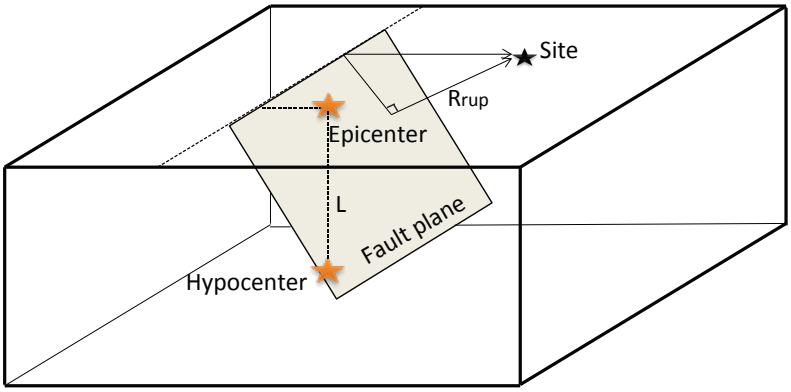

Figure 6.5 – Schematic explanation of a fault.

1. Values of M, R_{rup}, V_s and F are selected as input by the user according to the list of recorded earthquakes. These values are connected to a vector of auxiliary variables v_i through stochastic equations:

$$v_c = \mathscr{F}(M, F, R_{rup}, V_s, \epsilon) + e_c \tag{6.9}$$

where $\mathscr{F}$ is a selected predictive formula for the conditional mean of v_c given the earthquake and site characteristics, ϵ is the vector of regression coefficients and e_c represents the regression error that is zero-mean normally distributed.

These equations are the result of a regression analysis from the selected database of records. Each equation has error terms which correspond to the elements of a zero mean Gaussian vector, e_c, whose covariance matrix has been defined through the regression analysis. Having chosen the values of M, R_{rup}, V_s and F and knowing the covariance matrix of the errors, sample realizations of the vector v_c can be obtained using a multivariate random algorithm, where $c = 1, ..6$. This is the first level where stochasticity is introduced in the model.

2. Having obtained a realization of the vector v_c, the input of the model can be obtained by using the following equation:

$$\rho_c = \Phi_{\rho_c}^{-1}(\Phi(v_c)) \tag{6.10}$$

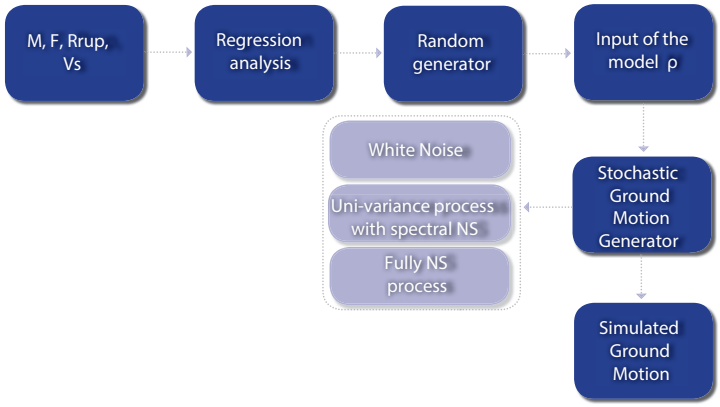

Figure 6.6 – Schematic explanation of the model. NS defines the Non-Stationarity of the process.

where Φ_{ρ_c} is cumulative density function of parameter ρ_c. The ϕ for each parameter is obtained by fitting selected ϕ to the data obtained from the selected list of earthquakes. The parameters ρ_c used can be separated to parameters related to the time records defined in equation (6.11): the Arias Intensity I_a, effective duration of the record D_{5-95} and time to the middle strong-shaking phase t_{mid}, and model specific parameters of the stochastic model: ω_{mid} and ω' defining the frequency of the filter at any time, t, as $\omega_{mid} + \omega'(t - t_{mid})$ and ξ_f defining the damping ratio of the filter.

$$\begin{aligned} D_{5-95} &= t_{95} - t_5 \\ t_{mid} &= t_{45} \end{aligned} \tag{6.11}$$

where t_{95}, t_{45} and t_5 are the instants at which the 95%, 45% and 5% of the Arias intensity are reached.

3. The procedure for simulating the synthetic ground motion can be completed once the parameter vector ρ_c is defined. To relate the parameters of the modulation function to ρ_c, a normalized filtered white noise time-varying process is time and frequency modulated to obtain the fully Non-Stationary process, $u(t)$ as shown in Figure 6.6. The time-envelope is defined by a gamma modulating function which gamma modulation

parameters a_1, a_2 and a_3 which are related to I_a, D_{5-95} and t_{mid} [44]. The linear filter with time-varying parameters depends on ω_{mid} and ω' whereas ξ_f is assumed to be constant. Therefore, for a given set of parameters one may obtain an arbitrary number of records through the use of a different realization of a standard Gaussian vector. This is the second level of introducing stochasticity in the model.

6.4.2 Simulation of biaxial ground motions

Following the discussion in Section 6.2, the directions at which the components are recorded in the horizontal plane are rotated such as the principal axis maximizes the Arias intensity. This work further focuses on the two horizontal components, ignoring for simplicity, but without any loss of generality, the vertical component which is assumed to also be a principal component as in [56].

The method presented in [56] extends the algorithm presented in [44], discussed earlier in Section 6.4.1, for obtaining biaxial inputs along the two principal horizontal axes, which following the convention in [56], are denoted as the major (I) and intermediate principal axes (II). Following the work in [100] the component with the largest Arias intensity is defined as the major component whereas the smallest Arias intensity defines the intermediate component.

As in the previous case, there are six model parameters to be calibrated for each earthquake. This is achieved using the same list of selected earthquakes as in [44] with the exception that from each earthquake the corresponding pair of horizontal axes is rotated to obtain time histories along the principal horizontal axes, before following the regression analysis for calibrating the stochastic equations that connect the seismic quantities M, R_{rup}, V_s and F to the parameters of the model.

Once the input of the model, ρ_c is calculated, the normalized filtered white noise time-varying is also time and frequency modulated to obtain $u(t)$ as defined in Figure 6.6. As a

result, the method generates synthetic pairs of horizontal ground motion components along the principal axes.

The models in [44, 56] provide the tool to control the seismological properties of the synthetic time histories. The physical characteristics of the process are achieved by using developed equations which provide the inputs to the stochastic process to generate ground motions. However, this model is enclosed to predefined equations which might not correspond to the underlying physical model. Moreover, each generated ground motion is governed by temporal and spectral modulation functions which only allow to the new records to have one peak of acceleration and a decayed predominant frequency.

In terms of design, the models presented in [44, 56] provides without any ambiguity the tools to design in terms of seismological properties. While the values of R_{rup} and V_s can be measured from the specific area, the value of M is directly obtained from the Gutenberg and Richter formula [109].

6.5 Data driven approach

This Section aims to explain the KL expansion. The main goal of this technique is that, without involving any predefined model, it generates artificial earthquakes taking as an input a set of recorded earthquakes [49, 110, 51]. The methodology is explained in this Section for biaxial case but it performs with equal steps for one direction of the earthquake. The only difference is that, for the case of two components, each earthquake is rotated to obtain the time histories along the principal horizontal axes as explained in [52].

The approach pursues the following steps also shown in Figure 6.7:

1. A recorded database containing n accelerograms is selected containing N_T acceleration samples in each horizontal orthogonal directions x and y. The components of x and y are defined as X_I and Y_{II}, respectively, corresponding to the principal axis I and

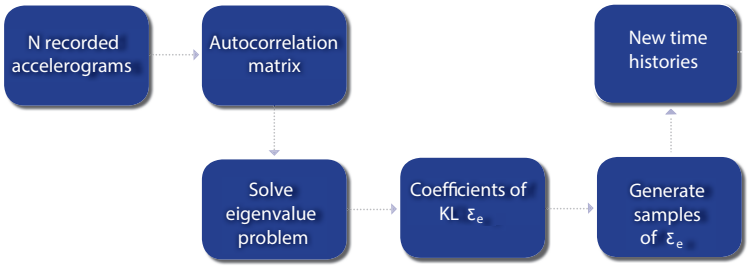

Figure 6.7 – Schematic explanation of the model used.

intermediate axis II. For each recorded accelerogram, a vector U of length $2n$ is constructed:

$$U^{(N_T)} = \left\{ \begin{array}{c} X_I^{(N_T)} \\ \\ Y_{II}^{(N_T)} \end{array} \right\} \quad N_T = 1, 2... \tag{6.12}$$

where N_T defines the number of records used.

2. To take into account the correlation between the two components, the empirical correlation matrix R_U is computed:

$$R_U = \frac{1}{n} \sum_{l=1}^{n} U^{(l)} U^{(l)T} \tag{6.13}$$

3. The eigenvalue problem is solved and the eigenvectors $V_{e,j}$ and eigenvalues D_e are found with $e = 1, .., 2n$ referring to the corresponding eigenmode and $j = 1, ..., 2n$ referring to the sample points. It is not necessary to compute the $2n$ coefficients. Only the eigenvalues that represent the major part of the energy are necessary to generate a process that matches well the data [51]. The KL expansion is constructed from N_T recorded records hence, all eigenvalues beyond D_{N_T} are zero [111] and maximum number of eigenvalues p is equal to N_T. Following the approach of [51], in this study p is chosen such that:

$$\frac{\sum_{e=1}^{p} D_e}{\sum_{e \geqslant 1} D_e} \geqslant 99\% \tag{6.14}$$

4. The coefficients of the KL expansion are computed as follows:

$$\varsigma_e^{(l)} = \frac{1}{\sqrt{D_e}} \sum_{j=1}^{2n} U^{(l)}(j) V_{(e,j)} \tag{6.15}$$

5. New samples, $\hat{\varsigma}_e^o$, are generated using the corresponding empirical distribution of ς_e, with $o = 1, 2..., N_o$ being N_o the total number of synthetic time histories. In this study, these samples generated are assumed to be independent and are generated using the tool defined in [112]. In [51] it has been observed that if those variables are independent, the new set could lead with errors. However, here the assumption that $\hat{\varsigma}_e^o$ are independent is kept without any loss of generality.

6. New time histories are generated using the following equation:

$$E_{N_o}(j, o) = \sum_{e=1}^{q} \hat{\varsigma}_e^{(o)} \sqrt{D_e} V_{(e,j)}^T \tag{6.16}$$

The vector E_{N_o} is composed with the principal and intermediate component of the generated time histories. Thus, the principal E_I and intermediate E_{II} components are calculated as:

$$\begin{aligned} E_I &= E_N(1 : n, o) \\ E_{II} &= E_N(n : 2n, o) \end{aligned} \tag{6.17}$$

For the biaxial generated time histories, the synthetic earthquakes are again rotated to correct any error. For the uniaxial case, the process is exactly the same without rotating the only component used. Therefore, the generated motion is in an horizontal random direction χ such as the earthquake is calculated as $E_\chi = E_{N_o}(n, o)$.

The KL decomposition involves the estimation of the probability density function of the random variables representing the KL parameters. This is due to the inability of the nowadays procedures to capture its real probability distribution structure using only a few records. In [51], several methods to generate these random variables are compared noticing that, although the models are highly efficient and accurate, for both, artificially generated earthquakes and measure data, most of the methods lead to an error on the standard deviation, overestimating the level of confidence in the results. Despite that, the KL expansion is a great tool to enrich databases from a specific area.

6.6 Conclusion

When studying models for generating artificial time histories for the purpose of characterising the risk of rocking bodies, there are a few viable options beside the feasible and, nowadays, generally impossible one of using real recorded earthquakes. However, identifying the most suitable method of generating or selecting recorded ground motions that produces the most realistic estimates is not an easy task. Different models in the literature have attempted to perform the best alternatives. This Chapter has summarized some of the most representative models in the earthquake engineering community focusing on the advantages and disadvantages of each of the methods for rocking bodies.

In terms of design, the GV procedure uses seismic design codes and RK-N is directly implemented with seismological data. Thus, time histories generated from RK-N are more realistic than earthquakes from GV as they have been created from a model that is trained from real records. This is also true when comparing RK-N and KT-CP. The latter is related to the physical parameter S_0. However, this value cannot be found easily whereas R_{rup} and V_s can be measured and M can be estimated from the Gutenberg and Richter model [109].

Nonetheless, RK-N model has the disadvantage of using a specific stochastic model. In contrast, the KL expansion does not used any predefined model. However, while RK-N produces earthquakes for a chosen M, R_{rup} and V_s, the KL expansion does not provided a connection with any seismological properties or response spectrum. In the next Chapter the KL expansion model is formulated in association with physically interpretable parameters capable to characterise the complex evolutionary nature of the earthquake phenomenon. This novel technique aims to capture the main features of real recorded ground motions in the synthetic generated time histories based on the advantages of [44]. Its successful application would have valuable benefits for the earthquake engineering community as the KL expansion avoids the used of any predefined model to describe these random phenomena behaviour.

Chapter 7

KL expansion with a specified earthquake and site characteristics

7.1 Introduction

Earthquakes generated with the KL expansion are obtained from data analysis and hence, should have similar statistical properties than toreal earthquakes used. However, even if the KL expansion uses recorded earthquakes, the generated ground motions do not have a known connection with seismological properties or response spectrum. Consequently, one of the key challenges of this Chapter is to relate these generated earthquakes to seismological properties.

A previous model which is particularly relevant to this problem is the one of [44]. As explained in Section 6.4, this model implements a regression analysis between parameters of the model and seismological properties. For this aim, predictive equations are developed for the model parameters in terms of F, M, R_{rup} and V_s. Following the inverse of this approach, predictive equations are developed in this Chapter using a set of real recorded earthquakes to estimate M, R_{rup} and V_s by fitting the model to the record properties I_a, D_{5-95} and t_{mid}. Thus, computing these sample observations for each generated earthquake, M, R_{rup} and V_s are captured.

However, one of the main purposes of this thesis is to characterise the risk of rocking bodies in order to generate the probability of failure curves for an intensity measure. The default KL expansion provides earthquakes that are not necessarily compatible with any specific target in terms of M, R_{rup} and V_s. It can be claimed that using real recorded earthquakes with the same characteristics as the target as an input to the KL expansion, synthetic earthquakes would retain these properties. However, this is not guaranteed. If what is needed for characterising the risk is a set of earthquakes with the same seismological properties, there is a need of selecting the ground motions generated with the KL expansion which have the target seismological properties.

The novel technique of computing rejection sampling methods [113] to select earthquakes is applied to overcome these difficulties. Two types of rejection sampling methods are proposed in this Chapter: one is based on a threshold distance and the other on an envelope distribution. Both models allow the user to generate the probability of failure curves given an intensity measure in terms of M, R_{rup} and V_s.

This Chapter is structured in three main parts. The first part is focused on estimating M, R_{rup} and V_s from a time series. The second part introduces the rejection sampling methodologies proposed and describes how each of them can be applied to the earthquake generation problem. In the third part, a validation study of the models proposed is presented and a comparison between them with [44] is illustrated.

7.2 Estimation of M, R_{rup} and V_s

It was shown in [114] that the seismological quantities, M, R_{rup} and V_s can be chosen as suitable intensity measures. It is therefore the purpose of this Section to propose a model to estimate the corresponding values of $\hat{M}$, $\hat{R}_{rup}$, $\hat{V}_s$ and $\hat{F}$ of the generated earthquakes. In this thesis the superscript "ˆ" refers to the estimated values and "" to the target values.

To reduce unknown variables, one can make sure that the generated time series correspond

to a reverse or a strike fault by selecting from the originally set N real recorded earthquakes from either a reverse or a strike fault. Thus, only M, R_{rup} and V_s need to be estimated.

7.2.1 Strong motion database

For this study, a subset of the recorded earthquakes database from the PEER library [115] is selected. This subset is available online ($http://www.eng.ox.ac.uk/nldyn/on-line-resources/AppendixI-II.pdf/view$. Last access date:21/12/2018). It shows a summary of the selected earthquakes from the NGA database within the following limits:

- The database is limited to large earthquakes with $M > 5$ therefore, this study is customized for ground motions that are capable of causing damage and non-linear behaviour [44].
- To separate the effects of near-fault ground motions, which might dominate, the spectral content of the time series [116] only $R_{rup} > 5$ Km and $V_s > 160$ m/s are considered.

Thus, the database consist of 397 pairs of horizontal recordings from 36 earthquakes for strike-slip type of fault and 2289 pairs of horizontal recordings from 30 earthquakes for reverse type of fault.

To avoid long stretches of zero motion at the beginning of the recorded earthquakes, a time shift, as explained in [44], is applied. The data is uniformly sampled at 100 samples per second, and all the records contain 10000 acceleration samples.

7.2.2 Methodology to develop predictive equations

The interest of this Section is to estimate site and earthquake characteristics from synthetic motions generated using the KL-expansion. To develop a predictive model of the seismological properties, it is necessary to relate the model parameters to the earthquake. For this purpose, three variables directly measured from the time series, I_a, D_{5-95} and t_{mid}, are selected to

represent its properties. Those are calculated using equation (6.11). A regression model is then constructed to relate these variables in terms of M, R_{rup}, V_s.

Denoting ρ_c as the ith parameter in the set (I_a, D_{5-95}, t_{mid}), $CDF_{\rho_c}(\rho_c)$ as the marginal cumulative distributions fitted to the data for ρ_c and Φ^{-1} as the inverse of the standard normal cumulative probability function, the marginal transformation is defined as [44]:

$$v_c = \Phi_N^{-1}[\Phi_{F\rho_c}(\rho_c)], \qquad c = 1, ..., 3 \tag{7.1}$$

Equation (7.1) transforms ρ_c to v_c. Therefore, v_c is regressed against variables defining earthquake and site characteristics [44]. This leads to predictive equations of the form:

$$\begin{bmatrix} v_1 \\ v_2 \\ v_3 \end{bmatrix} = \mathscr{F} \begin{bmatrix} M \\ R_{rup} \\ V_s \end{bmatrix}; \qquad \begin{bmatrix} M \\ R_{rup} \\ V_s \end{bmatrix} = \mathscr{F}^{-1} \begin{bmatrix} v_1 \\ v_2 \\ v_3 \end{bmatrix} \tag{7.2}$$

where $\mathscr{F}$ defines the system of equations to obtain v_c given M, R_{rup} and V_s and $\mathscr{F}^{-1}$ defines the inverse system of equations to obtain M, R_{rup} and V_s given v_c.

The probability distributions of the parameters ρ_c appearing in equation (7.1) for the database defined in Section 7.2.1 are assigned. It is normal to work with the logarithm of the data in order to satisfy the normality requirement of the error [44]. However, this requires the implementation of the log-normal distributions for each variable. Similar to what was observed in [44], the data for several of the model parameters show a non-log-normal behaviour (Figure 7.1). As a consequence, the histograms of each model parameter are built and marginal probability distributions are assigned.

Figure 7.1 illustrates the normalised frequency diagrams of the fitted model parameters for the entire database. The probability distributions of the six ρ_c defined in [44] are shown for use in future Sections. However, only the parameters related to the time records I_a, D_{5-95} and t_{mid} are implemented for the predictive equations (7.2). It is observed that I_a follows a log-normal distribution whereas D_{5-95}, t_{mid} and ξ_f a beta distribution, ω_{mid} a gamma distribution and ω' a two sided truncated exponential.

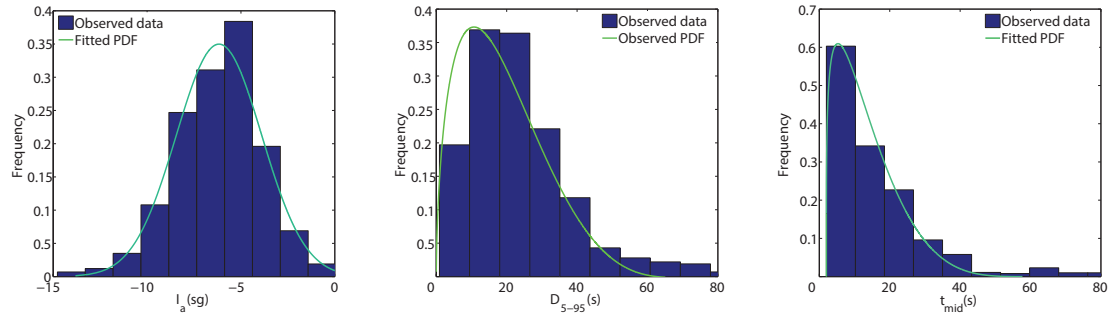

(a) I_a (b) D_{5-95} (c) t_{mid}

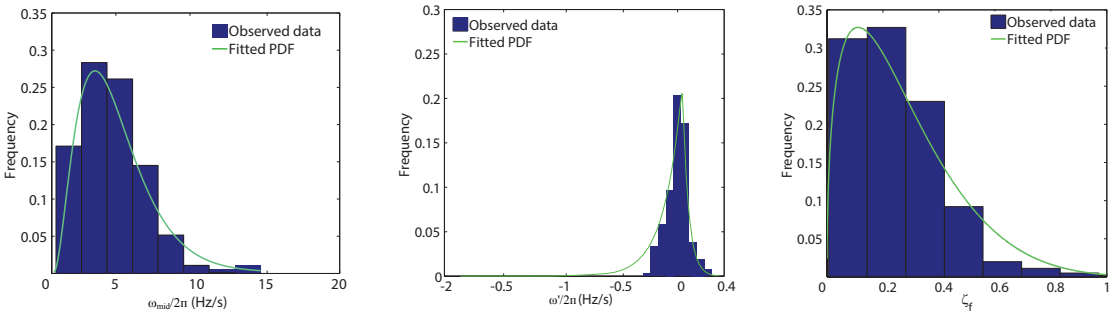

(d) ω_{mid} (e) ω' (f) ξ_f

Figure 7.1 – Probability density functions fitted to the observed normalised frequency of a) I_a (log-normal), b) D_{5-95} (beta), c) t_{mid} (beta) d) ω_{mid} (gamma), e) ω' (two-sided truncated) and f) ξ_f (beta). Normalised frequency: Total number of earthquakes:4592. Uniaxial case.

7.2.3 Empirical equations

This Section aims to construct empirical equations in terms of the model parameters v_c. The system of equations to be solved is defined in equation (7.2). These equations are used to solve $\mathscr{F}$ and are given in [44, 56]:

$$\begin{aligned} v_1 =& \beta(1,0) + \beta_R(1,1)F + \beta_R(1,2)\frac{M}{7.0} + \beta_R(1,3)\ln\left(\frac{R_{rup}}{25}\right) + \beta_R(1,4)\ln\left(\frac{Vs}{750}\right) + \eta_1 + \epsilon_1 \\ v_c =& \beta_R(i,0) + \beta_R(c,1)F + \beta_R(c,2)\frac{M}{7.0} + \beta_R(c,3)\frac{R_{rup}}{25} + \beta_R(c,4)\frac{Vs}{750} + \eta_c + \epsilon_c \end{aligned} \tag{7.3}$$

where $c = 2, ..., 6$, $\beta_R(c,k)$ is the vector of the regression coefficients and η_c and ϵ_c are the zero mean white noise errors with standard deviation δ^2 and σ^2, respectively. The regression

coefficients $\beta_R(i,k)$, η and ϵ are estimated for the database defined in Section 7.2.1. These values are reported in Tables 1 and 2 for the uniaxial and in Tables 3 and 4 for the biaxial case in Appendix II: New coefficients.

However, the aim of this study is to obtain the values M, R_{rup} and V_s knowing v_c. Therefore, the predictive equations are in the form of $\mathscr{F}^{-1}$ defined in equation (7.2). For the model in [44], the equations are uncoupled; however, for this inverse problem, there is a coupling between them. As the equations in terms of v_2 and v_3 are linear, they can be solved analytically in terms of two of the two variables $[M, R_{rup}, V_s]$. The two variables can then be replaced in the equation of v_1, resulting into a non linear equation of a single variable. The following equations (7.4), (7.5), (7.6) define the occurring non-linear equations for determining $\hat{M}$, $\hat{R}_{rup}$ and $\hat{V}_s$ respectively.

$$\begin{aligned} v_1 =&\kappa_{M,1} + \kappa_{M,2}F + \kappa_{M,3}M + \kappa_{M,4}ln(\kappa_{M,5}+ \\ &\kappa_{M,6}v_2 + \kappa_{M,7}v_3 + \kappa_{M,8}F + \kappa_{M,9}M)+ \\ &\kappa_{M,10}ln(\kappa_{M,11} + \kappa_{M,12}v_2 + \kappa_{M,13}v_3+ \\ &\kappa_{M,14}F + \kappa_{M,15}M) \end{aligned} \tag{7.4}$$

$$\begin{aligned} v_2 =&\kappa_{R_{rup},1} + \kappa_{R_{rup},2}F + \kappa_{R_{rup},3}v_2 + \kappa_{R_{rup},4}v_3+ \\ &\kappa_{R_{rup},5}R_{rup} + \kappa_{R_{rup},6}lnR_{rup} + \kappa_{R_{rup},7}ln(\kappa_{R_{rup},8}+ \\ &\kappa_{R_{rup},9}v_2 + \kappa_{R_{rup},10}v_3 + \kappa_{R_{rup},11}F + \kappa_{R_{rup},12}R_{rup}) \end{aligned} \tag{7.5}$$

$$\begin{aligned} v_3 =&\kappa_{Vs,1} + \kappa_{Vs,2}F + \kappa_{Vs,3}v_2 + \kappa_{Vs,4}v_3+ \\ &\kappa_{Vs,5}Vs + \kappa_{Vs,6}ln(\kappa_{Vs,7} + \kappa_{Vs,8}v_2+ \\ &\kappa_{Vs,9}v_3 + \kappa_{Vs,10}F + \kappa_{Vs,11}Vs) + \kappa_{Vs,12}lnVs \end{aligned} \tag{7.6}$$

where $\kappa_{\mathbb{M},k}$ are the coefficients for the equations being $\mathbb{M} = [M,\ R_{rup}, V_s]$. These coefficients are optimized using regression analysis with the tool of [117].

Once the coefficients are optimized, the estimated values of $\hat{M}$, $\hat{R}_{rup}$ and $\hat{V}_s$ are obtained

from:

$$\hat{M} = \mathscr{F}_M^{-1}(v_c) \qquad \hat{R}_{rup} = \mathscr{F}_{R_{rup}}^{-1}(v_c) \qquad \hat{V}_s = \mathscr{F}_{V_s}^{-1}(v_c) \tag{7.7}$$

Also, M, R_{rup} and V_s are estimated as:

$$\begin{aligned} M =& \mathscr{F}_M^{-1}(v_c) + \epsilon_M + \eta_M \\ R_{rup} =& \mathscr{F}_{R_{rup}}^{-1}(v_c) + \epsilon_{R_{rup}} + \eta_{R_{rup}} \\ V_s =& \mathscr{F}_{V_s}^{-1}(v_c) + \epsilon_{V_s} + \eta_{V_s} \end{aligned} \tag{7.8}$$

where $\mathscr{F}_M^{-1}(v_c)$, $\mathscr{F}_{R_{rup}}^{-1}(v_c)$ and $\mathscr{F}_{V_s}^{-1}(v_c)$ are deterministic and define the procedure of solving equations (7.4), (7.5) and (7.6), respectively and ϵ_M, $\epsilon_{R_{rup}}$ and ϵ_{V_s} and η_M, $\eta_{R_{rup}}$ and η_{V_s} are corresponding Gaussian white noise error terms.

The residuals are defined as the difference between the real and the predicted values. The total residual S is the sum of $\eta_{\mathbb{M}}$ and $\epsilon_{\mathbb{M}}$. These residuals have zero mean normally distributed error terms with variances $\delta_{\mathbb{M}}^2$ and $\sigma_{\mathbb{M}}^2$. The total error is a zero mean total distributed random variable with variance $\delta_{\mathbb{M}}^2 + \sigma_{\mathbb{M}}^2$. To calculate this error, the maximum likelihood technique is used. Note that in this method, only $\delta_{\mathbb{M}}^2$ and $\sigma_{\mathbb{M}}^2$ are calculated in the likelihood analysis. The likelihood function assumes the form:

$$L(\delta_{\mathbb{M}}^2, \sigma_{\mathbb{M}}^2) = \frac{1}{|\Sigma_{\mathbb{M}}|^{1/2}} e^{(-0.5 S^T \Sigma_{\mathbb{M}}^{-1} S)} \tag{7.9}$$

where $\Sigma_{\mathbb{M}} = \sigma_{\mathbb{M}}^2 I_N + \delta_{\mathbb{M}}^2 (\Sigma_{j=1\ldots N}^{+} 1Nj)$. The values of $\kappa_{\mathbb{M},k}$, $\delta_{\mathbb{M}}^2$, $\sigma_{\mathbb{M}}^2$ and the correlation matrices are reported in Appendix III: Predictive equations constants in Tables 5 and 7 for the uniaxial case.

This methodology to predict M, R_{rup} and V_s can be also extended to biaxial motions. For this aim, the earthquake components are rotated using [52]. However, only the major component of the principal axis is taken into account, as in reality both components have the same values for M, R_{rup} and V_s. The estimated regression coefficients for the biaxial case are reported in Appendix III: Predictive equations constants in Tables 6 and 8.

Figure 7.2 shows the characteristic scatter plots of the residuals versus the number of samples used for the uniaxial and biaxial case. The residuals are represented above and

below zero with no obvious systematic trends.

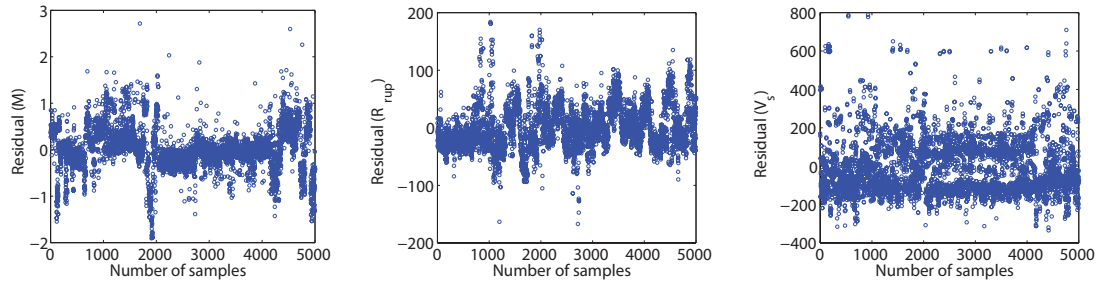

(a) M Uniaxial (b) R_{rup} Uniaxial (c) V_s Uniaxial

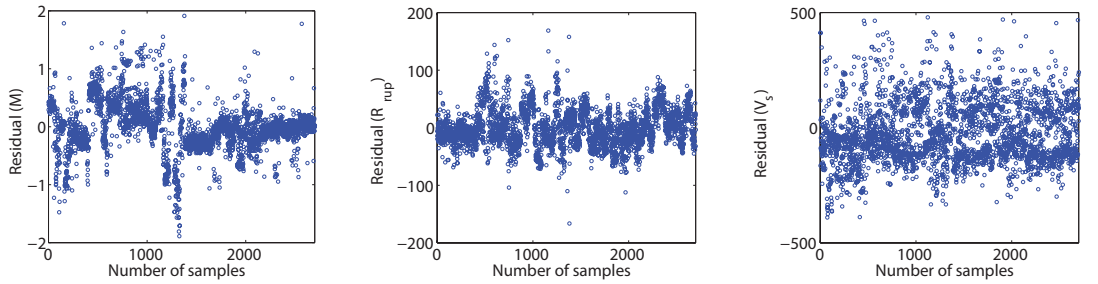

(d) M Biaxial (e) R_{rup} Biaxial (f) V_s Biaxial

Figure 7.2 – Scatter plots of the residuals against the number of samples for the uniaxial method a) M b) R_{rup} and c) V_s and for the biaxial method d) M e) R_{rup} and f) V_s.

7.3 Rejection Methods

The method presented in the previous Section provides an estimation of the values of the realization vector $\hat{\mathbb{M}} = [\hat{M}, \hat{R}_{rup}, \hat{V}_s]$ for each artificial earthquake. However, to generate probability of failure curves, one would need time series compatible with a target vector, in this case, $\tilde{\mathbb{M}}$. Nonetheless, it is not likely that values of $\hat{\mathbb{M}}$ for a generated record with the KL expansion would be the same as $\tilde{\mathbb{M}}$. Indeed, values of $\hat{\mathbb{M}}$ could be sufficiently far away from $\tilde{\mathbb{M}}$ having a minimal contribution and should instead be ignored for the purpose of the probability of failure curves. This selection of time series to be rejected is not trivial.

Rejection sampling methods provide useful techniques to achieve this rejection of unsuitable earthquakes. It is a basic approach used to generate samples from an observation. The

sample is either accepted or rejected by an adequate test of the ratio of two ϕs. The accepted samples are then distributed according to the target density [118]. It is therefore the aim of this Section to present two rejection techniques for selecting earthquakes: one based on a selected distance for which any value above a threshold results in the selection of the earthquake and the other based on an envelope distribution criterion for which only earthquakes inside this distribution are accepted.

7.3.1 Threshold method

The threshold model was developed to fit data with the assumption of an unobservable continuous character called "liability" [119]. On this scale, there was a threshold value and if the liability was above it a value of "1" was given, or "0" if it was below the threshold. It does not matter what happens when the liability is exactly at the threshold values, because this case is infinitely improbable.

The technique in [119] can be implemented for selecting earthquakes: values of $\hat{\mathbb{M}}$ that are bellow a threshold value, $\mathbb{K}$, are rejected. For this aim, both values need to be defined.

In Section 7.2, an estimated vector $\hat{\mathbb{M}}$ consisting of the estimates $\hat{M}$, $\hat{R}_{rup}$ and $\hat{V}_s$ is associated to the real value of $\mathbb{M}$ through equations (7.8) and (7.7). In these equations, the relationship between the values of $\hat{\mathbb{M}}$ and $\mathbb{M}$ is in terms of zero mean Gaussian errors. Thus, given an estimated $\hat{\mathbb{M}}$, the real value $\mathbb{M}$ is not deterministic and it also follows a multivariate Gaussian distribution with a density function $\mathscr{N}_\phi$:

$$\mathscr{N}_\phi(\mathbb{M}, \hat{\mathbb{M}}, \Sigma) = \frac{1}{\sqrt{|\Sigma_e|(2\pi)^u}} e^{(-\frac{1}{2}(\mathbb{M}-\hat{\mathbb{M}})\Sigma^{-1}(\mathbb{M}-\hat{\mathbb{M}}))} \tag{7.10}$$

where $\hat{\mathbb{M}}$ is the mean, Σ is the covariance matrix and u is the dimension of Σ. Following equation (7.8), $\mathscr{N}_\phi(\mathbb{M}, \hat{\mathbb{M}}, \Sigma)$ is evaluated at $\mathbb{M} = \tilde{\mathbb{M}}$.

Once the distribution is defined, the threshold value $\mathbb{K}$ at the same distribution is computed evaluating $\mathbb{M} = \hat{\mathbb{M}} + D\sigma$:

$$\mathbb{K} = \mathscr{N}_\phi(\hat{\mathbb{M}} + D\sigma, \hat{\mathbb{M}}, \Sigma) \tag{7.11}$$

where D is a scalar defining the distance and σ is the square root diagonal of Σ_e.

The values of the ϕ at a specific point are hence obtained from equations (7.10) evaluated at $\mathbb{M} = \tilde{\mathbb{M}}$ and (7.11). Once these two values are calculated, the threshold sampling criteria is implemented: any earthquake with $\mathscr{N}_\phi(\tilde{\mathbb{M}}, \hat{\mathbb{M}}, \Sigma)$ below $\mathbb{K}$ is rejected:

$$\mathscr{N}_\phi(\tilde{\mathbb{M}}, \hat{\mathbb{M}}, \Sigma) < \mathscr{N}_\phi(\hat{\mathbb{M}} + D\sigma, \hat{\mathbb{M}}, \Sigma) \tag{7.12}$$

Figure 7.3 tries to explain the idea under the threshold model for a bivariate case graphically (only M and R_{rup} are used). For the aim of the figure, ten thousand earthquakes are generated and $\hat{\mathbb{M}}$ is obtained for each of them. Each earthquake is evaluated using equation 7.12 in which $\tilde{M}$ varies between 5.8 to 6.6 and $\tilde{R}_{rup}$ between 50 to 90 Km and $D = 0.4$. Only the accepted earthquakes are plotted in Figure 7.3. It is observed that these accepted values define the threshold criterion which in this case takes the form of an ellipse. Thus, any value of $\mathscr{N}_\phi(\tilde{\mathbb{M}}, \hat{\mathbb{M}}, \Sigma)$ outside this ellipse is rejected.

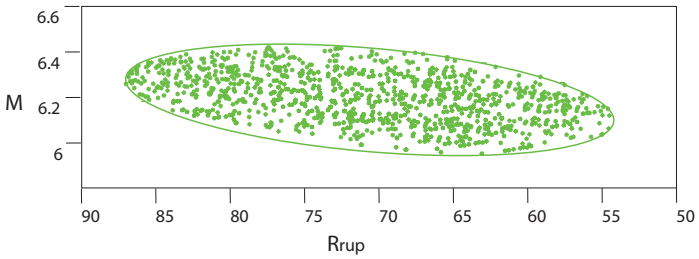

Figure 7.3 – Threshold criteria for a bivariate case. Ten thousand $\hat{\mathbb{M}}$ are evaluated for a $\tilde{\mathbb{M}} = [5.8, 70]$ and $D = 0.4$.

A summary of the steps followed in this procedure are presented in Figure 7.4 and defined as:

1. Generate an earthquake using the KL expansion and estimate its $\hat{\mathbb{M}}$ using the predefined equations in Section 7.2.

2. Define the threshold value $\mathbb{K}$.

3. Define $\mathscr{N}_\phi(\tilde{\mathbb{M}}, \hat{\mathbb{M}}, \Sigma)$ for each earthquake. Only accept earthquakes that satisfy equation

(7.12).

4. Repeat these steps until a record is accepted.

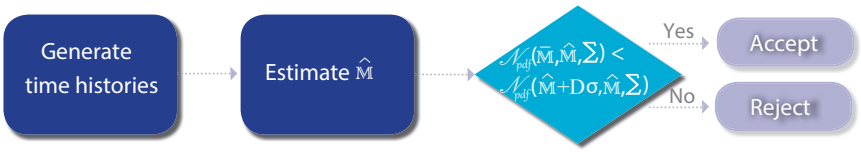

Figure 7.4 – Schematic explanation of the threshold rejection method.

7.3.2 Envelope distribution sampling method

Alternatively to the threshold sampling method, there are other rejection sampling methods that could be applied for this problem. From equation (7.3), it is observed that for a specific target $\tilde{\mathbb{M}}$, v_c is a Gaussian random vector with a known mean and covariance. However, there is not an easy way of generating samples directly from that target distribution. Instead, the regular KL expansion method can be thought of as the proposal distribution from which samples are drawn and the target distribution of the v_c, $\mathcal{N}_t(\mu_t, \Sigma_t)$, is defined using equation (7.3); where μ_t and Σ_t are defined by the v_c and the correlation coefficients, η_c and ϵ_c, respectively.

In general, this envelope rejection method follows the idea of sampling from an easy distribution $r(x)$ and applies a rejection criterion such as distributing the accepted samples according to the target distribution $d(x)$. To reject samples from $r(x)$ such they are sampled from $d(x)$, $r(x)$ must envelop the distribution $d(x)$. This is generally done by choosing a constant $C > 1$ such that $Cr(x) > d(x)$ for all x. For this reason, $cr(x)$ is often called the envelope distribution [120]. A typical criterion for accepting samples from $x \sim r(x)$ is based on the ratio of the target distribution and the envelope distribution. The samples are accepted only if:

$$\frac{d(x)}{Cr(x)} > unif \tag{7.13}$$

where $unif \sim Unif(0,1)$, and otherwise, rejected. If this ratio is close to one, then $d(x)$ should have a large amount of probability mass around x and that sample is more likely to be accepted. In contrast, if the ratio is small, $d(x)$ has less probability mass around x and the sample should be less likely to be accepted. An example of this criterion is illustrated in Figure 7.5.

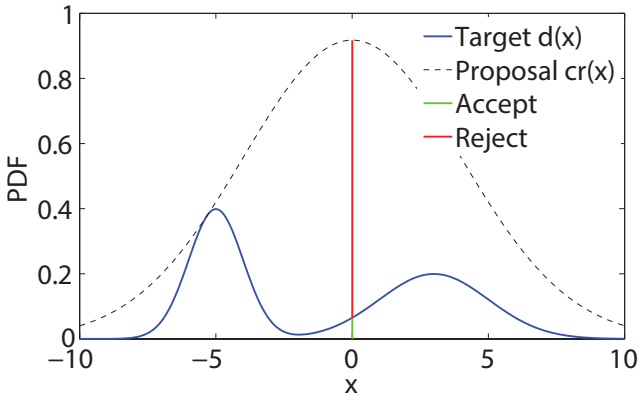

Figure 7.5 – Rejection sampling with a Normal proposal distribution.

To implement the envelope criterion to the earthquake problem, the proposal distribution needs to be denoted. To calculate this distribution of v_c, its probability distribution $\mathscr{S}_p$ needs to be specified. For this aim, a hundred thousand earthquakes from the KL expansion are generated using the recorded earthquakes for any of the faults as an input. For each of the records its ρ_c is calculated. In Figure 7.6, the normalised frequency diagrams of ρ_c for the set of generated earthquakes using the KL expansion are reported, as well as the distributions observed in Figure 7.1 for the recorded motions. These distributions are in agreement with the ones proposed in [44]: I_a follows a log normal distribution whereas D_{5-95}, t_{mid} and ξ_f a beta distribution, ω_{mid} a gamma distribution and ω' a two sided truncated exponential. Therefore, in this case the proposal distribution $\mathscr{S}_p$ is represented with the non-linear transformation defined in equation (7.1) with μ_p being the mean of the v_c and Σ_p being the covariance matrix of the v_c. This process gives the proposal distributions of the v_c. It should further be commented that the target and proposal distributions are different and hence, rejection

methods need to be implemented.

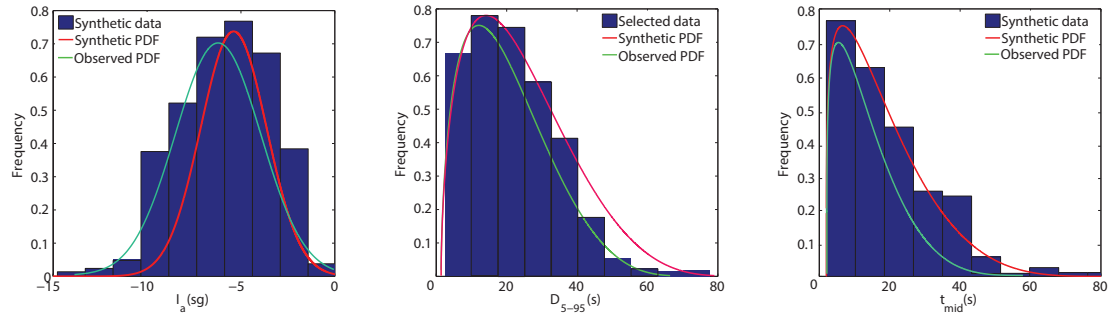

(a) I_a (b) D_{5-95} (c) t_{mid}

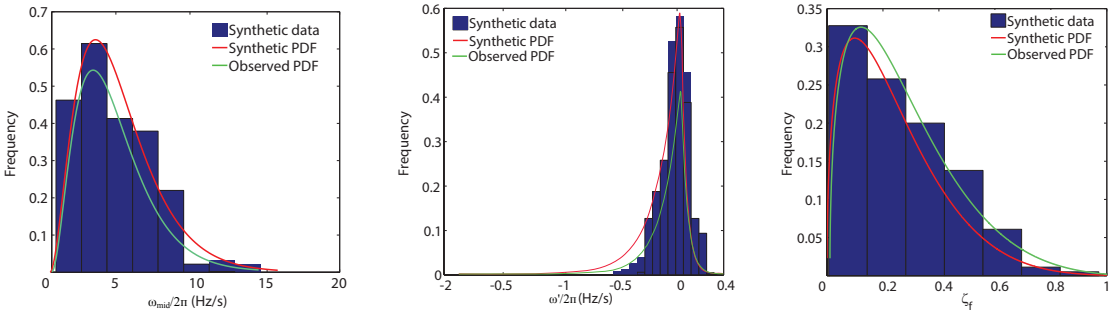

(d) ω_{mid} (e) ω' (f) ξ_f

Figure 7.6 – Probability density functions fitted to the generated normalised frequency of a) I_a (log-normal), b) D_{5-95} (beta), c) t_{mid} (beta), d) ω_{mid} (gamma), e) ω' (two sided exponential) and f) ξ_f (beta). Normalised frequency: Total:100000. Observed and synthetic data.

In this rejection model, the number of v_c implemented is decided by the user varying from 1 to 6 depending on the number of iterations that it is willing to do. A schematic explanation of how to implement the envelope procedure is presented in Figure 7.7 and following explained bellow:

1. Define the proposal distribution $\mathscr{S}_p$.

2. Define the target distribution $\mathscr{N}_t(\mu_t, \Sigma_t)$.

3. Calculate C.

4. Generate a random sample $unif$ from a uniform distribution from zero to one.

5. Generate an earthquake using the KL expansion.

6. Calculate its v_c using equation (7.1).

7. Evaluate this v_c as:

$$\frac{\mathcal{N}_t(v_c, \mu_t, \Sigma_t)}{C\mathcal{S}_p(v_c, \mu_p, \Sigma_p)} > u \tag{7.14}$$

8. The sample is accepted if equation (7.14) is satisfied.

9. The last five steps are repeated until a sample is accepted.

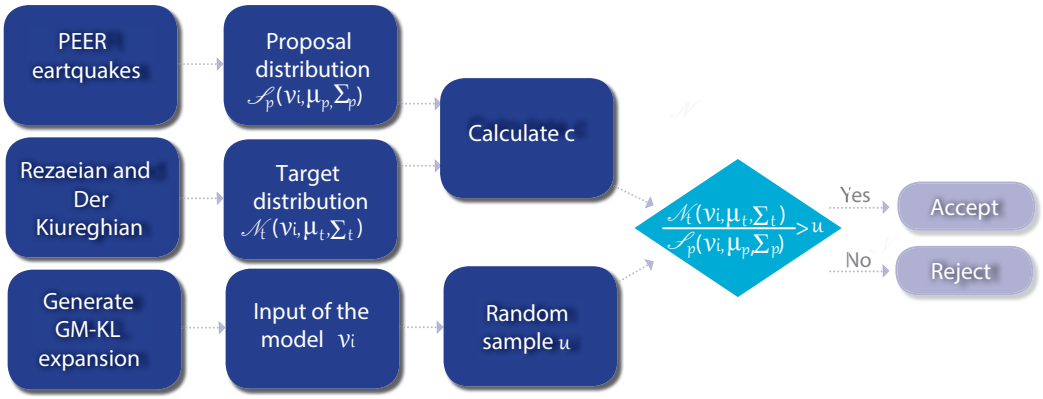

Figure 7.7 – Schematic explanation of the envelope rejection method. GM refers to Ground Motion.

7.4 Estimation of $\hat{\mathbb{M}}$

In this Section, earthquakes generated with the KL expansion are first presented. These earthquakes are computed using the data set previously defined, using enough eigenvalues to capture 99 % of the total energy as in equation (6.14).

Figure 7.8 illustrates two uniaxial ground motions, one recorded earthquake from the PEER library and one generated using the KL expansion. Similarly, Figure 7.9 illustrates a pair of recorded and generated earthquakes, respectively, for the biaxial case. For this

case, the real records were rotated to their principal components. It can be observed in both, Figures 7.8 and 7.9, that the generated accelerograms are slightly different from one to another, as expected.

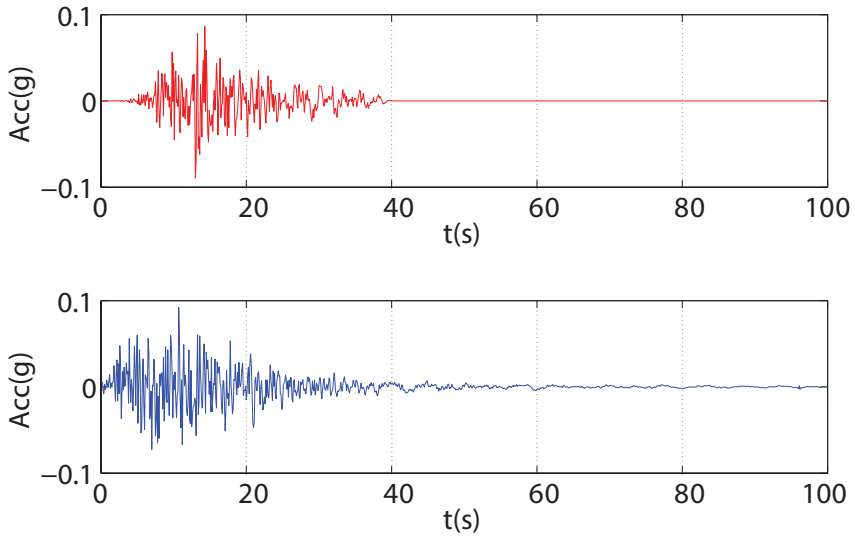

Figure 7.8 – Recorded (above) and synthetic (below) ground motions (GM) corresponding to a reverse fault.

The remainder of this Section aims to generate earthquakes with the KL and estimate the values M, R_{rup} and V_s using the methodology presented in Section 7.2. For this purpose, a seismic event with a large number of earthquakes is selected to be the input of the KL, i.e., Northridge earthquake (1994), which has 156 recordings. The magnitude, M, of this seismic event for the set is 6.69 whereas V_s and R_{rup} vary of station in station ($R_{rup} = [5.19 - 147.55]$ Km and $V_s = [160.6 - 2016.1]$ m/s). It should be noted that the KL expansion preserves the underlying stochastic process of the real records through the autocorrelation matrix. This does not mean that, because the set used has the same M, this value should also be preserved.

Figure 7.10 illustrates the histograms of M, R_{rup} and V_s for the set of recorded earthquakes and the estimated values of $\hat{M}$, $\hat{R}_{rup}$ and $\hat{V}_s$ of the uniaxial and biaxial artificial earthquakes. Figures 7.10(a), 7.10(b) and 7.10(c) represent the uniaxial results and Figures 7.10(d), 7.10(e)

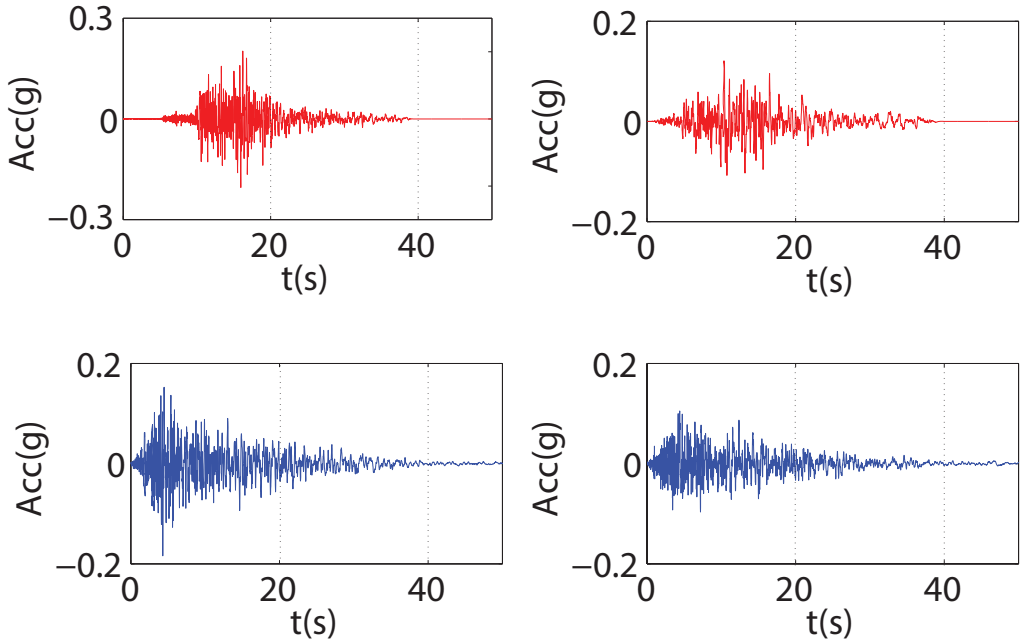

Figure 7.9 – Recorded (above) and synthetic (below) ground motions corresponding to a reverse fault.

and 7.10(f) the biaxial ones. Note that for M (Figures 7.10(a) and Figures 7.10(d)) the histogram of the magnitudes of recorded earthquakes has the same value of 6.69. It is observed that the values of $\hat{M}$ varies between 6 and 7.5 for both uniaxial and biaxial cases. For R_{rup} and V_s it is observed that, for the estimated earthquakes, large values of $\hat{R}_{rup}$ and $\hat{V}_s$ are not obtained using equations (7.4), (7.5) and (7.6). However, the number of recorded earthquakes with those large characteristics are a minority in this selected set.

Because two of the three parameters previously estimated vary between stations, only the difference between $\hat{M}$ and $M = 6.69$ is investigated. This difference, S_{est}, can be expressed as:

$$\hat{M} = M_{event} + S_{est} \tag{7.15}$$

where M_{event} is, in this case, 6.69 and $\hat{M}$ refers to the estimated value using equation (7.4). S_{est} is obtained for each artificial time series and can be then defined in terms of its mean

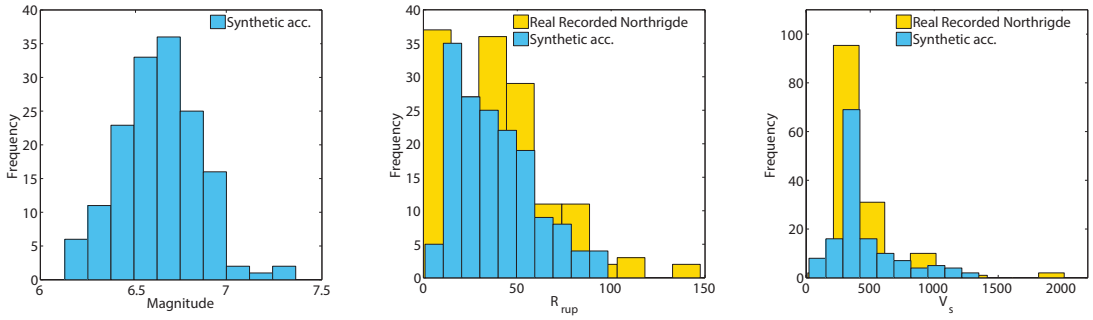

(a) M Uniaxial (b) R_{rup} Uniaxial (c) V_s Uniaxial

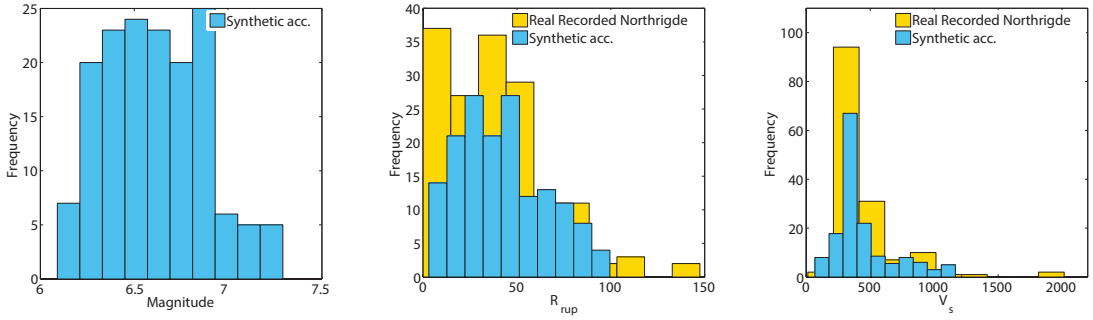

(d) M Biaxial (e) R_{rup} Biaxial (f) V_s Biaxial

Figure 7.10 – Histograms of the estimated values of M, R_{rup} and V_s for the uniaxial method a), b) and c) and for the biaxial method d), e) and f).

μ_{est} and its standard deviation σ_{est}. These values correspond to $\mu_{est} = 0.2322$, $\sigma_{est} = 0.3075$ and $\mu_{est} = 0.2493$, $\sigma_{est} = 0.4011$ for the uniaxial and biaxial case, respectively. Figure 7.11 shows the diagnostic scatter plots of the residuals for each sample generated for uniaxial and biaxial motions. These scatters again illustrate that there are no obvious trends and that the residuals are uniformly scattered above and bellow zero.

From the histograms (Figure 7.10) and scatter plots (Figure 7.11), it is observed that the value of $\hat{M}$ is not tremendously far from 6.69. It is therefore important to comment that the KL expansion provides an acceptable result without trying to preserve the value of M. However, note that only 156 records were used as an input to the KL, which is not enough. These problems are relaxed using rejection methods which allow selecting earthquakes from a target and a large number of records can be used as an input to the KL.

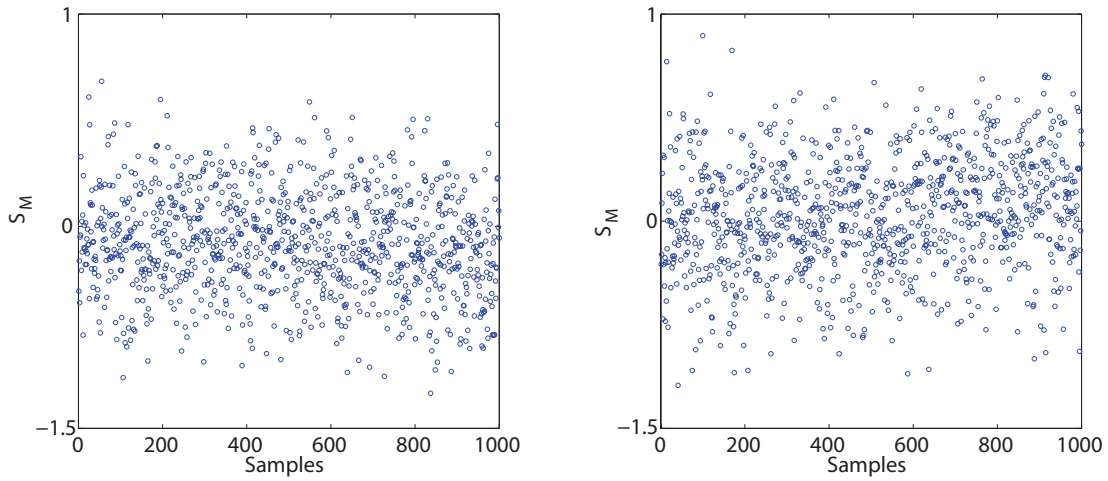

(a) Uniaxial

(b) Biaxial

Figure 7.11 – Scatter plots of residuals per sample generated. a) Uniaxial and b) biaxial motions.

7.5 Application of rejection methods

The purpose of this Section is to evaluate the models presented in Section 7.3. From now on, earthquakes generated with the KL expansion and selected with the threshold model are called KL-T. Similarly, earthquakes generated with the KL expansion and selected with the envelope model are called KL-ER Case I, when the first three ρ_c or v_c are used, and KL-ER Case II when all ρ_c or v_c are implemented.

7.5.1 Threshold model for the selection of ground motions

This Section aims to study the properties of earthquakes resulting from the KL-T. First, a number of artificial ground motions are accepted with the threshold sampler method, for a chosen design scenario expressed in terms of M, R_{rup} and V_s. Figure 7.12 provides typical samples accepted with the threshold sampler for a chosen $D = 0.4$ for three different targets $\tilde{\mathbb{M}} = [6, 10, 600]$, $\tilde{\mathbb{M}} = [7, 10, 600]$ and $\tilde{\mathbb{M}} = [8, 10, 600]$ manifesting the randomness of the simulated accelerograms.

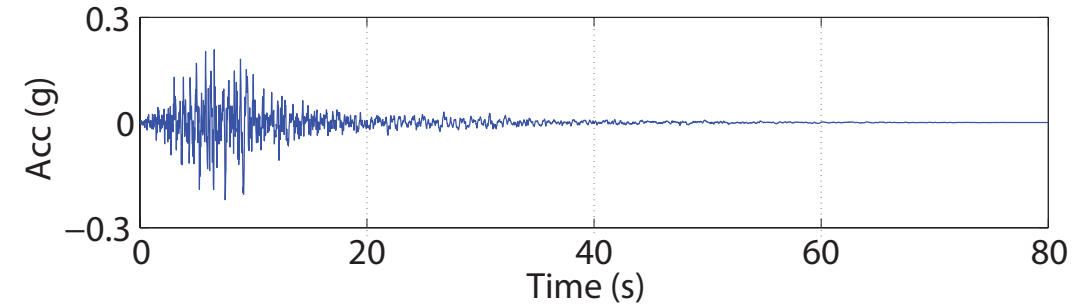

(a)

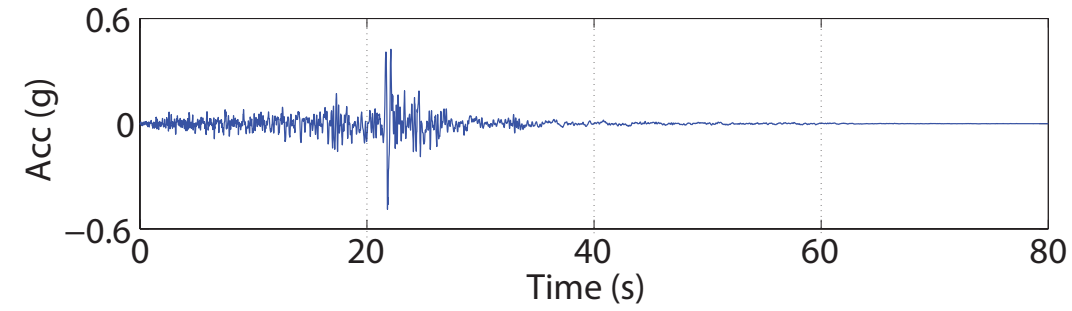

(b)

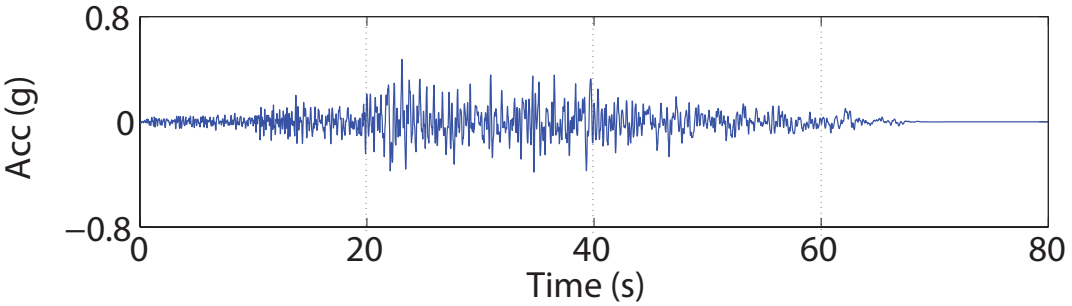

(c)

Figure 7.12 – Synthetic motions accepted using the threshold sampler model for a reverse fault type: a) $\tilde{\mathbb{M}} = [6, 10, 600]$, b) $\tilde{\mathbb{M}} = [7, 10, 600]$ and c) $\tilde{\mathbb{M}} = [8, 10, 600]$.

In the KL-T approach, accepting or rejecting samples depends on the parameters M, R_{rup} and V_s. Therefore, it is expected that the rejection procedure accepts earthquakes only if the records are consistent with the threshold value $\mathbb{K}$. Therefore, the residuals of the accepted earthquakes are mainly affected by the distance D chosen. For this reason, the relevance of this model is presented in terms of the distribution of its v_c.

For this aim, a set of 4000 earthquakes is selected using the KL-T for $\tilde{\mathbb{M}}$. The v_c of each

selected earthquake is calculated, using equation (7.1). Its distribution is calculated, which is Gaussian with a mean, μ_a, and a covariance matrix, Σ_a. Similarly, the target distribution is expressed by its mean μ_t and its covariance matrix Σ_t, calculated using equation (7.3).

Once these distributions are obtained, the difference between distributions is studied in terms of the absolute mean vector as $\mu_{SKL} = \mu_t - \mu_a$, and the covariance matrices as $\Sigma_{S_{KL},\mathbb{M}_j} = \Sigma_t + \Sigma_a$; with j referring to the M of the three targets studied: $[6, 10, 600]$, $[7, 10, 600]$ and $[8, 10, 600]$. These statistical properties are:

$$\mu_{S_{KL},\mathbb{M}_6} = \begin{bmatrix} 0.2341 \\ -0.3122 \\ -0.2650 \end{bmatrix} \quad \Sigma_{S_{KL},\mathbb{M}_6} = \begin{bmatrix} 0.0315 & -0.0011 & -0.0031 \\ -0.0012 & 0.0081 & -0.0025 \\ -0.0020 & -0.0012 & 0.1930 \end{bmatrix} \tag{7.16}$$

$$\mu_{S_{KL},\mathbb{M}_7} = \begin{bmatrix} 0.3891 \\ 0.0377 \\ 0.0381 \end{bmatrix} \quad \Sigma_{S_{KL},\mathbb{M}_7} = \begin{bmatrix} 0.2590 & -0.0122 & 0.0239 \\ 0.0029 & 0.5991 & -0.0125 \\ 0.0105 & -0.0114 & 0.5862 \end{bmatrix} \tag{7.17}$$

$$\mu_{S_{KL},\mathbb{M}_8} = \begin{bmatrix} 0.5931 \\ 0.2712 \\ 0.2167 \end{bmatrix} \quad \Sigma_{S_{KL},\mathbb{M}_8} = \begin{bmatrix} 0.3125 & 0.0021 & 0.0354 \\ 0.0038 & 1.2563 & -0.0163 \\ 0.0523 & -0.0232 & 2.369 \end{bmatrix} \tag{7.18}$$

From the above results, it can be observed that the diagonal terms of the covariance matrix are substantially bigger than the off diagonal terms, which are mostly zero. This observation means that the errors between the v_c are weakly correlated hence, they appear to be almost independent (errors). In terms of the mean, the absolute error, $\mu_{S_{KL},\mathbb{M}_j}$ increases while M takes larger values. The relative mean error $\epsilon_{\mu_{v_c}}$ of the method is also presented in Table 7.1 in the form of percentages. This relative error is calculated dividing $\mu_{S_{KL},\mathbb{M}_j}$ over the target v_c for each $\mathbb{M}_j$ obtained using equation (7.3). As expected, the error increases for larger magnitudes, probably due to the lack of records for greater M. In Table 7.1, it is also seen that the model has a large mean relative error. It should further be commented that even though the KL expansion coupled with the threshold method does not try to preserve

the v_c properties, these relative errors are too large and this model should be seen with some scepticism. One could argue that this error could be decreased setting D with a small value however, the computational cost would highly increase.

Table 7.1 – Relative error $\epsilon_{\mu_{v_c}}$ for the threshold rejection model (%).

	$\epsilon_{\mu_{v_1}}$	$\epsilon_{\mu_{v_2}}$	$\epsilon_{\mu_{v_3}}$
$M = 6$	29.62	27.69	31.60
$M = 7$	33.64	28.41	33.10
$M = 8$	38.70	31.49	36.18

7.5.2 Envelope distribution sampling method for the ground motions selection

This Section studies the relevance of the KL-ER Case II. As with KL-T, for specified earthquake and site characteristics, a number of artificial ground motions are accepted with KL-EN Case II. Figure 7.13 provides three earthquakes accepted with the envelope sampler method for the same scenarios as KL-T: $\tilde{\mathbb{M}} = [6, 10, 600]$, $\tilde{\mathbb{M}} = [7, 10, 600]$ and $\tilde{\mathbb{M}} = [8, 10, 600]$. For this rejection model, the randomness of the simulated accelerograms is also manifested in Figure 7.13.

As with the KL-T, the randomness of the model is investigated. In this approach, accepting or rejecting samples depends on the probability distribution of a target v_c. Therefore, it is expected that the rejection procedure accepts earthquakes only if the records are consistent with the distribution of the target v_c. To compare the truthfulness of the method, Figure 7.14 represents the fitted distribution of ρ_c of the accepted earthquakes using the KL-ER Case II model as well as the target distributions when $\tilde{M} = 6.2$, $\tilde{R}_{rup} = 10$ Km and $\tilde{V}_s = 600$ m/s where it can be seen that the distributions are in agreement. These distributions of the selected time series are obtained calculating the ρ_c of each earthquake, then generating the

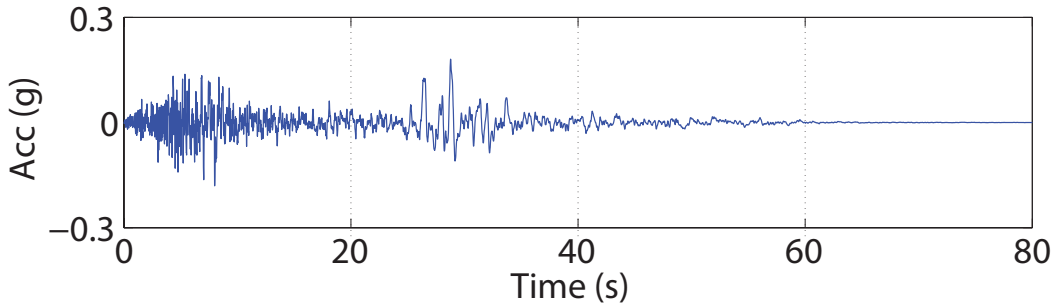

(a)

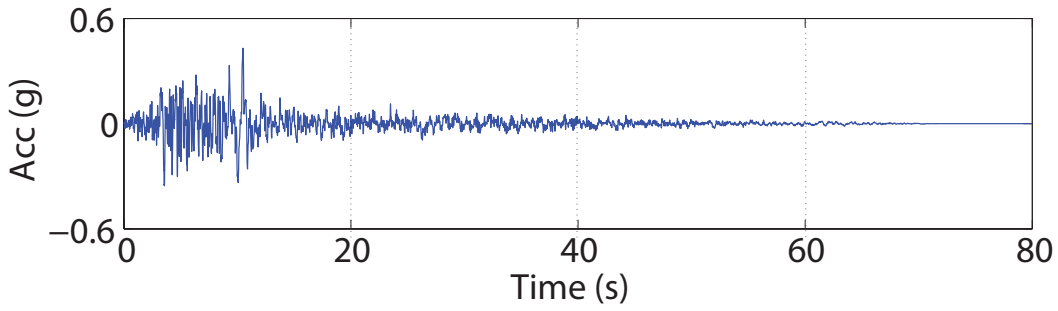

(b)

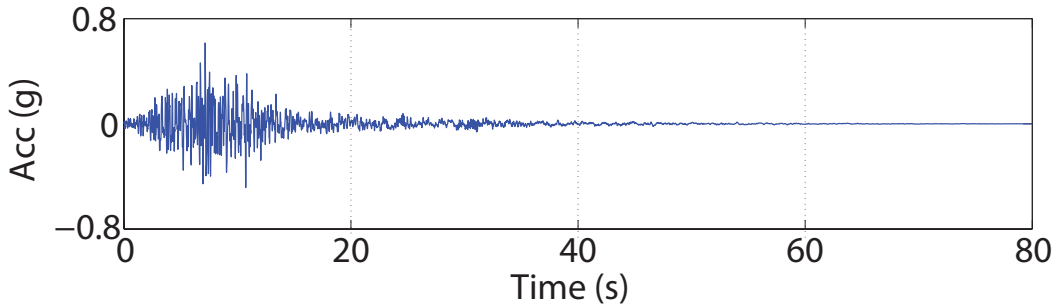

(c)

Figure 7.13 – Synthetic motions accepted using the envelope sampler model for reverse fault type a) $\tilde{\mathbb{M}} = [6, 10, 600]$, b) $\tilde{\mathbb{M}} = [7, 10, 600]$ and c) $\tilde{\mathbb{M}} = [8, 10, 600]$.

histograms and finally, fitting a distribution. For the target distribution, the v_c is calculated from equation (7.3). Samples are generated and then ρ_c is calculated. It is observed in Figure 7.14 that, in fact, these values are very well preserved in KL-ER Case II. It should further be commented that to achieve the similitude between the distributions, 8000 accepted earthquakes of 8000 samples each used.

As a consequence of the similitude between the target and proposal distributions, residuals

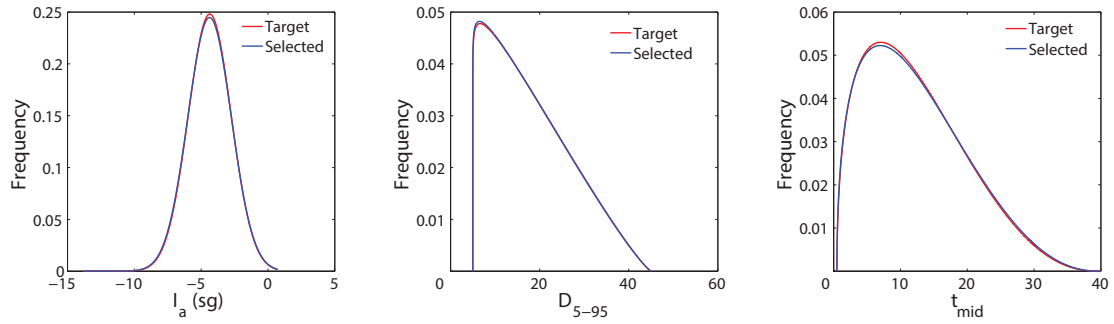

(a) I_a (b) D_{5-95} (c) t_{mid}

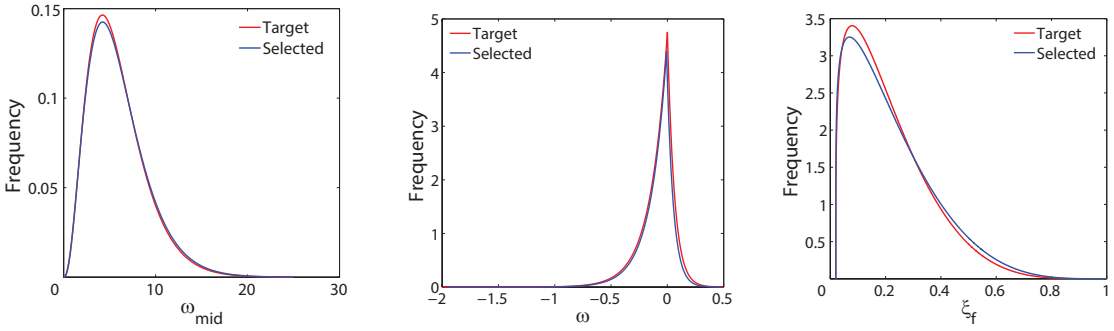

(d) ω_{mid} (e) ω' (f) ξ_f

Figure 7.14 – Probability density functions of the target distributions and selected earthquakes for the case of $M = 6.2$, $R_{rup} = 10$ Km and $V_s = 600$ m/s using the KL-ER Case II. a) I_a (log-normal), b) D_{5-95} (beta), c) t_{mid} (beta), d) ω_{mid} (gamma), e) ω' (two sided exponential) and f) ξ_f (beta).

are defined in terms of $\hat{\mathbb{M}}$ and $\tilde{\mathbb{M}}$. For this purpose, equation (7.15) is extended to the vector variables as:

$$\hat{\mathbb{M}} = \mathbb{M}_{event} + S_{est} \tag{7.19}$$

In terms of the generation of records, the model simulates earthquakes that are equal to the target with an error of the model ε_{KL} (which comes from the specific KL rejection method used) in the form of:

$$\mathbb{M}_{event} = \tilde{\mathbb{M}} + \varepsilon_{KL} \tag{7.20}$$

Combining equations (7.19) and (7.20):

$$\hat{\mathbb{M}} = \tilde{\mathbb{M}} + E \tag{7.21}$$

where $E = \varepsilon_{KL} + S_{est}$. This error is calculated extracting the target $\tilde{\mathbb{M}}$ from each $\hat{\mathbb{M}}$. Their properties such as the absolute mean $\mu_{E,\mathbb{M}_j}$ with j referring to the M of the three targets, the correlation coefficients $C_{E,\mathbb{M}_j}$ and the standard deviation, $\sigma_{E,\mathbb{M}_j}$ are presented bellow. Note that $\sigma_{E,\mathbb{M}_j}$ is normalised with the $\tilde{\mathbb{M}}$.

$$\mu_{E,\mathbb{M}_6} = \begin{bmatrix} 0.0410 \\ 0.3752 \\ 27.8412 \end{bmatrix} \quad C_{E,\mathbb{M}_6} = \begin{bmatrix} 1 & 0.0195 & -0.0425 \\ & 1 & 0.0059 \\ & & 1 \end{bmatrix} \quad \sigma_{E,\mathbb{M}_6} = \begin{bmatrix} 0.0833 \\ 0.0500 \\ 4.0812 \end{bmatrix} \tag{7.22}$$

$$\mu_{E,\mathbb{M}_7} = \begin{bmatrix} 0.0659 \\ 0.4354 \\ 34.6912 \end{bmatrix} \quad C_{E,\mathbb{M}_7} = \begin{bmatrix} 1 & 0.0141 & -0.0139 \\ & 1 & 0.0059 \\ & & 1 \end{bmatrix} \quad \sigma_{E,\mathbb{M}_7} = \begin{bmatrix} 0.2000 \\ 0.0536 \\ 3.7672 \end{bmatrix} \tag{7.23}$$

$$\mu_{E,\mathbb{M}_8} = \begin{bmatrix} 0.1392 \\ 0.4809 \\ 41.2561 \end{bmatrix} \quad C_{E,\mathbb{M}_8} = \begin{bmatrix} 1 & -0.0177 & 0.0397 \\ & 1 & -0.0059 \\ & & 1 \end{bmatrix} \quad \sigma_{E,\mathbb{M}_8} = \begin{bmatrix} 0.2250 \\ 0.0753 \\ 4.9267 \end{bmatrix} \tag{7.24}$$

From the above results, it is clearly observed that in the three cases, there is not a large correlation between errors. Hence, they are practically independent. Also, the three cases present a small $\sigma_{E,\mathbb{M}_j}$ for the first two values (M and R_{rup}). This means that the residuals almost fit the data. However, the third value, which correspond to V_s, takes large values of $\sigma_{E,\mathbb{M}_j}$. Similar results are obtained for $\mu_{E,\mathbb{M}_j}$: while the first two values have a small absolute mean, the third value has a larger one. Note that this results correspond to absolute errors and decrease for relative errors.

Similar to KL-T, the relative mean error, $\epsilon_{\mu_{\mathbb{M}_c}}$, is calculated and presented in Table 7.2. This error is estimated dividing $\mu_{E,\mathbb{M}_c}$ over the target $\tilde{\mathbb{M}}_c$. As observed in Table 7.1, the

error increases for greater values of $\mathbb{M}$. Note that for the case of V_s the relative error is tiny (the reader should remember that this component corresponds to $\tilde{V}_s = 600$ m/s). Thus, the previous absolute error is minimal.

Comparing the value of the errors from Tables 7.1 and 7.2, even if the errors refer to different quantities, it is clearly observed that the envelope rejection model has a smaller relative error than KL-T. Therefore, the results of the envelope distribution sampling method appear generally more accurate in comparison to the KL-T.

Table 7.2 – Relative error $\epsilon_{\mu_{M_c}}$ for the envelope rejection model (%).

	$\epsilon_{\mu_{M_1}}$	$\epsilon_{\mu_{R_{rup}}}$	$\epsilon_{\mu_{V_s}}$
$M = 6$	0.68	3.75	4.64
$M = 7$	0.94	4.35	5.78
$M = 8$	1.74	4.81	6.87

7.6 Comparison between the envelope method and RK-N

The aim of this Section is to evaluate the models presented in [44] and KL-ER Case I and II. KL-T is not implemented in this Section due to the large relative errors observed in Table 7.1. The following comparison is going to be, first, in terms of the peak ordinates of the generated earthquakes, second, through the response of a linear system and finally, the spectral and temporal characteristics of the earthquakes are compared.

7.6.1 Peak Ordinates and ρ_c

This Section focus on three quantities that are representative of a ground motion, PGA, PGV and PGD. The peak ordinates are computed for one accelerogram as follows:

$$\begin{aligned} PGA_j &= max|a_j(t)|, \quad j = 1, 2 \\ PGV_j &= max|\int_0^t a_j(t)dt|, \quad j = 1, 2 \\ PGD_j &= max|\int_0^t \int_0^t a_j(t)dtdt|, \quad j = 1, 2 \end{aligned} \tag{7.25}$$

where j defines the number of components.

For this purpose, a set of 5000 synthetic earthquakes from RK-N and KL-ER Case I and II are chosen varying M and for a fix $R_{rup} = 10$ Km and $V_s = 600$ m/s. As the interest is focused on the overall behaviour of the set, the mean of those three quantities over the whole data set is illustrated in Figure 7.15 for the uniaxial case. These mean values are calculated for each magnitude by averaging the peak ordinates of the set. It is observed that the PGA, PGV and PGD do not have a uniform trend between the models while M increases. However, it should be noted that even though these parameters are not intended to be retained, the peak ordinates are extreme values and the results could probably be improved with more accelerograms.

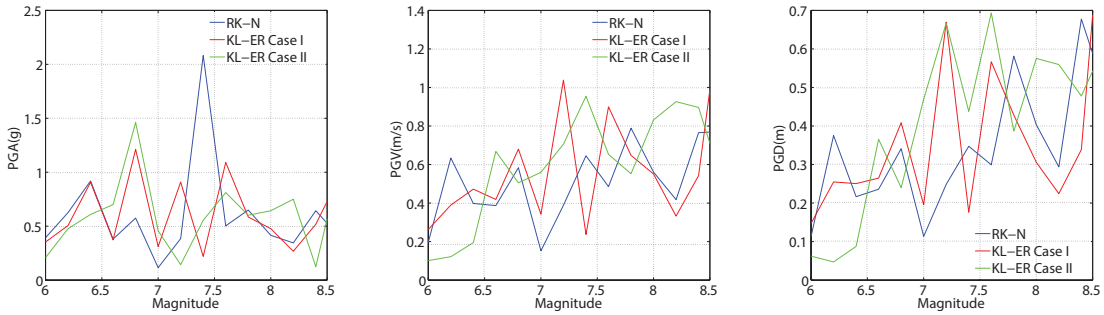

(a) PGA (b) PGV (c) PGD

Figure 7.15 – Comparison between KL-ER Case I and II and RK-N containing 5000 uniaxial accelerograms per magnitude. a) PGA, b) PGV and d) PGD.

7.6.2 Elastic response spectrum

For design purposes, the engineering community is often interested in the PGA. For this aim, the elastic response spectrum of linear SDOF structures with varying periods is studied in this Section for the three models: RK-N, KL-ER Case I and Case II. This comparison is going to be in terms of the peak amplitude, the period of the peak amplitude and the behaviour of the response at larger periods. It should be expected that KL-ER Case II and RK-N would have a close response because both build the damping and the frequency of the ground in a similar manner whereas KL-ER Case I does not preserve these properties.

To compute the elastic response spectrum, 300 uniaxial artificially generated earthquakes for a chosen realization of the vector $\mathbb{M}$ using the models excite to a 5% damped SDOF system. The pseudo absolute acceleration is computed for different values of the natural period. Results are presented in Figures 7.16, 7.17 and 7.18 for $\mathbb{M} = [6, 10, 600]$, $\mathbb{M} = [7, 10, 600]$ and $\mathbb{M} = [8, 10, 600]$, respectively. The elastic response spectrum is plotted in terms of the mean, μ, and the mean plus or minus the standard deviation, σ, of each set of accelerograms.

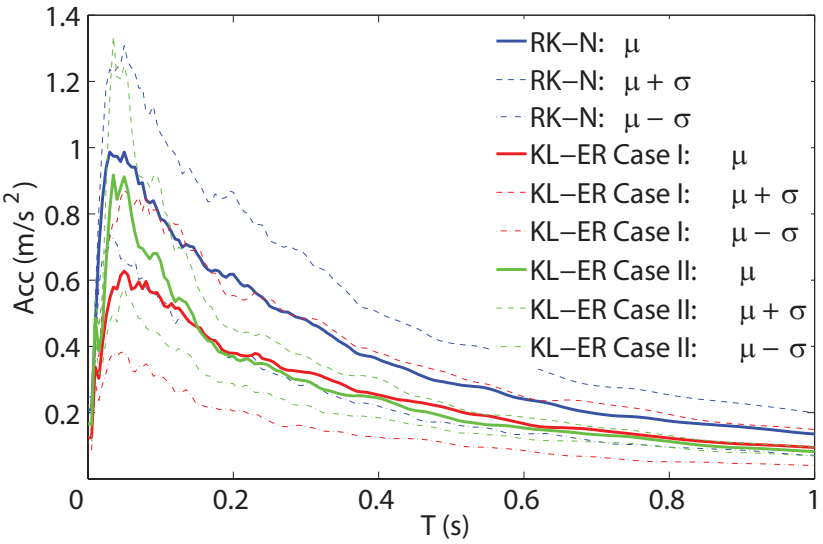

Figure 7.16 – Elastic response spectrum obtained using 300 uniaxial generated earthquakes from RK and KL-ER models for $\mathbb{M} = [6, 10, 600]$, $\xi = 5\%$.

In Figure 7.16 for $M = 6$, the maximum peak amplitude of the three models is obtained

at near periods. In Figure 7.17 for $M = 7$, the period of the peak amplitude in KL-ER Case I and Case II is slightly shifted to the left in comparison with RK-N. As expected, the peak amplitude of KL-ER Case II and RK-N has a similar behaviour while M is increasing. This is not preserved in Figure 7.18 for $M = 8$ however, results from this magnitude should be taken with some scepticism.

In terms of the peak amplitude, Figure 7.16 RK-N and KL-ER Case II present a similar peak amplitude acceleration, contrasting with KL-ER Case I which appears to have approximately two thirds of this amplitude. In Figure 7.17 for $M = 7$, this peak amplitude of the three models is close to each other; it appears between 1.7 and 2.1 m/s^2. A different behaviour is observed for $M = 8$ in Figure 7.18: KL-ER Case I and II have a closer amplitude whereas RK-N has a substantially larger one. However, as previously explained, cases of $M = 8$ probably do not correspond with the right behaviour.

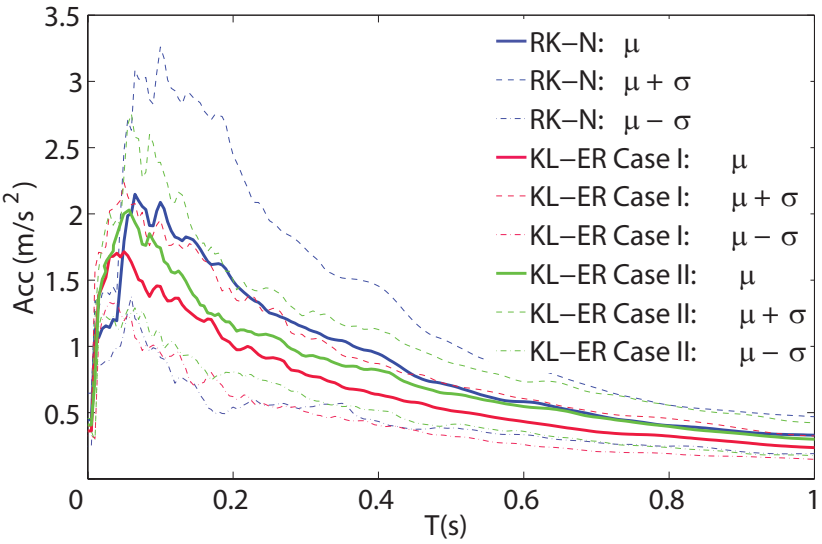

Figure 7.17 – Elastic response spectrum obtained using 300 uniaxial generated earthquakes from RK and KL-ER models for $\mathbb{M} = [7, 10, 600]$, $\xi = 5\%$.

It is observed in Figure 7.16 for $M = 6$, that RK-ER Case I and II present a similar behaviour at larger periods of the structure. This is also observed for $M = 8$ in Figure 7.18. In contrast, in Figure 7.17, RK-N and KL-ER Case II become similar at larger periods. In

general, the results at larger periods of the SDOF for the three earthquake models are in a agreement. This is of extremely importance for rocking bodies because they are more prone to fail at short periods.

Also, as explained in [44], the damping is a measure of the bandwidth of the ground motion and tends to increase with the magnitude. Therefore, the decay of the peak response should be steeper for larger magnitudes. This trend is verified as the magnitude is increased in Figures 7.16, 7.17 and 7.18. The decay of acceleration for RK-N, KL-ER Case I and Case II is steeper for $M = 8$ than for $M = 6$.

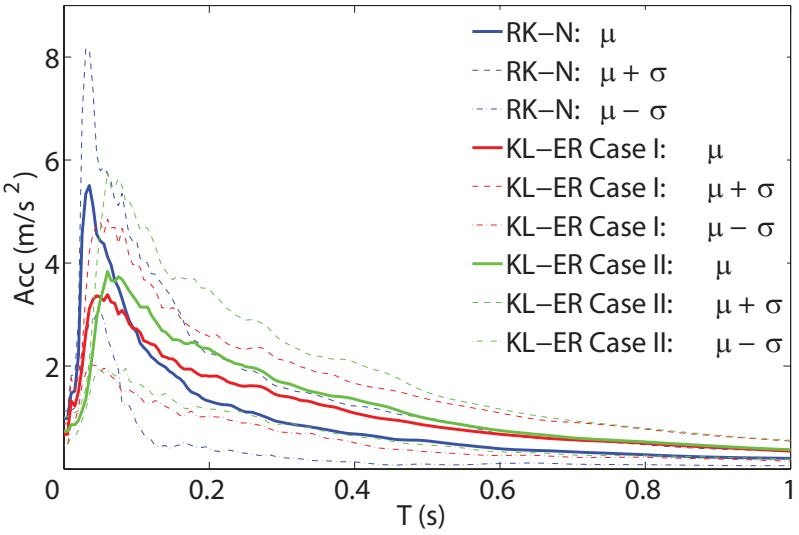

Figure 7.18 – Elastic response spectrum obtained using 300 uniaxial generated earthquakes from RK and KL-ER models for $\mathbb{M} = [8, 10, 600]$, $\xi = 5\%$.

It has been observed in this Section that the responses of RK-N, KL-ER Case I and Case II are, in general, similar throughout the period range considered. The variability observed between the three models is representative of the variability inherent in the given earthquake and site characteristics and the stochastic process implemented. Moreover, this variability was expected because of the differences observed between the models in Figure 7.15.

It should be further commented that for synthetic earthquakes accepted with KL-ER Case I model, only the first three v_c are considered. Therefore, the parameters related with

the frequency content are randomly obtained. However, even though the frequency content of the ground has a significant response on the system and it should be taken into account, the response from KL-ER Case I is fairly similar to KL-ER Case II.

In terms of comparing KL-ER Case I and II with RK-N, the generated accelerograms do not match the mean elastic response. However, this was not the intent of the methods. Both models try to approximate seismological properties but they generate earthquakes from a different stochastic model where the frequency and temporal characteristics are not equally computed. It is therefore the aim of the next Section to study these characteristics.

7.6.3 Temporal characteristics

It is well-known that ground motions are non-stationary in the time domain. Temporal non-stationarity refers to the variation in the intensity of the ground motion in time. Therefore, for the intended comparison between the models, these non-stationarities are investigated in this Section but only for RK-N and KL-ER Case II.

The envelope of the amplitudes of the earthquakes generated with RK-N follow a Gamma modulation function. This means that each of the generated earthquakes follow this distribution with random parameters which control the intensity of the process, the shape of the modulation function and the duration of the motion. In contrast, the KL expansion does not use any predefined amplitude modulation function and hence, each of these synthetic earthquakes has a different time envelope for the amplitude.

Figures 7.19(a) and 7.19(b) illustrate the mean envelopes for the amplitude for three different targets for RK-N and KL-ER Case II models, respectively. These envelopes are obtained from a set of 300 accelerograms for different $\tilde{\mathbb{M}}$. The envelope for each time series is calculated using the Hilbert transform [121]. After that, the mean of the 300 resulting envelopes is calculated. The smooth lines denote the imposed envelope function in RK-N for each set calculated by the Gamma distribution function defined in [44], whereas the lines

with fluctuations are the envelopes generated from the artificial earthquakes.

It can be seen in Figures 7.19(a) and 7.19(b) that RK-N follows the same Gamma function for each target whereas KL-ER Case II envelopes are described by a common feature: each set has a different envelope shape. In Figure 7.19(b) it is observed that these time envelopes of KL-ER Case II behave different than RK-N ones allowing the records to have multiple peaks and random envelope distributions.

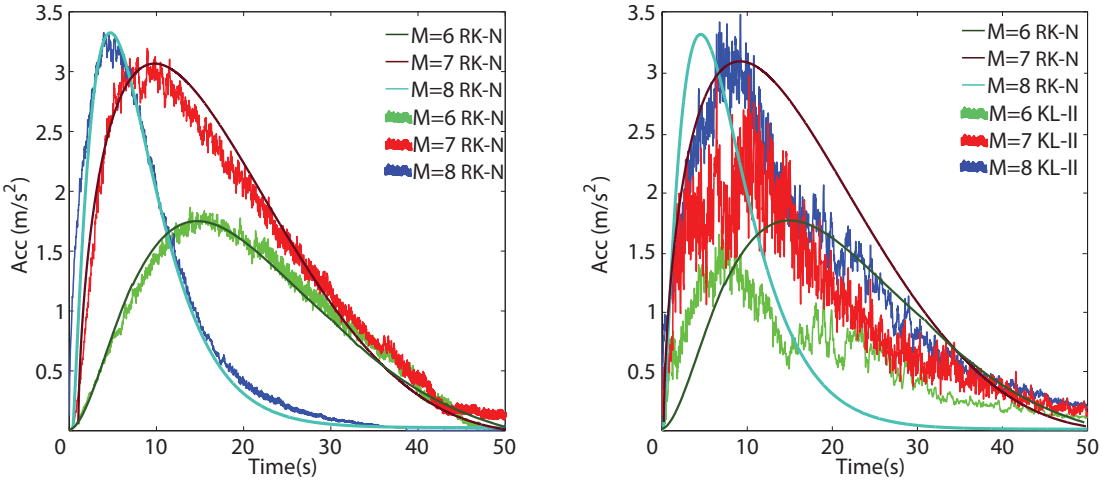

(a) RK-N

(b) KL-ER Case II

Figure 7.19 – a) Mean envelope of RK-N model [44] and b) Mean envelope of KL-ER Case II (in the legend is referred as KL-II) model for $M = 6$, $M = 7$, $M = 8$, $R_{rup} = 10$ Km and $V_s = 600$ m/s. The straight lines refer to the envelope modulation function for each set using the RK-N model and the lines with fluctuations denote the mean envelope of the generated earthquakes for both models.

In this Section, the temporal non-stationarities have provided a significant difference between both model envelopes. Figure 7.19(a) reflects that indeed, RK-N only provides one peak acceleration and it is fixed to a Gamma distribution function whereas more than one peak is observed for KL-ER Case II in Figure 7.19(b). Even though it is recognised that earthquakes have a predominant peak acceleration occurring during the earthquake

shaking, in nature, it has also been observed that earthquakes could have more than one peak acceleration, as in the case of Hachinohe or Northridge earthquakes. The envelope of the amplitudes is tremendously important in the non-linear response analysis. Therefore, modelling synthetic earthquakes which deem realistic temporal non-stationarities is crucial for the seismic risk analysis. To alleviate the problem of RK-N, in [44] a multi-degree of freedom filter is proposed to have multiple peaks. However, additional parameters need to be introduced and identified.

7.6.4 Spectral characteristics

In the previous Section, the envelope of the amplitudes of both models were studied. However, ground motions are also non-stationary in the frequency domain. Spectral non-stationarity refers to the variation of the frequency content of the ground motion over time. In this Section, the spectral characteristics of RK-N and KL-ER Case II are studied.

Similar to the amplitude envelopes, in KL-ER Case II the variation of the dominant ground frequency content is not forced to follow a specific function. However, RK-N adopts a theoretical linear function for the dominant ground frequency, ω_f of the form:

$$\omega_f(\tau) = \omega_{mid} + \omega'(\tau - t_{mid}) \tag{7.26}$$

To represent this theoretical frequency content in time for RK-N with $\tilde{\mathbb{M}} = [7, 10, 600]$, 300 synthetic earthquakes are generated. Then, the corresponding ω_{mid}, ω' and t_{mid} for each time series are calculated. After that, the mean of each variable is calculated to obtain the mean of $\omega_f(\tau)$ in equation (7.26). This theoretical representation of the frequency content is presented in Figure 7.20 with a green coloured dash. Observe that in this case, the frequency decreases linearly over time.

To represent the frequency content of the generated earthquakes with the two methods, the spectrogram function [78] is used. This tool returns the short-time Fourier transform of the time series where in each column an estimation of the short-term time-localized frequency

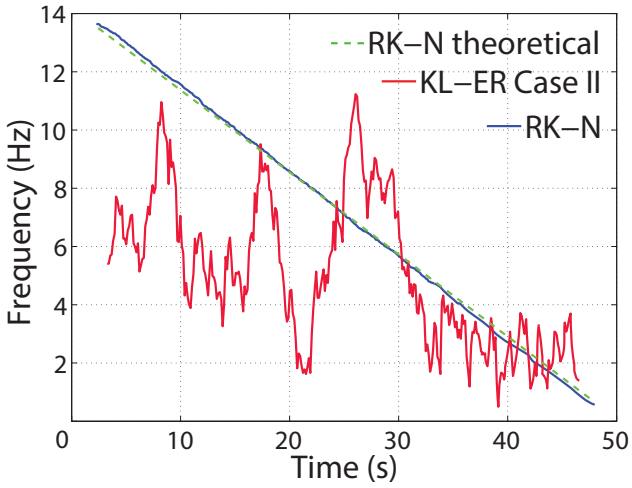

Figure 7.20 – Frequency content of RK-N and KL-ER Case II for $\tilde{\mathbb{M}} = [7, 10, 600]$.

content of the earthquake is contained. For this aim 300 earthquakes using RK-N and KL-ER Case II are selected for $\tilde{\mathbb{M}} = [7, 10, 600]$. Using the spectrogram tool, the frequency at which the maximum amplitude occurs per second is obtained for each time series. Then, the mean frequency value at each time is calculated. This is presented in Figure 7.20 for RK-N and KL-ER Case II. Comparing RK-N versus the theoretical RK-N, it is clearly seen that both functions behave similar following a decreasing linear trend. In contrast, comparing both RK-N and KL-ER Case II, no trend is observed. For KL-ER Case II the frequency increases and decreases over time without any systematic trend. The reason is again that the KL expansion does not use any predefined model.

In this Section, the spectral characteristics of both models are studied. Their differences are clearly observed: in RK-N the frequency behaves linearly due to the approximation of equation (7.26) and in KL-ER Case II the frequency content of these synthetic earthquakes has a random behaviour which may be defined by the statistics of the recorded ground motions.

7.7 Conclusion

In this Chapter a new site-based earthquake generation model is presented. Time series are simulated using the KL expansion using real records as inputs. Because the KL expansion does not provide any seismological properties, a new analytical technique to estimate M, R_{rup} and V_s of the artificial time series is presented.

The fact that engineers often want to use target values for generating ground motions leads to a probabilistic analysis based on rejection techniques. Such models filter the generated earthquakes and select only the ones in agreement with the target. Two rejection techniques are presented: the threshold model which appears to have a large relative error and the envelope sampling approach which significantly reduces the error.

Finally, a comparison between earthquakes generated with RK-N and the KL-ER Case I and II illustrate the differences between both models:

- Significant differences are observed with respect to the different peak ordinates. However, the peak ordinates are extreme values and probably with more accelerograms the results would be better. Nonetheless, it was not the intent of any of the models to approximate these parameters.

- The elastic response spectrum of the models appears to have the peak acceleration at approximately the same resonance period.

- The decay of acceleration on the elastic response spectrum is steeper for greater M in the three models. All the models compared agree with this conclusion.

- The average response of RK-N, KL-ER Case I and KL-ER Case II tends to be slightly similar even when the frequency content parameters are not introduced (KL-ER Case I). However, together with the temporal parameters, the KL-ER Case II model can provide a more lucid picture of the time series characteristics simulated and their effects on the

response of a SDOF system. The response spectra produced by RK-N and KL-ER Case II are similar at larger structural periods, however, that was not a systematic trend.

- The model parameters related to the temporal factors have shown important difference between the models. RK-N only produces earthquakes with one peak whereas the KL expansion can reproduce multiple peaks.

- The spectral characteristic of both models also appears to be considerably different. This is because the frequency content is fixed to an equation in RK-N whereas the KL expansion does not use any predefined model.

Chapter 8

Seismic risk analysis of rocking bodies

8.1 Introduction

In the previous Chapters, several earthquakes generation models were presented. However, characterising the risk not only requires an ensemble of ground motions to generate probability of failure curves but also a procedure to evaluate the seismic risk at a site. Estimations of the risk of rocking bodies have been presented in a series of papers. Each of them have used ground generation models previously defined; hence, the risk analysis might be affected by the disadvantages of these models. In [21] the generation of records is done using the SPM [32] with the TK-CP PSD [31]. In [122], estimations of the probability associated with the first overturning were presented using the hybrid approach of [123]. However, the blocks were subjected to synthetic waveforms. In [124], artificial motions were approximated to pulses and the probability of failure curves were generated versus intensity measures such as the PGA, PGV and PGD, using the source point model of [41] and [125]. However, the probability of failure of a rocking body depends on the whole motion and not on few characteristics or intensity measures. This Chapter presents methods for generating probability of failure

curves versus an intensity measure for the earthquake generation models proposed in Chapters 6 and 7.

It is also the purpose of this Chapter to present a method to calculate probability of failure for a period of interest and a method to calculate the lifespan of a body using seismological data. Both require the use of probability of failure curves. This seismic risk methodology proposed makes it possible to put design for earthquakes on a basis comparable to that presently used by engineers. The first part of this Chapter is therefore dedicated to explain this suggested engineering risk analysis.

For the aim of creating probability of failure curves, earthquakes are generated for a region using the models explained in Chapters 6 and 7. These earthquakes are subjected to a rocking body that is simulated using the IPM explained in Chapter 2. Probability of failure curves are created for varying intensity measures. The methodology is later extended to produce the probability of failure against a lifespan of interest. This is illustrated using suitable chosen examples and the methodology's ability to predict the probability of failure of a rocking body in an area.

8.2 Planar response of a Rocking Body

In Chapter 6, uniaxial and biaxial earthquake generations models were presented. It is hence the purpose of this Section to explain how these earthquakes excite the IPM.

The time histories generated using the methods described in Sections 6.4 and 6.5 can be associated using Figure 8.1(a). For instance, the method of Section 6.4.2 generates a pair of time histories, E_I and E_{II}, along the principal directions I and II, respectively, while the method of Section 6.4.1 generates a single time history, E_χ, along an axis χ which forms some random angle ψ with axis I. It is further worth mentioning that this angle ψ is different for each of the uniaxial time histories generated by the method of Section 6.4.1.

As discussed in [18] the response of rocking bodies is a general 3D rocking response, even

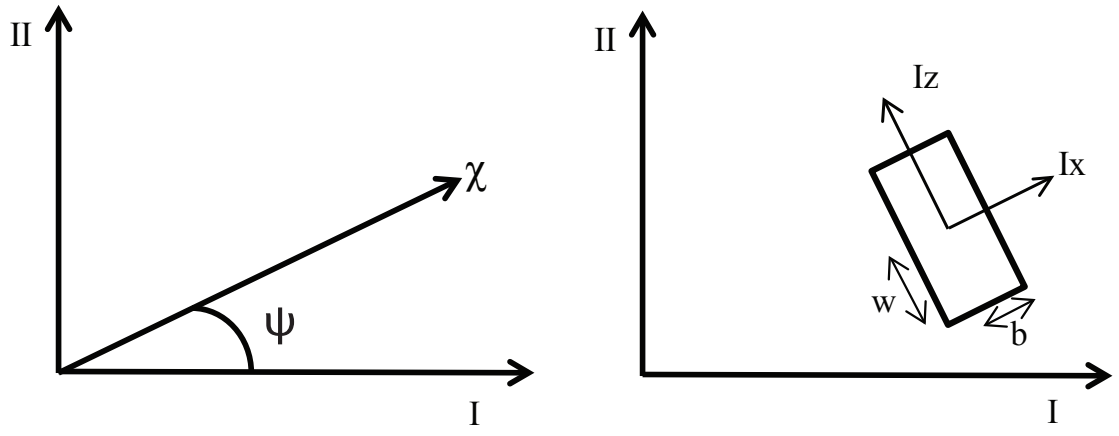

(a) (b)

Figure 8.1 – a) Principal axes. I and II correspond to the major and intermediate axes, respectively. χ is the angle with ψ. b) Prism as shown from above indicating the dimensions where w is the half-length and b is the half base.

for uniaxial horizontal inputs, unless the body is symmetric and the axis of excitation happens to be parallel with one of the axes of symmetry of the body. This work further demonstrated that the case of planar rocking is not the most conservative scenario for the body. An exception to this is when the third dimension of the body, considered to be a rectangular prism, its length, $2w$, is substantially bigger than the width, $2b$, and comparable or bigger to the height, $2h$. This is presented in Figure 8.1(b) for a body as shown from above along $x-z$ plane. In that case, planar rocking becomes a conservative assumption as practically only the component of excitation parallel to the axis, x, of the body induces rocking. If sliding is neglected, as is the assumption of the current work, then the perpendicular component, along the z axis, can be ignored. In this work, the assumption that $w >> b$ and $w \simeq h$ is used, together with the rest of the assumptions attributed to the IPM allow for examining planar rocking as a conservative scenario.

The ground motions generated are the inputs of the IPM. The method of Section 6.4.1 is used to generate the uniaxial horizontal inputs which are assumed to be parallel to the axis

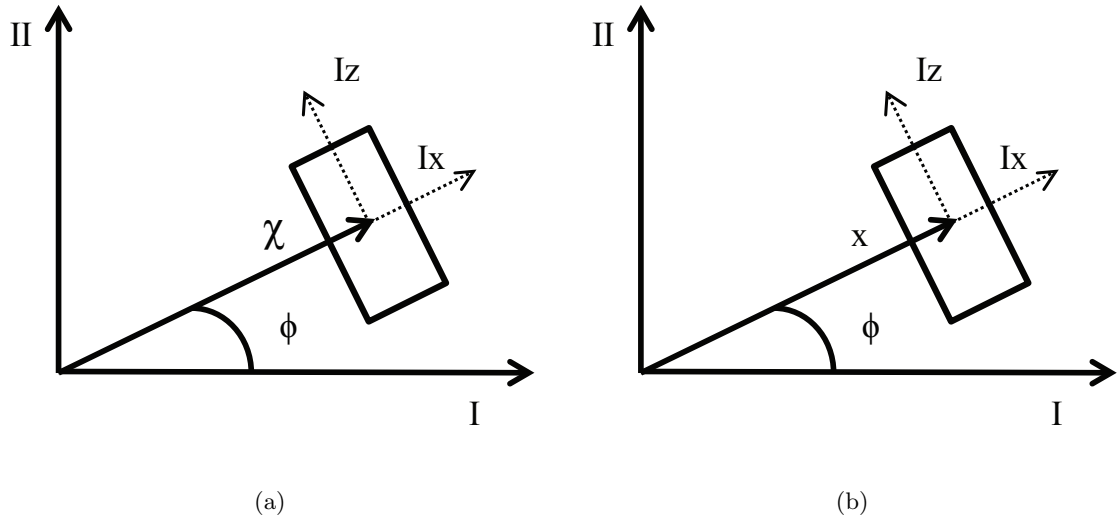

(a) (b)

Figure 8.2 – a) Rocking body parallel to χ. b) Rocking body twisted along the vertical axes y.

of the body, χ as illustrated in Figure 8.2(a). In this case, and under the previously defined assumptions, the input to the IPM is simply $\ddot{x}_g$.

The method of Section 6.4.2 is used to generate the biaxial inputs along the horizontal principal axes, assuming that the rocking body is twisted along the vertical axis so that its axis, x, forms an angle ϕ_b with the axes I as shown in Figure 8.2(b). The input to the IPM in that case is:

$$\ddot{x}_g = E_I cos\phi_b + E_{II} sin\phi_b \tag{8.1}$$

while the perpendicular horizontal component parallel to z is ignored, as explained above.

8.3 Engineering risk seismic analysis

This Section introduces a method for the evaluation of the probability of failure of a rocking body taking into account the seismic or design properties of the region where it is located. To achieve so, a methodology to produce probability of failure curves versus an intensity measure is presented.

8.3.1 Probability of failure curves versus intensity measures

A general approach to study the risk associated with rocking bodies is to create probability of failure curves, where the probability of occurrence of an event is mapped as a function of some parameters of interest. In the context of a rocking body, the event of interest is the survival or failure of the block, whereas the parameters of interest might depend on the earthquake generation model chosen. For instance, for the KT-CP PSD, the probability of failure is calculated after varying $\sqrt{S_0}$ whereas for RK-N are M, R_{rup} and/or V_s.

In a general case, the probability of failure of a rocking body, P_F, can be expressed in terms of a realization of the vector $\mathbb{A}$ as $P_F(\mathbb{A})$ where $\mathbb{A}$ refers to any intensity measure. To compute $P_F(\mathbb{A})$, a suit of earthquakes compatible with $\mathbb{A}$ are subjected to the IPM as described in Section 8.2. Then, $P_F(\mathbb{A})$ is calculated using a Monte Carlo simulation approach as the number of records for which failure occurs, N_F, over the total number of records compatible with the vector $\mathbb{A}$, N_T:

$$P_F(\mathbb{A}) = \frac{N_F}{N_T} \tag{8.2}$$

The probability of survival is simply calculated as $P_S(\mathbb{A}) = 1 - P_F(\mathbb{A})$.

8.3.2 Probability of failure over a period of interest

In the previous Section a methodology to calculate the probability of failure of a body versus a vector $\mathbb{A}$, which is used as an intensity measure, was defined. However, engineers are often more directly concerned with the probability of failure of a rocking body versus a time period of interest, T, $P_F(t = T)$:

$$P_F(t = T) = 1 - \sum_{n_e}^{\infty} P_S(N_T = n) P(N_T = n_e | t = T) \tag{8.3}$$

where t and N_T are, respectively, the variables for time and the number of earthquakes, $P_S(N_T = n_e)$ is the probability of survival of a block for a number, n_e, of earthquakes and $P(N_T = n_e | t = T)$ is the probability of occurrence of n_e earthquakes within the period of time, T.

Statistical modelling of earthquakes.

The number of occurring earthquakes in a period T is assumed to follow a Poison distribution [126] with the distribution parameter defined as c_p and the period of interest T. Therefore, $P(N_T = n_e|t = T)$ can be calculated as follows:

$$P(N_T = n_e|t = T) = \frac{e^{-c_p T}(c_p T)^{n_e}}{n_e!} \qquad n_e = 0, 1, 2, 3... \tag{8.4}$$

where the time units for equation (8.4) are in years. It is further assumed that the occurrence of earthquakes of different magnitudes is defined by the Gutenberg Richter model [109]:

$$log_{10} N_M = \alpha_g - \beta_g M \tag{8.5}$$

where N_M is the number of earthquakes greater or equal than M that are expected to occur annually and the model parameters α_g and β_g are defined by the seismicity of the region.

The total number of annual earthquakes of any magnitude occurs from equation (8.5) setting $M = 0$ is the annual occurrence rate c_p:

$$c_p = 10^{\alpha_g} \tag{8.6}$$

The Φ and ϕ for M are defined from equation (8.5) as:

$$\Phi(M) = 1 - 10^{-\beta_g M} \qquad \phi(M) = 10^{-\beta_g M} \beta_g \ln(10) \tag{8.7}$$

Probability of failure for a given number of earthquakes

Since the deterministic model assumes that the rocking body and the ground are rigid and that sliding and uplifting are neglected, there is no accumulation of damage between successive earthquakes that the body survives. Thus, the survivals of the rocking body in successive earthquakes can be treated as independent events leading to:

$$P_S(N_T = n_e) = P_S(E_1 \cap E_2 \cap E_3...) = P_S(E_l)^{n_e} \tag{8.8}$$

where $E_1, E_2...$ denotes the successive earthquakes and $P_S(E_l)$ is the probability of surviving any of the earthquakes with $l \in [1, n_e]$.

Substituting equations (8.8) and (8.4) into equation (8.3) results in the formula for the probability of failure of a rocking body versus a time period of interest:

$$P_F(t=T) = 1 - P_S(t=T) = 1 - \sum_{n=0}^{\infty} P_S(E_l)_e^n \frac{e^{-c_p T}(c_p T)^{n_e}}{n_e!} \tag{8.9}$$

which has an analytical expression defined as:

$$P_F(t=T) = 1 - e^{c_p T(P_S(E_l)-1)} \tag{8.10}$$

To compute the summation in equation (8.9), it is necessary to evaluate the probability of surviving any one earthquake, $P_S(E_l)$, in the region of interest. The total probability theorem gives:

$$P_S(E_l) = \int_{\mathbb{A}_1}^{\mathbb{A}_{end}} P_S(\mathbb{A} = \mathbb{A}_n)\phi(\mathbb{A})d\mathbb{A} \tag{8.11}$$

8.3.3 Lifespan

Lifespan is denoted as the variable indicating the time spent until the failure of the body occurs. Let L_t denote the variable for the lifespan, L_T a value of interest for the lifespan and N_t the number of failures that have occurred at a time t. By definition, the following conditions are equivalent:

$$P(L_t > L_T) = P(N_t - N_{t+T} = 0) \tag{8.12}$$

where the event $N_t - N_{t+T}$ implies that no failure has occurred yet in the time interval $[t, t+T]$, i.e., the body has survived during the time period T. This results in the following equation:

$$P(N_t - N_{t+T} = 0) = P_S(t=T) = e^{c_p T(P_S(E_l)-1)} \tag{8.13}$$

Rewriting equation (8.13) in terms of Φ:

$$P(L_t < L_T) = 1 - P(L_t > L_T) = 1 - e^{c_p T(P_S(E_l)-1)} \tag{8.14}$$

Note that for this case, the Φ of the lifespan of a body being equal to T (equation (8.14)) and the probability of failure during this period of interest, T (equation (8.10)) result in the same equation.

Unlike the probability of failure over a period of interest, the lifespan is a continuous variable hence, its ϕ can be defined as follows:

$$\phi(T) = \frac{d(\Phi(L_T))}{dT} = c_p T(P_S(E_l - 1)e^{c_p T(P_S(E_l)-1)} \tag{8.15}$$

8.3.4 Defining parameters α_g and β_g

The previously defined methods to compute the lifespan and probability of failure curves for a period of interest depend on α_g, β_g, the probability of failure of a block and the probability distributions of $\mathbb{A}$. While the last two can be determined using the methodology defined in the previous Section, α_g and β_g are provided through seismological data [127, 126].

The aim of this Section is to define α_g and β_g from the PGA, PGV and PGD. To achieve this, the model of Cornell [126] is used. This method could be helpful because there are areas around the globe where α_g and β_g are not defined due to the lack of seismological data. However, the values of PGA, PGV and PGD for a specific area might be known from seismological codes [54, 55]. Additionally, engineers might want to follow a design code and be compatible with it. Design codes provide for a specific area a PGA, PGV and PGD for which the system should not collapse. Thus, α_g and β_g can be obtained by implementing the design peak ordinates in Cornell's model [126]. For the above reasons, the method in [126] is needed to estimate α_g and β_g from known PGA, PGV and PGD.

In [126] a relationship between ground motion parameters PGA, PGV and PGD and the Gutenberg-Richter parameters, α_g and β_g, together with the perpendicular depth, L_M, is developed. The mathematical development of the equations are shown in [126]. Here, only the final equations are illustrated.

Starting with the recommended relation of the PGA, PGV and PGD in [102, 128], Cornell [126] argues that for a period of interest, T, the average return period, $T_{p,i}$, with $i = [PGA, PGV, PGD]$ from a uniform line fault is given by the following equation:

$$T_{p,i} = \frac{1}{vTCG} i^{-Q/b_{i2}} \tag{8.16}$$

where $Q = \beta_g \ln 10$, $C = e^{Qm_0} b_{i1}^{Q/b_{i2}}$, $G = \frac{2\pi}{(2L)^\gamma} \frac{\Gamma(\gamma)}{[\Gamma((\gamma+1/2)]^2}$ and $\gamma = Qb_{i3}/b_{i2} - 1$. The parameters b_{i1}, b_{i2} and b_{i3} are defined in [129].

It should further be noted that while the PGA, PGV and PGD depend on the period studied, α_g and β_g do not depend on it. Thus, equation (8.16) is independent of T.

Equation (8.16) relates the values of α_g, β_g and L_M with the PGA, PGV and PGD of a region. Therefore, knowing the values of PGA, PGV and PGD from an area of interest, α_g, β_g and L_M can be estimated. It is a system of three equations and three unknowns. Similarly, the opposite study can be carried out when the values of spectra coordinates are unknown and α_g, β_g and L_M known.

It should be reminded that the models in Sections 6.4 and 6.5 do not directly use the hypocentral depth, L_M, as an input parameter. Hence, unlike the specification implied in the regulations, the generated earthquakes are compatible with the values of α_g and β_g, but not with this depth. Instead, the generated earthquakes in reality correspond to a distribution of L_M that is compatible with the selected list of earthquakes, for a chosen realization of M, R_{rup} and V_s. Nonetheless, the process suggested results in defining the values of α_g and β_g which are representative of the seismological area studied.

8.4 Seismic risk evaluation

This Section aims to produce probability of failure curves using the procedures explained in Section 8.3. The body selected for this study has the following dimensions: $h = 1.5565$m and $b = 0.3975$m. This body has been used in previous works [26, 11, 18, 57] and allows for comparisons. The uncertainty of the position of the vertical impulse discussed in Chapters 2, 4 and 3 is further investigated while subjecting the rocking body to simulated time histories using the proposed earthquake generation models.

8.4.1 Probability of failure curves using stochastic models.

Artificial earthquakes are, in this Section, generated using the methods described in Section 6.3. Each synthetic earthquake was produced with a sampling step of 0.614 and 2^{11} steps were used. The duration of each single artificial earthquake was 10.24 s.

The probability of failure of the body is calculated for different realizations of an intensity measure in units of m/s^2. For this, for a single realization of the intensity measure, a number of uniaxial artificial earthquakes were generated and introduced as inputs to the deterministic model as described in Section 8.2.

Probability of failure using KT-CP with SPM

This Section focuses on the implementation of the KT-CP explained in Section 6.3.1, together with the SPM of Section 6.3.2. This spectrum is defined for a firm soil with the following characteristics: $\omega_g = 15$ rad/sec, $\xi_g = 0.6$, $\omega_f = 1.5$ rad/sec, $\xi_f = 0.6$. To achieve non-stationarities, the time envelope defined in [33] is applied with parameters $t_1 = 1$ s, $t_2 = 9$ s and $\beta_g = 0.2$.

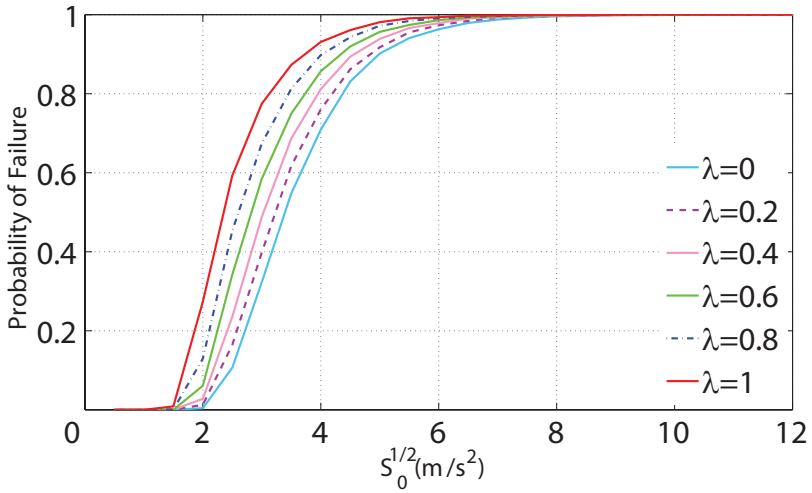

Figure 8.3 – Probability of failure for different values of $\sqrt{S_0}$ using 5000 artificial earthquakes for different values of λ for a body with $p = 2.1401$ and $\alpha = 0.3218$.

To quantify the risk of failure for the body, the probability of failure is calculated after

varying $\sqrt{S_0}$ as a measure of intensity hence, $\mathbb{A} = \sqrt{S_0}$. For this aim, 5000 earthquakes are generated for $S_0 = 1$ and are later uniformly scaled by multiplying the occurring amplitudes with $\sqrt{S_0}$. The probability of failure is calculated using the Monte Carlo analysis as in equation (8.2).

The effect of the propagation of the uncertainty of λ on the stability of rocking bodies subjected to earthquakes is also studied in this Section. Depending on the assumed value of λ, a different curve is produced, as shown in Figure 8.3. As expected, the probability of failure for a given λ increases as the value of the intensity measure, $\sqrt{S_0}$, increases. However, it should be noted that the probability of failure also increases for a given $\sqrt{S_0}$ when the assumed value of λ is increased. This indicates once again that the use of zero values for λ may potentially underestimate the probability of failure of the body, a conclusion compatible to the results seen earlier in Chapter 2 on cycloidal pulses and in [19].

These artificially generated time histories are also subjected to the case of two stacked bodies explained in Chapter 4 but in this case for a system with dimensions $h_1 = 0.5565$ m, $b_1 = 0.3970$ m, $h_2 = 0.3$ m and $b_2 = 0.15$ m. The body dimensions correspond to the bodies comprising a large monumental statue on a pedestal. They are also chosen as an example of a body where both λ_i have an equally important effect on the stability of the system. Depending on the assumed value of λ_i, a different curve is produced as shown in Figure 8.4.

As expected, it can be seen in Figure 8.4 that the probability of failure for a given value of $\sqrt{S_0}$ increases as either λ_i is increased. While in this specific system λ_2 appears to have a greater effect than λ_1, there are examples where this is reversed. For this system and for an earthquake type of excitation, the trend that has been observed in the previous examples of $\lambda_i = 0$ corresponding to a smaller probability of failure is observed again. Hence, as for a single rocking body, the choice of $\lambda_i = 0$ is the least conservative assumption, and modifications that cause a reduction in the values of λ_i in both interfaces are a desirable solution.

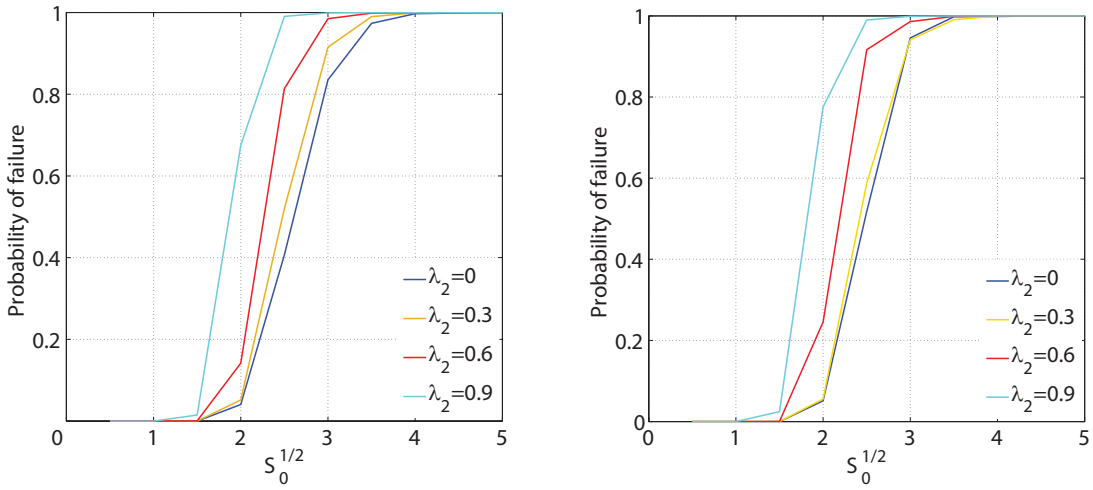

(a) $\lambda_1 = 0$

(b) $\lambda_1 = 0.3$

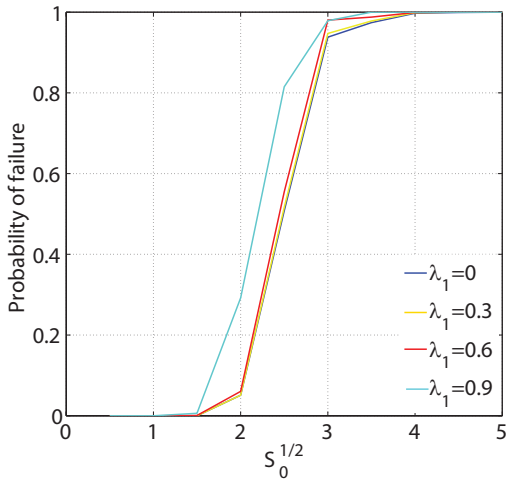

(c) $\lambda_2 = 0$

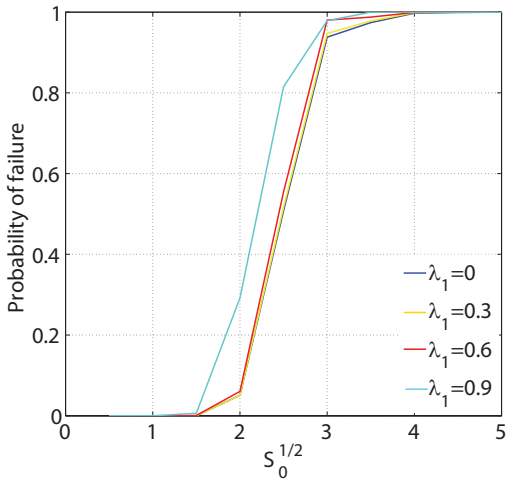

(d) $\lambda_2 = 0.3$

Figure 8.4 – Probability of failure curves for different values of λ_2, when a) $\lambda_1 = 0$, b) $\lambda_1 = 0.3$, and different values of λ_1 when c) $\lambda_2 = 0$ and d) $\lambda_2 = 0.3$ for bodies with dimensions $h_1 = 0.5565$, $b_1 = 0.3970$, $h_2 = 0.3$ and $b_2 = 0.15$.

Probability of failure using GV

This Section aims to produce probability of failure curves compatible with Eurocode 8. Thus, the GV approach explained in Section 6.3.3 is employed for the generation of artificially generated ground motion. As a starting PSD, the KT-CP spectrum for a firm soil is implemented. A single ground motion is obtained using the SPM. The time history generated is subjected

to an elastic SDOF system with a damping of 0.2. The corresponding response spectra is computed and compared versus the design spectrum. To ensure consistency with KT-CP, an horizontal elastic design spectrum for soil type A is chosen. The spectral density is adjusted iteratively using the scale factors defined in Section 6.3.3. This process was repeated until 5000 earthquakes were generated.

As previously explained, implementing GV procedure, S_0 is the initial guess in the iterative process hence, the final spectrum has little to do with this starting guess. Therefore, to quantify the risk, S_0 cannot be used as an intensity measure. However, one could use the design ground acceleration a_g [54], which is equal to the reference PGA of type A ground times the important factor γ_I:

$$a_g = \gamma_I PGA \tag{8.17}$$

The synthetic time histories are generated using $PGA = 1$ and are later uniformly scaled by multiplying by γ_I. Note that the recommended values of γ_I in [54] are $\gamma_I = [0.8 \quad 1.0 \quad 1.2 \quad 1.4]$. However, the range has been increased to have a broader view of the probability of failure. As in the previous approach, probability of failure curves are calculated using Monte Carlo analysis as in equation (8.2) where $\mathbb{A} = a_g$.

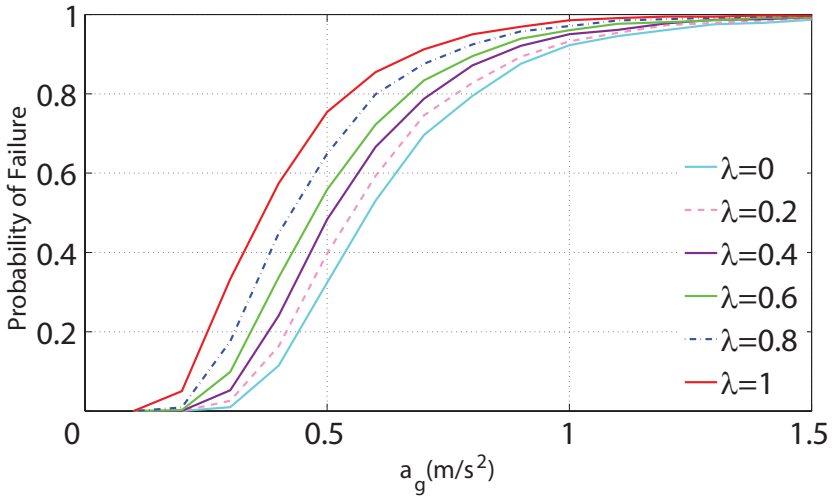

Figure 8.5 – Probability of failure for different values of PGA using 5.000 artificial earthquakes for different values of λ for a body with $p = 2.1401$ and $\alpha = 0.3218$.

Figure 8.5 represents the different curves produced for each value of λ. As in the case of Figure 8.3, for a given λ the probability of failure increases as the value of a_g increases. Moreover, for a given a_g, the probability of failure also increases, as the assumed value of λ is increased. This is again a compatible conclusion with the above results using the KT-CP joined with the SPM.

Figures 8.3 and 8.5 can be compared as both probability of failure curves are expressed versus an intensity in units of m/s^2. Consider for example the point of intensity at 0.5 m/s^2: in Figure 8.3, the probability of failure for $\lambda = 0$ is zero whereas in Figure 8.5 is 0.77. Therefore, the model of [35] highly increases the probability of failure, while matching individual time histories with a target response. As previously mentioned, matching the response spectrum of each time history to a target response spectrum ends in unrealistic earthquakes; hence, even the short frequency components are increased, which are the ones that conduct the rocking bodies into failure (as observed in the stability diagrams in Chapter 2). Therefore, probability of failure curves for rocking bodies using the GV procedure should be considered as an overly conservative estimate.

8.4.2 Probability of failure curves using hybrid approaches.

Artificial earthquakes are, in this Section, generated using the methods described in Section 6.4. The earthquakes used in the following examples are generated for M between 3 and 8.5, for a reverse fault, assuming a $V_s = 600$ m/s and $R_{rup} = 10$ Km. Only earthquakes with a magnitude greater than 3 are used in this Section as no failure was observed for smaller magnitudes.

The probability of failure of the body is calculated for different realizations of the vector $\mathbb{M} = [M, R_{rup}, V_s]$ hence, $\mathbb{A} = \mathbb{M}$. For this end, for a realization $[M, R_{rup}, V_s]$ a number of artificial earthquakes were generated and introduced as inputs to the deterministic model as described in Section 8.2.

Probability of failure using uniaxial motions from RK-N

In this Section, uniaxial inputs from RK-N are used and subjected to the body as described in Section 6.4.1. In Figure 8.6(a), the probability of failure of the body with $\lambda = 0$ is studied for different values of M and for $R_{rup} = 10$ Km and $V_s = 600$ m/s. To produce the probability of failure, the same number of earthquakes is used per magnitude.

It should be noted in Figure 8.6(a) that the curves become more similar and convergence of the estimated probability is gradually achieved as the number of earthquakes used for each magnitude is increased. For the case examined here in Figure 8.6(b), it should be noted that the generation of approximately 6000 earthquakes per magnitude are required in order to estimate all probabilities with an accuracy of 2%.

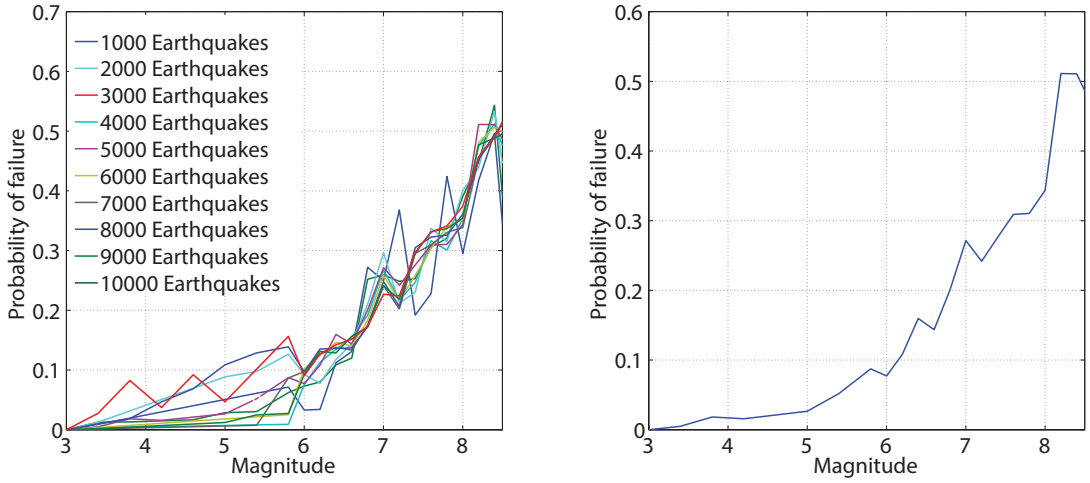

(a) (b)

Figure 8.6 – Probability of failure curves using the uniaxial method (RK-N), a) for different number of earthquakes and b) the probability of failure when the method convergences. Both figures assume that $\lambda = 0$, $R_{rup} = 10$ Km and $V_s = 600$ m/s.

Figure 8.6(b), i.e., the probability of failure occurring for 6000 earthquakes per magnitude, is used to further discuss properties of the curve. As expected, the larger probabilities of failure of the body are detected in the region of larger values of M. However, due to the non-

lineartity of the problem, a monotonic increase of the probability of failure is not observed. In fact, there are cases where the curve locally decreases as M increases as for example in the interval $[7, 7.5]$.

Figure 8.6 makes the assumption that $\lambda = 0$. However, as discussed earlier, there is an uncertainty over the location of the vertical impulse during impact and the value of λ. Figure 8.7 examines how different values of λ affect the probability of failure curves. For the aim of Figure 8.7 and the following figures, unless stated otherwise, 6000 generated earthquakes per magnitude are used. Similar to what was observed in the previous Section for earthquakes generated using the TK-CP Spectrum [31] together with the SPM, the probability of failure increases for larger values of λ. Thus, there is a need to take into account the uncertainty related to the assumption of how energy is lost during impacts. The average uncertainty between $\lambda = 0$ and $\lambda = 1$ for the uniaxial curve is calculated as the sum of the difference between the probabilities for each magnitude over the number of magnitudes used. In this case the uncertainty of λ is 8.03%.

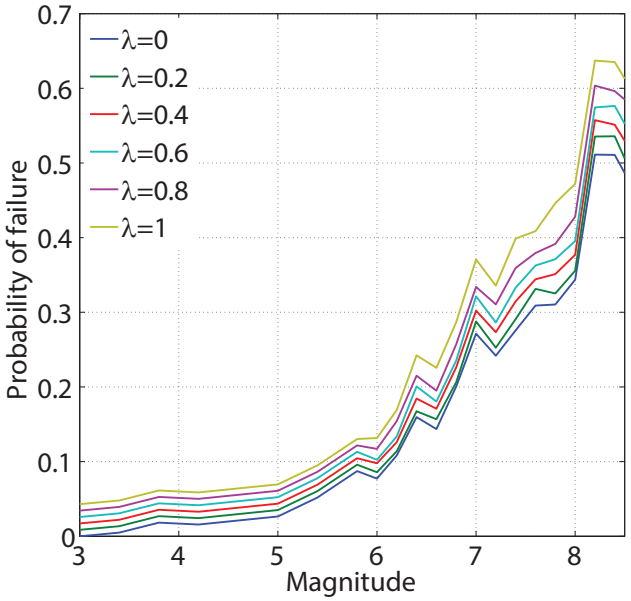

Figure 8.7 – Probability of failure curves for the specified body when the value of λ is varied using 6000 earthquakes.

It is of further interest to investigate how the probability of failure changes for varying R and V_s. For this aim, earthquakes are generated by varying the values of R_{rup} between 10 and 90 Km and V_s between 600 and 1500 m/s. Figure 8.8 represents the probability of failure surfaces for three cases in which a different subset of M, R_{rup} and V_s are varied: case A: M and R_{rup} are varied (Figure 8.8(a)) for $V_s = 1500$ m/s, case B: M and V_s are varied (Figure 8.8(b)) for $R_{rup} = 10$ Km and case C: V_s and R_{rup} are varied (Figure 8.8(c)) for $M = 8.5$.

First, in case A the probability of failure, in general, rises as R_{rup} decreases or M increases without a monotonic trend. In case B, as M is increased, the probability of failure is growing in a non-monotonic manner. Finally for case C, the body is, generally, more prone to fail as R_{rup} is closer to the fault. These results are expected as the proximity to the fault and high magnitudes cause the most damage. On the other hand, for the variable V_s, it does not seem to be a clear trend. This can be predicted as V_s is the velocity of the propagation of waves through the ground, and qualitatively, it reflects the resonant frequency of the soil. It is then expected that the response is not proportional to the increase or decrease of V_s, but instead local maxima are observed.

Probability of failure using biaxial motions from RK-N

As mentioned in Section 6.4.2, the biaxial inputs from RK-N are generated along both horizontal principal axes, while it is assumed that the rocking body is twisted so that its local x axis forms an angle ϕ_b with axis I. Due to the double symmetry of the body only values of ϕ_b in the interval $[0^\circ, 90^\circ]$ are examined in this Section.

Figure 8.9(a) shows the probability of failure curves for different values of the initial twist ϕ_b, using M as an intensity measure, $R_{rup} = 10$ Km and $V_s = 600$ m/s. As ϕ_b is increased, it can be seen that the probability of failure decreases practically for any value of M. This is, of course, expected as the assumption that $\phi_b = 0^\circ$ corresponds to the scenario where the weak axis of the body, z, is perpendicular to the major principal axis of the earthquake, while the

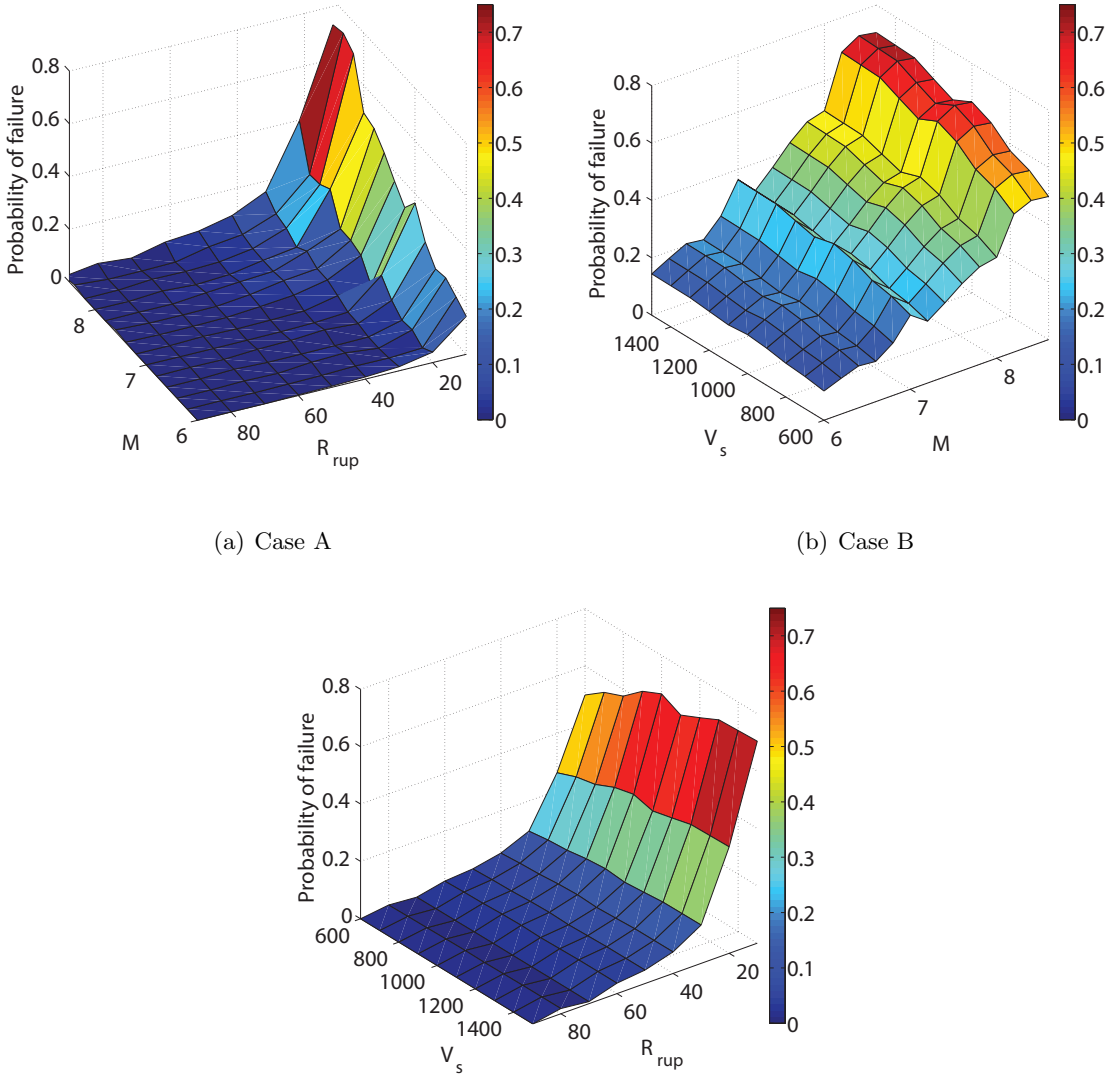

(a) Case A

(b) Case B

(c) Case C

Figure 8.8 – Probability of failure surfaces generated using the uniaxial method for different values of a) Case A: M and R_{rup} when $V_s = 1500$ m/s, b) Case B: M and V_s when $R_{rup} =$ 10Km and c) Case C: V_s and R_{rup} when $M = 8.5$. 6000 earthquakes are subjected to the IPM.

case of $\phi_b = 90°$ where it corresponds to the strong axis of the body x, being perpendicular to the major principal axis. Both scenarios are, of course, not very likely to happen in practice and hence, the corresponding probabilities of failure for $\phi_b = 0°$ and $\phi_b = 90°$ should be seen as the upper and lower bounds of the expected probability of failure.

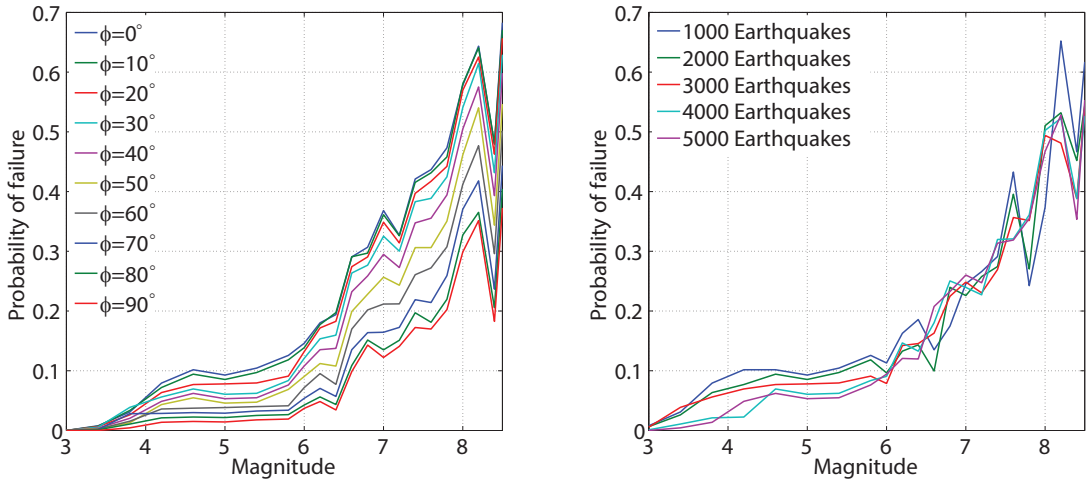

(a) (b)

Figure 8.9 – a) Probability of failure curves generated using the biaxial method for different values of ϕ_b (RK-N). b) Probability of failure generated using the biaxial method for different number of earthquakes.

In reality, the initial twist of the body ϕ_b is a random variable. We can further assume that this is a uniformly distributed random variable between 0° and 360° (or between 0° and 90° after making use of symmetry). The probability of failure of the body for a magnitude M, P_M, follows equation (8.18).

$$P_M = \int_{\phi_b=0°}^{\phi_b=90°} P_{M|\phi_b} f(\phi_b) dx \tag{8.18}$$

where, making use of the double symmetry of the body, its ϕ is: $f(x) = 1/90°$. The integral of equation (8.18) is computed numerically using a trapezoid integration rule.

Therefore, using Equation (8.18), the probability curves are plotted varying the number of pairs of earthquakes used and the results are presented in Figure 8.9(b). Convergence is achieved using 4000 pairs of earthquakes along the principal directions for each value of M. At this point, it should be reminded that the probability calculated from equation (8.18) and shown in Figure 8.9(b) is directly comparable to the probabilities obtained from the

uniaxial inputs shown in Figure 8.6. In both cases, the probability of failure for the body is obtained for different values of M taking into account the randomness of the twist of the body with respect to the principal axes. However, in the case of the uniaxial inputs, each new generated sample accounts for both, the randomness in the underlying ground motion stochastic process and the twist of the body. On the other hand, for the case of the biaxial inputs used in Section 6.4.2, these two sources of randomness are treated independently: no new ground motions need to be generated for different values of ϕ_b.

Table 8.1 shows the maximum error of the probability of failure for different number of ϕ_b angles taken into account for equation (8.18). The error, ε_1, is calculated for $\phi_b = 0, 5, 10, ..., 90^\circ$ and ε_2 for $\phi_b = 0, 10, 20, ..., 90^\circ$ as the maximum difference of the probabilities calculated by varying the numbers of pairs used. Retaining the same number of generated pairs of earthquakes, the maximum error of the probability of failure decreases as more angles are taken into account. This allows for reducing the number of ground motions generated to achieve a desired level of convergence, by instead increasing the number of the values of ϕ_b used. The focus of the latter strategy is not to reduce the overall computational cost, although there are methods that might result into computational benefits from separating the two sources of uncertainty, but rather to reduce the required number for the generated ground motions. The latter is desirable, as the generation of several pairs of earthquakes from a small number of experimental data results into theoretical problems [51].

Table 8.1 – Error Biaxial Method

Number of earthquakes	1000 - 2000	2000 - 3000	3000 - 4000	4000- 5000
ε_1 $(\phi_b = 0, 5, 10, ..., 90^\circ)$	6.82	4.11	2.52	1.26
$\varepsilon_2(\phi_b = 0, 10, 20, ..., 90^\circ)$	7.14	4.23	2.60	1.43

To account for the effect of the energy loss during impacts, similar to the uniaxial case,

the values of λ are varied and the corresponding $P_M(\phi_b)$ is calculated. Figure 8.10 represents a sequence of probability of failure curves in which the value of λ has been increased. It is observed that again in this problem, the location of the vertical impulse during impacts significantly affects the stability of the rocking body. Similar to uniaxial inputs, the mean uncertainty between $\lambda = 0$ and $\lambda = 1$ is calculated and is 8.77%.

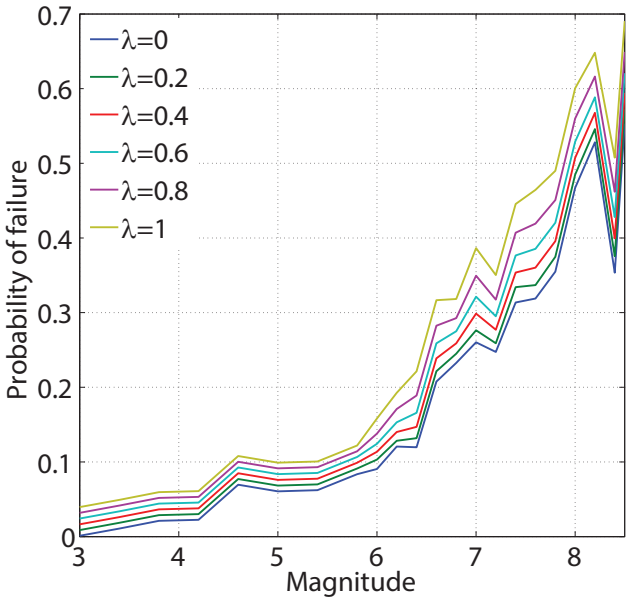

Figure 8.10 – Probability of failure curves for the specified body when the value of λ is varied for the biaxial case using 4000 earthquakes per ϕ_b.

Probability of failure curves for different intensity measures are presented in Figure 8.11. The cases of study presented for the uniaxial inputs are also illustrated for biaxial inputs. Similar to what was observed in Figure 8.8 while comparing case A, B and C, for biaxial inputs (Figures 8.11(a) and 8.11(b)), failure increases with increasing M and decreasing R_{rup}. Also, there are local maxima as V_s is varied.

A comparison of the uniaxial and biaxial methods for varying M and $R_{rup} = 10$ Km and $V_s = 600$ m/s is presented in Figure 8.12(a), where it can be seen that the probability of failure from the uniaxial method and the biaxial methods are both enveloped from the estimates of the biaxial method for angles $\phi_b = 0°$ and $\phi_b = 90°$. It should be noted that

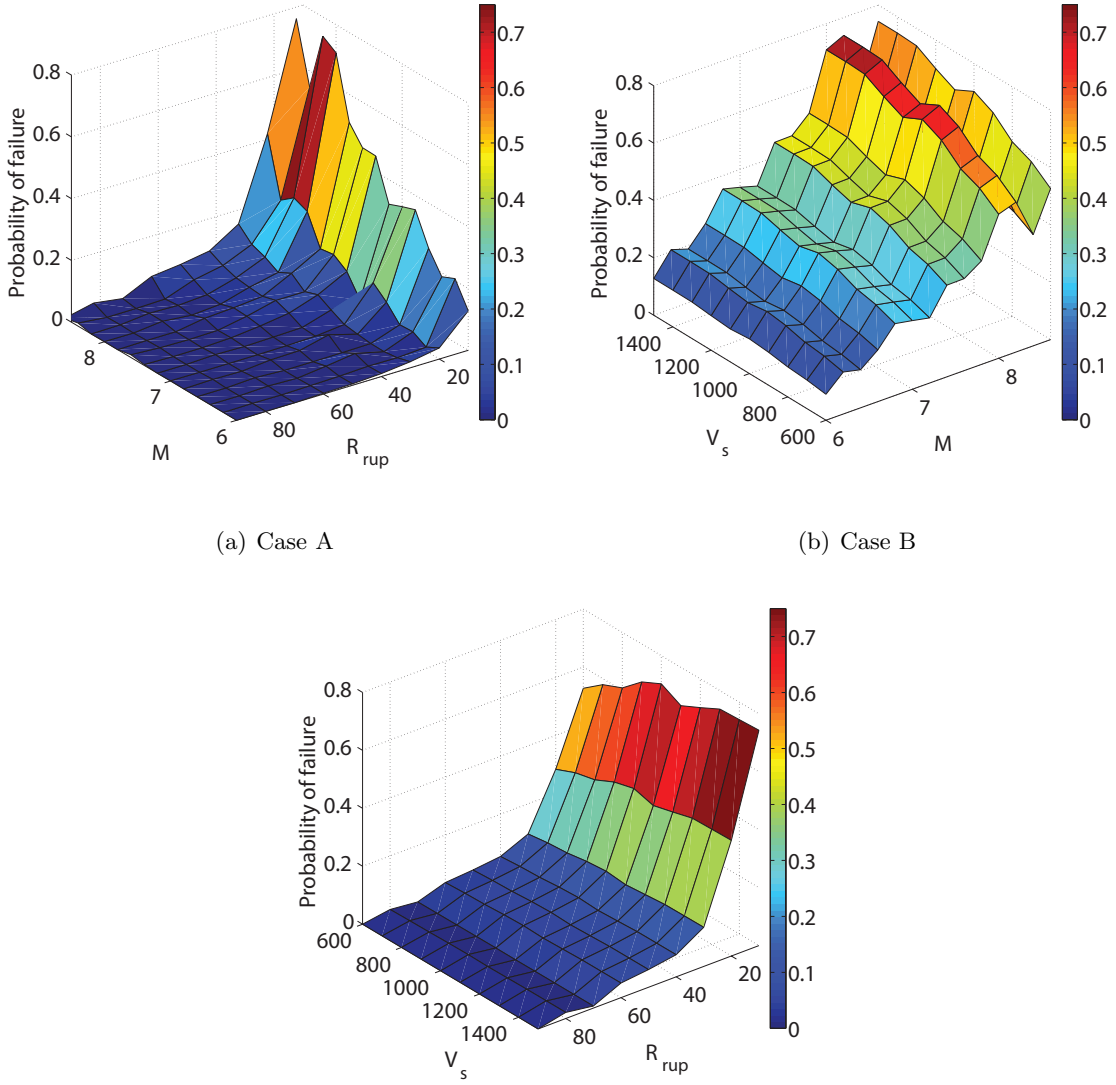

(a) Case A

(b) Case B

(c) Case C

Figure 8.11 – Probability of failure surfaces generated using the biaxial method for different values of a) Case A: M and R_{rup} when $V_s = 1500\text{m/s}^2$, b) Case B: M and V_s when $R_{rup} =$ 10Km and c) Case C: V_s and R_{rup} when $M = 8.5$. 4000 earthquakes are subjected to the IPM for $\phi_b = 0, 10, ..., 90°$.

the curves predicted by the two methods are very similar with a mean absolute error of 2.34%. This error is calculated as the sum of the difference between the probabilities of each magnitude over the number of magnitudes used. An exception of this similitude occurs near the maximum M of 8.5, which is to a point expected as the list of earthquakes used

to calibrate both models contains very few earthquakes with $M > 8$ and hence, the results obtained in that region should be addressed with some scepticism, as previously mentioned.

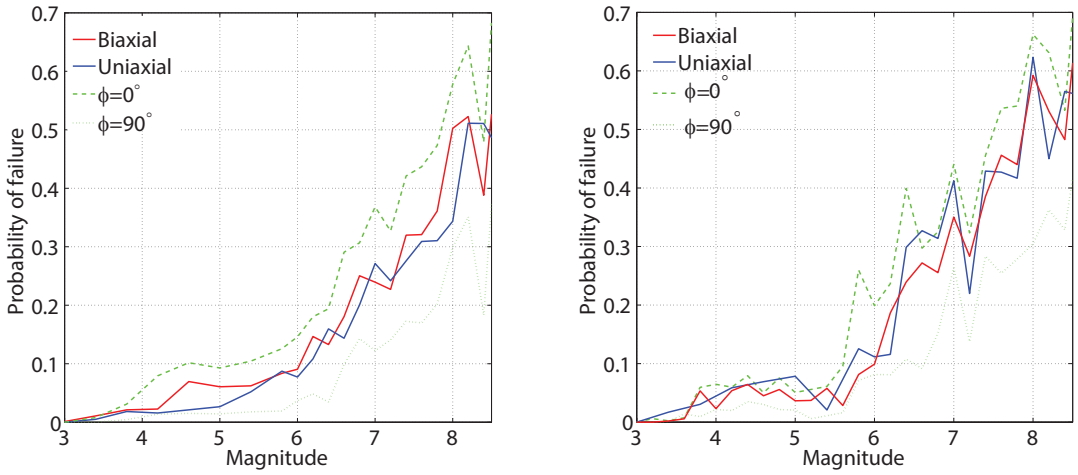

(a) (b)

Figure 8.12 – Comparison between the convergence of uniaxial and biaxial method with the biaxial method for angles $\phi_b = 0°$ and $\phi_b = 90°$ a) $\alpha = 0.25$, $p = 3.14$, $R_{rup} = 10$ Km and $V_s = 600$ m/s and b) $\alpha = 0.19$, $p = 8.96$, $R_{rup} = 20$ Km and $V_s = 650$ m/s.

Figure 8.12(b) illustrates the probability of failure curves for another body with dimensions $h = 0.8064$ m, $b = 0.1551$ m, $\alpha = 0.19$ and $p = 8.96$. The intensity measure chosen is M and $R_{rup} = 15$ Km and $V_s = 650$ m/s. Both uniaxial and biaxial curves are presented as well as the curves for $\phi_b = 0°$ and $\phi_b = 90°$. Contrasting with Figure 8.12(a), where convergence is achieved with 6000 and 4000 earthquakes for uniaxial and biaxial inputs, respectively, for Figure 8.12(b) convergence is achieved with 8000 earthquakes and 5000 earthquakes for the uniaxial and biaxial case, respectively. Therefore, convergence depends on the properties of the body and the seismological properties chosen (M, R_{rup} and V_s). Comparing Figures 8.12(a) and 8.12(b), it is observed that, qualitatively, the results for both bodies have similar trends: both probability of failures increase with a non-monotonic trend. Also, both bodies uniaxial and biaxial inputs give similar results with an absolute mean error of 6.17%. In Figure 8.12(b) the uniaxial curve is in general enveloped from the estimates of the biaxial

method for angles $\phi_b = 0°$ and $\phi_b = 90°$, except for $M < 5$. This can be explained as the list of earthquakes that were used to calibrate both models does not contain earthquakes with $M < 6$.

It is observed from Figures 8.12(a) and 8.12(b) that for both bodies examined, uniaxial and biaxial probability of failure curves are close to each other. These methods appear to be in agreement in terms of the probability of failure of rocking bodies, even though they were not forced to do so by construction: while in both the coefficients of the uniaxial and biaxial models are derived from the same list of earthquakes, the regression analyses are independent. The two models try to capture the same underlying stochastic process; hence, if the models perfectly captured this process, the coefficients would be equivalent and the results would be identical. The fact that probability of failure curves appear to be reasonably close, for a problem as sensitive to details as the toppling of a rocking body, illustrates that the two models are consistent and appear to practically capture the same physical process. This permits having a greater confidence in the results obtained with either of the methods.

In order to compare the probability of failure curves using the KT-CP and the GV procedure with RK-N, the magnitude of the seismic event is changed to PGA. For this aim, the PGA for each of the earthquakes generated per magnitude is calculated. After that, the mean PGA per magnitude is obtained. Figure 8.13 illustrates the probability of failure curve versus the PGA for the KT-CP, the GV procedure and RK-N for $\lambda = 0$. The differences between the models are clearly seen. As previously explained, GV produces larger probabilities of failure for smaller PGA than KT-CP. Comparing K-T versus RK-N, it was observed that for PGA between 0 and 3, RK-N estimates more failure than K-T, i.e., for $a_g = 2$ m/s^2, RK-N has a probability of failure of 0.27 and KT-CP of zero. In contrast, for values of $a_g > 3$ m/s^2 the KT-CP has larger probabilities of failure than RK-N, i.e., for $a_g = 6$ m/s^2, RK-N has a probability of failure of 0.5 and KT-CP of 0.96. In general, in Figure 8.13 it is observed that, contrasting with Figure 8.12(a), the curves of the three models are not close between them.

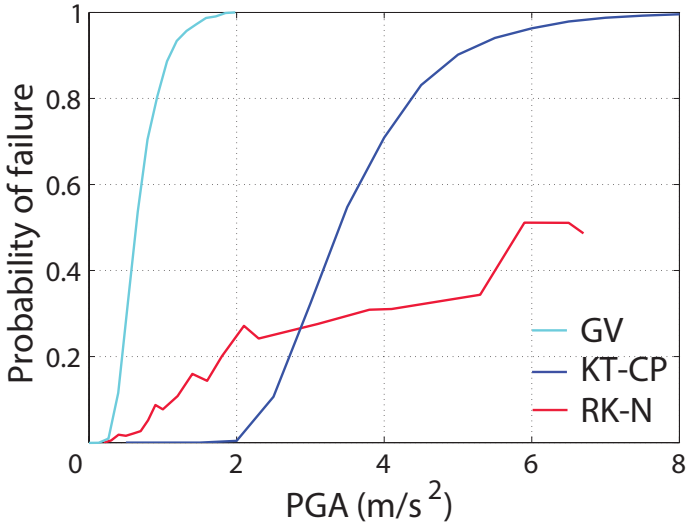

Figure 8.13 – Probability of failure curve versus the PGA for KT-CP, GV and RK-N for $\lambda = 0$.

Probability of failure using the KL-T.

In this Section, uniaxial and biaxial inputs are generated using the KL expansion and selected with the threshold sampling method explained in Section 7.4. To start, an ensemble of one hundred thousand uniaxial earthquakes was generated using the KL expansion. To calculate probability of failure curves, the threshold sampling criteria are applied.

The construction of a pertinent threshold filter is crucial for the generation of probability of failure curves. Thus, there is a need to choose a meaningful scale constant D for equation (7.12). An irrelevant value of D can lead to inaccuracies, i.e., if the $D\sigma$ is too large, that could potentially end in not selecting realistic earthquakes for each target, as most targets would end using the same time histories. Besides, if $D\sigma$ is small, most of the earthquakes would be rejected; hence, there is not enough earthquakes for the generation of the probability of failure curves.

In attempting to understand the behaviour of this distance to the target, Figure 8.14(a) varies D. For larger distances i.e., 3σ, 2σ, σ, most of the samples have been accepted producing that each target has the same probability of failure as the others. In contrast,

when the distance is decreasing, the probability of failure potentially becomes more realistic, as only the earthquakes close to each target are taking into consideration. Nonetheless, when the distance is decreased until i.e., 0.1, there are not enough earthquakes for each target as only few or none are accepted. Therefore, more initial samples need to be generated, and this could become computationally expensive.

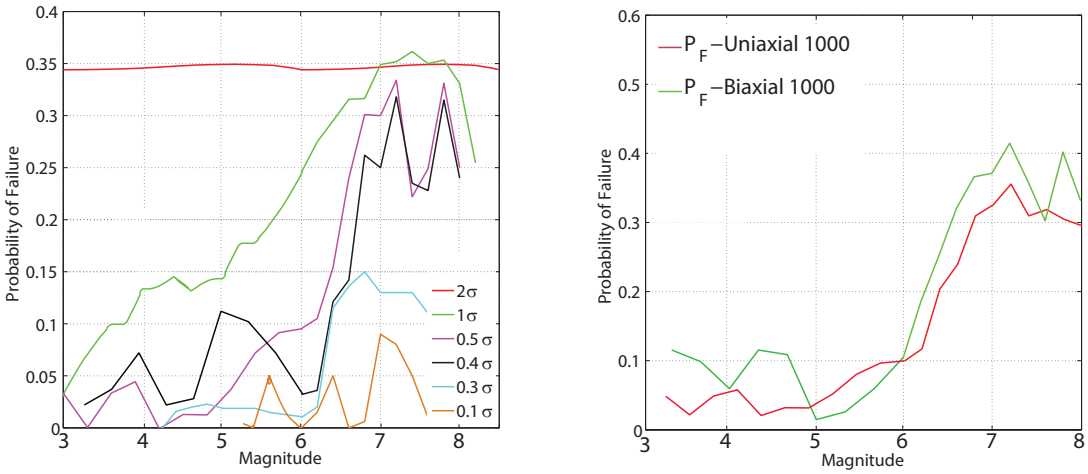

(a) (b)

Figure 8.14 – a) Probability of failure curve using different rejection rules. b) Probability of failure curves for 1000 one and two dimensional selected earthquakes for each M, $D = 0.4$. It is assumed that $\lambda = 0$, $R_{rup} = 10$Km and $V_s = 600$m/s.

Table 8.2 illustrates the samples accepted for each threshold distance for $\tilde{\mathbb{M}} = [6, 10, 600]$. Comparing the amount of earthquakes accepted, one could conclude that, as mentioned above, the threshold method does depend on the specific distance. Decreasing D turns out to not only reduce the error but also the samples accepted, whereas increasing D rises the error and most of the samples are accepted.

Since the number of samples for each magnitude have a wide range using the threshold sampling method, a number of accepted earthquakes is set to 1000 time histories for each target. Figure 8.14(b) illustrates the probability of failure curve while the rocking body is

Table 8.2 – Threshold method - D. $\tilde{\mathbb{M}} = [6, 10, 600]$.

D	$3\ \sigma$	$2\ \sigma$	σ	$0.5\ \sigma$	$0.4\ \sigma$	$0.3\ \sigma$	$0.1\ \sigma$
Samples Accepted	98,955	95,551	35,448	1,277	666	277	13

subjected to uniaxial and biaxial ground motions. Similar to Figure 8.12(a), a similar trend can be appreciated between the inputs using KL-T. In most cases, the biaxial curve envelopes the uniaxial one. An exception is observed at $M = 7.6$.

Results from Figure 8.14(a) using the threshold sampling method indicate that the methodology is extremely sensitive to the selection of D. A bad estimation of this parameter can lead to a poor representation of the overall probability of the failure curve. Although precision can be achieved only using small values of D, there may be practical constraints in terms of the availability and computational time. However, it seems that uniaxial and biaxial inputs have a good agreement while using the model to produce the curves.

Probability of failure using KL-EN Case I and KL-EN Case II.

In this Section, uniaxial and biaxial inputs are generated using the KL expansion and selected with the envelope sampling method from Section 7.3.2.

Figure 8.15 illustrates probability of failure curves using uniaxial inputs for both KL-ER Case I and Case II. For the case examined in Figure 8.15, it should be noted that the generation of approximately 8000 earthquakes per magnitude are required to estimate all probabilities with an accuracy of 2%. It is observed that both models have a similar probability of failure curve (absolute mean error of 3.46%) even if KL-ER Case I does not preserve the frequency components.

Figures 8.16(a) and 8.16(b) show the probability of failure curves for different values of the initial twist ϕ_b using KL-ER Case I and KL-ER Case II, respectively. As in Figure 8.12(a), as ϕ_b is increased, the probability of failure practically decreases for any value of M.

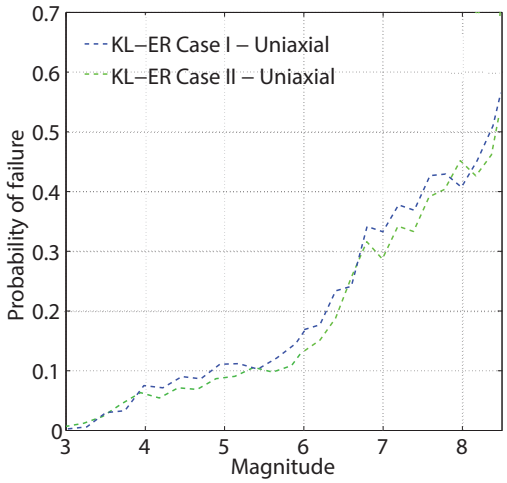

Figure 8.15 – Probability of failure curves using the uniaxial method for different number of earthquakes using KL-ER Case I and KL-ER Case II. $R_{rup} = 10$ Km and $V_s = 600$ m/s.

Probability of failure curves are plotted varying the number of pairs of earthquakes used in Figure 8.17. Convergence is achieved with 6000 and 7000 earthquakes for KL-EN Case II and Case I, respectively. Observe that the fact of introducing more model parameters while selecting earthquakes does not present significant differences on the curves. The probability of failure curve for uniaxial components is also presented in Figure 8.17. It is observed that both, KL-ER Case I and KL-ER Case II, appear to have a good agreement between them for all M and between uniaxial and biaxial inputs as presented in Table 8.3.

Table 8.3 – Absolute mean error KL-ER Case I and Case II. Uni refers to uniaxial and Bi to biaxial.

	Case I Uni. - Case II Uni.	Case I Bi. - Case II Bi.	Case I Uni. - Case I Bi.	Case II Uni. - Case II Bi.
Error (%)	3.46	7.59	8.67	8.23

The previous figures in this Section make the assumption that $\lambda = 0$. Figure 8.18 presents the variability of λ when the earthquakes are generated using the KL-ER Case I and Case II.

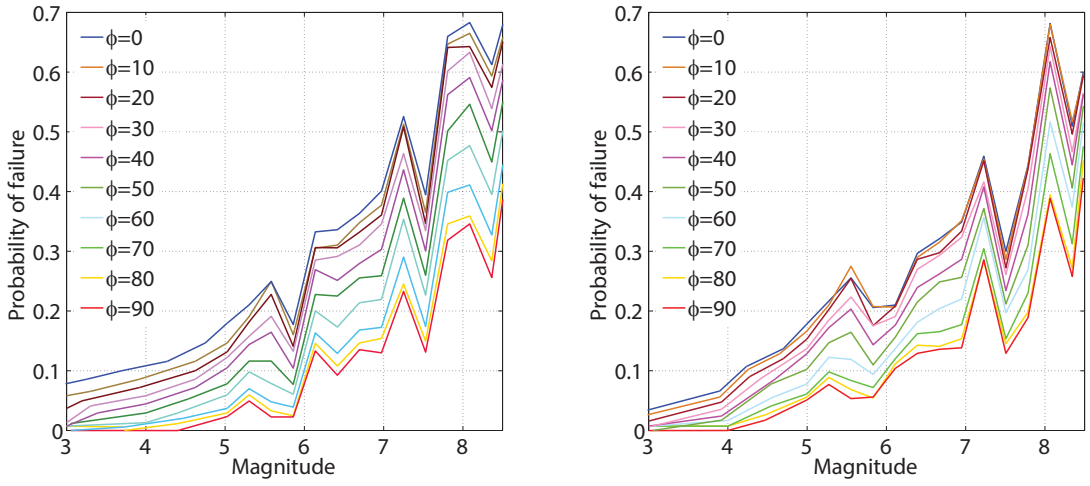

(a) (b)

Figure 8.16 – Probability of failure curves comparing a) Case I and b) Case II for the biaxial method for different values of ϕ_b. $R_{rup} = 10$ Km and $V_s = 600$ m/s.

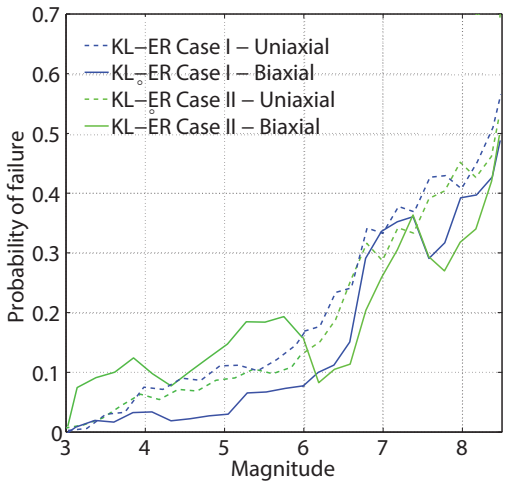

Figure 8.17 – Probability of failure curves comparing uniaxial and biaxial case using the KL-ER Case I and KL-ER Case II.

Similar to previous results, it is observed that as the value of λ increases, the probability of failure rises. The average uncertainty between $\lambda = 0$ and $\lambda = 1$ is calculated and presented in Table 8.4.

It is important to comment in this Section that, while there is an uncertainty related to the earthquake generation process between KL-ER Case I and Case II, the uncertainty of the

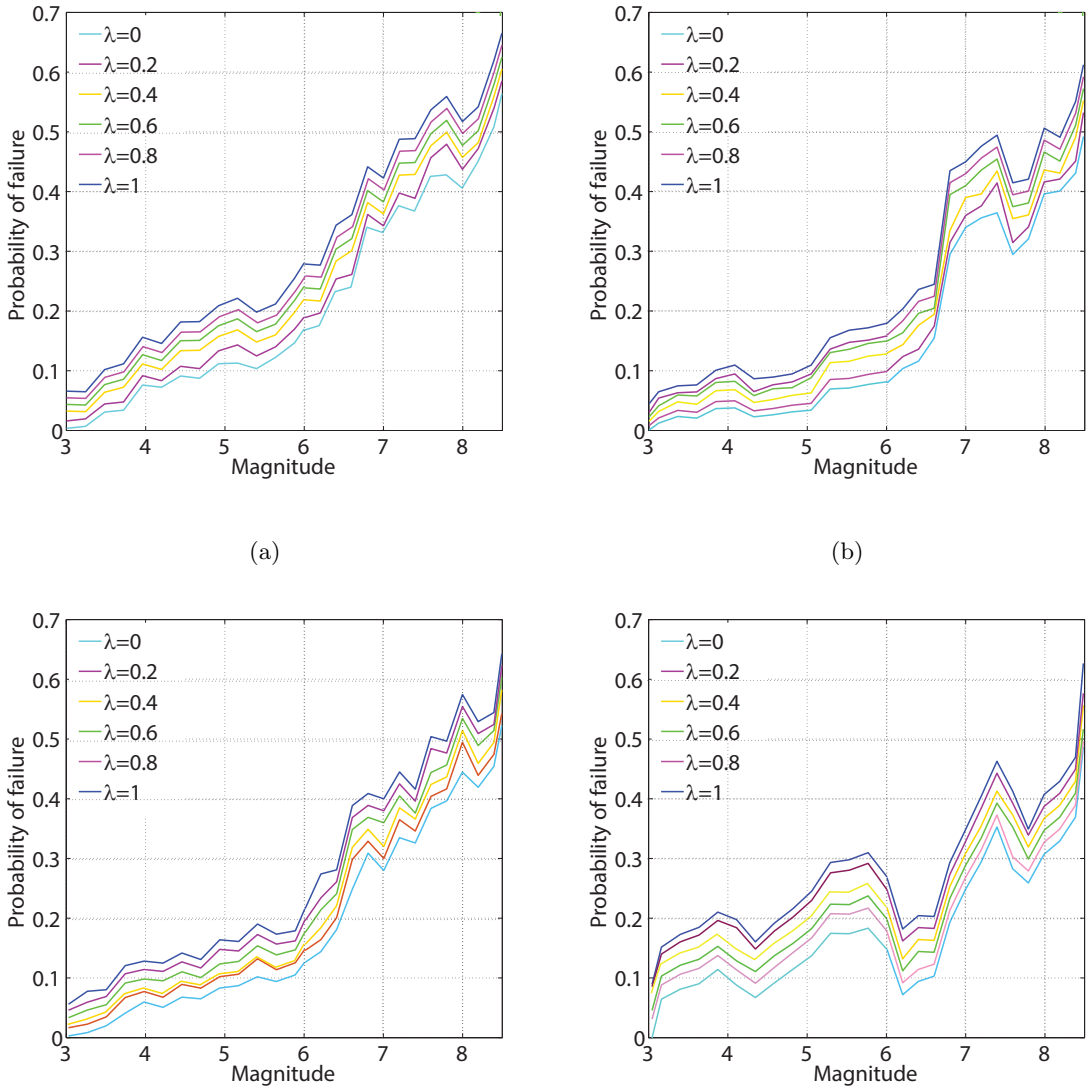

Figure 8.18 – Probability of failure curves for the specified body when the value of λ is varied for KL-ER Case I a) uniaxial and b) biaxial case and KL-ER Case II c) uniaxial and d) biaxial 4000 earthquakes, respectively. It is assumed that $R_{rup} = 10$ Km and $V_s = 600$ m/s.

IPM model related to λ has a larger variability as it was observed in Table 8.4. Therefore, even if the input earthquake models presented in 7.3.2 are not perfect, the uncertainty of λ should be a priority while working in the rocking body problem.

Table 8.4 – Uncertainty of λ KL-ER Case I and Case II and RK-N. Uni refers to uniaxial and Bi to biaxial.

	Case I Uni.	Case II Uni.	Case I Bi.	Case II Bi.	RK-N Uni.	RK-N Bi.
Error (%)	10.52	11.07	10.03	10.86	8.03	8.77

Comparison between KL-ER Case I and Case II and RK-N

A comparison between probability of failure curves varying M using RK-N, KL-ER Case I and KL-ER Case II is illustrated in Figure 8.19. In Figure 8.19(a) for uniaxial records, it is observed that KL-ER Case I and KL-ER Case II are more prone to failure than RK-N for M between 3 and 8. For $M > 8$, the maximum probability of failure fluctuates between the three models. These fluctuations are probably related to the fact that a few earthquakes with $M > 8$ are used as inputs to the models. The absolute mean error between the models are presented in Table 8.5.

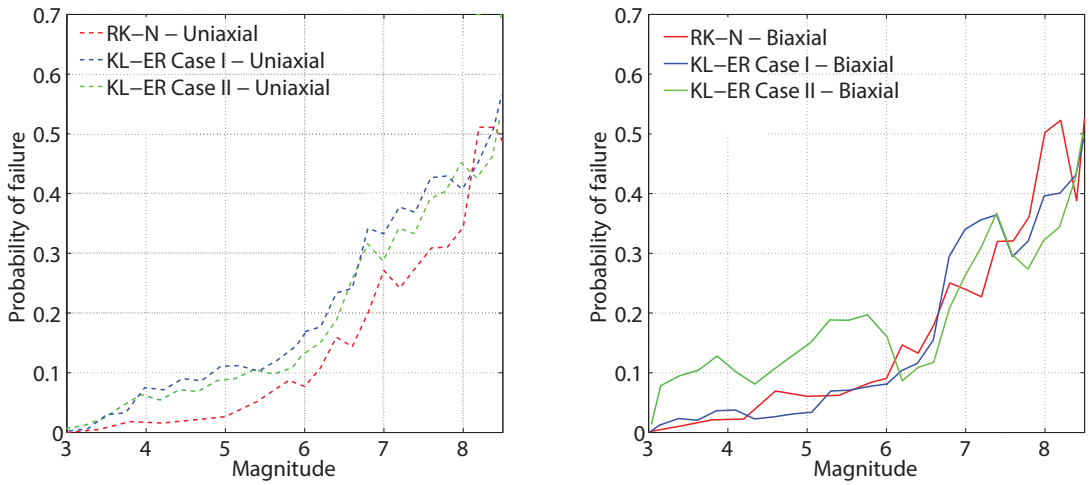

(a) (b)

Figure 8.19 – Probability of failure curves comparing a) uniaxial and b) biaxial cases using RK, KL-ER Case II and KL-ER Case I. $R_{rup} = 10$ Km and $V_s = 600$ m/s.

In contrast, for the biaxial case in Figure 8.19(b), there is no systematic trend that

produced more failure. It is observed that KL-ER Case II is substantially more prone to failure for $M < 6$ than KL-ER Case I and RK-N. This latter comment should not be taken as a conclusion due to the lack of earthquakes of $M < 5$ on the database. For values of M between 6.2 to 8, the three models seems to have a similar trend. This is an excellent result because the database is mainly composed with earthquakes with M between 6-8. The absolute mean errors between the models are presented in Table 8.5. Comparing uniaxial and biaxial curves of the three methods, biaxial curves seem, in general, more consistent than uniaxial models for $M > 6$.

Table 8.5 – Absolute mean error KL-ER Case I and Case II and RK-N. Uni refers to uniaxial and Bi to biaxial.

	Case I Uni. - RK-N Uni.	Case I Bi. - RK-N Bi.	Case II Uni. - RK-N Uni.	Case II Bi. - RK-N Bi.
Error (%)	6.29	4.56	5.54	8.73

Figure 8.20 illustrates the probability of failure curves for another body with dimensions $h = 0.8064$ m, $b = 0.1551$ m, $\alpha = 0.19$ and $p = 8.96$. The intensity measure M is varied and $R_{rup} = 15$ Km and $V_s = 650$ m/s. For this example, KL-ER Case I is avoided because RK-N and KL-ER Case II are more general cases. Both uniaxial and biaxial curves are presented for both RK-N and KL-ER Case II. Similar to the previous body, KL-ER Case II generally appears to produce more failure in comparison with RK-N for uniaxial and biaxial components. However, it appears that both models are in a better agreement for the biaxial case as the curves are closer to each other for magnitudes between $[6 - 8]$.

In this Section, probability of failure curves of KL-EN Case I and Case II and RK-N have been presented. The absolute errors presented in Table 8.5 are acceptable. Therefore, it appears that the differences noted in the previous Chapter seem to be less important

for the probabilities of failure. Due to this last observation, if an engineer wants to generate probability of failure curves with one of these presented methods, it would be better to choose RK-N; as both, KL-EN Case I and Case II, are computationally expensive.

Another important feature observed in this Chapter is the uncertainty of λ. This uncertainty between $\lambda = 0$ and $\lambda = 1$ was presented in Table 8.4. Comparing that Table with Table 8.5, it can be observed that the uncertainty of λ is greater than the input uncertainty.

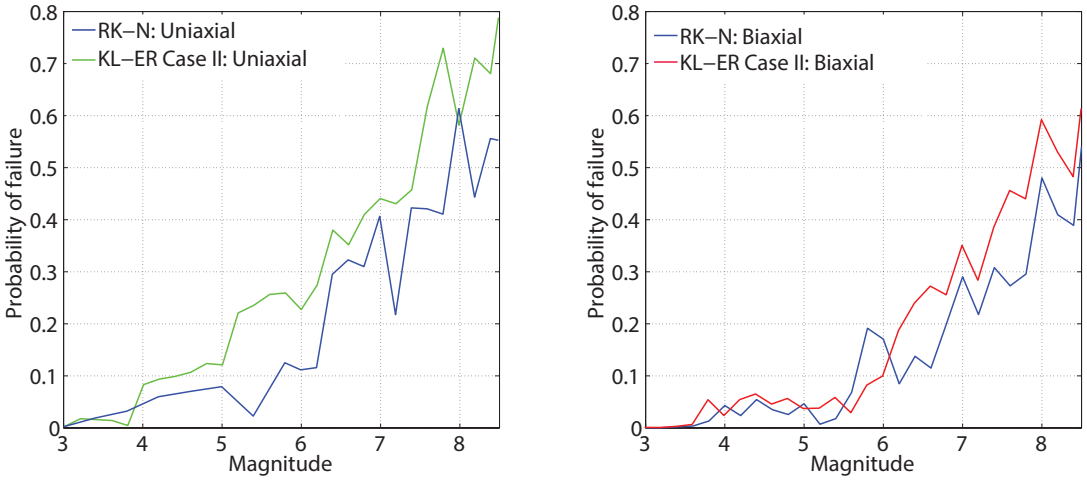

(a) (b)

Figure 8.20 – Probability of failure curves comparing a) uniaxial and b) biaxial case using the KL-ER Case II and RK-N methods for a body defined $h = 0.8064$ m, $b = 0.1551$ m and $R_{rup} = 15$ Km and $V_s = 650$ m/s.

Predicting the lifespan

The previous Section generates probability of failure curves for varying M, R_{rup} or V_s. However, as discussed earlier, it is often interesting to present this probability of failure for a rocking body versus a time period of interest. This Section studies the generation of probability of failure curves for a time period of interest in a region with defined seismological properties, as defined through the Gutenberg Richter parameters α_g and β_g [126].

To use the results in Section 8.4.2, lets substitute in equation (8.11) $\mathbb{A}$ for the realization

vector $\mathbb{M}$:

$$P_S(E_l) = \int_{\mathbb{M}_1}^{\mathbb{M}_{end}} P_S(\mathbb{M} = \mathbb{M}_n)\phi(\mathbb{M})d\mathbb{M} = \int_{M_l}^{M_u}\int_{R_{rup_l}}^{R_{rup_u}}\int_{V_{s_l}}^{V_{s_u}} P_S(M, R_{rup}, V_s)\phi(M)\phi(R_{rup})\phi(V_s)dMdR_{rup}dV_s \tag{8.19}$$

where l and u are, respectively, the lower and upper bounds of each variable. To reduce complexity, R_{rup} and V_s are assumed to be deterministically known.

Consider first the previously examined body with $b = 0.3975$ m and $h = 1.5565$ m to be located near the San Fernando fault in Southern California with $R_{rup} = 10$ Km and $V_s = 600$ m/s. The original values of α_g and β_g used are 1.93 and 0.3 respectively as defined in [127]. Figure 8.21 represents how the probability of failure $P_F(t = T)$ changes within 20 years. Uniaxial and biaxial inputs are investigated for RK-N and KL-ER Case II. In Figure 8.21 differences between the prediction using the uniaxial and biaxial inputs are almost negligible due to their similarities in the corresponding curves presented in Figure 8.19.

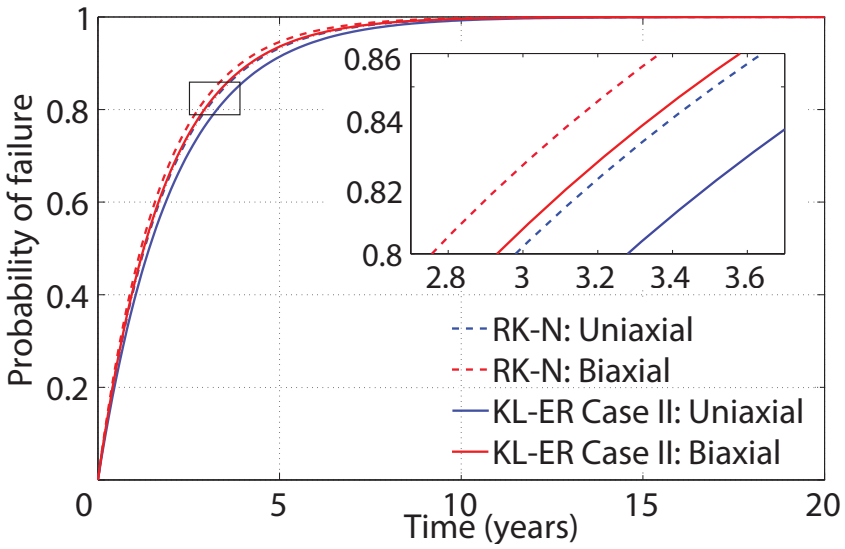

Figure 8.21 – Lifespan of the rocking body using uniaxial and biaxial generated earthquakes, $\alpha_g = 1.93$ and $\beta_g = 0.3$.

To directly compare with design codes, the lifespan of the body for $T = 20$ years is calculated using equation (8.14). As explained, the CDF for lifespan for both cases using

uniaxial and biaxial inputs results in Figure 8.21.

Next, a case is considered where α_g and β_g are not defined directly from seismological measurements, but through the use of known design codes values of PGA, PGV and PGD. To define α_g and β_g in this case, the methodology in Section 8.3.4 is applied. The values of the PGA, PGV and PGD for a ground type A are taken from [126] being 85.395 cm/s^2, 8.243 cm/s and 21.361 cm, respectively, with $T_{p,i} = 200$ years. These values together with the parameters b_{i1}, b_{i2} and b_{i3} defined in [129] as $[2000, 0.8, 2]$, $[16, 1.0, 1.7]$ and $[7, 1.2, 1.6]$ for the acceleration, velocity and displacement, respectively, are introduced in equation (8.16). Numerically, solving the systems of equations results in the following values of α_g, β_g and L_M: 5.51, 0.644 and 44.532 Km, respectively. It should be reminded that the value of L_M is not used in the generation of earthquakes or for the seismic risk analysis proposed in this work.

Similar to what was shown in Figure 8.21, the lifespan of the body for a period of 20 years is calculated using the new seismological parameters $\alpha_g = 5.51$ and $\beta_g = 0.644$ in Figure 8.22. Comparing the lifespan of the rocking body for different values of α_g and β_g (Figures 8.21 and 8.22), it is observed that, for the case presented in this Section, high values of α_g and β_g increase the probability of failure.

In this Section, probability of failure curves for a given lifespan are presented. It is then of interest to compare these results with design codes. Considering the framework of Eurocode 8 [54], the recommended probability of exceedance for a reference seismic action for ordinary structures is 22% for 50 years with an average return period of 200 years. In a simplified assumption, it can be considered that if this probability is exceeded, the structure is expected to fail. Therefore, it can be compared against the probability of failure from Figure 8.22. In this Figure, the probability of failure for the specific body is close to 100% in 10 years whereas the recommended value from Eurocode is 22% in 50 years. Thus, this structure does not pass the specifications of Eurocode 8. This discussion holds for any curve in Figure 8.22

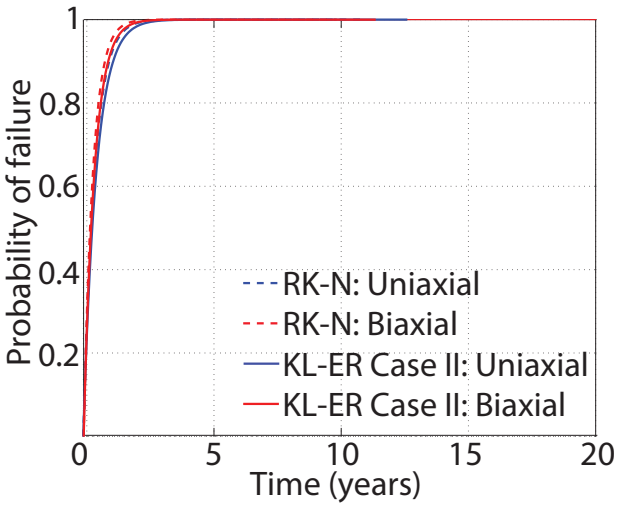

Figure 8.22 – Lifespan of the rocking body using uniaxial and biaxial generated earthquakes. $\alpha_g = 5.51$ and $\beta_g = 0.644$.

as the probability of failure for a given lifespan is extremely similar for uniaxial and biaxial inputs of both models.

Finally, the above discussion assumes that the location of the vertical impulse is located at $\lambda = 0$. However, it was previously mentioned that there is a related uncertainty about λ. Figure 8.23 represents the probability of failure versus T for different values of λ with $\alpha_g = 1.93$ and $\beta_g = 0.3$ for RK-N. As expected, as λ is increased the probability of failure rises. Observe that varying the location of the impact results in a larger increase of the probability of failure than the uniaxial versus biaxial inputs. Thus, the uncertainty in λ matters more than the input uncertainty of the two models.

8.5 Conclusions

The purpose of this Chapter was to present qualitative guideline methods for evaluating the seismic risk of rocking bodies at a particular site. This methodology represents an important step in creating the necessary basis for a risk seismic analysis in rocking bodies. In its current format, rocking bodies reliability profiles should be simulated and predicted based

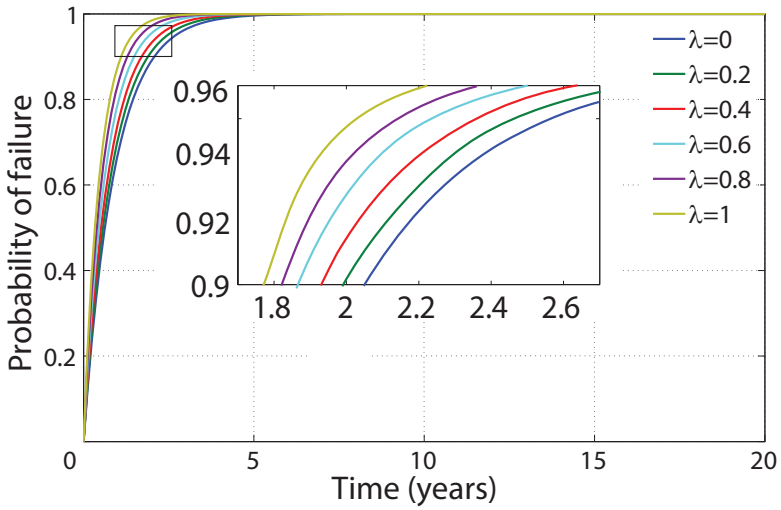

Figure 8.23 – Lifespan of the rocking body using uniaxial generated earthquakes for different values of λ, $\alpha_g = 1.93$ and $\beta_g = 0.3$.

on appropriate earthquake generation models necessary for the development of the approach. Four earthquake generation methods were used to produce probability of failure curves: the KT-CP joint with the Spectral representation method, GV procedure, RK-N and the KL expansion.

In terms of rocking, the uniaxial methods generate ground records that are not in general parallel to any of the principal axes. Taking into account the random twist of the rocking body with respect to the axes it can be assumed that the weak (planar rocking) axis of the body is aligned with this direction. In that sense, the methods attempt to depict both the underlying stochastic nature of the earthquakes and the uncertainty of the initial twist of the body by generating more samples. It is then seen that in order for the method to converge within a desired margin of tolerance, several time histories are required to be generated.

In contrast, the biaxial methods generate a pair of records along the principal axes. The uncertainty about the twist of the body with respect to those axes is treated independently by introducing the uniformly distributed twist ϕ_b. This approach allows for providing limit estimates of the probability of failure by using the extreme values of $\phi_b = 0°$ and $\phi_b = 90°$.

The separation of the sources of uncertainty further allows to achieve convergence of the probability of failure within a window of tolerance by using more values of ϕ_b while retaining or even reducing the necessary for convergence number of pairs of generated earthquakes.

In terms of the risk, a comparison between KT-CP and GV has shown that the GV approach overestimates the probability of failure curves for the same ground type. Thus, the trends are not close. Between KT-CP and RK-N an opposite behaviour is observed: for smaller values of the intensity measure, KT-CP underestimates failure over RK-N while for larger values this trend reverses. It should be noted that RK-N does not try to preserve the PGA. In general, the three models do not present any significant similitude between curves.

The probability of failure curves using RK-N, KL-T and KL-Case I and II have also been presented. While the threshold sampler model highly depends on the parameter D, the envelope procedure has illustrated a good match with RK-N curves. It was shown that similar to what has been noticed for cycloidal pulses [26, 57], the probability of failure does not monotonically increase as an intensity measure, such as M increases. A comparison between uniaxial probability of failure curves illustrated that KL-ER Case I and Case II produce more failure than RK-N although the errors were minimal. Biaxial curves have a similar behaviour between the models studied, although without any systematic trend.

The framework is later extended to calculate the probability of failure of a rocking body versus a time period of interest in an area with defined seismological properties. This probability was also connected to the distribution of the lifespan of a rocking body. For this purpose the Gutenberg Richter model [109] is used, with parameters α_g and β_g, together with the Poison model for earthquake arrivals. This methodology requires knowledge of α_g and β_g; which can be known from seismological data. In lack of such data, or in cases where results have to be compared versus Design Codes, a method was presented to define the PGA, PGV and PGD often available in the regulations.

The methodologies RK-N and KL-ER Case I and II were shown to have appealing features

for calculating the probability of failure of rocking bodies. Unlike previous methods, they do not aim at being conservative and hence, overestimate such probabilities, but attempt to quantify them given the seismological properties of a region. The fact that the three models have produced similar probability of failure curves is of extreme importance for the rocking community. The model in [44] is a great approach for the generation of earthquakes even if spectral and temporal characteristics depend on models. While the KL-ER Case II approach does not use any predefined model and seems to be in agreement with the RK-N, its computational cost is significantly higher. Therefore, if the conclusions drawn in this work still hold for different R_{rup}, V_s and different bodies; it is suggested that, nowadays, for the rocking problem, the model from [44] is the most suitable one for calculating the risk.

Chapter 9

Conclusions and future work

9.1 A summary of the conclusions

The objective of this dissertation was to develop a methodology that allows to calculate realistic probability of failure curves for rocking bodies. To do so, initially the deterministic models used were re-examined. The assumption involved in modelling the loss of energy during impact in the IPM was investigated. It was shown that the location of the vertical impulse during impact could be applied at any point between the post-impact rocking corner of the body and the midpoint of the base, without violating any of the assumptions of the model. It was illustrated that the assumed value of λ significantly affects the stability of rocking bodies and that the, common in the literature, assumption of $\lambda = 0$ is the least conservative assumption compatible with the assumptions of the IPM as shown in Chapters 2 and 4. This location is affected, among other things, for the base geometries as discussed in Chapter 3. Experimental results on the shake table for two almost identical bodies apart from their base geometries verified that, indeed this location varies between the bodies: a body with feet on the edges closely models the IPM [1]; hence, the location of the vertical impulse is really close to the future rocking corner. In contrast, this location moves for bodies with a flat base.

A practical application derives for Chapter 5. It was observed that the differences shown between the waveform of the instruments highly affected the response of the artifacts. In terms of different instruments notes, it was concluded that the nowadays common technique of creating artificial music with synthesisers has proved to be the least safe one in terms of the stability of the artifact.

Chapters 6, 7 and 8 were dedicated to estimate the risk of rocking bodies. A summary of the existing methodologies to select or generate earthquakes was presented in Chapter 6. It was discussed that the KL-CP with the SPM is very easy to use but often hard to associate to physical or design quantities. This problem can be alleviated with GV approach however, rocking bodies do not have a resonance period. In terms of seismological data, RK-N is a great tool to generate artificial time histories. Nonetheless, the model assumes modulation functions to address spectral and temporal characteristics of the excitation: the frequency content of synthetic earthquakes is assumed to decrease over time and generated time histories only have one peak. These were alleviated with the KL expansion which does not use any predefined model and preserves the statistical properties of the input. Thus, the frequency is generated with these preserved properties and earthquakes can have multiple peaks.

In Chapter 7, a novel technique of estimating the values of M, R_{rup} and V_s from the accelerograms was presented. Two techniques were developed to generate probability of failure curves versus an intensity measure using the KL expansion: KL-T and KL-EN Case I and Case II. Both techniques allow to generate earthquakes for a target $\tilde{\mathbb{M}}$. It was observed that KL-T has a large relative error which depends on the distance selected. Hence, this model was not considered suitable for the selection of earthquakes. In contrast KL-EN Case I and Case II have shown to select earthquakes with distributions extremely close to the target one.

In Chapter 8, a framework to calculate probability of failure curves for an intensity mea-

sure was developed. It was observed that the GV overestimates the probability of failure while comparing with KT-CP and RK-N. A comparison between uniaxial and biaxial probability of failure curves using RK-N showed that uniaxial and biaxial curves were similar. Therefore, both independent models accurately obtain the same components of the physical process.

A comparison between uniaxial and biaxial inputs for RK-N and KL-EN Case II concluded that the curves have similar behaviour. Therefore, the differences between temporal and spectral characteristics might matter up to a point. This conclusion is of significant importance for the rocking community, due to the lack of a suitable earthquake generation model. However, it should be further commented that while the KL-ER Case II model does not use any predefined model, its computational cost is significantly higher than RK-N (note that the computational cost of the RK-N is also expensive). Therefore, if for different bodies the conclusions drawn in this work still hold, it is suggested that, nowadays, for the rocking problem, the model from [44] is the most suitable one to calculate the risk.

The above discussion was studied for different values of λ. It was observed that varying the location of the impact, the probability of failure increases more than the uncertainty produces between uniaxial and biaxial inputs. Thus, the uncertainty of λ seems to matter more than the input uncertainty.

9.2 Future work

In terms of rocking models, one would explore a way of relaxing the rigidity assumptions for the body and base. This direction would require the combination of discrete and finite element methods as described in [130].

The calculation of probability of failure curves using other models should also be explored. A recent investigation of site based model [47] has related the KT-CP with site and earthquake characteristics. Thus, it might be possible that this model and RK-N produce similar trends.

However, it is expected that this model would also be computational expensive hence, there is a need to reduce this computational cost.

As pointed in section 6.5, the generation of earthquakes with the KL expansion is controlled by the parameter ξ_e of the KL expansion. Thus, knowing the conditional probability of each mode, one could generate earthquakes for different values of $\mathbb{M}$ as in the work of [44, 56]. This problem might be solved with models which allow finding the probability distribution based on non-sampling methods or interpolation as the Polynomial Chaos expansion [131] or Kriging [132], respectively. An improvement of the KL expansion with rejection models presented in this thesis can be done using the work in [133]. In this work, the KL expansion is used to construct a Polynomial Chaos representation by matching a target joint probability density function based on a sequence of conditional probability relations. Therefore, using as an input the recorded earthquakes, the conditional probability of ξ_e could be defined. That would reduce the computational cost.

Another important direction towards future work is to extend the methodology to create probability of failure curves for a lifespan to bodies that accumulate damage. Hence, one would be able to investigate whether rocking can be used as a design principle (or not).

Appendices

Appendix I: Momentum equations

Pattern 1

From pattern 1a to 2b,

$$A_1 = I_{O_1} - (2-\lambda_1)m_1{b_1}^2 + m_2 l R_2 \cos(\theta_2+\beta-\alpha_2) + 2m_2 l h_1 \cos\beta - \big((1-\lambda_1)b_1+b_2\big)m_2 l \sin\beta \qquad A_2 = m_2 l R_2 \cos(\theta_2+\beta-\alpha_2)$$

$$B_1 = I_{O_2} + 2m_2 R_2 h_1 \cos(\alpha_2-\theta_2) - \big((1-\lambda_1)b_1+b_2\big)m_2 R_2 \sin(\alpha_2-\theta_2) \qquad B_2 = I_{O_2}$$

$$C_1 = I_{O_1} - \lambda_1 m_1{b_1}^2 + m_2 l' R_2 \cos(\theta_2-\beta'-\alpha_2) + 2m_2 l' h_1 \cos\beta' + \big((1-\lambda_1)b_1+b_2\big)m_2 l' \sin\beta' \qquad C_2 = m_2 l' R_2 \cos(\theta_2-\beta'-\alpha_2)$$

$$D_1 = I_{O_2} + 2m_2 R_2 h_1 \cos(\alpha_2-\theta_2) - \big((1-\lambda_1)b_1+b_2\big)m_2 R_2 \sin(\alpha_2-\theta_2) \qquad D_2 = I_{O_2}$$

From 1a to 4a: $\dot{\theta}_1^+ = 0$, hence,

$$\begin{aligned} \dot{\theta}_2^+ &= \frac{A_2}{D_2}\,\dot{\theta}_1^- + \dot{\theta}_2^- \\ \lambda_1 &= \frac{A_3\dot{\theta}_1^- + B_3\dot{\theta}_2^- + C_3\dot{\theta}_2^+}{D_3\dot{\theta}_1^- + E_3\dot{\theta}_2^- + F_3\dot{\theta}_2^+} \end{aligned} \tag{1}$$

where,

$$A_3 = -(I_{O1} - 2m_1 b_1^2 + m_2 l R_2 \cos(\theta_2+\beta-\alpha_2) + 2m_2 l h_1 \cos\beta - (b_1+b_2)m_2 l \sin\beta)$$

$$B_3 = -(I_{O2} + 2m_2 R_2 H_1 cos(\alpha_2-\theta_2) - (b_1+b_2)m_2 R_2 \sin(\alpha_2-\theta_2))$$

$$C_3 = I_{O2} + 2m_2 R_2 h_1 \cos(\alpha_2-\theta_2) - (b_1+b_2)m_2 R_2 \sin(\alpha_2-\theta_2)$$

$$D_3 = m_1 b_1^2 + b_1 m_2 l \sin\beta$$

$$E_3 = b_1 m_2 R_2 \sin(\alpha_2-\theta_2)$$

$$F_3 = -(b_1 m_2 R_2 \sin(\alpha_2-\theta_2)$$

By symmetry this analysis holds for the transition from pattern 1b to 2a and 4b, though it should be noted that the sign of θ_2 must change.

From pattern 1a to 2a,

$$A_1 = I_{O_1} + m_2 l^2 + m_2 l R_2 \cos(\alpha_2 - \beta) \qquad A_2 = m_2 l R_2 \cos(\alpha_2 + \beta) + \lambda_2 m_2 l b_2 \sin\beta$$

$$B_1 = I_{O_2} + m_2 l R_2 \cos(\alpha_2 - \beta) \qquad B_2 = I_{G_2} + m_2 {R_2}^2 \cos(2\alpha_2) + \lambda_2 m_2 R_2 b_2 \sin\alpha_2$$

$$C_1 = I_{O_1} + m_2 {l'}^2 + m_2 l' R_2 \cos(\alpha_2 + \beta') \qquad C_2 = m_2 l' R_2 \cos(\alpha_2 + \beta') + \lambda_2 m_2 l' b_2 \sin\beta'$$

$$D_1 = I_{O_2} + m_2 l' R_2 \cos(\alpha_2 + \beta') \qquad D_2 = I_{O_2} - \lambda_2 m_2 R_2 b_2 \sin\alpha_2$$

From 1a to 3a: $\dot{\theta}_2^+ = \dot{\theta}_1^+$

$$\begin{aligned} \dot{\theta}_1^+ =& \frac{A_1}{C_1 + D_1}\ \dot{\theta}_1^- + \frac{B_1}{C_1 + D_1}\dot{\theta}_2^- \\ \lambda_2 =& \frac{A_3\dot{\theta}_1^- + B_3\dot{\theta}_2^- + C_3\dot{\theta}_1^+}{D_3\dot{\theta}_1^- + E_3\dot{\theta}_2^- + F_3\dot{\theta}_1^+} \end{aligned} \tag{2}$$

where,

$$A_3 = m_2 l R_2 \cos(\alpha_2 + \beta) \qquad B_3 = I_{G2} + m_2 R_2^2 \cos(2\alpha_2)$$

$$C_3 = -(m_2 l' R_2 \cos(\alpha_2 + \beta') + I_{O2}) \qquad D_3 = -(m_2 l b_2 \sin\beta)$$

$$E_3 = -(m_2 R_2 b_2 \sin\alpha_2) \qquad F_3 = m_2 l' b_2 \sin\beta' - m_2 R_2 b_2 \sin\alpha_2$$

By symmetry this analysis holds for the transition from pattern 1b to 2b or 3b.

Pattern 2

From pattern 2a to 1b,

$$A_1 = I_{O_1} - (2 - \lambda_1) m_1 {b_1}^2 + m_2 {l'}^2 + m_2 l' R_2 \cos(\theta_2 + \alpha_2 + \beta') - (2 - \lambda_1) m_2 l' b_1 \sin\beta' \qquad A_2 = m_2 l' R_2 \cos(\theta_2 + \alpha_2 + \beta')$$

$$B_1 = I_{O_2} + m_2 l' R_2 \cos(\theta_2 + \alpha_2 + \beta') + (2 - \lambda_1) m_2 R_2 b_1 \sin(\alpha_2 + \theta_2) \qquad B_2 = I_{O_2}$$

$$C_1 = I_{O_1} - \lambda_1 m_1 {b_1}^2 + m_2 l^2 + m_2 l R_2 \cos(\theta_2 + \alpha_2 - \beta) - \lambda_1 m_2 l b_1 \sin\beta \qquad C_2 = m_2 l R_2 \cos(\theta_2 + \alpha_2 - \beta')$$

$$D_1 = I_{O_2} + m_2 l R_2 \cos(\theta_2 + \alpha_2 - \beta) - \lambda_1 m_2 R_2 b_1 \sin(\alpha_2 + \theta_2) \qquad D_2 = I_{O_2}$$

From 2a to 4b: $\dot{\theta}_1^+ = 0$

$$\begin{aligned}\dot{\theta}_2^+ =& \frac{A_2}{D_2}\ \dot{\theta}_1^- + \dot{\theta}_2^- \\ \lambda_1 =& \frac{A_3\dot{\theta}_1^- + B_3\dot{\theta}_2^- + C_3\dot{\theta}_2^+}{D_3\dot{\theta}_1^- + E_3\dot{\theta}_2^- + F_3\dot{\theta}_2^+}\end{aligned} \tag{3}$$

where,

$$A_3 = I_{O1} - 2m_1b_1^2 + m_2l\prime^2 + m_2l'R_2\cos(\theta_2+\alpha_2+\beta') - 2m_2l\prime b_1\sin\beta'$$

$$B_3 = I_{O2} + m_2l'R_2\cos(\theta_2+\alpha_2+\beta') + 2m_2R_2b_1\sin(\alpha_2+\theta_2)$$

$$C_3 = -(I_{O2} + m_2lR_2\cos(\theta_2+\alpha_2-\beta))$$

$$D_3 = -(m_1b_1^2 + m_2l'b_1\sin\beta')$$

$$E_3 = m_2R_2b_1\sin(\alpha_2+\theta_2)$$

$$F_3 = -m_2R_2b_1\sin(\alpha_2+\theta_2)$$

By symmetry this analysis is valid for the transition from pattern 2b to 1a or 4a, though it should be noted that the sign of θ_2 must change.

From pattern 2a to 1a,

$$A_1 = I_{O_1} + m_2{l'}^2 + m_2l'R_2\cos(\alpha_2+\beta')$$

$$A_2 = m_2l'R_2\cos(\beta'-\alpha_2) - \lambda_2m_2l'b_2\sin\beta'$$

$$B_1 = I_{O_2} + m_2l'R_2\cos(\alpha_2+\beta')$$

$$B_2 = I_{G_2} + m_2{R_2}^2\cos(2\alpha_2) + \lambda_2m_2R_2b_2\sin\alpha_2$$

$$C_1 = I_{O_1} + m_2l^2 + m_2lR_2\cos(\alpha_2-\beta)$$

$$C_2 = m_2lR_2\cos(\alpha_2-\beta) - \lambda_2m_2lb_2\sin\beta$$

$$D_1 = I_{O_2} + m_2lR_2\cos(\alpha_2-\beta)$$

$$D_2 = I_{O_2} - \lambda_2m_2R_2b_2\sin\alpha_2$$

From 2a to 3a: $\dot{\theta}_2^+ = \dot{\theta}_1^+$

$$\begin{aligned}\dot{\theta}_1^+ =& \frac{A_1}{C_1+D_1}\ \dot{\theta}_1^- + \frac{B_1}{C_1+D_1}\dot{\theta}_2^- \\ \lambda_2 =& \frac{A_3\dot{\theta}_1^- + B_3\dot{\theta}_2^- + C_3\dot{\theta}_1^+}{D_3\dot{\theta}_1^- + E_3\dot{\theta}_2^- + F_3\dot{\theta}_1^+}\end{aligned} \tag{4}$$

where,

$$A_3 = m_2l'R_2\cos(\beta'-\alpha_2)$$

$$B_3 = IG2 + m_2R_2^2\cos(2\alpha_2)$$

$$C_3 = -(m_2lR_2\cos(\alpha_2-\beta) + I_{O2})$$

$$D_3 = m_2l'b_2\sin\beta'$$

$$E_3 = -m_2R_2b_2\sin(\alpha_2)$$

$$F_3 = -m_2lb_2\sin\beta - m_2R_2b_2\sin\alpha_2$$

By symmetry this analysis is valid for the transition of pattern 2b to 1b or 3b. Since the post impact angular velocities are independent of $\theta_1 = \theta_2$ the relationships are identical.

Pattern 3

By symmetry the analysis in section Special transition cases holds for the transitions from pattern 3b to 1a, 3a or 4a.

Pattern 4

From pattern 4a to 1b,

$$A_1 = 0 \qquad A_2 = 0$$

$$B_1 = I_{G_2} + m_2 R_2 (2h_1 + h_2)\cos\alpha_2 - (1-\lambda_1) m_2 R_2 b_1 \sin\alpha_2 \qquad B_2 = I_{O2} - (2-\lambda_2) m_2 {b_2}^2$$

$$C_1 = I_{O_1} - \lambda_1 m_1 {b_1}^2 + m_2 l (2h_1 + h_2)\cos\beta + (1-\lambda_1) m_2 l b_1 \sin\beta \qquad C_2 = m_2 l h_2 \cos\beta + (1-\lambda_2) m_2 l b_2 \sin\beta$$

$$D_1 = I_{G_2} + m_2 R_2 (2h_1 + h_2)\cos\alpha_2 + (1-\lambda_1) m_2 R_2 b_1 \sin\alpha_2 \qquad D_2 = I_{O_2} - \lambda_2 m_2 {b_2}^2$$

From pattern 4a to 4b: $\dot{\theta}_1^+ = 0$

$$\begin{aligned} \dot{\theta}_2^+ &= \frac{I_{O_2} - (2-\lambda_2) m_2 b_2^2}{I_{O_2} - \lambda_2 m_2 b_2^2} \dot{\theta}_2^- \\ \lambda_1 &= \frac{A_3 \dot{\theta}_2^- + B_3 \dot{\theta}_2^+}{C_3 \dot{\theta}_2^- + D_3 \dot{\theta}_2^+} \end{aligned} \tag{5}$$

where,

$$A_3 = -(I_{G2} + m_2 R_2 (2h_1 + h_2)\cos\alpha_2 - m_2 R_2 b_1 \sin\alpha_2) \qquad B_3 = I_{G2} + m_2 r_2 (2h_1 + h_2)\cos\alpha_2 + m_2 R_2 b_1 \sin\alpha_2$$

$$C_3 = m_2 R_2 b_1 \sin\alpha_2 \qquad D_3 = m_2 R_2 b_1 \sin\alpha_2$$

From pattern 4a to 3b, $\dot{\theta}_2^+ = \dot{\theta}_1^+$

$$\begin{aligned} \dot{\theta}_1^+ =& \frac{B_1}{I_O - \lambda_1 M {b_1}^2}\ \dot{\theta}_2^- \\ \lambda_2 =& \frac{A_3\dot{\theta}_1^+ + B_3\dot{\theta}_2^-}{C_3\dot{\theta}_2^- + D_3\dot{\theta}_1^+} \end{aligned} \tag{6}$$

where,

$$A_3 = -(I_{O_2} - 2m_2 b_2^2) \qquad B_3 = I_{O_2} + m_2 l h_2 \cos\beta + m_2 l b_2 \sin\beta$$

$$C_3 = m_2 b_2^2 \qquad D_3 = m_2 b_2 (l \sin\beta + b_2)$$

Note that this analysis is valid for the transition of pattern 4b to 1a, 4a or 3a.

Appendix II: New coefficients

Table 1 – Estimates of the regression coefficients and standard error components. Uniaxial case.

i	$\beta_{i,0}$	$\beta_{i,1}$	$\beta_{i,2}$	$\beta_{i,3}$	$\beta_{i,4}$	δ_i	σ_i
1	-1.621	-0.091	2.635	-0.958	-0.135	0.172	0.694
2	-6.399	-0.512	6.956	0.234	-0.421	0.575	0.496
3	-4.825	-0.318	-2.015	-0.158	0.100	0.245	0.614
4	2.395	-0.021	-2.015	-0.158	0.10	0.529	0.832
5	-2.298	0.011	2.168	0.054	0.062	0.221	0.541
6	-0.378	-0.421	1.021	-0.358	0.412	0.541	0.772

Table 2 – Sample correlation coefficients between the transformed model parameters of the horizontal ground motion component

	v_1	v_2	v_3	v_4	v_5	v_6
v_1	1	-0.21	0.04	-0.19	0.15	-0.03
v_2		1	0.67	0.09	0.12	-0.31
v_3			1	-0.31	-0.15	-0.29
v_4				1	-0.16	0.31
v_5					1	-0.03
v_6						1

Table 3 – Estimates of the regression coefficients and standard error components. Biaxial case.

i	$\beta_{i,0}$	$\beta_{i,1}$	$\beta_{i,2}$	$\beta_{i,3}$	$\beta_{i,4}$	δ_i	σ_i
1_{maj}	-1.621	0.091	2.935	-0.958	-0.135	0.171	0.714
1_{inter}	-2.399	-0.12	3.456	-1.234	-0.221	0.581	0.549
2	-5.625	-0.818	5.998	0.322	-0.455	0.657	0.356
3	-4.895	-0.231	4.415	0.458	-0.100	0.369	0.515
4	2.198	-0.051	-1.158	-0.254	0.062	0.418	0.621
5	-3.378	0.021	3.321	-0.058	-0.112	0.321	0.533
6	0.542	-0.584	0.198	-0.251	0.200	0.681	0.612

Table 4 – Sample correlation coefficients between the transformed model parameters of two horizontal ground motion component.

		Major component						Intermediate component					
		v_1	v_2	v_3	v_4	v_5	v_6	v_1	v_2	v_3	v_4	v_5	v_6
Major	v_1	1	-0.21	0.03	-0.23	0.27	-0.04	0.9	-0.32	-0.05	-0.13	0.07	0.05
	v_2		1	0.71	-0.09	-0.31	-0.24	-0.28	0.91	0.66	-0.22	-0.21	-0.2
	v_3			1	-0.27	-0.29	-0.23	0.08	0.75	0.84	-0.31	-0.35	-0.31
	v_4				1	-0.21	0.29	-0.18	-0.18	-0.21	0.92	-0.1	0.41
	v_5					1	-0.05	0.22	-0.24	-0.32	-0.15	0.46	-0.23
	v_6						1	-0.03	-0.21	-0.21	0.31	-0.06	0.69
Inter.	v_1							1	-0.39	0.01	-0.12	0.09	-0.01
	v_2								1	0.59	-0.3	-0.25	-0.19
	v_3									1	-0.33	-0.36	-0.32
	v_4										1	-0.21	0.31
	v_5											1	-0.02
	v_6												1

Appendix III: Predictive equations constants

Table 5 – Maximum estimates of the regression coefficients and standard error components for the uniaxial method.

$\mathbb{M}$	**M**	R_{rup}	V_s
$\kappa_{\mathbb{M},1}$	4.409	65.353	4.027x10ˆ3
$\kappa_{\mathbb{M},2}$	-4.813	25.918	-2.561x10ˆ3
$\kappa_{\mathbb{M},3}$	4.571	2.995	-912.316
$\kappa_{\mathbb{M},4}$	-2.967	2.377	193.324
$\kappa_{\mathbb{M},5}$	-8.303x10ˆ3	-0.120	-15.716
$\kappa_{\mathbb{M},6}$	-866.667	-1.349	171.170
$\kappa_{\mathbb{M},7}$	-1.061x10ˆ3	-4.712	187.732
$\kappa_{\mathbb{M},8}$	12.712	-123.342x10ˆ3	317.108
$\kappa_{\mathbb{M},9}$	890.150	-30.103x10ˆ3	307.429
$\kappa_{\mathbb{M},10}$	-1.755	-7.299x10ˆ3	36.871
$\kappa_{\mathbb{M},11}$	-625.452	-1155.396x10ˆ3	150.203x10ˆ3
$\kappa_{\mathbb{M},12}$	-55.583	912.959	-1.610
$\kappa_{\mathbb{M},13}$	58.272	-	-
$\kappa_{\mathbb{M},14}$	-500.518	-	-
$\kappa_{\mathbb{M},15}$	173.071	-	-
$\sigma_{\mathbb{M}}$	0.445	35.024	165.499
$\delta_{\mathbb{M}}$	0.076	5.496	11.490

Table 6 – Maximum estimates of the regression coefficients and standard error components for the biaxial method.

$\mathbb{M}$	**M**	R_{rup}	V_s
$\kappa_{\mathbb{M},1}$	2.646	67.814	2.480x10ˆ3
$\kappa_{\mathbb{M},2}$	-3.855	14.019	-2.889x10ˆ3
$\kappa_{\mathbb{M},3}$	4.875	1.079	-983.381
$\kappa_{\mathbb{M},4}$	-2.865	2.025	226.628
$\kappa_{\mathbb{M},5}$	-8.472x10ˆ3	-0.104	-15.820
$\kappa_{\mathbb{M},6}$	-704.148	-0.144	260.896
$\kappa_{\mathbb{M},7}$	-1.238x0ˆ3	-5.177	326.749
$\kappa_{\mathbb{M},8}$	-323.912	-1.319x10ˆ5	272.801
$\kappa_{\mathbb{M},9}$	951.943	-240.257	634.080
$\kappa_{\mathbb{M},10}$	-1.963	7.051x10ˆ3	-25.146
$\kappa_{\mathbb{M},11}$	-554.827	-3.003x10ˆ3	1.079x10ˆ-5
$\kappa_{\mathbb{M},12}$	-25.948	491.810	-1472
$\kappa_{\mathbb{M},13}$	51.702	-	-
$\kappa_{\mathbb{M},14}$	-584.546	-	-
$\kappa_{\mathbb{M},15}$	173.727	-	-
$\sigma_{\mathbb{M}}$	0.322	30.636	158.553
$\delta_{\mathbb{M}}$	0.129	17.088	58.110

Table 7 – Sample correlations between the error terms of the model parameters for the uniaxial case.

	M	R_{rup}	V_s
M	1	0.13	0.13
R_{rup}		1	0.06
V_s			1

Table 8 – Sample correlations between the error terms of the model parameters for the biaxial case.

	M	R_{rup}	V_s
M	1	0.13	0.17
R_{rup}		1	0.07
V_s			1

Bibliography

[1] G. W. Housner, "The behavior of inverted pendulum structures during earthquakes," *Bulletin of the Seismological Society of America*, vol. 53, pp. 403–417, 1963.

[2] F. Prieto and P. B. Lourenco, "On the rocking behavior of rigid objects," *Meccanica*, vol. 40, pp. 121–133, 2005.

[3] R. Plaut, W. Fielder, and L. Virgin, "Fractal behavior of an asymmetric rigid block overturning due to harmonic motion of a tilted foundation," *Chaos, Solitons & Fractals*, vol. 7, no. 2, pp. 177–196, 1996.

[4] Y. Ishiyama, "Motion of rigid bodies and criteria for overturning by earthquake excitations," *Journal of Earthquake Engineering and Structural Dynamics*, vol. 10, no. 10, pp. 635–650, 1982.

[5] H. Shenton and N. Jones, "Base excitation of rigid bodies. 1: Formulation," *Journal of Engineering Mechanics*, vol. 117, pp. 2286–2306, 1991.

[6] A. Pompei, A. Scalia, and M. A. Sumbatyan, "Dynamics of rigid block due to horizontal ground motion," *Journal of Engineering Mechanics*, vol. 124, pp. 713–717, 1998.

[7] P. Lipscombe and S. Pellegrino, "Free rocking of prismatic blocks," *Journal of engineering mechanics*, vol. 119, no. 7, pp. 1387–1410, 1993.

[8] I. N. Psycharis and P. C. Jennings, "Rocking of slender rigid bodies allowed to uplift," *Earthquake Eng Struct Dyn*, vol. 11, no. 11, pp. 57–76, 1983.

[9] P. D. Spanos and A. Koh, "Analysis of block random rocking," *Soil Dynamics and Earthquake Engineering*, vol. 5, pp. 178–183, 1986.

[10] A. Palmeri and N. Makris, "Response analysis of rigid structures rocking on viscoelastic foundation," *Earthquake Engineering and Structural Dynamics*, vol. 37, pp. 1039–1063, 2008.

[11] M. N. Chatzis and A. W. Smyth, "Robust modeling of the rocking problem," *Journal of Engineering Mechanics*, vol. 3, pp. 247–262, 2012.

[12] R. H. Allen, I. J. Oppenheim, A. R. Parker, and J. Bielak, "On the dynamic response of rigid body assemblies," *Earthquake Engineering & Structural Dynamics*, vol. 14, no. 6, pp. 861–876, 1986.

[13] P. D. Spanos, P. C. Roussis, and N. P. Politis, "Dynamic analysis of stacked rigid blocks," *Soil Dynamics and Earthquake Engineering*, vol. 21, no. 7, pp. 559 – 578, 2001.

[14] G. J. Kounadis, A. N. Papadopoulos and M. Cotsovos, "Overturning instability of a two-rigid block system under ground excitation," *Math. Mech.*, vol. 92, no. 9, pp. 536557,, 2012.

[15] N. Makris and M. F. Vassiliou, "Are some top-heavy structures more stable?," *Journal of Structural Engineering*, vol. 140, no. 5, p. 06014001, 2014.

[16] L. Papaloizou and K. Komodromos, "Planar investigation of the seismic response of ancient columns and colonnadeswith epistyles using a custom-made software.," *Soil Dynamics and Earthquake Engineering*, vol. 29, no. 11-12, pp. 1437–1454, 2009.

[17] D. Zulli, A. Contento, and A. D. Egidio, "3d model of rigid block with a rectangular base subject to pulse-type excitation," *International Journal of Non-Linear Mechanics*, vol. 47, no. 6, pp. 679 – 687, 2012.

[18] M. N. Chatzis and A. W. Smyth, "Modeling of the 3d rocking problem," *International Journal of Non-Linear Mechanics*, vol. 47, pp. 85–98, 2012.

[19] D. Kalliontzis, S. Sritharan, and A. Schultz, "Improved coefficient of restitution estimation for free rocking members," *Journal of Structural Engineering*, vol. 142, no. 12, p. 06016002, 2016.

[20] H. Zhang, B. Brogliato, and C. Liu, "Study of the planar rocking-block dynamics with coulomb friction: Critical kinetic angles," *Journal of Computational and Nonlinear Dynamics*, vol. 8', July 2012.

[21] C.-S. Yim, A. K. Chopra, and J. Penzien, "Rocking response of rigid blocks to earthquakes," *Earthquake Engineering & Structural Dynamics*, vol. 8, no. 6, pp. 565–587, 1980.

[22] E. G. Dimitrakopoulos and M. J. DeJong, "Revisiting the rocking block: closed-form solutions and similarity laws," *Proceedings of the Royal Society of London A: Mathematical, Physical and Engineering Sciences*, 2012.

[23] E. Voyagaki, I. Psycharis, and G. Mylonakis, "Complex response of a rocking block to a full-cycle pulse," *Journal of Engineering Mechanics*, vol. 140, no. 6, p. 04014024, 2014.

[24] M. A. ElGawady, Q. Ma, J. W. Butterworth, and J. Ingham, "Effects of interface material on the performance of free rocking blocks," *Earthquake Engineering & Structural Dynamics*, vol. 40, no. 4, pp. 375–392, 2011.

[25] R. L. Nigbor, S. Masri, and M. Agbabian, "Seismic vulnerability of small rigid objects.," in *Proceedings of the 5th U.S. natural Conference of Earthquake Engineering,*, no. 725-734, 1994.

[26] J. Zhang and N. Makris, "Rocking response of free-standing blocks under cycloidal pulses.," *Journal of Engineering Mechanics*, vol. 127, no. 5, pp. 473–483, 2001.

[27] J. Baker, "Conditional mean spectrum: Tool for ground motion selection.," *Journal of Engineering Mechanics*, vol. 7, no. 2, pp. 177–196, 2011.

[28] C. Haselton, A. Whittaker, A. Hortacsu, J. Baker, J. Bray, and D. Grant, "Selecting and scaling earthquake ground motions for performing response-history analyses," in *Proceedings of the 15th World Conference on Earthquake Engineering*, 2012.

[29] N. Jayaram, T. Lin, and J. W. Baker, "A computationally efficient ground-motion selection algorithm for matching a target response spectrum mean and variance," *Earthquake Spectra*, vol. 27, no. 3, pp. 797–815, 2011.

[30] M. D. Shields, *Simulation of stochastic processes: Applications in civil engineering.* Columbia University, 2010.

[31] R. W. Clough and J. Penzien, *Dynamics of Structures.* Mcgraw-Hill, 1975.

[32] M. Shinozuka and G. Deodatis, "Simulation of stochastic processes by spectral representation," *American Society of Mechanical Engineering*, vol. 44, no. 4, pp. 191–204, 1991.

[33] P. Jennings, G. W. Housner, and N. C. Tsai, *Simulated Earthquake Motions.* 1968.

[34] S. Rezaeian and A. Der Kiureghian, "A stochastic ground motion model with separable temporal and spectral nonstationarities," *Earthquake Engineering & Structural Dynamics*, vol. 37, no. 13, pp. 1565–1584, 2008.

[35] D. Gasparini and E. H. Vanmarcke, *Simulated earthquake motions compatible with prescribed response spectra.* Massachusetts Institute of Technology. Department of Civil Engineering. Constructed Facilities Division: Natural Science Foundation (U.S). Division of Advanced Environmental Research and Technology., 1976.

[36] P. Cacciola and G. Deodatis, "A method for generating fully non-stationary and spectrum-compatible ground motion vector processes," *Soil Dynamics and Earthquake Engineering*, vol. 31, no. 3, pp. 351–360, 2011.

[37] K. Aki, "Scaling law of seismic spectrum," *Journal of Geophysics*, vol. 72, pp. 1217–1231, 1697.

[38] J. N. Brune, "Tectonic stress and the spectra of seismic shear waves from earthquakes," *Journal of geophysical research*, vol. 75, no. 26, pp. 4997–5009, 1970.

[39] H. Miyake, T. Iwata, and K. Irikura, "Source characterization for broadband ground-motion simulation: Kinematic heterogeneous source model and strong motion generation area," *Bulletin of the Seismological Society of America*, vol. 93, no. 6, pp. 2531–2545, 2003.

[40] J. Ruiz, D. Baumont, P. Bernard, and C. Berge-Thierry, "New approach in the kinematic k- 2 source model for generating physical slip velocity functions," *Geophysical Journal International*, vol. 171, no. 2, pp. 739–754, 2007.

[41] G. P. Mavroeidis and A. S. Papageorgiou, "A mathematical representation of near-fault ground motions," *Bulletin of the Seismological Society of America*, vol. 93, no. 3, pp. 1099–1131, 2003.

[42] H. Aochi and E. Fukuyama, "Three-dimensional nonplanar simulation of the 1992 landers earthquake," *Journal of Geophysical Research: Solid Earth*, vol. 107, no. B2, 2002.

[43] K. Olsen, R. Madariaga, and R. Archuleta, "Three-dimensional dynamic simulation of the 1992 landers earthquake," *Science*, vol. 278, no. 5339, pp. 834–838, 1997.

[44] S. Rezaeian and A. Der Kiureghian, "Simulation of synthetic ground motions for specified earthquake and site characteristics," *Earthquake Engineering & Structural Dynamics*, vol. 39, no. 10, pp. 1155–1180, 2010.

[45] G. Pousse, L. F. Bonilla, F. Cotton, and L. Margerin, "Nonstationary stochastic simulation of strong ground motion time histories including natural variability: Application to the k-net japanese database," *Bulletin of the Seismological Society of America*, vol. 96, no. 6, pp. 2103–2117, 2006.

[46] F. Sabetta and A. Pugliese, "Estimation of response spectra and simulation of nonstationary earthquake ground motions," *Bulletin of the Seismological Society of America*, vol. 86, no. 2, pp. 337–352, 1996.

[47] C. Vlachos, K. G. Papakonstantinou, and G. Deodatis, "A multi-modal analytical nonstationary spectral model for characterization and stochastic simulation of earthquake ground motions," *Soil Dynamics and Earthquake Engineering*, vol. 80, pp. 177–191, 2016.

[48] J. Alamilla, L. Esteva, J. Garcia-Perez, and O. Diaz-Lopez, "Evolutionary properties of stochastic models of earthquake accelerograms: Their dependence on magnitude and distance," *Journal of seismology*, vol. 5, no. 1, pp. 1–21, 2001.

[49] I. Zentner and F. Poirion, "Enrichment of seismic ground motion databases using karhunenlove expansion," *Earthquake Engineering & Structural Dynamics*, vol. 41, no. 14, pp. 1945–1957, 2012.

[50] A. W. Smyth and S. F. Masri, "The robustness of an efficient probabilistic data-based tool for simulating the non-stationary response of non-linear systems," *International Journal of Non-Linear Mechanics*, vol. 39, no. 9, pp. 1453–1461, 2004.

[51] A. Olivier and A. W. Smyth, "Trade offs between statistical agreement and data reproduction in the generation of synthetic ground motions," *Probabilistic Engineering Mechanics*, vol. 43, pp. 36–49, 2016.

[52] M. W. J. Penzien, "Characteristics of 3-dimensional earthquake ground motions," *Earthquake Engineering & Structural Dynamics*, vol. 13, pp. 1–12, 1975.

[53] N. Abrahamson, G. Atkinson, D. Boore, Y. Bozorgnia, K. Campbell, B. Chiou, I. Idriss, W. Silva, and R. Youngs, "Comparisons of the nga ground-motion relations," *Earthquake Spectra*, vol. 24, no. 1, pp. 45–66, 2008.

[54] *Eurocode 8, Design of Structures for Earthquake Resistance*. London: British Standars Institutions, 2005.

[55] FEMA, *Document Control Procedures Manual*. September 2006.

[56] S. Rezaeian and A. Der Kiureghian, "Simulation of orthogonal horizontal ground motion components for specified earthquake and site characteristics," *Earthquake Engineering & Structural Dynamics*, vol. 41, no. 2, pp. 335–353, 2012.

[57] M. N. Chatzis, M. Garcia-Espinosa, and A. W. Smyth, "Examining the energy loss in the inverted pendulum model for rocking bodies," *Engineering Mechanics*, 2016.

[58] L. Virgin, W. Fielder, and R. Plaut, "Transient motion and overturning of a rocking block on a seesawing foundation," *Journal of Sound and Vibration*, vol. 191, no. 1, pp. 177 – 187, 1996.

[59] A. Chatterjee and A. Ruina, "A new algebraic rigid-body collision law based on impulse space considerations," *Journal of Applied Mechanics*, vol. 65, no. 4, pp. 939–951, 1998.

[60] J. Dormand and P. Prince, "A family of embedded runge-kutta formulae," *Journal of Computational and Applied Mathematics*, vol. 6, no. 1, pp. 19 – 26, 1980.

[61] L. F. Shampine and M. K. Gordon, *Computer solution of ordinary differential equations: the initial value problem*. WH Freeman San Francisco, 1975.

[62] P. Bogacki and L. F. Shampine, "A 3 (2) pair of runge-kutta formulas," *Applied Mathematics Letters*, vol. 2, no. 4, pp. 321–325, 1989.

[63] C. Robert, "Simulation of truncated normal random variables," *Statistics and Computing*, vol. 5, pp. 121–125, 1995.

[64] S. C.-S. Yim and A. K. Chopra, "Dynamics of structures on two-spring foundation allowed to uplift," *Journal of the Engineering Mechanics Division*, vol. 110, no. EM7, pp. 1124–1146, 1984.

[65] U. Andreaus and P. Casini, "On the rocking-uplifting motion of a rigid block in free and forced motion: influence of sliding and bouncing," *Acta Mechanica*, vol. 138, pp. 219–241, 1999.

[66] P. D. Spanos, A. Di Matteo, A. Pirrotta, and M. Di Paola, "Rocking of rigid block on nonlinear flexible foundation," *International Journal of Non-Linear Mechanics*, 2017.

[67] H. P. Mouzakis, I. N. Psycharis, D. Y. Papastamatiou, P. G. Carydis, C. Papantonopoulos, and C. Zambas, "Experimental investigation of the earthquake response of a model of a marble classical column," *Earthquake Engineering & Structural Dynamics*, vol. 31, pp. 1681–1698, 9 2002.

[68] A. Baratta, I. Corbi, and O. Corbi, "Towards a seismic worst scenario approach for rocking systems: analytical and experimental set-up for dynamic response," *Acta Mechanica*, vol. 224, no. 4, p. 691, 2013.

[69] Y. Chen, T. Larkin, and N. Chouw, "Experimental assessment of contact forces on a rigid base following footing uplift," *Earthquake Engineering & Structural Dynamics*, 2017.

[70] T. Taniguchi, "Experimental and analytical study of free lift-off motion induced slip behavior of rectangular rigid bodies," *TRANSACTIONS-AMERICAN SOCIETY OF*

MECHANICAL ENGINEERS JOURNAL OF PRESSURE VESSEL TECHNOLOGY, vol. 126, no. 1, pp. 53–58, 2004.

[71] C. Mathey, C. Feau, I. Politopoulos, D. Clair, L. Baillet, and M. Fogli, "Behavior of rigid blocks with geometrical defects under seismic motion: an experimental and numerical study," *Earthquake Engineering & Structural Dynamics*, vol. 45, no. 15, pp. 2455–2474, 2016. eqe.2773.

[72] R. J. Greenbaum, A. W. Smyth, and M. N. Chatzis, "Monocular computer vision method for the experimental study of three-dimensional rocking motion," *Journal of Engineering Mechanics*, vol. 142, no. 1, p. 04015062, 2015.

[73] M. A. ElGawady, Q. Ma, J. W. Butterworth, and J. Ingham, "Effects of interface material on the performance of free rocking blocks," *Earthquake Engineering & Structural Dynamics*, vol. 40, no. 4, pp. 375–392, 2011.

[74] D. Physics, "Signalstar engine simulator controller," 2016.

[75] M. A. C. A. Mota, *Shake table acceleration tracking performance impact on dynamic similitude*, vol. 73. 2011.

[76] T. L. Trombetti and J. P. Conte, "Shaking table dynamics: results from a test-analysis comparison study," *Journal of Earthquake Engineering*, vol. 6, no. 04, pp. 513–551, 2002.

[77] Sorbothane, "Sorbothane." `https://www.sorbothane.com/`. Accessed: 2017-08-28.

[78] A. V. Oppenheim, *Discrete-time signal processing*. Pearson Education India, 1999.

[79] J. M. Bernardo and A. F. Smith, "Bayesian theory," 2001.

[80] M. Chatzis, M. García Espinosa, C. Needham, and M. Williams, "Energy loss in sys-

tems of stacked rocking bodies," *Journal of Engineering Mechanics*, vol. 144, no. 7, p. 04018044, 2018.

[81] I. N. Psycharis, "Dynamic behaviour of rocking two-block assemblies," *Earthquake Engineering & Structural Dynamics*, vol. 19, no. 4, pp. 555–575, 1990.

[82] E. G. Dimitrakopoulos and A. I. Giouvanidis, "Seismic response analysis of the planar rocking frame," *Journal of Engineering Mechanics*, vol. 141, no. 7, p. 04015003, 2015.

[83] P. Harvey Jr, "Behavior of a rocking block resting on a rolling isolation system," *Journal of Engineering Mechanics*, vol. 143, no. 8, p. 04017045, 2017.

[84] M. F. Vassiliou and N. Makris, "Analysis of the rocking response of rigid blocks standing free on a seismically isolated base," *Earthquake Engineering & Structural Dynamics*, vol. 41, no. 2, pp. 177–196, 2012.

[85] M. N. Chatzis and A. W. Smyth, "The 3d dynamics of a rigid body with wheels on a moving base," *Journal of Engineering Mechanics*, vol. In Press, doi: 10.1061/(ASCE)EM.1943-7889.0000456, 2012.

[86] F. Nikfar and D. Konstantinidis, "Shake table investigation on the seismic performance of hospital equipment supported on wheels/casters," *Earthquake Engineering & Structural Dynamics*, vol. 46, no. 2, pp. 243–266, 2017.

[87] C. E. Wittich and T. C. Hutchinson, "Experimental modal analysis and seismic mitigation of statue-pedestal systems," *Journal of Cultural Heritage*, vol. 20, pp. 641–648, 2016.

[88] D. T. Greenwood, *Advanced dynamics*. Cambridge University Press, 2003.

[89] A. W. Smyth, P. Brewick, R. Greenbaum, M. Chatzis, A. Serotta, and I. Stünkel, "Vibration mitigation and monitoring: a case study of construction in a museum," *Journal of the American Institute for Conservation*, vol. 55, no. 1, pp. 32–55, 2016.

[90] P. R. Lipscombe and S. Pellegrino, "Free rocking of prismatic blocks," *Engineering Mechanics*, vol. 119, pp. 1387–1410, 1991.

[91] M. Chatzis and A. Smyth, "Preliminary investigation of the randrandom in the outcome of a die throw," *Proceedings ICOSSAR 2013 11th International Conference on Structural Safety and Reliability*, June 16-20, 2013, Columbia University, New York, NY, USA.

[92] M. Agbabian, F. Masri, R. Nigbor, and W. Ginel, "Seismic damage mitigation concepts for art objects in museum," in *Proceeding of ninth world conference on earthquake engineering*, 1988.

[93] G. Augusti, M. Ciampoli, and L. Airoldi, "Mitigation of seismic risk for museum contents: An introductory investigation," in *Proceedings of the 10th World Conference on Earthquake Engineering, Madrid, Spain*, pp. 19–24, 1992.

[94] C. C. Spyrakos, C. A. Maniatakis, and I. M. Taflampas, "Application of predictive models to assess failure of museum artifacts under seismic loads," *Journal of Cultural Heritage*, vol. 23, pp. 11–21, 2017.

[95] A. P. Johnson, W. Robert Hannen, and F. Zuccari, "Vibration control during museum construction projects," *Journal of the American Institute for Conservation*, vol. 52, no. 1, pp. 30–47, 2013.

[96] A. Zureick, "Vibration surround us: The science of music," December 1 2010.

[97] D. Lapp, "The physics of music and musical instruments," January 14 2002.

[98] J. O. Smith, *Physical audio signal processing: For virtual musical instruments and audio effects*. W3K Publishing, 2010.

[99] S. S. Rao and F. F. Yap, *Mechanical vibrations*, vol. 4. Prentice Hall Upper Saddle River, 2011.

[100] W. Smeby and A. Der Kiureghian, "Modal combination rules for multicomponent earthquake excitation," *Earthquake Engineering & Structural Dynamics*, vol. 13, no. 1, pp. 1–12, 1985.

[101] Cygres, "Cignus research international," 1992.

[102] K. Kanai, "An empirical formula for the spectrum of strong earthquake motions," *Bulletin of the earthquake research institute*, vol. 39, pp. 85–95, 1961.

[103] A. Zerva, *Spatial Variation of Seismic Ground Motions: Modeling and Engineering Applications*. Taylor & Francis, 2010.

[104] B. R. Ellingwood and M. E. Batts, "Characterization of earthquake forces for probability-based design of nuclear structures," tech. rep., National Bureau of Standards, Washington, DC (USA). Center for Building Technology, 1982.

[105] N. A. Kiureghian, A. D., "Response spectrum method for multi-support seismic excitations," *Earthquake Engineering & Structural Dynamics*, vol. 21, pp. 713–740, 1992.

[106] M. Grigoriu, "To scale or not to scale seismic ground-acceleration records," *Journal of engineering mechanics*, vol. 137, no. 4, pp. 284–293, 2010.

[107] J. Kaklamanos, D. M. Boore, E. M. Thompson, and K. W. Campbell, "Implementation of the next generation attenuation (nga) ground-motion prediction equations in fortran and r," *US Geological Survey Open-File Report*, vol. 1296, p. 47, 2010.

[108] K. W. Campbell and Y. Bozorgnia, "Nga ground motion model for the geometric mean horizontal component of pga, pgv, pgd and 5% damped linear elastic response spectra for periods ranging from 0.01to10s," *Earthquake Spectra*, vol. 24, no. 1, pp. 139–171, 2008.

[109] B. Gutenberg and C. F. Richter, "Earthquake magnitude, intensity, energy, and accel-

eration (second paper)," *Bulletin of the seismological society of America*, vol. 46, no. 2, pp. 105–145, 1956.

[110] I. Zentner and F. Poirion, "Non-gaussian non-stationary models for natural hazard modeling," *Applied Mathematical Modelling*, vol. 37, no. 8, pp. 5938 – 5950, 2013.

[111] S. Masri, A. Smyth, and M.-I. Traina, "Probabilistic representation and transmission of nonstationary processes in multi-degree-of-freedom systems," *Journal of Applied Mechanics*, vol. 65, no. 2, pp. 398–409, 1998.

[112] D. L. Shrestha, "emprand." https://sites.google.com/site/durgalalshrestha/tools/matlab-tools/erand, October 2007.

[113] S. F. M. Lambert M. Surhone, Miriam T. Timpledon, *Rejection Sampling*. 2010.

[114] M. Garcia-Espinosa and M. Chatzis, "A preliminary investigation of methods for generating fragility curves for rocking bodies," *16th World Conference on Earthquake, 16WCEE*, no. 3778, 2017.

[115] P. E. E. R. Center, "Nga west."

[116] P. Tothong, C. A. Cornell, and J. Baker, "Explicit directivity-pulse inclusion in probabilistic seismic hazard analysis," *Earthquake Spectra*, vol. 23, no. 4, pp. 867–891, 2007.

[117] W. Dumouchel and F. O'Brien, "Integrating a robust option into a multiple regression computing environment," in *Computing and graphics in statistics*, pp. 41–48, Springer-Verlag New York, Inc., 1992.

[118] C. G. Robert, C.P., *Monte Carlo Statistical Methods*. Springer, Berlin, 2004.

[119] S. Wright, "An analysis of variability in number of digits in an inbred strain of guinea pigs," *Genetics*, vol. 19, no. 6, p. 506, 1934.

[120] G. Casella, C. P. Robert, and M. T. Wells, *Generalized Accept-Reject sampling schemes*, vol. Volume 45 of *Lecture Notes–Monograph Series*, pp. 342–347. Beachwood, Ohio, USA: Institute of Mathematical Statistics, 2004.

[121] J. F. Claerbout, *Fundamentals of geophysical data processing.* Citeseer, 1985.

[122] M. D. Purvance, A. Anooshehpoor, and J. N. Brune, "Freestanding block overturning fragilities: Numerical simulation and experimental validation," *Earthquake Engineering & Structural Dynamics*, vol. 37, no. 5, pp. 791–808, 2008.

[123] D. M. Boore, "Stochastic simulation of high-frequency ground motions based on seismological models of the radiated spectra," *Bulletin of the Seismological Society of America*, vol. 73, no. 6A, pp. 1865–1894, 1983.

[124] E. G. Dimitrakopoulos and T. S. Paraskeva, "Dimensionless fragility curves for rocking response to near-fault excitations," *Earthquake Engineering & Structural Dynamics*, vol. 44, no. 12, pp. 2015–2033, 2015. eqe.2571.

[125] S. Acikgoz and M. J. DeJong, "The rocking response of large flexible structures to earthquakes," *Bulletin of Earthquake Engineering*, vol. 12, no. 2, pp. 875–908, 2014.

[126] A. Cornell C., "Engineering seismic risk analysis," *Bulletin of the S*, vol. 58, no. 5, pp. 1583–1606, 1968.

[127] P. M. Herrera Suarex and A. J. Alfaro Castillo, "Caracterizacion sismica de fallas colombinas por analogia con fallas conocidas geologica y sismologicamente," *Revista de la Escuela Colombiana de Ingenieria*, vol. 95, pp. 37–46, Julio-Septiembre 2014.

[128] L. Esteva and E. Rosenblueth, "Spectra of earthquakes at moderate and large distances," *Soc. Mex. de Ing. Sismica, Mexico II*, pp. 1–18, 1964.

[129] L. Esteva, "Criteria for the construction of spectra for seismic design," in *Third Panamerican Symposium on Structures*, (Caracas, Venezuela), 1967.

[130] A. A. Munjiza, *The combined finite-discrete element method*. John Wiley & Sons, 2004.

[131] B. Sudret, "Polynomial chaos expansions and stochastic finite element methods," *Risk and reliability in geotechnical engineering*, pp. 265–300, 2015.

[132] P. Kersaudy, B. Sudret, N. Varsier, O. Picon, and J. Wiart, "A new surrogate modeling technique combining kriging and polynomial chaos expansions–application to uncertainty analysis in computational dosimetry," *Journal of Computational Physics*, vol. 286, pp. 103–117, 2015.

[133] S. Das, R. Ghanem, and S. Finette, "Polynomial chaos representation of spatio-temporal random fields from experimental measurements," *Journal of Computational Physics*, vol. 228, no. 23, pp. 8726–8751, 2009.